

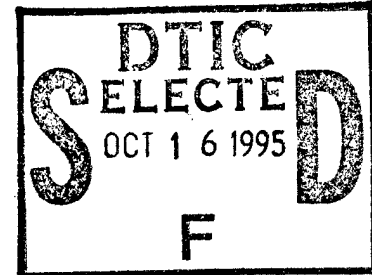
WL-TR-95-4078



**FATIGUE CRACK GROWTH BEHAVIOR OF A TITANIUM MATRIX COMPOSITE  
UNDER THERMOMECHANICAL LOADING**

A Thesis Submitted to the Facility of Purdue University  
in Partial Fulfillment of the Requirements for the Degree  
of Doctor of Philosophy

Paul Andrew Blatt



December 1993

Approved for public release; distribution is unlimited.

19951012 080

MATERIALS DIRECTORATE  
WRIGHT LABORATORY  
AIR FORCE MATERIEL COMMAND  
WRIGHT-PATTERSON AFB OH 45433-7734

DTIC QUALITY INSPECTED 6

## NOTICE

WHEN GOVERNMENT DRAWINGS, SPECIFICATIONS, OR OTHER DATA ARE USED FOR ANY PURPOSE OTHER THAN IN CONNECTION WITH A DEFINITELY GOVERNMENT-RELATED PROCUREMENT, THE UNITED STATES GOVERNMENT INCURS NO RESPONSIBILITY OR ANY OBLIGATION WHATSOEVER. THE FACT THAT THE GOVERNMENT MAY HAVE FORMULATED OR IN ANY WAY SUPPLIED THE SAID DRAWINGS, SPECIFICATIONS, OR OTHER DATA, IS NOT TO BE REGARDED BY IMPLICATION OR OTHERWISE IN ANY MANNER CONSTRUED, AS LICENSING THE HOLDER OR ANY OTHER PERSON OR CORPORATION, OR AS CONVEYING ANY RIGHTS OR PERMISSION TO MANUFACTURE, USE, OR SELL ANY PATENTED INVENTION THAT MAY IN ANY WAY BE RELATED THERETO.

THIS REPORT IS RELEASABLE TO THE NATIONAL TECHNICAL INFORMATION SERVICE (NTIS). AT NTIS, IT WILL BE AVAILABLE TO THE GENERAL PUBLIC, INCLUDING FOREIGN NATIONS.

THIS TECHNICAL REPORT HAS BEEN REVIEWED AND IS APPROVED FOR PUBLICATION.

P. Andrew Blatt  
PAUL ANDREW BLATT  
Materials Behavior Branch  
Metals and Ceramics Division

Allan W. Gunderson  
ALLAN W. GUNDERSON, Chief  
Materials Behavior Branch  
Metals and Ceramics Division

Walter M. Griffith  
WALTER M. GRIFFITH, Asst. Chief  
Metals and Ceramics Division  
Materials Directorate

IF YOUR ADDRESS HAS CHANGED, IF YOU WISH TO BE REMOVED FROM OUR MAILING LIST, OR IF THE ADDRESSEE IS NO LONGER EMPLOYED BY YOUR ORGANIZATION, PLEASE NOTIFY, WL/MLLN, WRIGHT-PATTERSON AFB OH 45433-7817 TO HELP US MAINTAIN A CURRENT MAILING LIST.

COPIES OF THIS REPORT SHOULD NOT BE RETURNED UNLESS RETURN IS REQUIRED BY SECURITY CONSIDERATIONS, CONTRACTUAL OBLIGATIONS, OR NOTICE ON A SPECIFIC DOCUMENT.

# **DISCLAIMER NOTICE**



**THIS DOCUMENT IS BEST  
QUALITY AVAILABLE. THE  
COPY FURNISHED TO DTIC  
CONTAINED A SIGNIFICANT  
NUMBER OF PAGES WHICH DO  
NOT REPRODUCE LEGIBLY.**

## REPORT DOCUMENTATION PAGE

FORM APPROVED  
OMB NO. 0704-0188

Public reporting burden for this collection of information is estimated to average 1 hour per response, including the time for reviewing instructions, searching existing data sources, gathering and maintaining the data needed, and completing and reviewing the collection of information. Send comments regarding this burden estimate or any other aspect of this collection of information, including suggestions for reducing this burden, to Washington Headquarters Services, Directorate for Information Operations and Reports, 1215 Jefferson Davis Highway, Suite 1204, Arlington, VA 22202-4302 and to the Office of Management and Budget, Paperwork Reduction Project (0704-0188), Washington, DC 20503.

1. AGENCY USE ONLY (Leave blank)			2. REPORT DATE December 1993	3. REPORT TYPE AND DATES COVERED Thesis for December 1993
4. TITLE AND SUBTITLE  Fatigue Crack Growth Behavior of a Titanium Matrix Composite Under Thermomechanical Loading			5. FUNDING NUMBERS  C - N/A PE - 61102F PR - 2302 TA - P1 WU - 01	
6. AUTHOR(S)  Paul Andrew Blatt			8. PERFORMING ORGANIZATION REPORT NUMBER	
7. PERFORMING ORGANIZATION NAMES(ES) AND ADDRESS(ES)  Wright Laboratory/Materials Behavior Branch (WL/MLLN) Materials Directorate WPAFB OH 45433-7817			10. SPONSORING/MONITORING AGENCY REPORT NUMBER  WL-TR-95-4078	
9. SPONSORING/MONITORING AGENCY NAMES(ES) AND ADDRESS(ES)  Materials Directorate Wright Laboratory Air Force Materiel Command Wright-Patterson AFB OH 45433-7734				
11. SUPPLEMENTARY NOTES  N/A				
12a. DISTRIBUTION/AVAILABILITY STATEMENT  Approved for public release; distribution is unlimited.			12b. DISTRIBUTION CODE  A	
13. ABSTRACT (Maximum 200 words)  The crack growth characteristics of a 4-ply, unidirectional, titanium matrix composite, SCS-6/Ti-6Al-2Sn-4Zr-2Mo, subjected to thermomechanical fatigue were investigated. A linear summation model was developed to predict the isothermal and thermomechanical fatigue (TMF) crack growth rates of the composite. The linear summation approach assumes the total fatigue crack growth rate is a combination of a cycle-dependent and a time-dependent component. To assist the modeling effort, a series of isothermal, in-phase, and out-of-phase crack growth test were conducted. The test temperatures ranged from 150°C to 538°C and the fastest thermal frequency was 0.0083 Hz. With the exception of the 150°C isothermal test, the model was able to correlate all the baseline fatigue crack growth test data between $\Delta K$ of 50 to 90MPa. In addition, the model was able to predict the fatigue crack growth rate of a proof test which involved a continual change in temperature range and load range to produce a constant crack growth rate. The proof test began under isothermal conditions at the maximum temperature and ended under in-phase TMF conditions.				
14. SUBJECT TERMS  Thermomechanical fatigue, fatigue crack growth, linear summation model, time-dependent, cycle-dependent, SCS-6/Ti-6Al-2Sn-4Zr-2Mo, metal matrix composite			15. NUMBER OF PAGES 237	16. PRICE CODE
17. SECURITY CLASSIFICATION OF REPORT Unclassified	18. SECURITY CLASSIFICATION OF THIS PAGE Unclassified	19. SECURITY CLASSIFICATION OF ABSTRACT Unclassified	20. LIMITATION OF ABSTRACT Unlimited	

NSN 7540-01-280-5500

COMPUTER GENERATED

STANDARD FORM 298 (Rev. 2-89)  
Prescribed by ANSI Std. Z39-18  
298-102

## ACKNOWLEDGEMENTS

This project was completed under the auspices of the Senior Knight Program sponsored by the United States Air Force. All laboratory work was performed in the Materials Directorate, Materials Behavior Branch, at Wright-Patterson Air Force Base, Ohio. All course work was completed at Purdue University, West Lafayette, Indiana.

I would like to especially thank Professor A.F. Grandt, Jr. for serving as the chair of my thesis committee and for encouraging me to pursue the Senior Knight Program to fund my Ph.D. research. Thanks also goes to my three other committee members: Professors B.M. Hillberry, C.T. Sun, T.N. Farris. Their insightful comments and questions helped direct my research to its successful end. I would also like to thank Dr. Ted Nicholas, also on my committee, and Dr. Jim Larsen, my Senior Knight mentor, for their input to my project; my numerous questions were always followed by a lengthy discussion and often an answer.

Several others are now recognized for their unselfish giving of time and effort in order that this project be completed successfully: the entire University of Dayton Research Institute technical staff, especially George Hartman, for developing the software to simplify and automate the test procedure; and all the other research engineers at the Materials Behavior Branch. Captain John Pernot is also especially thanked for the many hours he spent explaining the finer points of his TMF crack growth model.

Availability Codes	
Dist	Avail and/or Special
A-1	

## TABLE OF CONTENTS

	Page
<b>LIST OF TABLES.....</b>	<b>vi</b>
<b>LIST OF FIGURES.....</b>	<b>vii</b>
<b>ABSTRACT .....</b>	<b>xiii</b>
<b>CHAPTER 1 - INTRODUCTION .....</b>	<b>1</b>
<b>CHAPTER 2 - BACKGROUND .....</b>	<b>7</b>
<b>2.1 Definition of Terms.....</b>	<b>7</b>
2.1.1 Thermal and Mechanical Cycling Terminology .....	7
2.1.2 Crack Growth Rate Terminology.....	9
2.1.3 Composite Material Fabrication Techniques .....	11
2.1.4 Coefficient of Thermal Expansion .....	12
<b>2.2 Crack Bridging.....</b>	<b>13</b>
<b>2.3 Modeling of Thermomechanical Fatigue Crack Growth.....</b>	<b>16</b>
<b>2.4 Historical Development of Monolithic Ti-6Al-2Sn-4Zr-2Mo .....</b>	<b>21</b>
<b>CHAPTER 3 - EXPERIMENTAL SET-UP AND TEST PROCEDURE.....</b>	<b>28</b>
<b>3.1 Material .....</b>	<b>28</b>
<b>3.2 Specimen Description .....</b>	<b>29</b>
<b>3.3 Test Apparatus .....</b>	<b>30</b>
3.3.1 Mechanical Loading Description.....	31
3.3.2 Heating and Cooling System.....	33
3.3.3 Crack Length Measurement.....	36
<b>CHAPTER 4 - INITIAL CHARACTERIZATION OF THE SCS-6/Ti-6Al-2Sn-4Zr-2Mo .....</b>	<b>52</b>
<b>4.1 Specimen Identification.....</b>	<b>52</b>
<b>4.2 Nondestructive Evaluation .....</b>	<b>53</b>
4.2.1 Ultrasonic C-scan .....	53
4.2.2 Radiographs.....	54
<b>4.3 Metallographic Analysis .....</b>	<b>54</b>

	Page
4.4 Monotonic Material Properties .....	55
4.4.1 Tension Tests.....	55
4.4.2 Modulus and CTE as a Function of Temperature.....	56
CHAPTER 5 - A SYSTEMATIC CHECK OF MATERIAL QUALITY.....	65
5.1 Material Evaluated.....	66
5.2 Nondestructive Evaluation .....	66
5.2.1 Ultrasonic C-scans .....	67
5.2.2 Radiographs.....	69
5.3 Tension Tests .....	69
5.4 Metallographic Analysis .....	70
5.5 Summary of Findings.....	72
CHAPTER 6 - DEVELOPMENT OF A NEW STRESS INTENSITY FACTOR SOLUTION .....	80
6.1 Available LEFM Solutions.....	81
6.2 Finite Element Analysis .....	83
6.3 Experimental Validation .....	86
6.3.1 Material and Test Specifications .....	87
6.3.2 Validation of Compliance Solution .....	88
6.3.3 Validation of K Solution.....	89
6.4 Discussion of Findings.....	89
CHAPTER 7 - RESULTS AND DISCUSSION OF FATIGUE CRACK GROWTH TESTS.....	103
7.1 Summary of Tests Performed.....	103
7.2 Fatigue Crack Growth Data of SCS-6/Ti-6Al-2Sn-4Zr-2Mo .....	104
7.2.1 Reduction of Crack Length-Cycle Data.....	105
7.2.2 Isothermal Fatigue Crack Growth Data .....	107
7.2.3 Thermomechanical Fatigue Crack Growth Data .....	111
7.3 Additional Crack Growth Tests.....	112
7.3.1 Cyclic Temperatures and Static Loading.....	113
7.3.2 Correlation of Crack Growth Rates with $\Delta K_{app}$ .....	115
CHAPTER 8 - MODELING OF TMF CRACK GROWTH IN SCS-6/Ti-6Al-2Sn-4Zr-2Mo .....	134
8.1 Development of the TMF Model.....	134
8.2 Explanation of TMF Modeling Expressions .....	135
8.2.1 Determination of the Cycle-Dependent Term .....	136
8.2.2 Determination of the Time-Dependent Term.....	138
8.2.3 Accounting for Frequency .....	141
8.2.4 Final Form of the TMF Linear Summation Model.....	144

	Page
8.3 Crack Growth Rate Correlations and Predictions .....	145
8.3.1 Isothermal Crack Growth Correlations .....	145
8.3.2 TMF Crack Growth Correlations .....	146
8.4 Experimental Proof of Linear Summation Model.....	146
8.4.1 Designing the Proof Test.....	147
8.4.2 Experimental Results of Proof Test .....	150
8.5 Parametric Study of Model.....	152
8.6 Computer Code for Modeling TMF Crack Growth .....	155
CHAPTER 9 - CONCLUSIONS .....	171
LIST OF REFERENCES.....	175
APPENDICES	
Appendix A - Tabulated Data: Cycles, Crack Lengths, and Crack Growth Rates .....	183
Appendix B - Computer Code to Predict TMF Crack Growth Rates.....	196
VITA.....	223

## LIST OF TABLES

Table	Page
3.1 Actual chemical composition (weight %) of the titanium alloy matrix in the SCS-6/Ti-6Al-2Sn-4Zr-2Mo used for this research.....	41
4.1 Monotonic tensile data for SCS-6/Ti-6242 (batch three).....	58
4.2 Longitudinal modulus and CTE data as a function of temperature for panel G1, a 4-ply, unidirectional panel of SCS-6/Ti-6242 composite.....	58
4.3 Transverse modulus and CTE data as a function of temperature for panel G1, a 4-ply, unidirectional panel of SCS-6/Ti-6242 composite.....	58
5.1 Monotonic tensile data for Sigma/Ti-6Al-2Sn-4Zr-2Mo. ....	74
5.2 Monotonic tensile data for SCS-6/Ti-6242 (batch two).....	75
6.1 Geometry correction factors (F) and nondimensionalized CMOD for an SE(T) with clamped ends H/W = 4.0 .....	91
6.2 Coefficients used to define F(a/W), a/W(U) and U(a/W).....	91
7.1 Summary of tests performed on the SCS-6/Ti-6Al-2Sn-4Zr-2Mo in the order in which they were completed.....	117
7.2 Summary of baseline crack growth test conditions for the SCS-6/Ti-6Al-2Sn-4Zr-2Mo.....	117

## LIST OF FIGURES

Figure	Page
2.1 Diagram of mechanical and thermal cycles (a) in-phase and (b) out-of-phase by some angle $\phi$ .....	23
2.2 Typical sigmoidal crack growth rate curve.....	24
2.3 Illustration of simultaneous fiber and matrix crack growth.....	25
2.4 Illustration of the crack bridging phenomenon in fiber reinforced composite material systems. ....	25
2.5 Damage tolerant map illustrating relationship between failure characteristics of composites in relation to the matrix toughness and interface strength or interface toughness [8]. .....	26
2.6 Influences of interface properties on fatigue crack growth characteristics (a) strong interface, (b) weak interface, and (c) frictional interface and crack bridging [8]. .....	27
3.1 Location of single-edge notch specimens in typical plate (G9A) of SCS-6/Ti-6242 composite.....	42
3.2 Schematic of single-edge notch specimen and corresponding dimensions. ....	43
3.3 Schematic of center cracked specimen and corresponding dimensions. ....	44
3.4 Photograph of the horizontal servo-hydraulic test frame set-up.....	45
3.5 Representation of the rigid grip system. ....	46
3.6 Percent bending as a function of applied load, confirming load train alignment. ....	46

Figure	Page
3.7 Comparison of crack growth ( $da/dN$ ) versus applied stress intensity factor range ( $\Delta K$ ) response of Ti-1100 obtained using SE(T) and C(T) geometries.....	47
3.8 Typical experimental set-up for TMF crack growth test. Note position of thermocouples, cooling jets and optical inspection slot.....	48
3.9 A 3-view schematic of the cooling system used on the thermomechanical fatigue crack growth tests.....	49
3.10 Plot of cyclic temperature profile over single edge notch specimen for a single 120 second temperature cycle between 538 and 150 °C (1000-300 °F). ....	50
3.11 Set-up for visual inspection of crack propagation.....	51
4.1 Schematic of the ultrasonic system used to evaluate the material for this study as well as the material described in Chapter 5.....	59
4.2 Representative ultrasonic reflector-plate C-scan of panel G9A, a 4-ply, unidirectional panel of SCS-6/Ti-6Al-2Sn-4Zr-2Mo composite.....	60
4.3 Representative radiograph (x-ray) of panel G9A, a 4-ply, unidirectional panel of SCS-6/Ti-6Al-2Sn-4Zr-2Mo composite.....	60
4.4 Schematic explaining location and orientation of the three different planes on which photomicrographs can be taken.....	61
4.5 3-D representation of the SCS-6/Ti-6Al-2Sn-4Zr-2Mo microstructure used in this study. ....	61
4.6 Transverse photomicrograph showing complete consolidation of the matrix around the fiber for SCS-6/Ti-6Al-2Sn-4Zr-2Mo. ....	62
4.7 Elastic modulus as a function of temperature for the 4-ply unidirectional SCS-6/Ti-6Al-2Sn-4Zr-2Mo.....	63
4.8 Coefficient of thermal expansion as a function of temperature for the 4-ply unidirectional SCS-6/Ti-6Al-2Sn-4Zr-2Mo.....	64
5.1 Representative ultrasonic reflector-plate C-scan of the 4-ply, unidirectional panel of Sigma/Ti-6Al-2Sn-4Zr-2Mo composite.....	76

Figure	Page
5.2 Representative ultrasonic reflector-plate C-scan of the 4-ply, unidirectional panel of SCS-6/Ti-6Al-2Sn-4Zr-2Mo composite (batch two) .....	76
5.3 Representative radiograph (x-ray) of the 4-ply, unidirectional panel of Sigma/Ti-6Al-2Sn-4Zr-2Mo composite.....	77
5.4 Representative radiograph (x-ray) of the 4-ply, unidirectional panel of SCS-6/Ti-6Al-2Sn-4Zr-2Mo composite (batch two).....	77
5.5 Photomicrographs of the (a) transverse, (b) longitudinal and (c) plane cross section of the Sigma/Ti-6Al-2Sn-4Zr-2Mo composite. ....	78
5.6 Photomicrograph of the transverse cross section of the SCS-6/Ti-6Al-2Sn-4Zr-2Mo composite (batch two).....	78
5.7 Photomicrograph of the longitudinal cross section of the SCS-6/Ti-6Al-2Sn-4Zr-2Mo composite (batch two).....	79
6.1 Schematic of SE(T) specimen with appropriate boundary conditions used for the finite element analysis.....	92
6.2 Geometry correction factor for a tension loaded SE(T) geometry with different boundary conditions and height-to-width ratios. ....	93
6.3 Effect of H/W on the ratio of geometry correction factors for a clamped SE(T) to a pin-loaded SE(T). ....	94
6.4 (a) Typical half-body finite element mesh ( $a/W = 0.5$ ) and (b) close-up view near the crack tip. ....	95
6.5 Nondimensional crack length as a function of the compliance. ....	96
6.6 Comparison of compliance crack length with optical measurements over the life of the Ti-1100 specimen.....	97
6.7 Comparison of compliance crack length with optical measurements over the life of the SCS-6/Ti-24Al-11Nb specimen.....	98
6.8 Correlation of compliance crack length with optically measured crack length. ....	99
6.9 Room temperature crack growth rate as a function of applied stress intensity factor range for Ti-1100 and SCS-6/Ti-24Al-11Nb. ....	100

Figure	Page
6.10 Comparison fatigue crack growth rate data obtained using the SE(T) and C(T) geometries for Ti-1100.....	101
6.11 Comparison fatigue crack growth rate data obtained using the SE(T) and C(T) geometries for SCS-6/Ti-24Al-11Nb.....	102
7.1 Crack length from DCEP and optical measurements as a function of applied cycles for specimen G9A-2-FCG.....	118
7.2 Crack length from DCEP and optical measurements as a function of applied cycles for specimen G8A-1-FCG.....	119
7.3 Crack length from DCEP and optical measurements as a function of applied cycles for specimen G9A-3-FCG.....	120
7.4 Crack length from DCEP and optical measurements as a function of applied cycles for specimen G9A-4-FCG.....	121
7.5 Crack length from DCEP and optical measurements as a function of applied cycles for specimen G8A-2-FCG.....	122
7.6 Crack length from DCEP and optical measurements as a function of applied cycles for specimen G8A-3-FCG.....	123
7.7 Crack length from DCEP and optical measurements as a function of applied cycles for specimen G8A-4-FCG.....	124
7.8 Crack length from DCEP and optical measurements as a function of applied cycles for specimen G8A-5-FCG.....	125
7.9 Crack length from DCEP and optical measurements as a function of applied cycles for specimen G7A-4-FCG.....	126
7.10 Fatigue crack growth data for SCS-6/Ti-6Al-2Sn-4Zr-2Mo at 150 and 538 °C and v = 0.0083 Hz.....	127
7.11 Comparison of fatigue crack growth data for SCS-6/Ti-6Al-2Sn-4Zr-2Mo generated at 538 °C and v = 0.0083 Hz and 0.83 Hz .....	128
7.12 Comparison of in-phase thermomechanical fatigue crack growth data for SCS-6/Ti-6Al-2Sn-4Zr-2Mo cycled between 150 and 538 °C at 0.0083 Hz and 0.00083 Hz.....	129
7.13 Comparison of out-of-phase thermomechanical fatigue crack growth data for SCS-6/Ti-6Al-2Sn-4Zr-2Mo cycled between 150 and 538 °C at 0.0083 Hz and 0.00083 Hz.....	130

Figure	Page
7.14 Comparison of in-phase and out-of-phase thermomechanical fatigue crack growth data for SCS-6/Ti-6Al-2Sn-4Zr-2Mo cycled between 150 and 538 °C at 0.0083 Hz.....	131
7.15 Comparison of in-phase and out-of-phase thermomechanical fatigue crack growth data for SCS-6/Ti-6Al-2Sn-4Zr-2Mo cycled between 150 and 538 °C at 0.00083 Hz.....	132
7.16 Comparison of SE(T) and M(T) geometries for out-of-phase thermomechanical fatigue crack growth data for SCS-6/Ti-6Al-2Sn-4Zr-2Mo cycled between 150 and 538 °C at 0.0083 Hz.....	133
8.1 Effect of varying $C_2$ in the Arrhenius function, f.....	157
8.2 Plot showing the accuracy of the correlation between the model and the SCS-6/Ti-6Al-2Sn-4Zr-2Mo fatigue crack growth data from the isothermal tests at 150 and 538 °C and 0.0083 Hz.....	158
8.3 Plot showing the accuracy of the correlation between the model and the SCS-6/Ti-6Al-2Sn-4Zr-2Mo fatigue crack growth data from the isothermal tests at 538 °C and 0.0083 Hz and 0.83 Hz.....	159
8.4 Plot showing the accuracy of the correlation between the model and the SCS-6/Ti-6Al-2Sn-4Zr-2Mo fatigue crack growth data from the in-phase tests at 0.0083 Hz and 0.00083 Hz.....	160
8.5 Plot showing the accuracy of the correlation between the model and the SCS-6/Ti-6Al-2Sn-4Zr-2Mo fatigue crack growth data from the out-of-phase tests at 0.0083 Hz and 0.00083 Hz.....	161
8.6 Influence of decreasing $T_{min}$ on the crack growth rates under constant $\Delta K_{app}$ conditions.....	162
8.7 Influence of decreasing $T_{min}$ on the crack growth behavior under constant crack growth rate conditions.....	163
8.8 Variation of $C^*$ as a function of the minimum cyclic temperature, $T_{min}$ .....	164
8.9 Experimental data verifying the minimum and maximum temperatures during the proof test followed the requested profiles.....	165
8.10 Experimental crack lengths from the proof test compared to the predicted values as a function of applied cycles.....	166

Figure	Page
8.11 Experimental crack growth rates from the proof test compared to the predicted values as a function of $\Delta K_{app}$ .....	167
8.12 Effect of load hold times at various frequencies on the fatigue crack growth rate of [0]4, SCS-6/Ti-6Al-2Sn-4Zr-2Mo.....	168
8.13 Effect of different isothermal temperatures at various frequencies on the fatigue crack growth rate of [0]4, SCS-6/Ti-6Al-2Sn-4Zr-2Mo. ....	169
8.14 Effect of varying $T_{min}$ at various frequencies on the in-phase fatigue crack growth rate of [0]4, SCS-6/Ti-6Al-2Sn-4Zr-2Mo. ....	170

## ABSTRACT

Blatt, Paul Andrew. Ph.D., Purdue University, December 1993. Fatigue Crack Growth Behavior of a Titanium Matrix Composite under Thermomechanical Loading. Major Professor: Dr. A.F. Grandt, Jr.

The fatigue crack growth characteristics of a 4-ply, unidirectional, titanium matrix composite, SCS-6/Ti-6Al-2Sn-4Zr-2Mo, subjected to thermomechanical loading was investigated. The majority of work conducted for this research project was of an experimental nature. A test frame was assembled to perform the fully-automated, computer-controlled thermomechanical fatigue crack growth tests. A series of isothermal, in-phase, and out-of-phase crack growth tests were run. The test temperatures ranged from 150 °C to 538 °C and the fastest thermal frequency was 0.0083 Hz. The baseline isothermal and TMF data suggested that the time-at-temperature and the maximum temperature experienced by the composite significantly influenced the fatigue crack growth rates. Isothermal conditions produced higher crack growth rates than either in-phase or out-of-phase conditions for equivalent mechanical frequencies. Fiber bridging during both the isothermal and TMF tests was limited to a region of approximately 2-3 fibers directly behind the advancing crack tip.

A linear summation approach was developed to model the effect of isothermal and thermomechanical cycling on the crack growth rates of the SCS-6/Ti-6Al-2Sn-4Zr-2Mo composite. The total fatigue crack growth rate was

decomposed into cycle-dependent and time-dependent components. The model was able to correlate all the baseline fatigue crack growth tests as well predict the fatigue crack growth rate of a test which began under isothermal conditions and ended under in-phase conditions.

## CHAPTER 1

### INTRODUCTION

Metal matrix composite (MMC) materials have been studied for over three decades. More recently, MMC have gained attention as promising material candidates for advanced high performance aerospace applications, like the Integrated High Performance Turbine Engine Technology Initiative (IHPTET) and the National Aero-Space Plane (NASP) program. The IHPTET program is a cooperative effort among the Air Force, Navy, Army, Defense Advanced Research Projects Agency (DARPA), National Aeronautics and Space Administration (NASA), and the turbine engine industry [1]. Its goal is to double turbine propulsion capability by the year 2000 using more efficient combustion and hotter flow paths [1, 2]. An equally ambitious program is NASP, which is jointly sponsored by the Department of Defense (Air Force, DARPA, and Navy) and NASA. The goal for NASP is the development a hypersonic vehicle able to take off from a runway and achieve earth orbit with a single stage, air-breathing propulsion system [1].

Both IHPTET and NASP require the development of high-temperature, lightweight materials in either a monolithic or thin-sheet composite form. These materials must possess good high temperature strength and creep resistance as well as sufficient ductility, fracture toughness, fatigue behavior and impact resistance at room temperature and, for hydrogen fueled

hypersonic vehicles, cryogenic temperatures [1]. For example, IHPTET requires a material capable of withstanding maximum temperatures of about 700 °C (1292 °F), while maintaining dimensional stability and mechanical strength [3, 4]. Only a few monolithic materials (titanium and titanium aluminide alloys) are practical candidates; however, even these few don't have sufficient strength and stiffness at elevated temperatures to satisfy the requirements of either IHPTET or NASP [4]. Metal matrix composites, however, using titanium alloys reinforced with silicon carbide fibers are excellent choices in these types of applications because they exhibit high modulus and high strength-to-weight ratio [3].

Although metal matrix composites were some of the earliest continuous fiber-reinforced composites studied, their use as production components has been limited. At one point the tubular struts on the United States space shuttle were the only production continuous fiber-reinforced metal matrix composite components in service [5]. Now other aerospace structures are being considered for metal matrix composite applications. The F-15 horizontal stabilator torque box, the F/A-18 landing gear and arresting hook, and components on the Advanced Tactical Fighter (ATF) are all structures being designed with MMC as a primary material [6].

One of the reasons that metal matrix composite materials have not been more widely used is the high cost of fibers and fabrication. Since these materials are inherently strong, cutting and drilling of these systems can be very expensive when compared to traditional metal shop operations [6]. Although MMC have much higher stiffness to weight ratios than conventional homogeneous structural metals and numerous other attractive properties, their cost could seldom be justified. Recently, certain research and development

projects, however, have embraced the use of metal matrix composites in order to complete their designed mission, accepting along the way the elevated cost.

In order that MMC be confidently utilized to their full potential, designers and engineers need a more thorough understanding of their behavioral characteristics. To accomplish this, experimental data and theoretical models must be generated to better clarify monotonic strength, fatigue behavior, fracture characteristics, environmental stability and durability of metal matrix composites. A difficulty in developing general models for all metal matrix systems is that each composite system can be significantly different. When different fibers are used with the identical matrix, strength and fatigue behavior can change dramatically. Likewise, as the matrix alloy material is altered from system to system (i.e. titanium matrix versus aluminum matrix) or through variations in the chemical composition, the behavior characteristics will change in a way that one model may not sufficiently predict the correct properties for all systems. For example, aluminum matrix composites strengthened by boron fibers (B/Al) develop fatigue cracks first in the matrix, while B/Ti and Al<sub>2</sub>O<sub>3</sub>/Al develop fatigue cracks in the fibers first indicating that each system has a lower fatigue strength in either the matrix or fiber [7].

The development of predictive models to accurately quantify the effect of thermal and mechanical loading on the metal matrix composites used for the IHPTET and NASP programs is mandatory. These applications will primarily use titanium matrix composites (TMC) reinforced with continuous silicon carbide fibers (e.g. SCS-6). Most early fatigue studies (1960's) of metal matrix composites, however, dealt with filamentary composites reinforced by steel, tungsten, beryllium, or molybdenum wires, with the matrix materials being Aluminum alloys and sometimes copper or silver [8]. As MMC progressed into

the early 70's, the combination of boron fibers with a 6061 aluminum matrix was considered to be the most advanced MMC [8]. During the 80's the systems being studied ranged from titanium, magnesium, nickel and aluminum alloys with various fiber reinforcements like tungsten, coated boron, alumina, silicon carbide, SCS-6, and Aramid fibers [8].

The past fatigue studies of MMC, regardless of the system investigated, discovered that there are four primary categories of failure mechanisms: (1) matrix dominated, (2) fiber dominated, (3) self-similar damage growth, and (4) fiber/matrix interfacial failure [9, 10]. A great deal of the MMC fatigue data base has been generated using the stress-life approach. This approach applies some repetitive stress to an initially undamaged specimen until failure (usually fracture) occurs. The stress-life technique yields useful information about the fatigue strength of a given material system, but produces limited data about fatigue crack growth behavior. The damage tolerant design concept used for military flight vehicles requires an accurate prediction of crack growth to determine service life and inspection intervals on both airframe and engine structural components [11].

In order to confidently predict the service life of aircraft components made of metal matrix composites, research efforts have recently concentrated on establishing a data base and models dealing with both stress-life behavior and fatigue crack growth. For the high temperature applications, IHPTET and NASP, most fatigue tests are conducted on titanium matrix composites at an elevated constant temperature with a cyclic applied stress [7, 12-14]. The majority of the data are generated with smooth specimens using the stress-life technique; that is, little attention is paid to the crack growth characteristics during the test. Limited data on crack growth behavior are slowly becoming

available, but most of it is at either room temperature or elevated isothermal conditions.

There is, however, a need to determine fatigue crack growth characteristics under thermomechanical loading. Thermomechanical fatigue (TMF) is defined as a cyclic change in temperature and applied load, not necessarily with the same frequency or period. Consequently, if the load and temperature reach their minimum and maximum at the same time, the cycle is defined as in-phase; if, however, the maximum load occurs at the minimum temperature and vice versa, the cycle is defined as out-of-phase. Thermomechanical loading is common in engine applications and in some advanced supersonic airframe designs; severe temperature excursions coupled with cyclic mechanical loading are experienced during each flight.

A key problem with analyzing fatigue damage and fracture in composites in general, is determining the crack driving force during crack propagation. With monolithic metallic materials, linear elastic fracture mechanics (LEFM) can often be successfully applied to predict crack tip stress intensity factors and, in turn, predict the crack growth rate for various loading conditions. For composite materials, and more specifically metal matrix composites, some questions arise as to whether LEFM is a valid approach. For some MMC, the lack of a dominant crack, crack branching, crack bridging, fiber fracture and interface decohesion [8] make the correlation of crack growth rates with the stress intensity range,  $\Delta K$ , suspect. A better understanding of the damage mechanisms under cyclic loading, both mechanical and thermal, must be reached before life prediction for MMC structures is reliable.

This dissertation investigates the thermomechanical fatigue crack growth characteristics of titanium matrix composites. The primary material

used for this study is Ti-6Al-2Sn-4Zr-2Mo reinforced with silicon carbide fibers (SCS-6). Unidirectional material, [0]4, is investigated under isothermal and in-phase and out-of-phase TMF conditions. The purpose of this work is two fold: (1) to develop a better understanding of the mechanisms (e.g., environmental attack, fiber bridging, etc.) that affect the fatigue crack growth behavior of SCS-6/Ti-6242 under isothermal and TMF conditions and (2) to develop a model to predict crack growth rates under TMF conditions using only isothermal fatigue crack growth data.

## CHAPTER 2

### BACKGROUND

This section represents a compilation of background information necessary to describe the basic work completed for this research project.

#### 2.1 Definition of Terms

There are several terms that will be used throughout the remainder of this thesis that warrant a brief description now to avoid later confusion. Although this section will cover most specialized terms, it is not an exhaustive list, and descriptions of other items will be presented later in the thesis to maintain continuity.

##### 2.1.1 Thermal and Mechanical Cycling Terminology

For thermomechanical cycling, both load and temperature vary cyclically, usually with the same period. That is, the time needed to complete one thermal cycle is the same needed to complete a mechanical cycle. Since thermomechanical fatigue tests for this study are run on standard servo-hydraulic closed-loop test frames, mechanical loads can be applied very quickly. The time, however, required to heat and cool a specimen in a controlled mode (i.e., triangular waveform) takes considerably longer; hence,

the test frequency or cycles completed per second is limited to the temperature cycle frequency.

Another key feature of the thermomechanical cycle is the phase angle ( $\phi$ ) between the load and temperature. The phase angle represents the shift in time between a minimum or maximum peak of temperature in relation to that of the load (see Fig. 2.1). For this study the load is considered to lead temperature by some angle  $\phi$ . Typically, a cycle in which the minimum/maximum load and minimum/maximum temperature occur simultaneously is referred to as in-phase. The cycle where the peak events do not occur together is referred to as out-of-phase. Unless otherwise noted, the term out-of-phase in this thesis refers to the case of  $\phi = 180^\circ$ . More specifically, the maximum load occurs when the temperature is a minimum and vice versa.

Hold times (load-dwell) are often incorporated into thermomechanical cycling. The hold portion of the cycle usually takes place at maximum temperature to assess the contribution to damage from sustained loading at elevated temperatures. No hold times are incorporated into the tests performed for this current study. Isothermal fatigue tests are accomplished by holding the temperature constant and applying only mechanical loading, allowing assessment of the fatigue process as a function of temperature. Ultimately, it would be preferred if the thermomechanical response of a material system could be predicted based on the data from isothermal tests alone. By doing so, fewer thermomechanical tests could be run, and the necessary data could be obtained from the faster (higher frequency) and less complicated (experimentally) isothermal fatigue tests.

### 2.1.2 Crack Growth Rate Terminology

Crack growth rates are often correlated with the stress intensity factor range applied to a test specimen. This functional relationship is commonly illustrated on a log-log plot of crack growth rate,  $da/dN$ , versus the cyclic stress intensity factor,  $\Delta K$ , as shown in Figure 2.2. Note the three distinct regions of the curve: Region I is threshold portion; Region II is the stable growth (Paris Law) regime; and Region III is the critical crack growth area. The crack growth rates observed in this current study are for the most part contained in the Region II or stable growth region.

There are several relationships that have been developed to describe  $da/dN$  as a function of  $\Delta K$ . The familiar Paris Law [15] is a power law that describes the linear portion or Region II as follows:

$$\frac{da}{dN} = C(\Delta K)^n \quad (2.1)$$

The coefficient,  $C$ , and the exponent,  $n$ , are material constants that are typically determined empirically. A multitude of crack growth relationships are available to account for mean load or load ratio,  $R$ , effects. One model that is commonly used to describe the effect of  $R$  is known as the Forman equation [16] and is given by:

$$\frac{da}{dN} = \frac{C(\Delta K)^n}{(1-R)(K_c - K_{max})} \quad (2.2)$$

Here,  $K_{max}$  is the maximum stress intensity of the fatigue cycle,  $K_c$  is the critical stress intensity (fracture toughness), and  $C$ , and  $n$  are material constants.

Other crack growth relationships have been developed to model all three crack growth regions of a  $da/dN$  vs.  $\Delta K$  curve. Two common models developed by Pratt and Whitney [17] and General Electric [18] are represented by hyperbolic sine and sigmodial functions, respectively.

Pratt and Whitney [17] established the following relationship:

$$\log\left(\frac{da}{dN}\right) = C_1 \sinh[C_2 (\log \Delta K + C_3)] + C_4 \quad (2.3)$$

where  $C_1$  and  $C_2$  scale the x and y axes and  $C_3$  and  $C_4$  define the inflection point in the curve. It should be noted that while  $C_1$  is a material constant,  $C_2$ ,  $C_3$ , and  $C_4$  can be expressed as functions of temperature, frequency, hold-time, and load ratio [19, 20].

General Electric [18] developed the sigmodial crack growth model that is given by:

$$\frac{da}{dN} = \exp(B) \left( \frac{\Delta K}{\Delta K_{th}} \right)^C \left[ \ln\left( \frac{\Delta K}{\Delta K_{th}} \right) \right]^Q \left[ \ln\left( \frac{\Delta K_c}{\Delta K} \right) \right]^D \quad (2.4)$$

The parameters B, C, Q, and D determine the shape of the curve and in general can be expressed in terms of temperature, frequency, and load ratio [21]. Also,  $\Delta K_{th}$  and  $\Delta K_c$  are constants which specify the threshold stress intensity range and critical stress intensity range, respectively. There are two primary advantages of the sigmodial model (Eq. 2.4) as compared to the sinh model (Eq. 2.3). First, regions I and III need not be symmetric since those regions are defined independently in Eq. 2.4, and second,  $\Delta K_{th}$  and  $\Delta K_c$  are defined explicitly in the sigmodial model [22].

### 2.1.3 Composite Material Fabrication Techniques

There are at least three methods by which titanium matrix composites can be fabricated. These techniques include powder cloth processing, foil-fiber-foil (F-F-F) and thermal spraying (induction plasma spray deposition) [23]. Powder cloth processing has been used successfully to fabricate SiC/Ti-24Al-11Nb. In this process, powder cloths are stacked in alternating layers with fiber mats. Then the composite panel is consolidated in a vacuum hot press (VHP). Because of problems with binder materials and scaling the composite plates to production sizes, the powder cloth process is not as widely used as the other two methods.

As the name foil-fiber-foil suggests, fiber mats are alternated with layers of thin foils of matrix material. The consolidation of the composite is achieved by hot isostatic pressing (HIP'ing) or vacuum hot pressing [23]. A key advantage to this method is that the matrix is fully densified, without the organic binders used in the powder cloth process. This technique is not without its disadvantages: such as the high cost of the matrix foil; difficulty of processing by standard wrought methods; and the excessive waste of the starting ingot material.

Induction plasma spray deposition (IPD) is also being developed as a viable technique to fabricate titanium matrix composite (TMC) [24]. The titanium matrix composite used for this current study was fabricated using the IPD technique. Molten droplets of the matrix material are applied to a single layer of SiC fiber that is wound around a drum. The resulting monotapes are then cut to size, stacked and consolidated by VHP or HIP'ing. This fabrication technique usually produces composite with more evenly spaced fibers and is a good choice for scaled-up production since no organic binders are needed.

Induction plasma spray, however, can damage (break) fibers during spraying and/or consolidation as well as detach the outer carbon coating on the SiC fiber.

While a recent General Electric study [25] has shown that material property data have less scatter when generated from F-F-F fabricated composites compared to IPD fabricated composites, the results of the IPD material used in this study showed little scatter for replicate tests. The reported scatter may be attributed to only partial densification (erratic porosity) of the matrix during the consolidation process of the IPD material. Recall, the fiber-foil-fiber fabrication technique begins with fully densified foil sheets prior to the consolidation process.

#### 2.1.4 Coefficient of Thermal Expansion

Most engineering materials have an associated coefficient of thermal expansion (CTE). The coefficient of thermal expansion is a measure of strain that accompanies a unit change in material temperature. Typically, the CTE is a positive quantity; that is, for a unit increase in material temperature the material will expand some finite amount. Consequently, for composite materials the CTE can be one of the most helpful and at the same time most damaging features of the laminate.

For titanium matrix composites reinforced with continuous SiC fibers, the CTE for the matrix ( $\sim 10 \times 10^{-6}/^{\circ}\text{C}$ ) is typically twice as high as the CTE for the fiber ( $\sim 4.9 \times 10^{-6}/^{\circ}\text{C}$ ). During consolidation the matrix and fiber are subjected to high temperatures and pressures. At the maximum processing temperature the fiber and matrix are pressed together into a stress-free condition. Upon cool down the matrix tends to contract more than the fiber because of the CTE

mismatch between the fiber and matrix. This contraction of matrix around the fiber leads to a state of radial compression and circumferential and axial tension in the matrix areas adjacent to the fiber [23]. The radial compressive stress of the matrix around the fiber is the primary feature that binds the matrix and fiber together. It is thought that chemical binding in this class of TMC is negligible in comparison to the mechanical binding.

This tri-axial state of stress, however, leads to property degradation under certain loading conditions. Moreover, thermomechanical loading of a composite produces both mechanical and thermal cyclic loads, and depending on the phase between the mechanical and thermal loading, can lead to excessive stress ranges in the matrix and/or the fiber. For monolithic materials, a thermomechanical load would merely produce a linear summation of the mechanical and thermal strains (or stresses) for the entire material with no non-uniformities throughout the material. Thermal residual stresses resulting from the composite fabrication can be lowered by reducing the consolidation temperature, using a compliant layer between the foil and fiber, or using diffusion barriers that limit the fiber/matrix reaction [23].

## 2.2 Crack Bridging

Damage tolerance characteristics of titanium matrix composites are a pivotal issue in their potential success in aerospace applications. The crack bridging phenomenon can dramatically affect the fracture toughness of ceramic or metal matrix composite material systems. Crack bridging refers to the condition established when an advancing matrix crack leaves in its wake unbroken fibers that bridge (hence the name) the two opposing crack surfaces. Examples of an unbridged and bridged continuous-fiber reinforced composite

are shown in Figures 2.3 and 2.4, respectively. The extent of the crack bridging wake is a function of the fiber and matrix material properties and, to a larger degree, the fiber/matrix interfacial strength.

Metal matrix composites with strong interfaces and weak fibers are, in general, prone to crack growth dominated by fiber and matrix fracture. This case is usually typified by no fiber bridging and a greater possibility of multiple damage sites. Conversely, MMC with weak interfaces and strong fibers are likely to have crack branching at the fiber/matrix interface. That is, a crack advancing perpendicular to the loading direction may, upon reaching the fiber/matrix interface, proceed to extend along the interface parallel to the loading direction. Crack bridging, however, tends to occur in MMC with strong fibers, a weak interface and compressive residual stresses at the fiber/matrix interface [8].

Damage tolerance of a composite material system is directly related to the interfacial characteristics. Low toughness composites (brittle matrices) have interfaces of low shear strength, while high toughness composites require a much greater interfacial strength. A damage tolerance map was compiled by Chan and Davidson (see Fig. 2.5) [8]. The trends of the map best represent those of a composite with a notch experiencing tension-tension cyclic loading. The damage map is divided into 5 separate regions, labeled I-V. In region I, fracture along the interface is dominant, i.e., transverse properties are poor. Region II, however, is considered the optimum region for damage tolerance; in this region, the combination of matrix toughness and interfacial strength yields composites with fiber bridging, the principal mechanism for imparting damage tolerance [8]. A more detailed discussion of the fiber bridging phenomenon is found in Ref. [26]. If the interfacial shear

strength is high (Region III), however, little crack bridging occurs, and the composite's fracture behavior is similar to that of the matrix. Virtually no debonding occurs in the presence of very strong interfaces (Region IV), where interfacial fracture is best described by a stress intensity factor for a crack along the interface. Region V describes fracture of particulate composites; cracks avoid growing in the interface, and matrix toughness dominates the composite.

Fatigue resistance in metal matrix composites in conjunction with damage tolerance is also important. The effects of the fiber's mechanical properties, the fiber/matrix interface strength, and the crack bridging phenomenon on fatigue crack growth rates [8] are summarized in Figure 2.6 (a), (b), and (c), respectively. This figure reiterates that optimizing the damage tolerance characteristics of a composite requires tailoring the properties of the fiber, the matrix, and the interface.

For monolithic, metallic materials that behave in a Hookean manner the fatigue crack propagation and the fracture behavior are most commonly evaluated using linear-elastic fracture mechanics (LEFM). Typically, the crack driving force is associated with a stress intensity factor range ( $\Delta K$ ) that can, in turn, be related to the fatigue crack growth rate (see Sec. 2.1.2). The stress intensity factor (SIF) is a function of the applied stress, crack length and the specimen geometry. Linear elastic fracture mechanics also provides the relation between crack surface displacement and SIF for a given set of conditions, so that the crack length can be computed from the crack-mouth opening displacement (CMOD).

Experimentally, the crack length at any given time can be computed using the material's compliance, for instance, from the crack-mouth opening displacement measured by some calibrated clip gage, extensometer, or strain

gage arrangement. This information is useful for automated testing systems that require knowledge of the crack length at all times in order to properly apply load so that a given  $\Delta K_{\text{applied}}$  can be maintained. The compliance technique often used to measure crack length in monolithic material systems is reliable, but assumes that crack surfaces are separated up to the crack tip. That is, there are no bridging ligaments that would tend to hold the crack shut and thereby reduce the CMOD and the resulting stress intensity factor.

Although crack bridging is common in the titanium matrix composites, like those used in the current study, crack tip shielding or bridging in SiC-reinforced aluminum-alloy composites also occurs. Crack bridging has been studied in aluminum-alloy laminates reinforced with epoxy-resin sheets impregnated with unidirectional Aramid fibers (ARALL® Laminates) [27] and with silicon carbide particulates [28]. The ARALL composite system has superior crack growth properties which are a result of the extensive crack bridging that occurs in the wake of the crack. In fact, the fiber/epoxy interfaces are weak enough to permit controlled delamination which leads to the bridging of unbroken fibers across the crack [27].

### 2.3 Modeling of Thermomechanical Fatigue Crack Growth

The study of thermomechanical fatigue crack growth has generally been limited to monolithic materials, and the author is unaware of TMF crack growth results for metal matrix composites in the open literature. This section discusses some of the modeling efforts used to predict TMF crack growth in monolithic nickel based superalloys and titanium-aluminide alloys. While many different modeling approaches are available, the following section focuses on the linear summation type used for the current study.

Simply put, the linear summation approach represents the total fatigue crack growth per cycle as a combination of the cycle-dependent and time-dependent phenomena. The Heil-Nicholas-Haritos Model (HNH) [11, 29] proposed a linear cumulative-damage model for TMF crack growth rates in Inconel 718 based on isothermal crack growth data in the following way:

$$\left. \frac{da}{dN} \right|_{total} = \left. \frac{da}{dN} \right|_{cycle-dependent} + \left. \frac{da}{dN} \right|_{time-dependent} \quad (2.5)$$

where  $a$  and  $N$  are crack length and number of cycles, respectively.

The cycle-dependent contribution in Eq. 2.5 was determined from low temperature and/or high frequency crack growth test data, and was assumed to be independent of temperature and frequency. The time-dependent term, however, was assumed to be affected by temperature and frequency based on the experimental results and model presented by Nicholas, et al [30] who investigated the creep/fatigue interactions in Inconel 718. Furthermore, the time-dependent term was calculated by integrating the sustained-load crack growth rate over only the loading portion of the cycle.

The HNH model was able to predict isothermal and non-isothermal fatigue crack growth rates for a variety of conditions within a factor of two. The Inconel 718 was cycled in a triangular waveform at 0.01 Hz between 427 and 649 °C. The model, however, was unable to successfully predict crack growth rates for the 270° out-of-phase data. To properly predict the 270° test data, the integration scheme was modified such that when the  $da/dt$  term (part of the time-dependent component in Eq. 2.5) from the sustained-load data decreased during a cycle the numerical integration was terminated.

Mall, et al [31] proposed a similar linear summation model to predict crack growth in a titanium-aluminide alloy under sustained load and sustained load with superimposed fatigue cycles at 700 °C, 750 °C, and 800 °C. In the study, the total crack growth rate of Ti-24Al-11Nb was successfully modeled based on a summation of cyclic damage due to fatigue cycles and due to creep (sustained load). The total crack growth rate, written in terms of crack extension per unit time, is given by

$$\frac{da}{dt} \Big|_{total} = \frac{1}{fT} \frac{da}{dt} \Big|_{fatigue} + \frac{T_H}{T} \frac{da}{dt} \Big|_{creep} \quad (2.6)$$

where  $f$  is frequency,  $T$  is total cycle time and  $T_H$  is the duration of the hold time. The predictions based on Eq. 2.6 correctly yielded the trends of the data, but did not capture the interactive damage occurring between fatigue cycling (crack sharpening) and hold times (crack tip blunting) at lower cycle times. Unlike the observations made in nickel-base superalloys [11], a hold time in titanium-aluminides appears to retard the fatigue contribution of the creep-fatigue cycle, and pure mechanical fatigue tends to accelerate the contribution of the creep portion of the cycle. By adding an interactive term, the crack growth predictions were significantly improved. Equation 2.6 was then modified as follows:

$$\frac{da}{dt} \Big|_{total} = \frac{F_1(T_H)}{6T} \frac{da}{dt} \Big|_{fatigue} + \frac{F_2(T_H)T_H}{T} \frac{da}{dt} \Big|_{creep} \quad (2.7)$$

where  $F_1(T_H)$  is the correction factor to account for retardation of fatigue crack growth which develops during the hold time and  $F_2(T_H)$  is the correction factor

to account for acceleration of the creep crack growth due to crack sharpening by the fatigue cycle. Mall, et al [31] assumed the following expressions for  $F_1(T_H)$  and  $F_2(T_H)$

$$\begin{aligned} F_1 &= \exp(-\alpha T_H) \\ F_2 &= 1 + \beta \exp(-\alpha T_H) \end{aligned} \quad (2.8)$$

Here  $\alpha$  and  $\beta$  are empirical constants determined from the experimental data.

In a follow-on study, Nicholas and Mall [32] attempted to extend the model presented in [31]. Their model had three terms: one for purely cyclic fatigue; one for environmentally enhanced fatigue; and one for sustained load growth. They also included an interactive term as Mall, et al [31] did. Thus, their model looked like the following:

$$\left. \frac{da}{dN} \right|_{total} = F_1(T_H) \left. \frac{da}{dN} \right|_{fatigue} + F_2(T_H) T^{\gamma-1} \left[ \int_{cycle} \frac{da}{dt} dt + T_H \frac{da}{dt} \right] \quad (2.9)$$

Here  $\gamma$  is an empirical constant and  $F_1(T_H)$  is defined by

$$F_1 = (1 + T_H)^{-\alpha} \quad (2.10)$$

and  $F_2(T_H)$  is again defined by Eq. 2.8. The model captures several features of fatigue crack growth in titanium-aluminide alloys. For instance, hold times tend to blunt the crack tip, reducing the crack growth rate, while environmental exposure over time accelerates crack growth. A unique feature of this model is its ability to predict a decrease in growth rate due to the addition of hold times.

This is not the case with other linear summation models no matter what correlating parameter is used.

The most recent model to predict fatigue crack growth behavior under elevated temperature as well as TMF conditions in Ti-24Al-11Nb was by Pernot [22] and Pernot, et al [33]. While other linear summation models [31, 32] used retardation coefficients to account for crack-tip blunting, these retardation coefficients are limited to a particular temperature. The model proposed by Pernot [22] incorporates retardation coefficients that vary continuously during a TMF cycle, resulting in effective cycle-dependent and time-dependent contributions. This model has the form:

$$\left. \frac{da}{dN} \right|_{tot} = \int_0^{t_{ul}} \beta(t) \left( \frac{2}{\tau} \right) \left( \frac{da}{dN} \right)_{ur \ cd} dt + \int_0^{t_{nd}} \beta(t) \left( \frac{da}{dt} \right)_{ur \ td} dt \quad (2.11)$$

where  $t_{ul}$  equals the uploading time,  $t_{nd}$  equals the sum of  $t_{ul}$  and  $t_{hd}$  ( $t_{hd}$  = time the load is held at  $P_{max}$ ),  $\beta(t)$  is the retardation coefficient,  $\tau$  is the cycle period  $(da/dN)_{ur \ cd}$  is the unretarded cycle-dependent crack growth rate and  $(da/dt)_{ur \ td}$  is the unretarded time-dependent crack growth. Since the retardation coefficient  $\beta(t)$  is a continually changing function, it took the following form:

$$\beta(t) = \beta(t_0) + \int_{t_0}^t \frac{d\beta}{dt} dt \quad (2.12)$$

The  $d\beta/dt$  term is expressed as the combination of an increasing (crack-tip sharpening) term and a decreasing (crack-tip blunting) term. These components were assumed to have the form:

$$\left( \frac{d\beta}{dt} \right)_{inc} = \begin{cases} C_1(1-\beta); & \text{for } \frac{dP}{dt} \neq 0 \\ 0 & ; \text{for } \frac{dP}{dt} = 0 \end{cases} \quad (2.13)$$

and

$$\left( \frac{d\beta}{dt} \right)_{dec} = -C_2 \left( \frac{P}{P_{max}} \right) (\beta - \beta_0) \quad (2.14)$$

where  $C_1$  is a polynomial function of frequency,  $C_2$  is a polynomial function of temperature,  $P$  is the instantaneous load,  $P_{max}$  is the maximum load during the cycle and  $\beta_0$  is the value of  $\beta$  during steady-state sustained-load crack growth. Predictions of test data over a wide range of test conditions correlated well. Test conditions included isothermal crack growth ( $T = 649^\circ\text{C}$ ) for 0.01, 0.1 and 5.0 Hz, isothermal crack growth at  $315^\circ\text{C}$ ,  $482^\circ\text{C}$ , and  $649^\circ\text{C}$  at 0.01 Hz, in-phase and out-of-phase tests at 0.01 Hz, and tests with hold times at various times in the cycle.

#### 2.4 Historical Development of Monolithic Ti-6Al-2Sn-4Zr-2Mo

The gas turbine industry has used Ti-6Al-2Sn-4Zr-2Mo (Ti-6242) as the workhorse elevated-temperature titanium alloy for over a decade [34]. The maximum use temperature of Ti-6242 is approximately  $540^\circ\text{C}$  ( $1000^\circ\text{F}$ ), but is generally limited to  $510^\circ\text{C}$  ( $950^\circ\text{F}$ ) [34, 35]. The overall success of this titanium alloy can be attributed to its excellent creep resistance, high strength, and its post-creep stability.

The initial development of high temperature titanium alloys dates back to the mid-1950's. The first titanium alloy to be commercially available for high

temperature applications was Ti-6Al-4V. It had by today's standards a meager maximum use temperature of only 350 °C (660 °F) [34]. During the early 1960's, however, Ti-7Al-4Mo and Ti-8Al-1Mo-1V were introduced with a maximum use temperature of roughly 400 °C (750 °F). Even these newly developed alloys suffered from embrittlement after sustained exposures to elevated temperatures. Continuing alloy research in the mid-1960's produced Ti-679 (Ti-11Sn-5Zr-1Mo-2.5Al-0.2Si) and Ti-6242 (Ti-6Al-2Sn-4Zr-2Mo) with maximum use temperatures of 480 °C (900 °F) and 510 °C (950 °F), respectively. It was not until the early 1970's that an additional 0.1% of silicon was added to Ti-6242 to extend its temperature range to 540 °C (1000 °F). Note that when the additional silicon was added the trade name was changed to Ti-6242-Si. Since the silicon is now assumed to be present in all commercially produced Ti-6242, however, the alloy is now commonly referred to as just Ti-6242 - dropping the Si suffix.

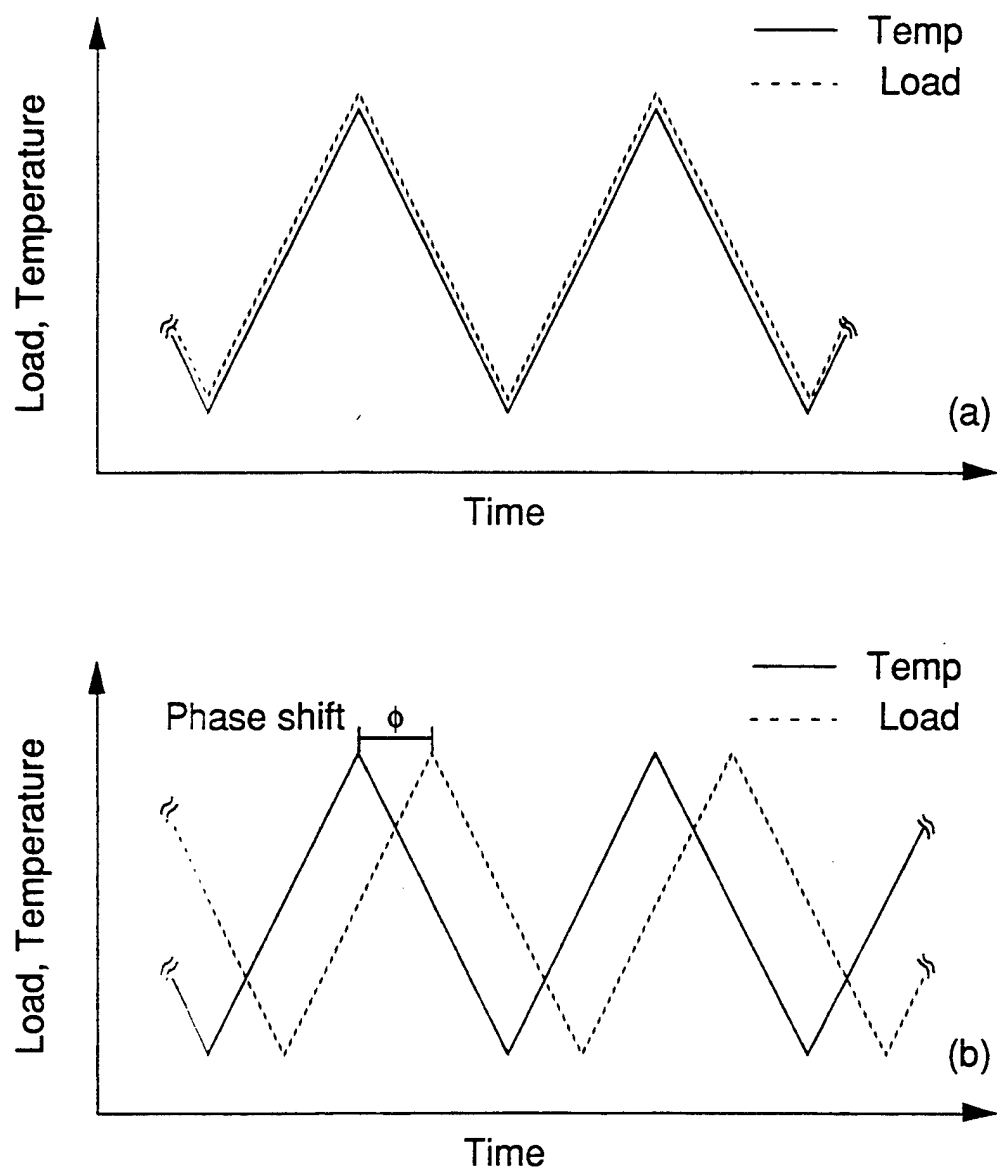


Figure 2.1 Diagram of mechanical and thermal cycles (a) in-phase and (b) out-of-phase by some angle  $\phi$ .

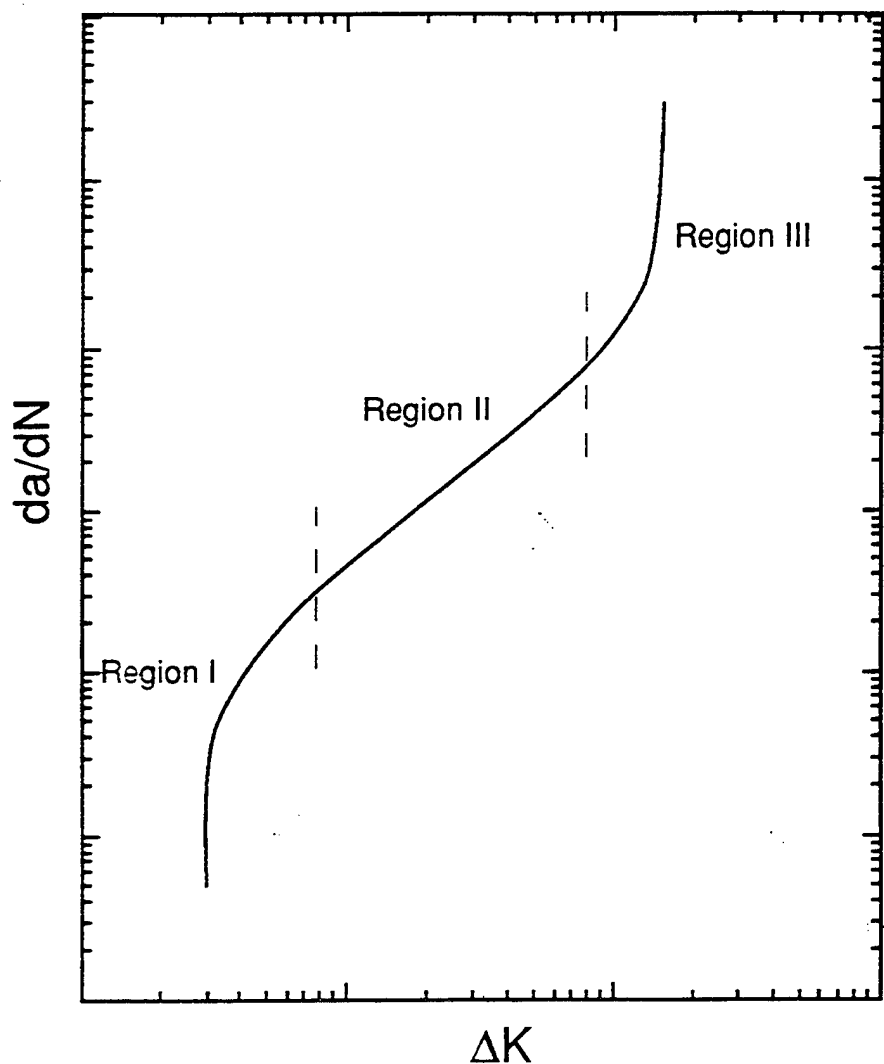


Figure 2.2 Typical sigmoidal crack growth rate curve.

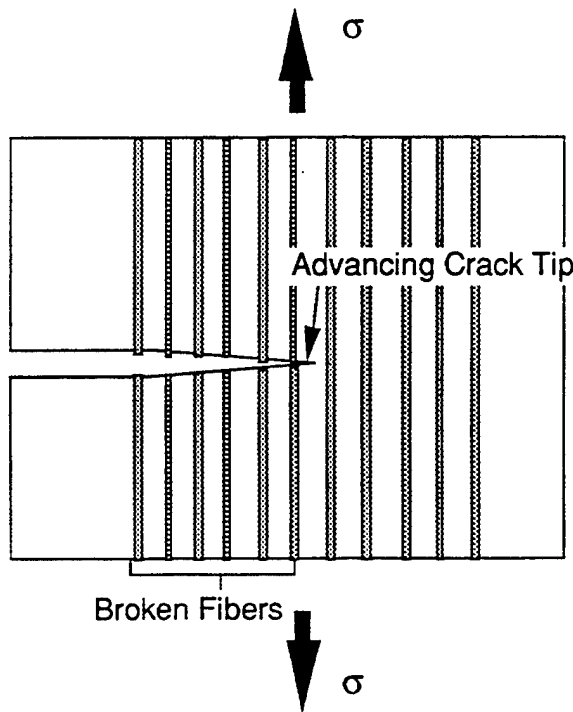


Figure 2.3 Illustration of simultaneous fiber and matrix crack growth.

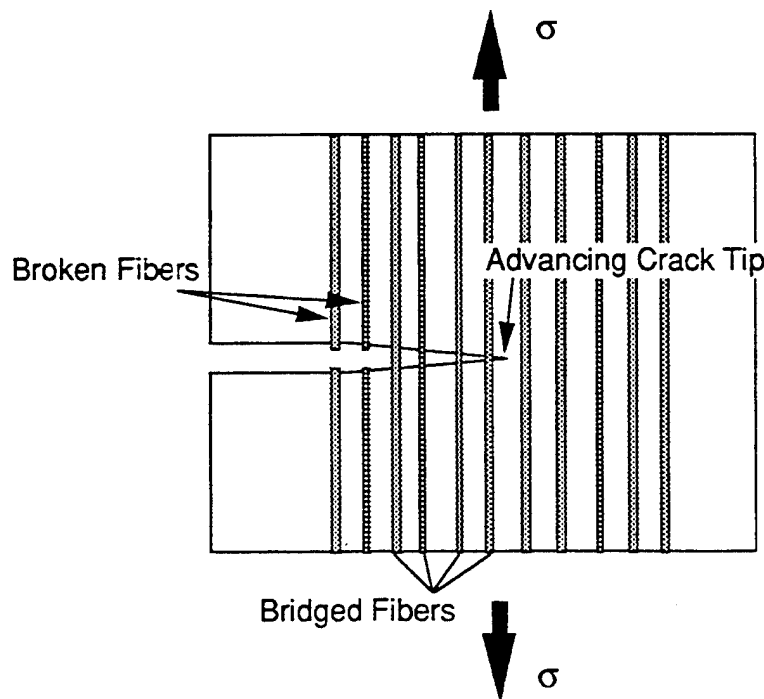


Figure 2.4 Illustration of the crack bridging phenomenon in fiber reinforced composite material systems.

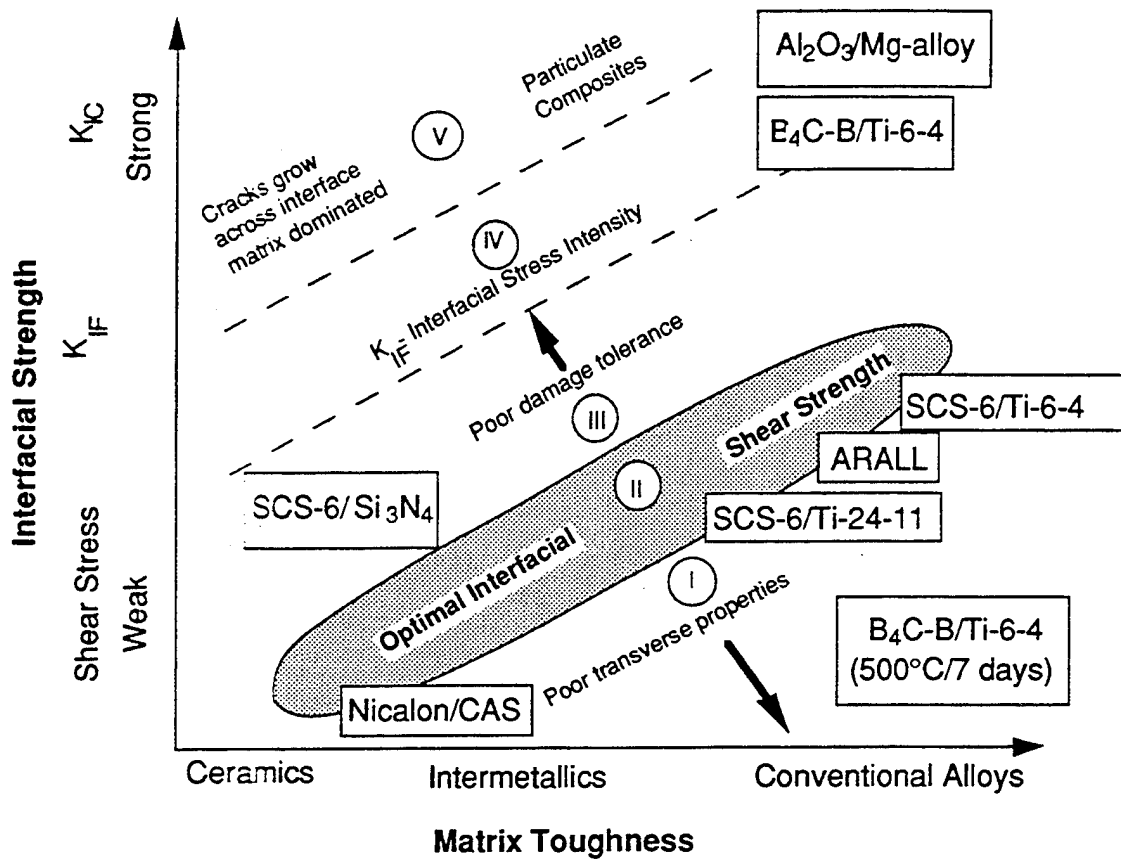
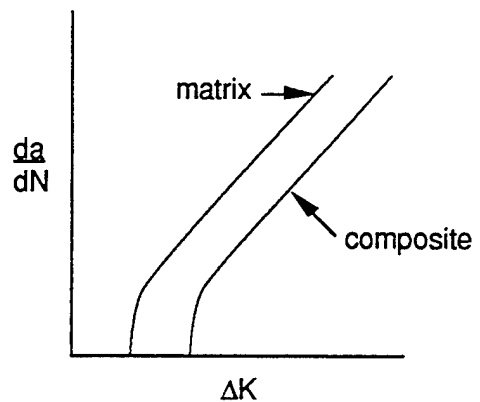
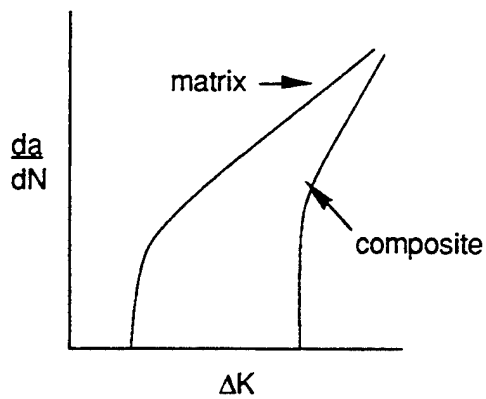


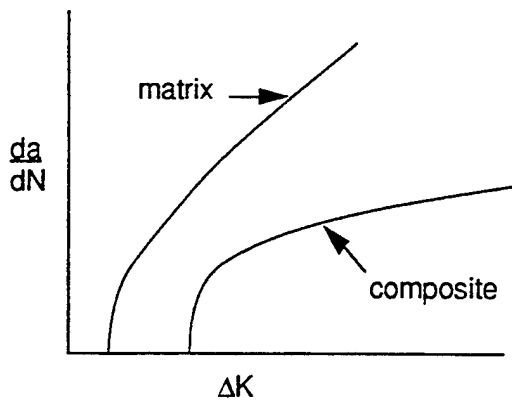
Figure 2.5 Damage tolerant map illustrating relationship between failure characteristics of composites in relation to the matrix toughness and interface strength or interface toughness [8].



(a) Strong Interface



(b) Weak Interface



(c) Frictional Interface and Crack Bridging

Figure 2.6 Influences of interface properties on fatigue crack growth characteristics (a) strong interface, (b) weak interface, and (c) frictional interface and crack bridging [8].

## CHAPTER 3

### EXPERIMENTAL SET-UP AND TEST PROCEDURE

The material, test equipment, experimental procedures, and data gathering techniques employed for the present study are discussed in this section. Additional background and terminology are presented in Chapter 2 of this thesis.

#### 3.1 Material

The material used in this study is a titanium based metal matrix composite reinforced with silicon-carbide fibers, SCS-6. The nominal composition (weight %) of the matrix alloy is Ti-6Al-2Sn-4Zr-2Mo-0.1Si (Ti-6242). The actual chemical composition (weight %) of the titanium alloy was determined using standard metallurgical techniques and compared to data sheets provided by the material supplier. The chemical composition is given in Table 3.1. The SCS-6 continuous reinforcing fibers developed by Textron Specialty Materials are composed of a silicon-carbide outer shell surrounding a core of carbon. The fibers are also subjected to a dual-pass carbon-rich coating to promote survivability in aggressive environments and limit the reaction between the SiC fiber and the Ti matrix.

### 3.2 Specimen Description

Specimens were electric discharge machined (EDM) from plates nominally 1 by 201 by 146 mm (0.039 by 7.91 by 7.75 in) of Ti-6Al-2Sn-4Zr-2Mo with a fiber volume fraction of 36 %  $\pm$ 1 % of SCS-6 continuous reinforcing fibers. The location of each specimen in a representative plate is illustrated in Figure 3.1. The plates were fabricated using the induction plasma spray deposition (IPD) technique (see Sec. 2.1.3) and then consolidated under hot isostatic pressure (HIP'ing). Electric discharge machining was also used to cut the edge notch in the SE(T) and center notch in the M(T) specimens. The width of the EDM notch is 0.370 mm (0.0146 in). A heat treatment commonly applied to the SCS-6/TIMETAL®21S composite system was not used for the material used in this study. The heat treatment was not deemed necessary to reduce mid-temperature embrittlement or to stabilize the matrix material as is required in similar composite systems.

A representative fatigue crack growth single-edge notch specimen, SE(T), is shown in Figure 3.2. An initial  $a/W$  of 0.3 was used for all specimens unless otherwise stated. With an  $a/W = 0.3$ , the applied load was sufficient to allow for a crack to initiate at the notch ( $\Delta K_{\text{applied}} > \Delta K_{\text{thrs}}$ ) but not slip in the friction grips ( $P_{\text{applied}} < P_{\text{grip-slip}}$ ). All single-edge notch specimens were nominally 1 by 25 by 136 mm (0.039 by 0.98 by 5.35 in) with an edge notch machined perpendicular to the loading axis at the center of the specimen length. Approximately 18 mm of each end was gripped with the rigid grip system described later.

The center notched geometry, M(T), shown in Figure 3.3 was also used in this study. It also had nominal dimensions of 1 by 25 by 136 mm (0.039 by 0.98 by 5.35 in) with the center notch machined perpendicular to the loading

axis at the geometric center of the specimen; the initial notch length,  $2a/W$ , was 0.25. The M(T) was loaded by gripping 18 mm of each end by the rigid-grip system (see Section 3.3.1). The stress intensity factor solution for the M(T) geometry assuming pin loading (i.e., uniform remote stress) were used even though it was rigidly gripped. Unlike the SE(T) stress intensity factor solution which is sensitive to end loading conditions, the fixed displacement constraint does not affect the stress intensity factor solution for the M(T) geometry for height-to-width ratios,  $H/W$ , greater than 1.0 [36]. The height-to-width ratio used in this study was 4.0.

### 3.3 Test Apparatus

By the nature of the tests run, a mechanical and temperature cycle was applied simultaneously to the specimen. The mechanical loads were applied by means of a closed-loop servo-hydraulic test frame whose load train was horizontal as opposed to vertical commonly used on conventional fatigue test frames. The temperature cycles, in turn, were applied with a quartz lamp radiant heating system coupled with forced air jets for "power-on" cooling. While loads were applied, the crack length and number of cycles were monitored and recorded so that crack growth rates could be computed in real time. A triangular waveform for both thermal and mechanical cycling was used for all fatigue crack growth tests with no hold times unless otherwise stated. In addition, some tests were run under isothermal conditions. To automate the test procedure, a micro-computer was used in conjunction with the servo-hydraulic test frame electronics and lamp controllers.

### 3.3.1 Mechanical Loading Description

The horizontal load frame has two primary advantages over the vertical load frame for TMF tests: 1) the quartz rod high-temperature extensometer is more readily mounted in the horizontal orientation, and 2) there is little chimney effect from the heating lamps that vertical systems experience. A photograph of the complete test station is shown in Figure 3.4. The primary components in this set-up are the 22 kN (5 kip) servo-hydraulic test frame, the MTS 458.20 microcontroller, and the Unisys 386 microcomputer.

The command signal for load to the specimen goes directly from the controlling software aboard the computer to the MTS microcontroller which then regulates the motion of the servo. The load signal contains information such as magnitude of load, frequency and loading shape. The load cell which is part of the load train sends its signal back to the MTS microcontroller so that a closed-loop control system is realized. This feedback loop allows the computer to monitor and correct the applied load so it more closely reflects the desired load.

A unique grip system was used to apply the mechanical loads. A detailed diagram of the rigid grip system is shown in Figure 3.5. The rigid grip system prevents end rotations or transverse displacements. The design of the rigid grips also allows the application of compression loading [3]. Bending stress, always a concern in axially loaded specimens, however, must be eliminated prior to mounting the specimen since the rigid grip system is not self aligning.

After the assembly of the horizontal test frame and before any material evaluation began, the alignment was checked and verified. To obtain the necessary alignment, that is, to minimize bending stresses, the load frame was

rotated to the vertical orientation. The Woods metal alignment pot was heated allowing the grip fixture to move freely. Precision angle irons were then placed around the grip's flat outer surface and the Woods metal was then allowed to cool, fixing the grip's position. Upon cool down, the load frame was returned to its original horizontal orientation. Using a traversing dial indicator along the precisely machined grip outer surfaces, the transverse alignment and angular alignment were found to be better than 0.025 mm and  $2 \times 10^{-4}$  rads, respectively.

The possibility for bending stresses was checked using a machined bar and an extensometer. The extensometer was positioned at each side of the bar, and four separate stress-strain data sets were collected. The stress-strain data were then reduced and converted to percent bending using *corrected* equations taken from ASTM Standard 1012-89 [37]. The results show that for this test frame, the percent bending is nominally less than 2% for any load greater than 0.5 kN (1.1 kip). A plot of percent bending as a function of applied load is shown in Figure 3.6. The ASTM standard for load train alignment stipulates that the bending stresses must be less than 5% of the maximum applied stress. Figure 3.6 confirms that for the designated test matrix, the bending stresses are well below the allowed limit.

In order to verify proper operation of the newly constructed test frame as well as the control software, a monolithic titanium alloy, Ti-1100, was used to perform crack growth tests at room temperature and elevated temperature (593 °C or 1100 °F). Crack growth data were then compared to recent studies [34, 35, 38] on the same alloy. The room temperature data shown in Figure 3.7 illustrate good correlation with published data. This consequently confirmed

that the test system was capable of generating valid crack growth data under the given test conditions.

### 3.3.2 Heating and Cooling System

One of the most challenging aspects of a thermomechanical fatigue test set-up is the successful heating and cooling of the test specimen in unison with the mechanical load. A four-zone, quartz-lamp, radiant heating system was used to heat the specimen in a controlled and uniform fashion. As shown in Figure 3.8, the lamps were oriented transverse to the specimen's longitudinal axis. This system was closed-loop, achieving feedback from four K type thermocouples spot welded in strategic locations on the specimen.

Several studies of thermal gradients and lamp control were performed prior to the start of the thermomechanical fatigue crack growth tests. The placement of the thermocouples on the specimen and was an iterative process. The final configuration was such that all lamps contribute equally (power supplied by each lamp was approximately equal) to heat the gage section and produce a relatively smooth temperature profile across the gage section. Figure 3.8 indicates the designated location of each of the four thermocouples. Thermocouples 1 and 2 were opposed 12.7 mm (0.5 in) from the specimen center, while thermocouples 3 and 4 were placed near the geometric center of the specimen with thermocouple 4 being attached to the bottom of the specimen. Thermocouples 3 and 4 were offset from the center of the specimen so they did not interfere with the propagating crack. This, of course, assumed that each crack would propagate in a self-similar fashion away from the edge notch perpendicular to the load direction.

In order to have a controlled, repeatable cooling side of the thermal cycle, passive over-the-specimen cooling air was implemented. The air flowed across the specimen to cool the specimen faster than the necessary programmed cycle. This meant the lamps output some radiant heat even on the cooling side of the thermal cycle. By doing so, the computer along with the lamp controllers produced a well defined triangular thermal cycle as requested. With additional cooling air over the specimen, shorter cycle times were realized, as opposed to letting the specimen cool under the influence of only natural convection.

A previous TMF study of unnotched titanium matrix composites with similar test equipment used a triangular cycle whose period was as long as 3 minutes [39]. Cooling air flow rates in those studies were nominally low, using only one cooling jet. For the current study, initially, two stainless steel cooling tubes were used to provide cool down control. It was discovered, however, that as faster and faster cycle times were sought (less than 180 sec/cycle), the less controlled the cyclic temperature profile became. More specifically, the inner zones (#'s 3 and 4) cooled adequately, but the outer zones (#'s 1 and 2) were unable to cool fast enough to follow the requested triangular waveform.

To ensure a faster controlled cycle a new method of cooling was developed. The new system provided even air flow over a wider region allowing even heating and cooling for cycles as fast as 90 sec/cycle from 150-650 °C (300-1200 °F). A schematic of the cooling system is shown in Figure 3.9. The goal with the two tubes with 5 evenly spaced holes was to use smaller amounts of air over a wider portion of the specimen, providing sufficient cooling to zones 1 and 2. The cooling system was also designed to blow the air from the same side as the high temperature extensometer. The

rationale was that if a cooled zone develops due to the forced air it would be limited to a small region along the edge of the notched side of the specimen. This would reduce the effect that any non-uniform temperatures would have on the advancing crack (or damage).

One drawback, however, of using cooling air, or at least excessive cooling air, was the possible generation of undesirable thermal gradients on the section of the specimen closest to the forced air. A thermal gradient study was conducted to asses the nature and severity, if any, of the temperature profile over a typical gage section. Thermocouples were placed in critical regions of the specimen (e.g. near the crack tip front), and the lamps were programmed to cycle between 150 and 538 °C (300-1000 °F) in a triangular waveform with cyclic periods varying between 180 to 90 seconds. Temperature readings from all attached thermocouples were recorded as well as the exact location of each thermocouple. Figure 3.10 shows a typical temperature profile over the specimen during such a cycle with a 120 second period. Note tha: zones 1-4 (the controlling zones) and zones 5 and 6 (along the notch line) follow the desired profile over the entire period. Also note that zone 8 (at the grip) remains almost at a constant temperature slightly above room temperature.

Various combinations of cyclic frequency and temperature range were monitored. For the 150-538 °C range the temperature profile was controlled adequately even with a 90 second period. However, this required significant air flow and generated excessive "flashing" by the quartz lamps trying to maintain the proper temperature. It was felt that although the system was capable of maintaining the desired temperature profile, it was too demanding and over long testing periods could greatly shorten the lives of the quartz lamp

bulbs. There was also the real possibility that while the exterior (surface) temperature appeared reasonable the interior temperature, especially that of the fiber, may have lagged behind in the very fast cycle regime. This could generate severe thermal gradients between the fiber and matrix and exacerbate the problem of thermal residual stresses that were already present after composite fabrication. If adverse thermal gradients did exist, the effective stress intensity factor,  $K$ , at the crack tip, all else being equal, could be quite damaging relative to a condition of a constant temperature distribution across the gage section.

With the above discussion in mind, the shortest cycle length used in this study was 120 seconds when cycling between 150 and 538 °C (300-1000 °F). This cycle time and temperature range combination as illustrated in Figure 3.10 yielded the best trade off between cycle time (fast as possible) and excessive air flow (adverse temperature gradients). At this rate thermomechanical cycles accumulated on the specimen at a pace of 5000 cycles per week.

### 3.3.3 Crack Length Measurement

The determination of crack length was accomplished using two independent methods: (1) optical inspection and (2) direct-current electric potential (DCEP). Elevated temperature extensometry was also considered for crack length determination, but was not used as discussed later. As each fatigue crack growth test progressed, a crack length was determined by each method at regular intervals. The frequency of data acquisitions depended on the length of the actual crack (and crack growth rate), where the data acquisition intervals were loosely based on the guide lines set-up by ASTM

E647 [40]. This standard suggests that crack length and cycle number should be recorded more frequently as the crack growth rate increases near the latter part of the test. The procedure used for the fatigue crack growth tests of this study called for a crack length measurement when crack extension  $\Delta a \approx 0.05$  mm (0.00197 in). Typically, data were taken at 1, 2 or 4 hour increments to meet the above required for crack extension. As expected, the time increment was dependent upon the crack growth rate. As the growth rate changed, the time increment was also updated. It should be noted that during each data acquisition the control software adjusts the load-temperature profile and corrects the phase angle between them. In order to maintain corrected profiles, more data samples are taken than are actually required by any governing standards.

Optical inspection to determine crack length is the oldest technique for data collection during a fatigue crack growth test. This technique is still widely used for verification of other more automated techniques like compliance and EPD as is the case in this study. The problem, however, of monitoring crack growth with the previously used quartz lamps is that the crack cannot be seen during a test. Normally, the regular (unslotted) lamps are positioned approximately 15 mm apart with the flat specimen sandwiched between (see Fig. 3.5). To alleviate this problem, the lamps were redesigned such that a slot was machined through the center of the lamps. The slot is 7 mm (0.2756 in) wide and 32 mm (1.2598 in) long. With the slot in combination with a mirror and a traversing telemicroscope, a visual inspection of the propagating crack was performed while the test was in progress. Figure 3.11 illustrates the typical experimental set-up of the lamp-mirror-telemicroscope combination. Although crack growth rates were not determined directly from crack lengths

obtained visually (primarily because it is difficult to automate this procedure), the telemicroscope allowed for verification and/or correlation of crack lengths computed by EPD. An attempt was made to photograph the crack propagation during the life of the test. However, lighting difficulties and lack of clarity resulted in photographs that were difficult to interpret. The exact location of the crack tip(s) was hard to determine in the photographs . Since the photographs returned very little useful data, the use of the photographic equipment was stopped.

The elevated temperature quartz-rod extensometer, used only on the SE(T) geometry, measured the crack-mouth-opening-displacement (CMOD) as a means of computing an effective crack length (recall crack bridging is possible). For Hookean, monolithic materials, CMOD can be used to yield the length of a crack by taking into account the specimen geometry, loading conditions and material properties. The control software, for example, can sample the extensometer output when appropriate and then calculate the crack length for that material and geometry. Accurate prediction of actual crack length assumes one dominant crack that is not bridged and fully open when the CMOD measurement is taken.

In metal matrix composites, however, the dominant crack will probably have a region just behind the advancing crack tip that is bridged by unbroken fibers. The effect of these bridged fibers (explained in more detail in Ch. 2) is to reduce the CMOD as compared to a crack that experiences no bridging. Consequently, any compliance technique (e.g. extensometry) used to determine crack length in a MMC must account for any bridged region that will tend to reduce the crack-mouth-opening-displacement. Since the extent of

crack bridging was unknown prior to testing, the CMOD was not used as a means of predicting the real time crack length.

Another method used to asses crack growth was the direct-current (d-c) electrical potential (DCEP). When an electric field is generated by an electric current in a conducting body, its field shape and intensity can be measured and calibrated to yield the crack length. The DCEP technique relies on the relationship between the DCEP field strength at the chosen measurement points and the geometric changes associated with a growing crack [41]. Determining the crack length in a monolithic material at room temperature using the DCEP method is straightforward and reliable. This method becomes more cumbersome at elevated temperatures, especially if the temperature varies cyclically. Significant errors in crack length measurement can occur at the elevated temperatures since the electric-field intensity measurements are affected by temperature and time-dependent material-property changes and thermoelectric effects [41]. The material resistivity (or conductivity) generally varies with time and temperature. By placing a second set of reference leads on the specimen where the field strength is not affected by crack length, the material resistivity can be detected independently of the DCEP voltage generated by the crack [41]. Consequently, the crack length can be measured accurately for the life of the test regardless of the time at temperature.

The thermal emf voltages, a by-product of any temperature difference between two joined dissimilar materials, adds to the voltage generated by the current flowing through the cracked specimen. Possible sources of thermal emf voltages are the leadwires used in DCEP measurements or the connectors on the DCEP amplifier/voltmeter. Interestingly, the thermal emf is still present even when the applied current is removed; consequently, it can be

independently measured with the DCEP current off and then subtracted from the measured DCEP voltage. This method is implemented in the isothermal and thermomechanical fatigue crack growth testing procedure. Fortunately, since the reinforcing fibers are nonconducting, the crack length computed with the DCEP technique yields a crack length that is equivalent to the matrix crack length regardless of the amount of bridging occurring. This fact is useful when attempting to ascertain the extent of bridging by comparing crack lengths computed with compliance (bridging dependent) and electric potential (bridging independent).

A constant current of 3 amps was applied to each specimen during each thermomechanical fatigue crack growth test. The DCEP pickup wires were attached at the corner of the notch for the SE(T) geometry with one lead on the top the other lead on the bottom. The DCEP pickup wires for the M(T) geometry were attached to the top of specimen 12.5 mm from the center notch along the centerline. The potential drop was directed through a multimeter and for the material tested was nominally 0.05 mV (uncycled at 23 °C = 73 °F). As the crack (damage) progressed the increase in potential drop was calibrated with the matrix crack length.

Table 3.1 Actual chemical composition (weight %) of the titanium alloy matrix in the SCS-6/Ti-6Al-2Sn-4Zr-2Mo used for this research.

Al	Sn	Zr	Mo	Ti
5.66	1.85	3.99	2.50	bal

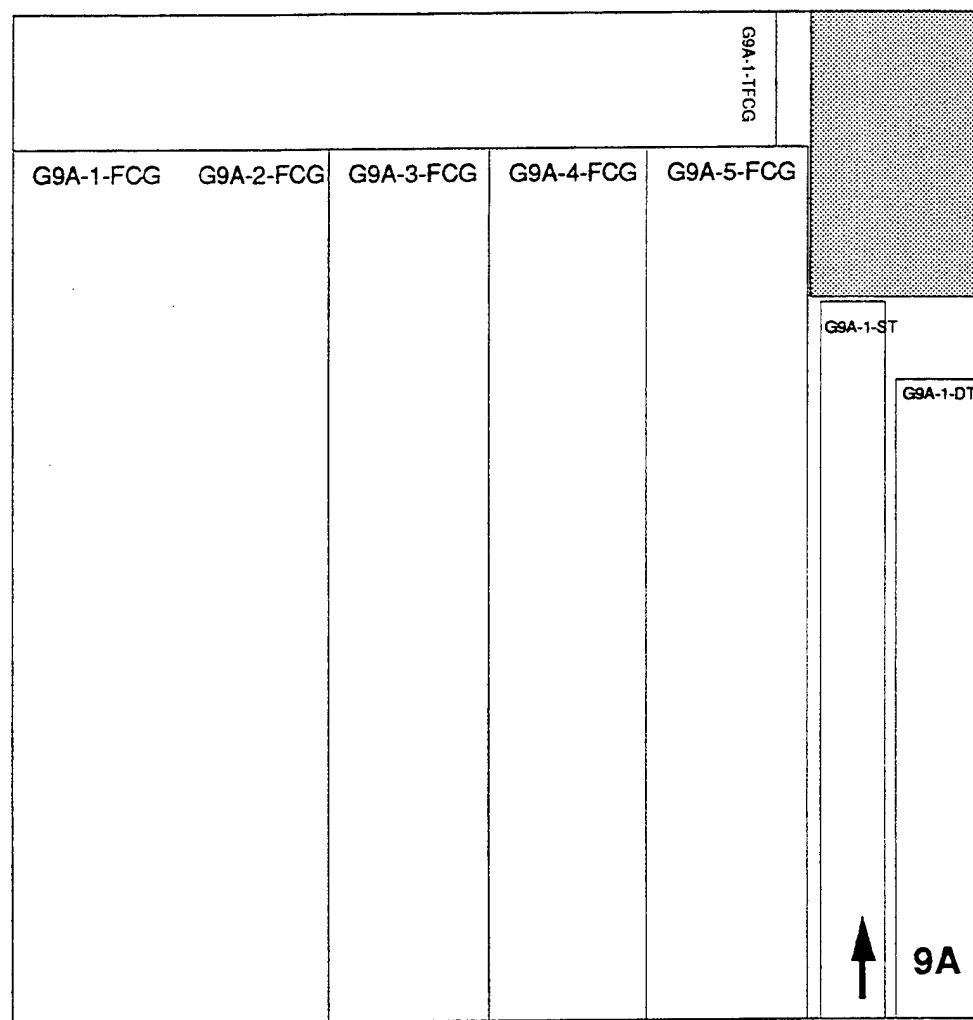


Figure 3.1 Location of single-edge notch specimens in typical plate (G9A) of SCS-6/Ti-6242 composite.

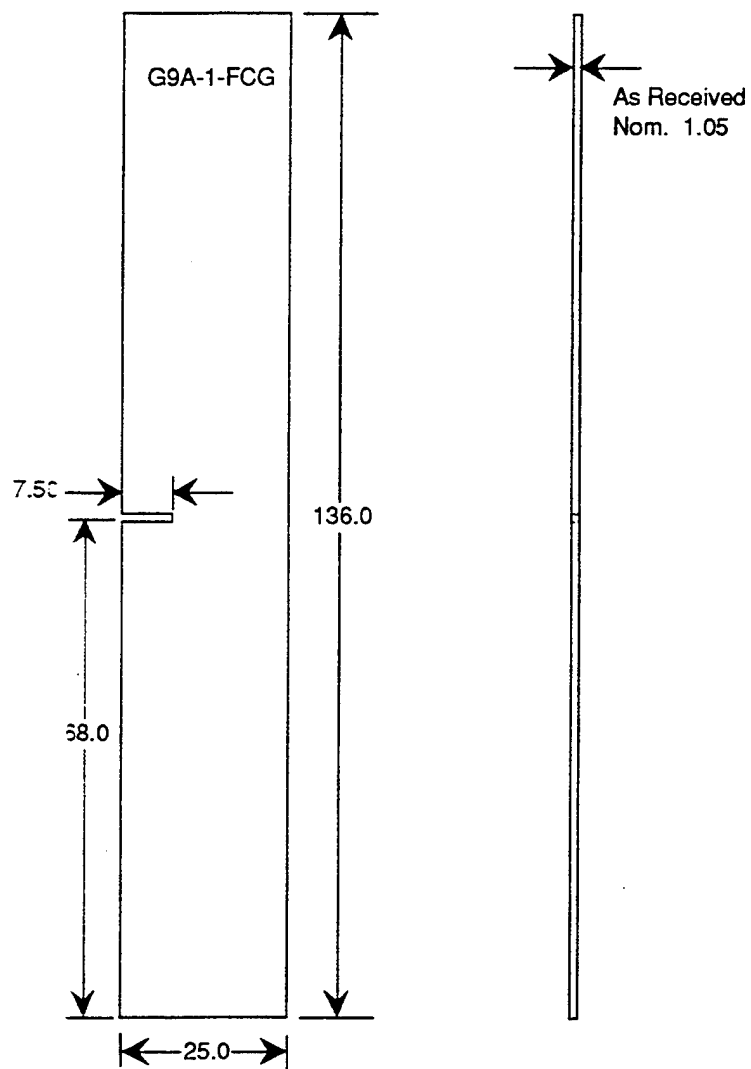


Figure 3.2 Schematic of single-edge notch specimen and corresponding dimensions.

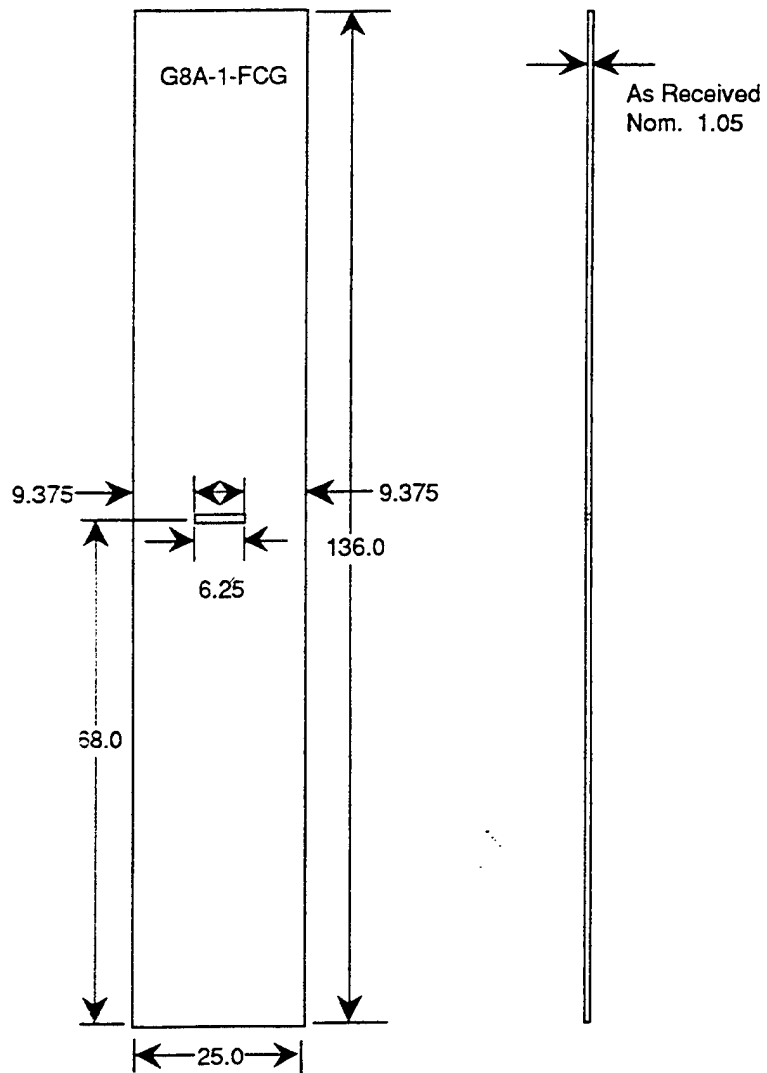


Figure 3.3 Schematic of center cracked specimen and corresponding dimensions.

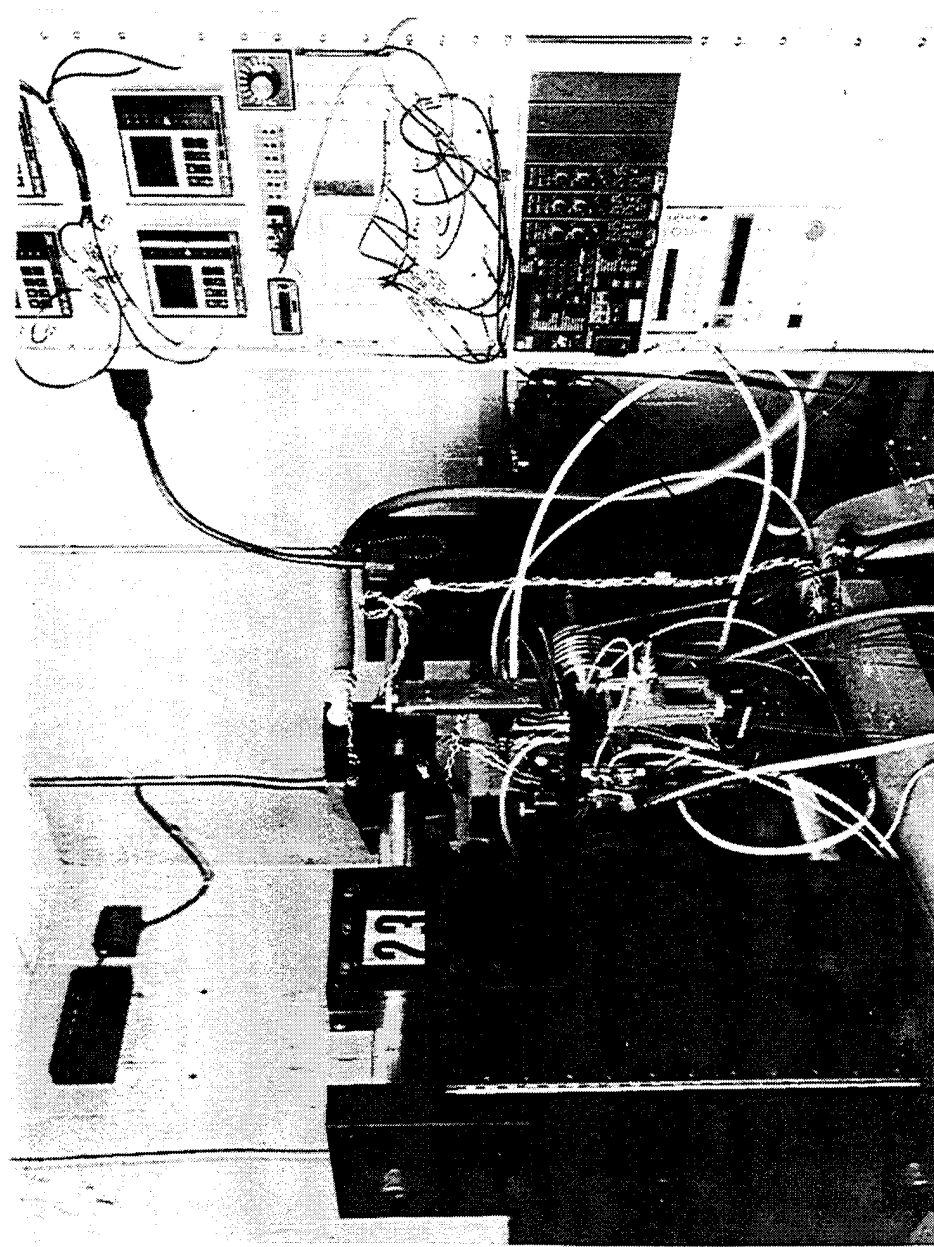


Figure 3.4 Photograph of the horizontal servo-hydraulic test frame set-up.

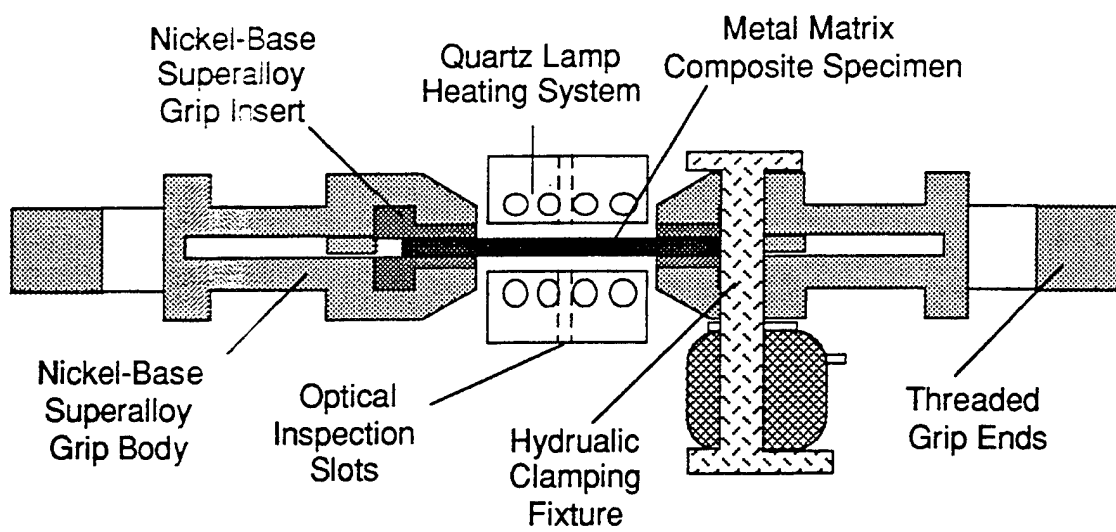


Figure 3.5 Representation of the rigid grip system.

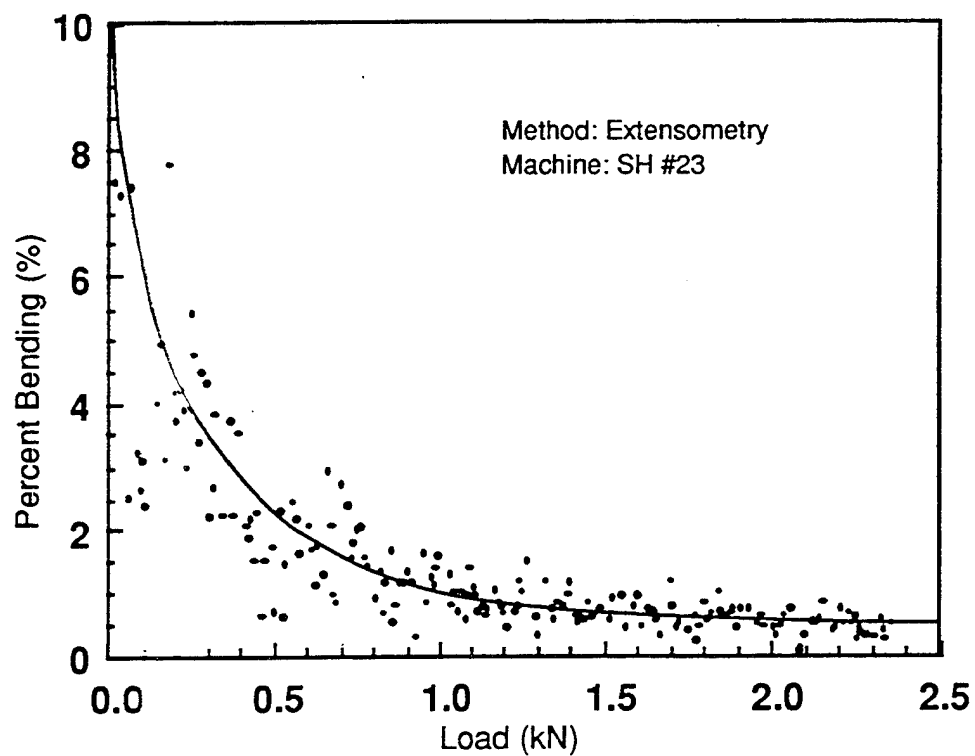


Figure 3.6 Percent bending as a function of applied load, confirming load train alignment.

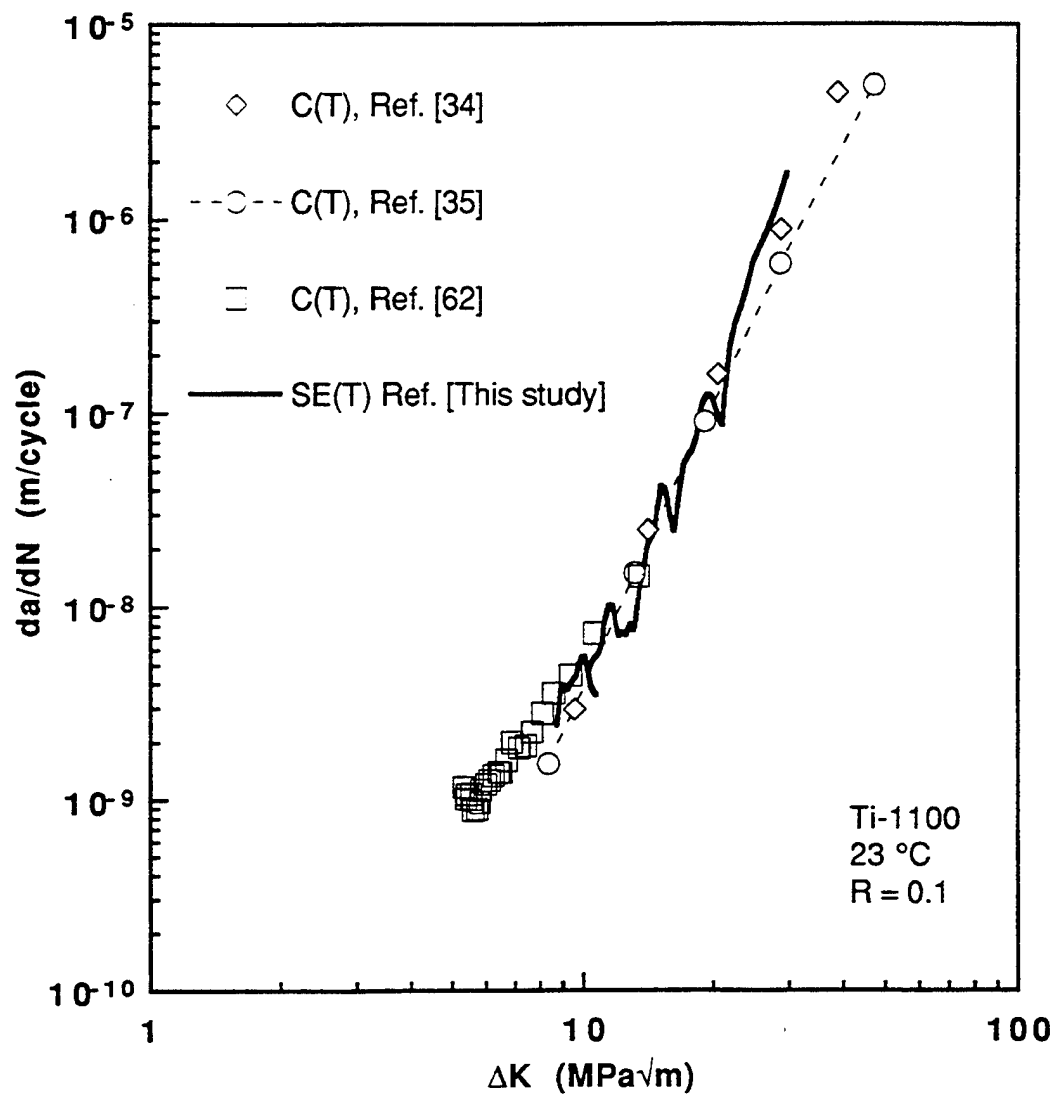


Figure 3.7 Comparison of crack growth ( $da/dN$ ) versus applied stress intensity factor range ( $\Delta K$ ) response of Ti-1100 obtained using  $SE(T)$  and  $C(T)$  geometries.

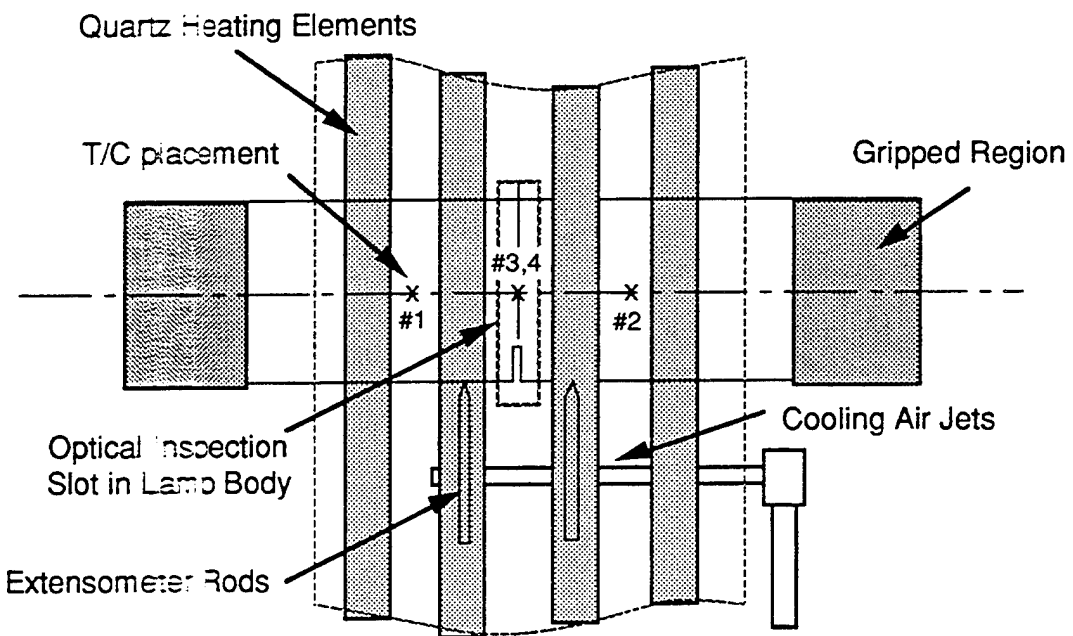


Figure 3.8 Typical experimental set-up for TMF crack growth test. Note position of thermocouples, cooling jets and optical inspection slot.

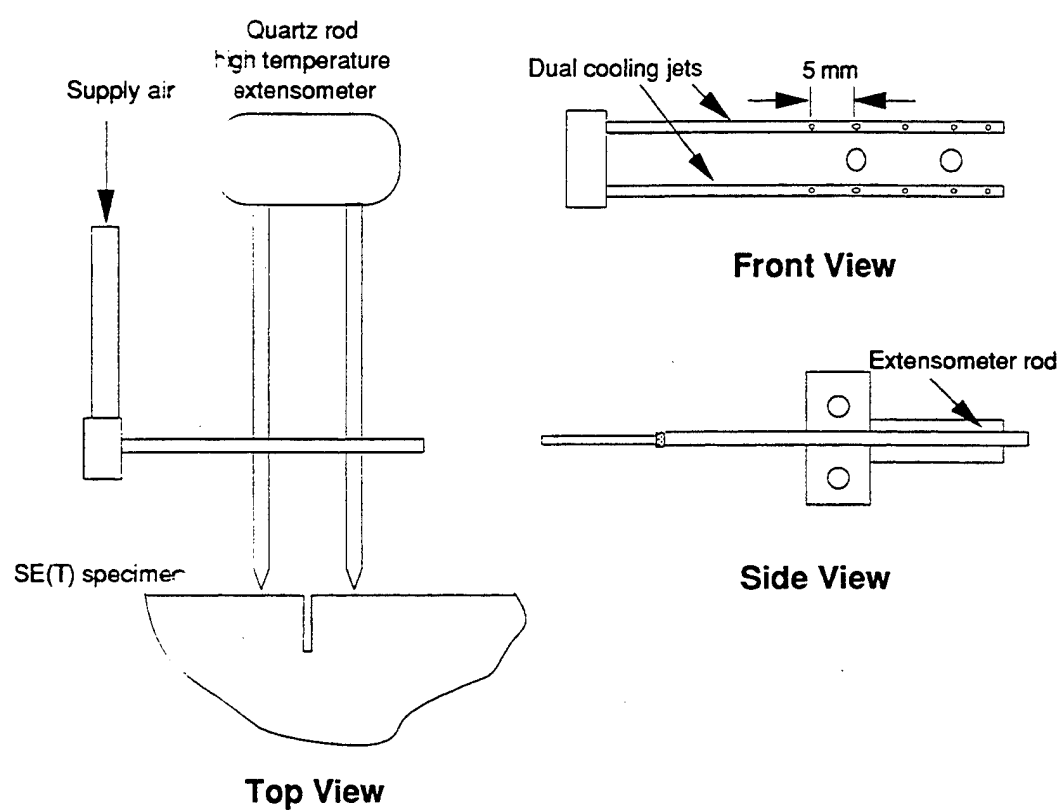


Figure 3.9 A 3-view schematic of the cooling system used on the thermomechanical fatigue crack growth tests.

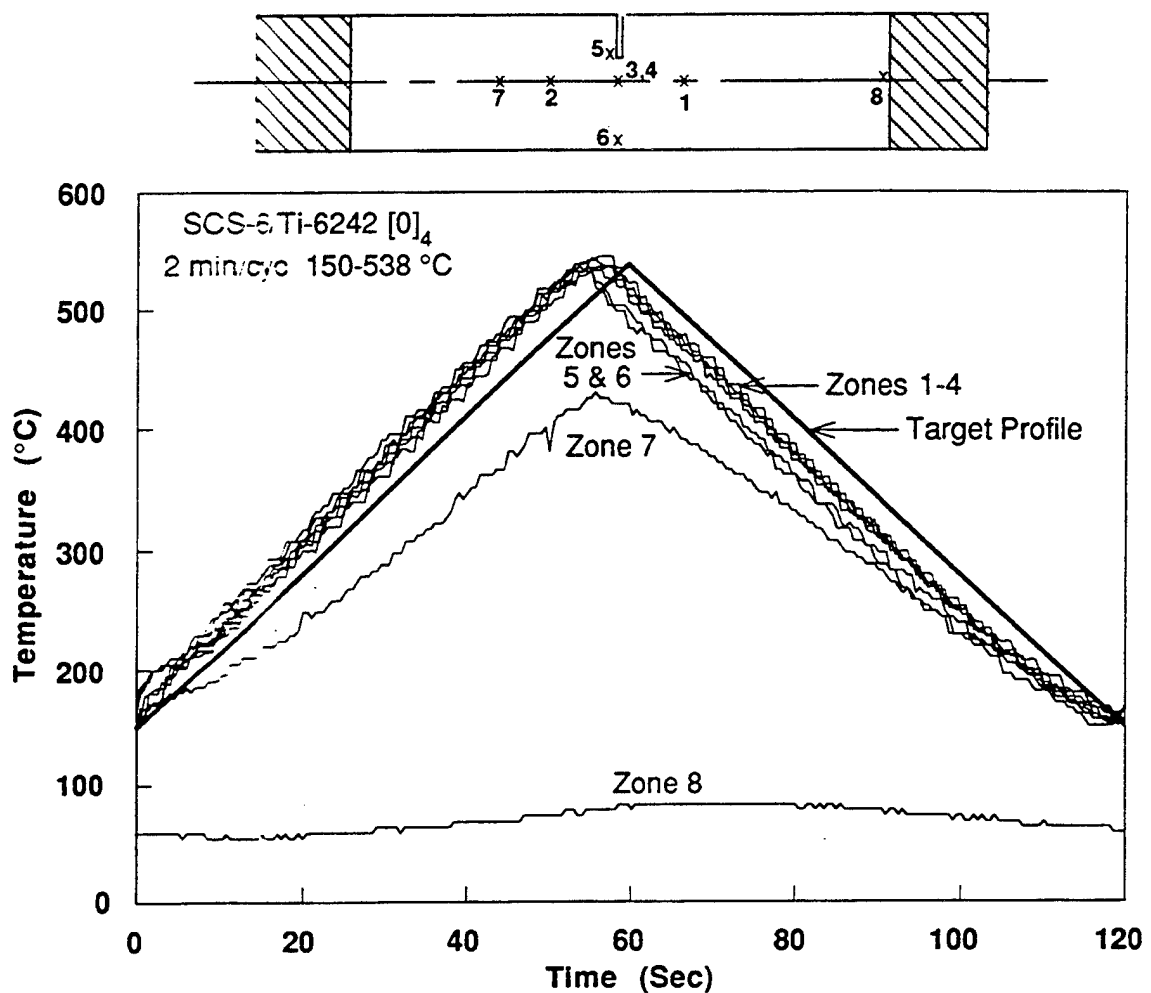


Figure 3.10 Plot of cyclic temperature profile over single edge notch specimen for a single 120 second temperature cycle between 538 and 150 °C (1000-300 °F).

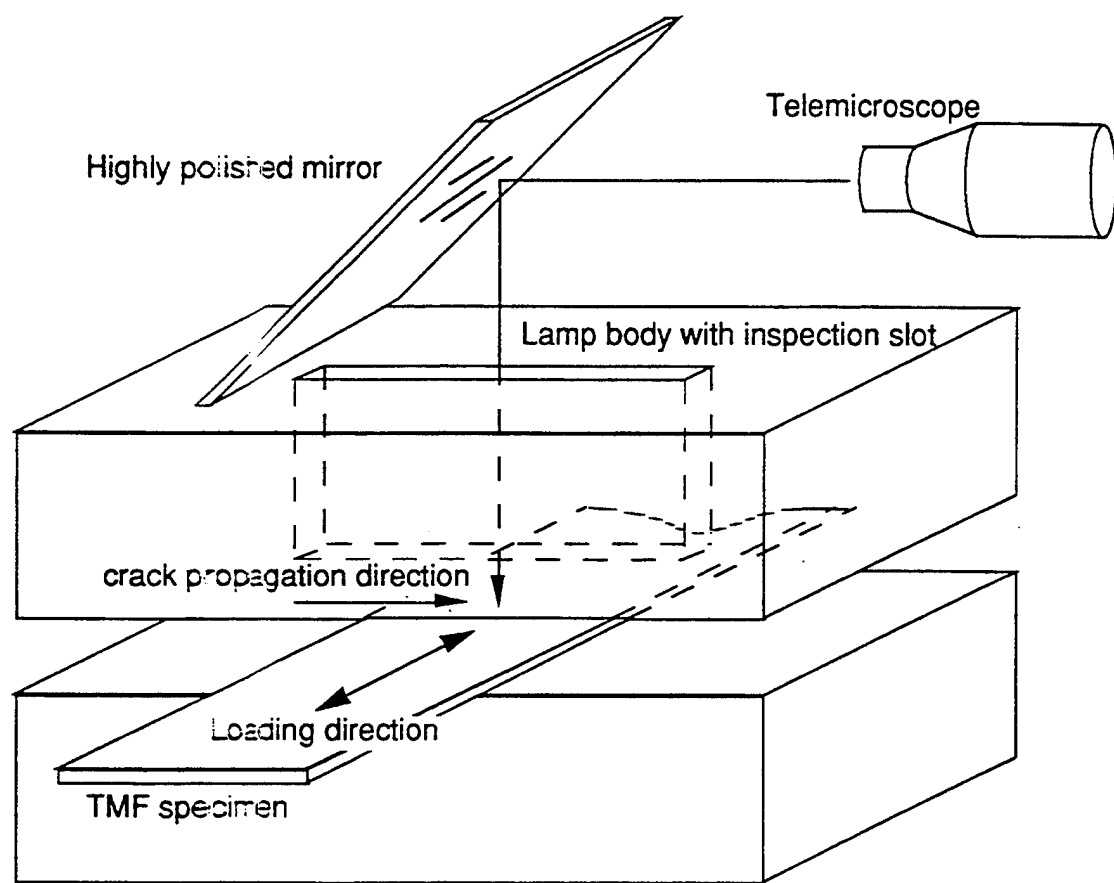


Figure 3.11 Set-up for visual inspection of crack propagation.

## CHAPTER 4

### INITIAL CHARACTERIZATION OF THE SCS-6/Ti-6Al-2Sn-4Zr-2Mo

Key material attributes of the SCS-6/Ti-6Al-2Sn-4Zr-2Mo used for this research effort were assessed by nondestructive evaluation and monotonic tests prior to any thermomechanical fatigue crack growth tests. These detailed evaluations gave credence to the assumption that the tested material was of "research quality." Prior experience with other "research material" has shown that a rigorous scrutiny of initial quality is essential to avoid the collection of batch-dependent data. For further discussion on the topic of composite material quality see Chapter 5 - A Systematic Check of Material Quality.

#### 4.1 Specimen Identification

An identification scheme was derived to track specimens used in the various tension, metallography, and fatigue crack growth studies. In the scheme, the panel number is first followed by a number representing the position of the specimen (numerically increasing from left to right) in the panel and then a letter designation to indicate what type of test was run with that specimen. The letter designations are as follows: M = metallography, ST = straight sidec tension, FCG = fatigue crack growth. For example, specimen G9A-3-FCG is the third fatigue crack growth specimen from a plate made by General Electric's Lynn, Massachusetts, Plant.

## 4.2 Nondestructive Evaluation

Nondestructive evaluation was the initial litmus test for the condition of the material after the consolidation process. As the name suggests, it is not harmful to the composite panel and can yield valuable information without altering the material's characteristics.

### 4.2.1 Ultrasonic C-scan

Each panel of the SCS-6/Ti-6242 was evaluated using a modified through-transmission technique called reflection plate inspection. These particular scans used a 10 MHz center frequency broadband transducer, 12.7 mm in diameter and spherically focused at 75 mm. Typical step sizes (distance between adjacent X,Y data acquisition locations) were 0.25 - 0.50 mm. This type of ultrasonic technique is often used to assess the consolidation quality of, and to detect defects in, metal matrix composites [42].

In this technique the panel is submerged in water and scanned with a sender/receiver ultrasonic transducer. The transducer's return signal is then processed, and results are shown in a color coded output of the panel that is used for interpretation. A schematic of the ultrasonic system used is shown in Figure 4.1. For a more detailed explanation of ultrasonic inspection see Ref. [43, 44]. A typical output (shown in gray scale format) of a single C-scan is shown in Figure 4.2. In the figure, panel G9A, a 4-ply unidirectional SCS-6/Ti-6242, is shown with shades ranging from light gray through spots of dark gray. Each shade represents some percent reduction of the sonic signal that is bounced back off the reflector plate to the transducer. The scale shown along with the panel in Figure 4.2 can be interpreted as white being a full return of

the original signal to the transducer (100% reflection) to black being nearly no return of the original signal to the transducer (100% absorption or scatter). Based on previous experience with composite panels and their C-scans, the ultrasonic signature of the panel in Figure 4.2 indicates that the mechanical properties should be uniform and that consolidation was successful.

#### 4.2.2 Radiographs

All panels were X-rayed prior to the machining of specimens as another form of nondestructive evaluation. Radiographs yield little information for fiberless panels; however, for fiber reinforced panels the fiber distribution becomes apparent. The radiographs are able to detect if fibers become bunched together or are somehow missing during consolidation. The x-ray for the G9A panel (Fig. 4.3) shows straight fibers with no apparent missing or bunching fibers. This information along with the data gathered from the ultrasonic C-scans indicates that this composite panel is of high quality.

#### 4.3 Metallographic Analysis

A representative sample of the G9A panel was mounted and polished to reveal the microstructure in three planar sections: the longitudinal, transverse and plane (Fig. 4.4). Photomicrographs were taken in each direction at different magnifications ranging from 100x to 500x. These micrographs were instrumental in determining the quality of the composite consolidation, as well as the condition of the microstructure. Figure 4.5 shows a 3-D view of the microstructure. As seen in the 3-D representation of the microstructure, the grain structure is similar in all views. There appears to be no texturing as a result of processing. The 300X magnification of fiber cross section in Figure

4.6 shows complete consolidation of matrix around the entire fiber circumference. This characteristic is an essential property of quality composite material.

#### 4.4 Monotonic Material Properties

Tensile properties, such as modulus and strain-to-failure, as well as coefficient of thermal expansion data as a function of temperature were collected. These data were necessary for modeling purposes, and for a cursory check of material quality.

##### 4.4.1 Tension Tests

Two room temperature tension tests were performed prior to any fatigue crack growth tests. The results of the tension tests are given in Table 4.1. For the tests where the final failure was outside the region monitored by the extensometer, the strain to failure was considered to be as great or greater than the strain measured by the extensometer, as indicated in Table 4.1 by use of the greater-than sign. The rule of mixture (ROM) values given in Table 4.1 for modulus and ultimate tensile strength were determined from the equations:

$$E_{comp} = v_f E_f + v_m E_m \quad (4.1)$$

and

$$\sigma_{ult,comp} = v_f \sigma_{ult,f} + v_m \sigma_{ult,m} \quad (4.2)$$

where f = fiber, m = modulus, comp = composite,  $v_f$  and  $v_m$  are the fiber and modulus volume fraction and  $v_f + v_m = 1$ . The fiber volume was determined by polishing with standard metallographic techniques a representative piece from

panel G9A and counting the number of fibers in a given cross section. The total fiber area was calculated, and a ratio of the total fiber area to the total cross sectional area was formulated; this represents the fiber volume fraction. The fiber volume fraction was determined to be 36.0 % which is within 2 % of the target volume fraction established by the manufacturer of  $38\% \pm 2\%$ . The modulus values at room temperature for the two composite specimens tested were nearly identical to those predicted by rule of mixtures. This fact, along with the results from the NDE and photomicrographs, reconfirmed that the SCS-6/Ti-6242 was well consolidated and research worthy material.

#### 4.4.2 Modulus and CTE as a Function of Temperature

The elastic modulus and coefficient of thermal expansion (CTE) properties of the composite were evaluated as a function of temperature. A straight sided specimen 5.57 mm (0.219 in) wide was loaded elastically in the longitudinal direction ( $\sigma_{max} \leq 200$  MPa (29 ksi)) at temperatures ranging from 22 to 815 °C (70-1500 °F). Similarly, another straight sided specimen 9.94 mm (0.391 in) wide was loaded elastically in the transverse direction ( $\sigma_{max} \leq 60$  MPa (8.7 ksi)) at temperatures ranging from 22 to 815 °C (70-1500 °F). In both cases a quartz rod high temperature extensometer was used to monitor composite displacement (strain). The specimen was allowed to stabilize and soak at temperature for approximately 5 minutes prior to application of the elastic load.

At room temperature and at zero load, a voltage was recorded from the extensometer that represented zero strain. At the higher isothermal temperatures the voltage was again read from the extensometer at zero load. The coefficient of thermal expansion was then calculated by taking the

difference in voltages, converting the difference to strain and dividing by the temperature difference between room and the elevated temperature.

The longitudinal data for modulus and CTE as functions of temperature are listed in Table 4.2. Likewise the data for the transverse properties are given in Table 4.3. In Figures 4.7 and 4.8 the data are plotted as a function of temperature for the modulus and CTE, respectively. Clearly, from Figure 4.7 the modulus for the longitudinal and transverse material decreases with increasing temperature as is normally expected. Also as expected the modulus is noticeably reduced for temperatures above 538 °C (1000 °F). The trend of the data for the CTE as a function of temperature given in Figure 4.8 follows predictions made for the same material by Bain [45].

Table 4.1 Monotonic tensile data for SCS-6/Ti-6242 (batch three).

Specimen ID	Temp °C (°F)	Layup	Modulus GPa (Msi)	UTS MPa (Ksi)	$\epsilon_f$ %
G1-1-DT	21 (70)	[0]4	221.20 (32.08)	>1778.46 (257.94)	>0.956
G1-2-DT	21 (70)	[0]4	210.55 (30.54)	1844.45 (267.51)	1.019
ROM	21 (70)	[0]4	216.81 (31.45)	1938.64 (281.18)	—

Table 4.2 Longitudinal modulus and CTE data as a function of temperature for panel G1, a 4-ply, unidirectional panel of SCS-6/Ti-6242 composite.

Temperature °C (°F)	Modulus GPa (Msi)	CTE (mm/mm/°C)
21 (70)	214.27 (31.08)	
150 (300)	211.78 (30.72)	5.271e-06
250 (482)	207.03 (30.03)	5.590e-06
350 (662)	200.87 (29.13)	5.957e-06
450 (842)	197.58 (28.66)	5.828e-06
538 (1000)	192.06 (27.86)	5.687e-06
650 (1200)	183.21 (26.57)	5.644e-06
760 (1400)	161.68 (23.45)	5.345e-06
815 (1500)	153.73 (22.30)	5.202e-06

Table 4.3 Transverse modulus and CTE data as a function of temperature for panel G1, a 4-ply, unidirectional panel of SCS-6/Ti-6242 composite.

Temperature °C (°F)	Modulus GPa (Msi)	CTE (mm/mm/°C)
21 (70)	145.79 (21.15)	—
150 (300)	140.68 (20.40)	6.900e-06
250 (482)	135.63 (19.67)	7.290e-06
350 (662)	130.76 (18.97)	7.810e-06
450 (842)	126.66 (18.37)	7.970e-06
538 (1000)	120.02 (17.41)	8.160e-06
650 (1200)	106.73 (15.48)	8.390e-06
760 (1400)	77.74 (11.28)	8.630e-06
815 (1500)	72.97 (10.58)	8.650e-06

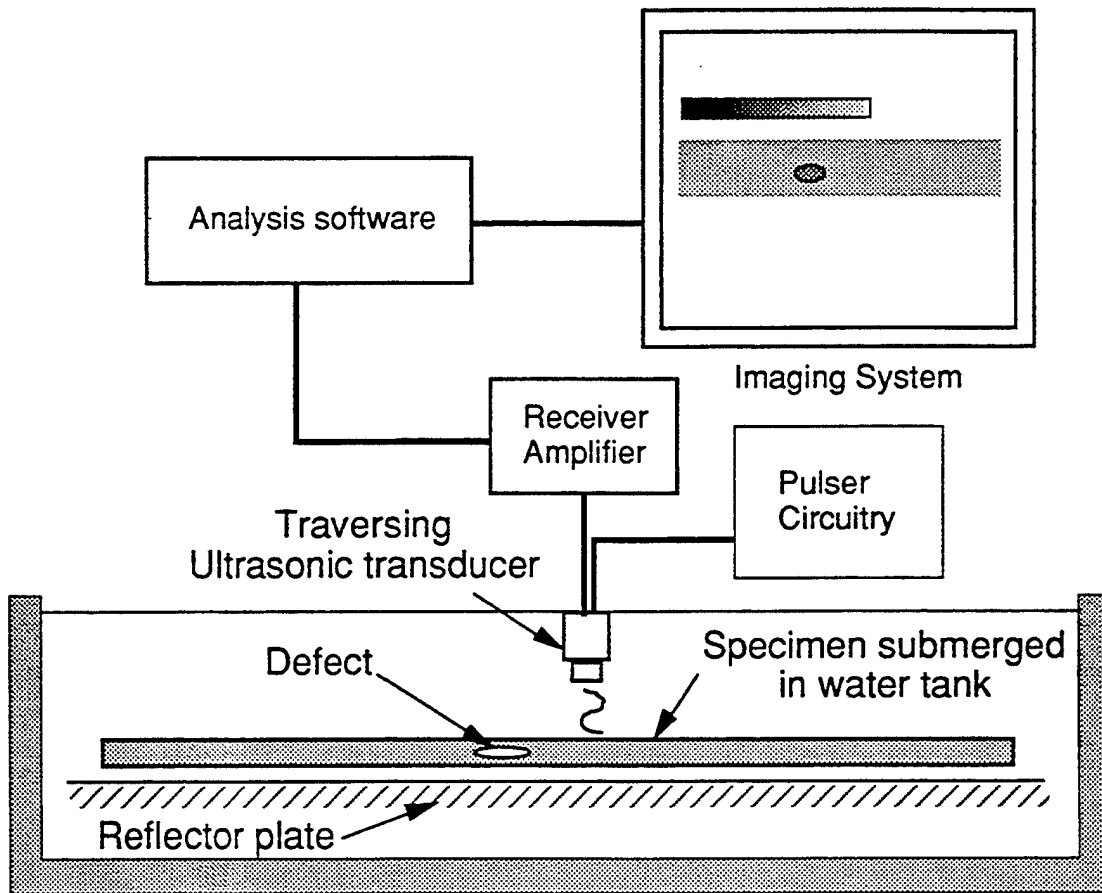


Figure 4.1 Schematic of the ultrasonic system used to evaluate the material for this study as well as the material described in Chapter 5.

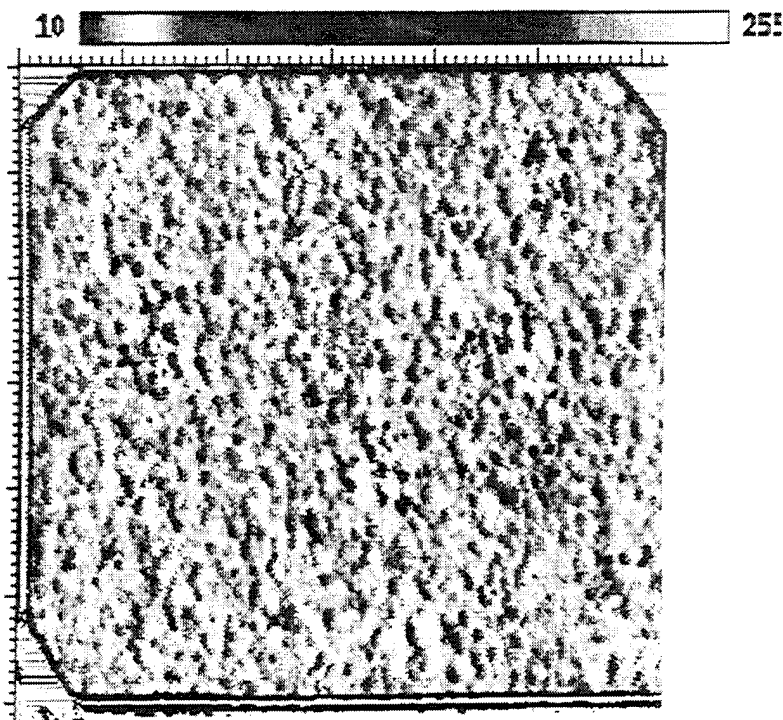


Figure 4.2 Representative ultrasonic reflector-plate C-scan of panel G9A, a 4-ply, unidirectional panel of SCS-6/Ti-6Al-2Sn-4Zr-2Mo composite.

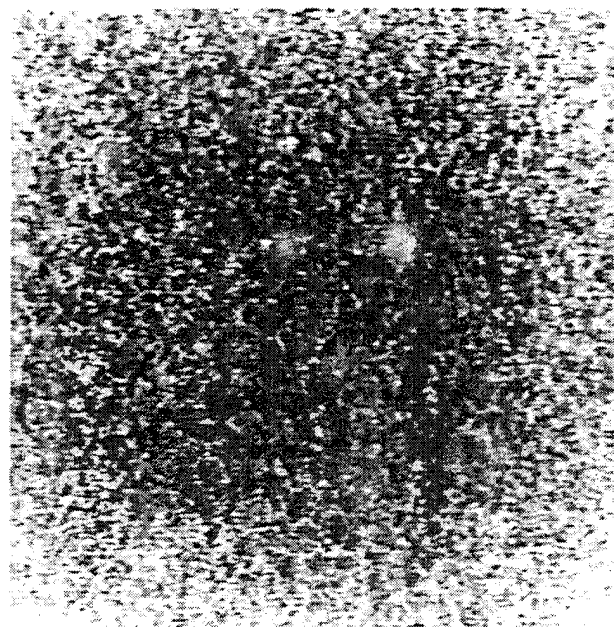


Figure 4.3 Representative radiograph (x-ray) of panel G9A, a 4-ply, unidirectional panel of SCS-6/Ti-6Al-2Sn-4Zr-2Mo composite.

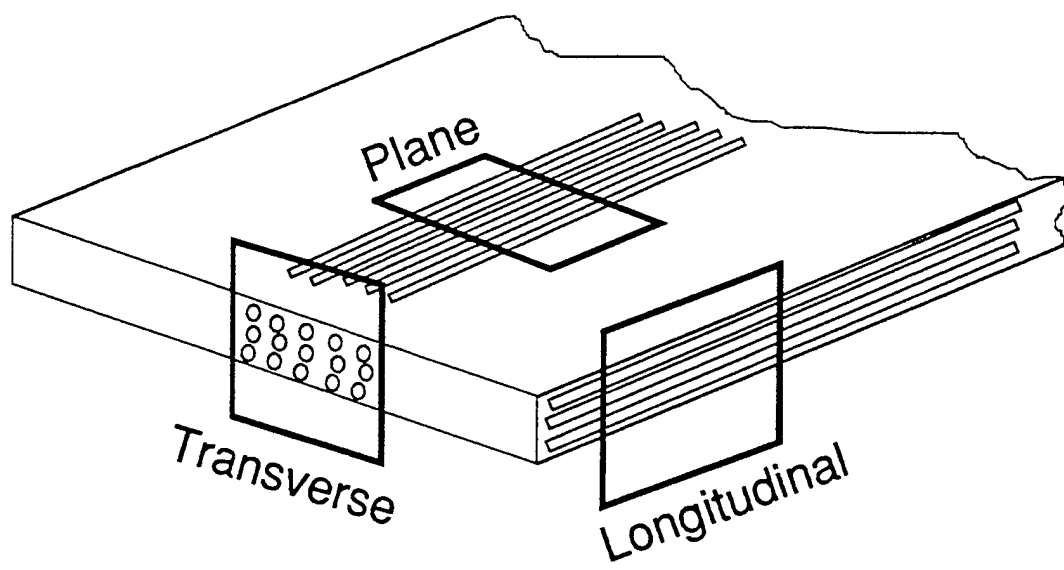


Figure 4.4 Schematic explaining location and orientation of the three different planes on which photomicrographs can be taken.

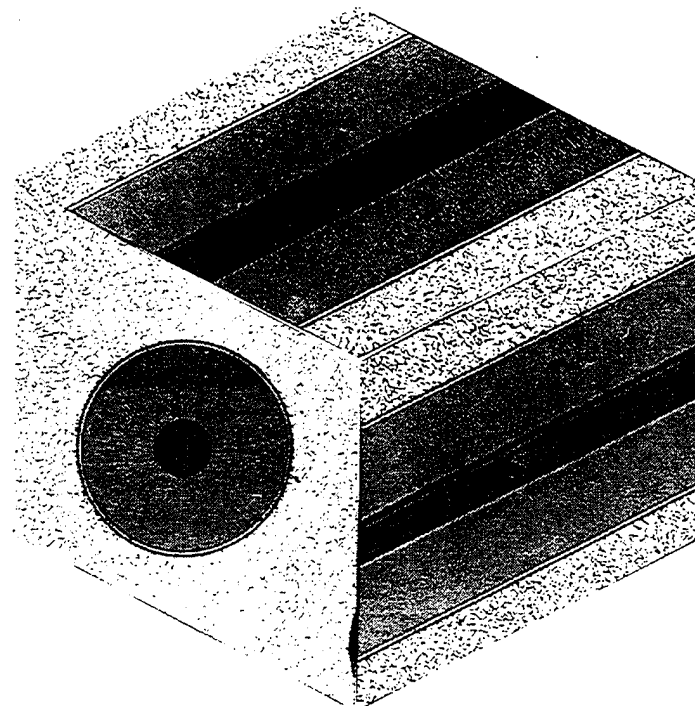


Figure 4.5 3-D representation of the SCS-6/Ti-6Al-2Sn-4Zr-2Mo microstructure used in this study.

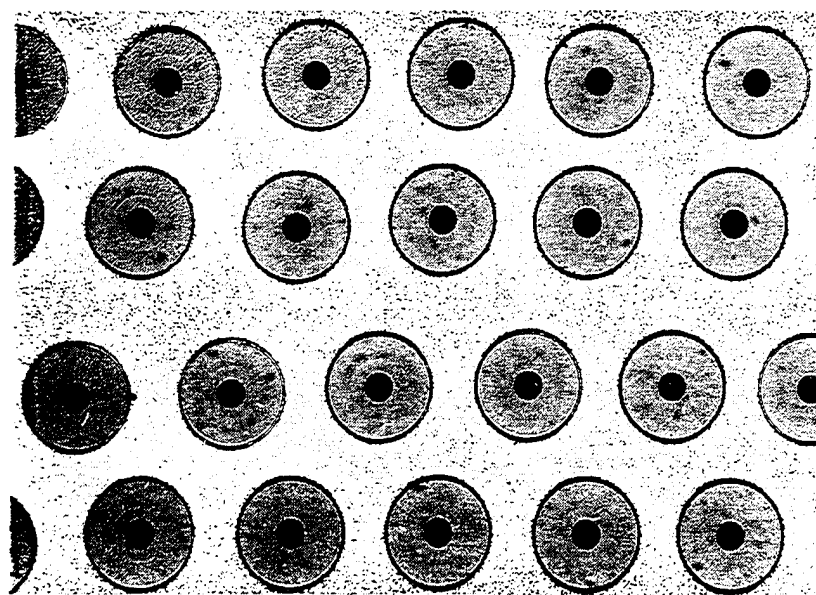


Figure 4.6 Transverse photomicrograph showing complete consolidation of the matrix around the fiber for SCS-6/Ti-6Al-2Sn-4Zr-2Mo.

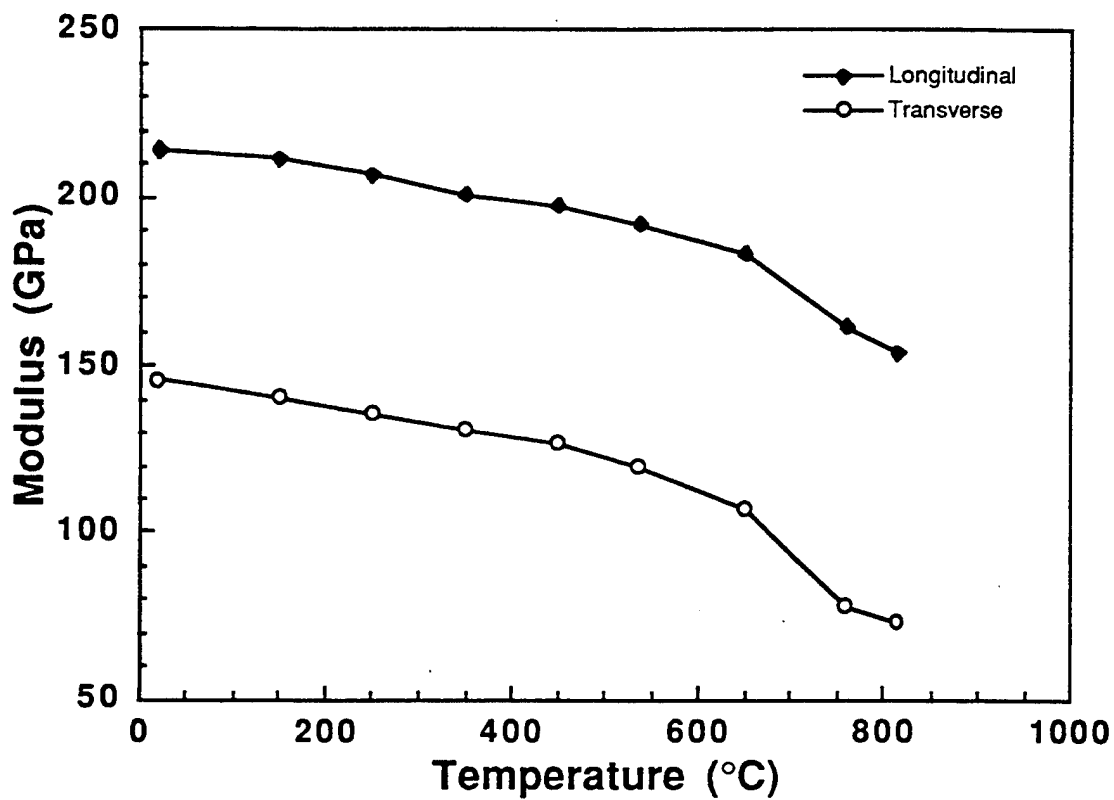


Figure 4.7 Elastic modulus as a function of temperature for the 4-ply unidirectional SCS-6/Ti-6Al-2Sn-4Zr-2Mo.

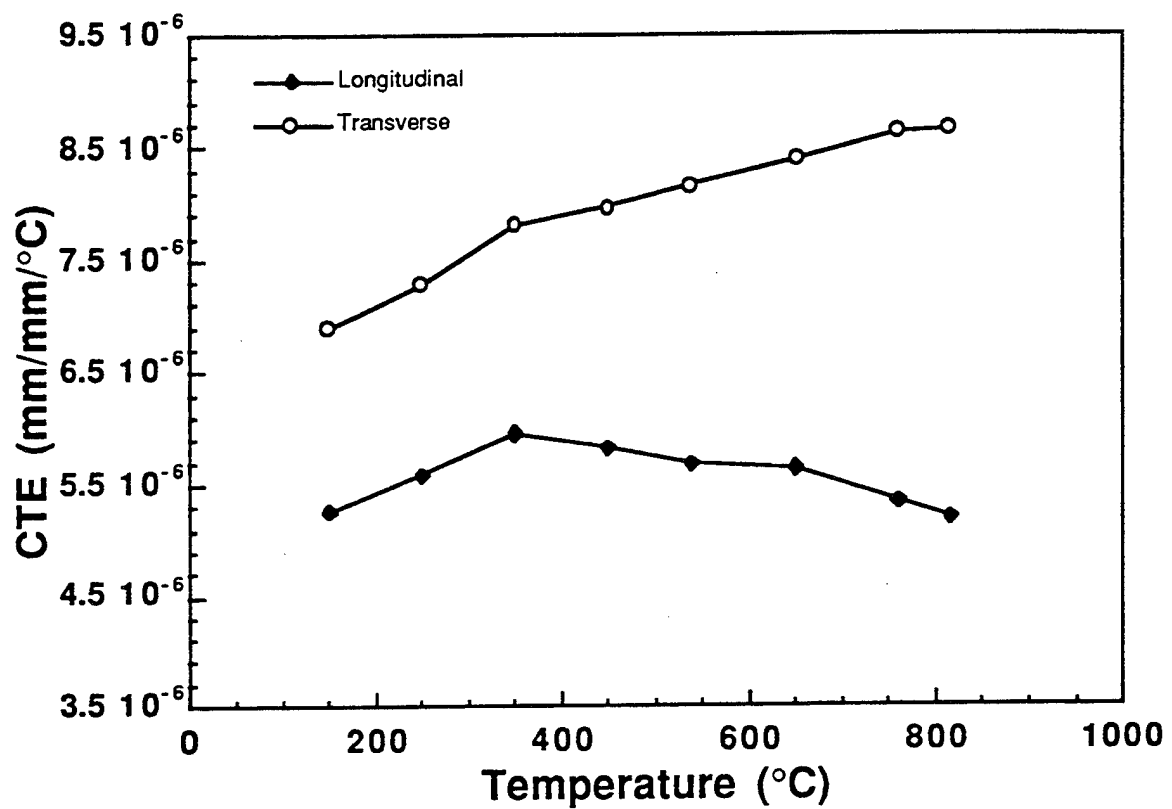


Figure 4.8 Coefficient of thermal expansion as a function of temperature for the 4-ply unidirectional SCS-6/Ti-6Al-2Sn-4Zr-2Mo.

## CHAPTER 5

### A SYSTEMATIC CHECK OF MATERIAL QUALITY

The technology for metal matrix composite manufacturing is still in the developmental stages, and variations in the consolidation process of the composite can greatly affects its mechanical properties. As testimony to the inability of manufacturers of metal matrix composites to consistently produce high quality material, the first two batches of material (from different sources) obtained for this research project were defective as a result of processing. The defects in these two batches consisted of incomplete consolidation of matrix around fiber and damage fibers due to processing. The third batch (again a different source) was properly manufactured with as-expected mechanical properties. This chapter explains in some detail the steps taken to assess the condition of each lot of MMC considered for this project. Nondestructive evaluation, metallographic analysis and tension tests were conducted to determine the quality of the composite material. These material evaluation procedures, although not inclusive, were able to give some indication of the material quality (e.g., stiffness, strength, consolidation uniformity, etc.) prior to the start of the thermomechanical fatigue crack growth tests.

### 5.1 Material Evaluated

Three different batches of metal matrix composite were considered for this research effort; chronologically, they were a foil-fiber-foil Sigma/Ti-6Al-2Sn-4Zr-2Mo, a plasma sprayed SCS-6/Ti-6Al-2Sn-4Zr-2Mo, and another plasma sprayed SCS-6/Ti-6Al-2Sn-4Zr-2Mo. Each batch was fabricated and consolidated by a different manufacturer. The first two batches contained defects due to improper consolidation while the third batch was correctly consolidated.

The first batch of material consisted of 15 plates 152 mm x 152 mm (6 in x 6 in) taken from four 305 mm x 305 mm (12 in x 12 in) panels. The layups of the 15 plates consisted of four fiberless, eight [0]4, and three [0/90]s. The second batch of material consisted of six 127 mm x 203 mm (5 in x 8 in) panels: three fiberless, three [0]4. The final batch of material was three 152 mm x 165 mm (6 in x 6.5 in) panels of [0]4. A more complete description of the pedigree of the final batch of material is found in Chapter 4 - Initial Characterization of the SCS-6/Ti-6Al-2Sn-4Zr-2Mo.

### 5.2 Nondestructive Evaluation

Before each material system was considered for use in this research project it was subjected to nondestructive evaluation to determine the quality of the material in the as-consolidated condition. Both ultrasonic inspection and radiography were used for this evaluation. The following discussion reveals that these methods provided necessary insight into the quality of each material system.

### 5.2.1 Ultrasonic C-scans

Each reinforced and fiberless panel of Ti-6242 was evaluated using an ultrasonic reflector plate C-scan technique. A more complete description of the ultrasonic system used is given in section 4.2.1. Typically, the ultrasonic system produces a color coded output that represents the extent of damage in a particular panel. The color output is often used to determine damage in the composite due to manufacturing. Recall from the discussion in section 4.2.1 the colors represent some percent reduction of the sonic signal that is bounced back off the reflector plate to the transducer, white being a full return of the original signal to the transducer (100% reflection) to blue (black in gray-scale) being nearly no return of the original signal to the transducer (100% absorption or scatter).

In work by Stubbs [46], the ultrasonic C-scans of composite isothermal fatigue specimens were able to indicate regions of poorly consolidated or damaged material prior to any mechanical testing. Stubbs correlated the location of fractured regions of the specimens and the percent reduction in residual strength from tension tests to regions where the ultrasonic signal was reduced by 50% or more. Stubbs' findings suggest that the mechanical properties (e.g., longitudinal ultimate strength) of a composite panel can be inhomogenous due only to processing conditions. The ultrasonic signature of a panel could, therefore, indicate regions having different mechanical properties (i.e., ultimate strength) because of nonuniform processing conditions (temperature, pressure and/or fiber spacing).

Representative ultrasonic C-scans of batches one, two, and three are shown in Figures 5.1, 5.2, and 4.2. The gray-scale shading shown in Figure 5.1 indicates attenuation (loss of return signal) is greater than 50 % for most of

the [0]4 plate. There also appears to be a pattern that is consistent with the three other plates that were cut from the same 152 mm x 152 mm (6 in x 6 in) panel. This pattern seems to be associated with the variation in temperature and/or pressure that occurred at the central portion of the panel and varied toward the outside edges. The shading pattern in Figure 5.1 and subsequent C-scans of other batch-one plates indicated a significant problem with the consolidation process used for this system. The metallographic discussion will further explain the problem with batch one.

The C-scans for the second batch of material (Fig. 5.2) contained randomly scattered spots of 50-70 % attenuation of ultrasonic signal. At first, these spots were attributed to the fairly irregular surface finish associated with the plasma-spray technique used for manufacturing this material system. The photomicrographs, however, uncovered the reason for the spots on the C-scans as discussed later in Section 5.4. Interestingly, the C-scans for batch one show a different color pattern than those of batch two, and in fact each batch suffers from different anomalies due to improper processing. The matrix material did not fully flow around the fiber in batch one, and the fibers were crushed during consolidation of batch two.

The material of batch three was clear of defects from an ultrasonic perspective. A more detailed discussion of the ultrasonic work for batch three is given in section 4.2.1. Incidentally, the fiberless material in batches one and two were also free of defects as indicated by their C-scans. This would tend to indicate that the presence of fibers complicates the processing and consolidation procedure.

### 5.2.2 Radiographs

Panels from each batch of material were X-rayed as another form of nondestructive evaluation. The radiographs yielded little, if any, information for the fiberless panels; however, for the fiber reinforced panels the fiber distributions became apparent. Representative radiographs of all batches are shown in Figures 4.3, 5.3, and 5.4. The radiographs are able to detect if, during consolidation, fibers become bunched together or are somehow missing. The fiber spacing phenomenon can and does lead to non homogeneity in material properties and is deemed undesirable. The radiographs for each batch of material show well aligned and evenly distributed fibers. This NDE technique does not indicate the same problems that the C-scans do; nonetheless the x-rays are an important technique to show common fiber abnormalities such as "fiber swimming" which leads to "fish eye" shaped regions in the fiber mats during consolidation.

## 5.3 Tension Tests

Although tension tests do not completely describe composite material quality, they do give some indication of the strength, stiffness, and strain-to-failure of the composite in a monotonic mode. Tension tests were performed on each batch of material. The tension test results (i.e., elastic modulus and ultimate strength) were compared, when applicable, to calculated values obtained from rule of mixtures (ROM). The appropriate formulas used in these calculations are given in Equations 4.1 and 4.2.

The tension data for each batch of material are presented in Tables 5.1, 5.2 and 4.1. For the Sigma/Ti-6242, the modulus values at room and elevated temperatures for both the fiberless and composite specimens were consistent

from panel to panel and within a particular panel. The average composite modulus at room temperature, however, was 12 % lower than that predicted by the rule of mixtures. Also, the average composite ultimate strength was 17 % lower than the rule of mixtures value. Again, these discrepancies indicated that batch one was not correctly consolidated and was not research worthy material. The phrase "not research worthy" also implies that it would not be, in most instances, suited for production components either.

The tension data obtained for batch two also indicated that the material did not have the expected mechanical properties. The data in Table 5.2 show that the modulus and ultimate tensile strength were lower than the ROM calculation by 13 % and 47 %, respectively. The strain to failure,  $\epsilon_f$ , was also only half of the expected strain to failure of about 1 %. Obviously these data illustrate that this batch of material had serious problems associated with its strength and strain-to-failure. The photomicrographs of this material make the tension data more understandable.

A complete description of the monotonic mechanical properties of the third batch of material is given in Section 4.4. These data show that the ultimate strength and modulus values are nearly equal to those predicted by ROM.

#### 5.4 Metallographic Analysis

Although the ultrasonic C-scans and radiographs yield useful information in a nondestructive manner, they are rarely conclusive without some further, usually destructive, analysis. One destructive technique employs photomicrographs commonly used to determine the condition of the microstructure and the quality of consolidation for composite systems.

Photomicrographs are high magnification photographs of highly polished representative samples of the material of interest. These photographs show great detail about the fiber/matrix interface and confirm complete consolidation, as well as the status of the fiber (i.e., fractured or not).

Each batch of material evaluated with nondestructive techniques was also evaluated with photomicrographs. The photomicrographs for the first batch of material are shown in Figure 5.5. The transverse cross section showing the fiber ends coming in and out of the page clearly indicate that the matrix does not fully encapsulate the fiber. This is the result of improper consolidation; that is, the temperature/pressure/time combination used during HIP'ing was not correct for this material system. Closer inspection of the matrix material tends to support the idea that the temperature during HIP'ing was too low and did not allow the matrix to flow around the fiber. The voids around the fiber help explain why the tension results (Table 5.1) were consistently lower than those computed by ROM. The ROM calculations did not assume part of the composite volume had zero modulus and strength. The photomicrographs confirmed the suspicions that the ultrasonic C-scans raised; this batch of material was unsuitable for the research effort considered in this thesis.

When the second batch of material became available, only the transverse cross section was inspected with the photomicrographs. The photomicrograph in Figure 5.6 shows complete consolidation of matrix around the fiber. After seeing this result, the conclusion was made that the spotty behavior of Figure 5.2 was due to the surface finish, and tension tests soon followed. The results of the tension tests (Table 5.2), however, prompted further investigation into the composite quality. The photomicrographs of the longitudinal view in Figure 5.7 again clearly show why the computed modulus

and strength differ from the experimental values. The fibers were severely damaged (broken and crushed) during the HIP'ing possibly due to excessive pressure or pressure applied at the incorrect time. This new information about this material's integrity ruled out this batch for use in this thesis study.

The photomicrographs in Figure 4.6 of the final batch of SCS-6/Ti-6242 indicate that this material was properly consolidated. Accordingly, the tension test results closely matched the ROM values (see Table 4.1). With the new understanding gained by the experiences of the first two batches of material, this third batch of material was deemed research worthy.

### 5.5 Summary of Findings

The manufacturing of metal matrix composites is a complex series of calculated steps that are supposed to produce consistent-quality composite material. Unfortunately, the current state of the technology requires that even the most trusted consolidation techniques be suspect and held accountable when producing any composite. The evaluation techniques described in the previous sections are essential for determining the integrity of a material's composition prior to investing effort in a particular research project or constructing composite structures. The nondestructive ultrasonic C-scans and radiographs provide efficient and relatively effortless methods to examine the internal condition of a composite without causing harm to the material. If the NDE work is then followed with metallographic analysis (photomicrographs) of the mutually orthogonal planes, the composite could then be judged suitable or not. Furthermore, tension test results can also confirm material quality based somewhat on their correlation to rule-of-mixture calculations.

To efficiently characterize the quality of a composite panel the following steps should be followed in sequence: 1) perform ultrasonic C-scans of *all* panels of interest, 2) make radiographs of all panels. 3) take photomicrographs on *all* planes of a representative section of material, 4) if steps 1-3 reveal no deficiencies, consider room temperature tension tests to check correlation with rule-of-mixture values for modulus and strength. If steps 1-4 produce no abnormalities the composite is most likely quality material.

Table 5.1 Tension test results for the fiberless Ti-6242 and Sigma/Ti-6242.

Specimen ID	Temp °C (°F)	Layup	Modulus GPa (Gsi)	UTS MPa (Ksi)	$\epsilon_f$ %
2-2DT	21 (70)	fiberless	100.506 (14.577)	898.819 (115.340)	25.88691
2-6DT	21 (70)	fiberless	100.670 (14.601)	859.607 (110.308)	*
2-8DT	21 (70)	fiberless	107.630 (15.610)	972.027 (124.734)	>21.95196
6-2DT	21 (70)	[0]4	171.926 (24.936)	1375.000 (176.446)	>0.92946
6-6DT	21 (70)	[0]4	179.194 (25.990)	1366.227 (175.320)	0.88713
8-2DT	21 (70)	[0]4	172.113 (24.963)	1524.554 (195.637)	>1.05135
6-4ST	21 (70)	[0]4	174.185 (25.263)†		
6-7ST	21 (70)	[0]4	170.059 (24.665)†		
8-5ST	21 (70)	[0]4	166.857 (24.200)†		
ROM	21 (70)	[0]4	196.400 (28.485)	1719.600 (249.407)	
6-4ST	538 (1000)	[0]4	154.536 (22.413)	1081.852 (138.828)	>0.79893
6-7ST	538 (1000)	[0]4	149.084 (21.623)	1009.570 (129.552)	0.74145
8-5ST	538 (1000)	[0]4	145.734 (21.137)	963.936 (123.696)	0.72668

† Room temperature modulus check for the straight sided geometry to be tested at elevated temperature.

Table 5.2 Monotonic tensile data for SCS-6/Ti-6242 (batch two).

Specimen ID	Temp °C (°F)	Layup	Modulus GPa (Msi)	UTS MPa (Ksi)	$\epsilon_f$ %
A1-DTL	21 (70)	[0]4	175.36 (25.43)	930.50 (134.95)	0.569
A2-DTL	21 (70)	[0]4	170.60 (24.74)	849.94 (123.27)	0.519
ROM	21 (70)	[0]4	199.42 (28.92)	1679.73 (243.62)	—

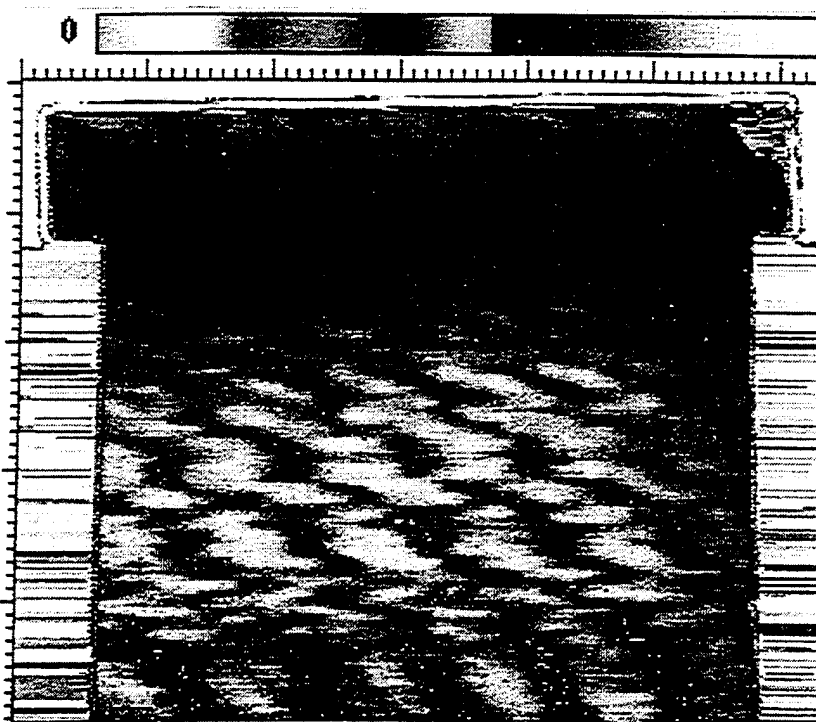


Figure 5.1 Representative ultrasonic reflector-plate C-scan of the 4-ply, unidirectional panel of Sigma/Ti-6Al-2Sn-4Zr-2Mo composite.

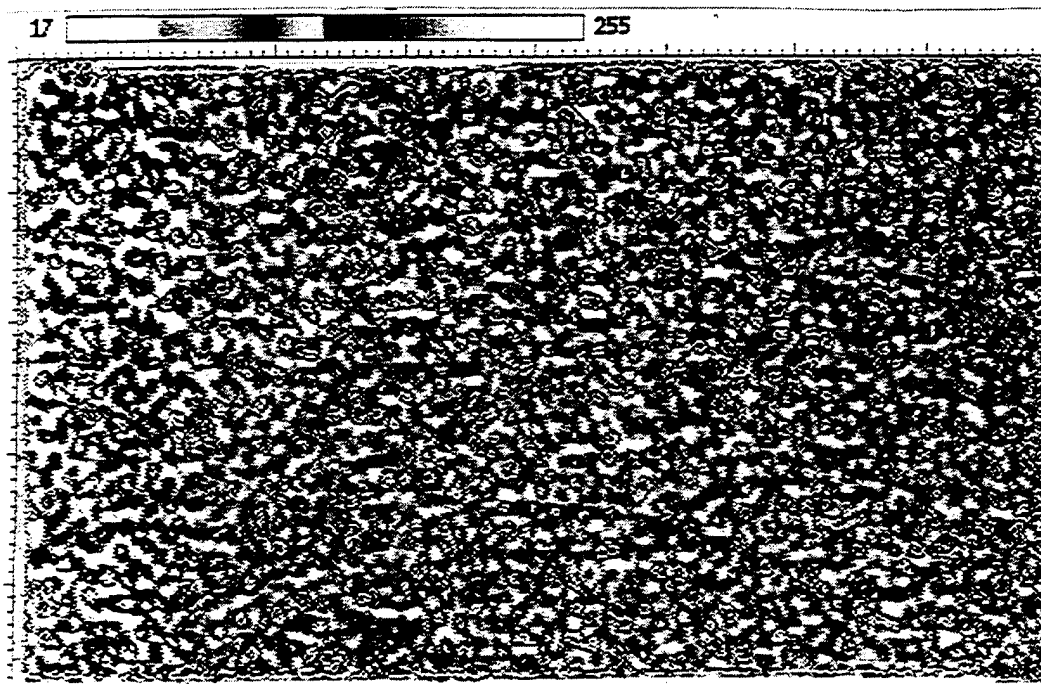
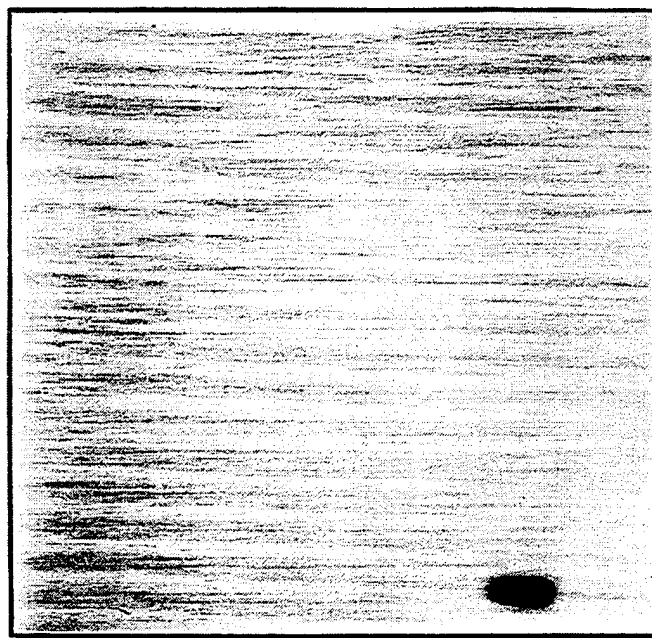
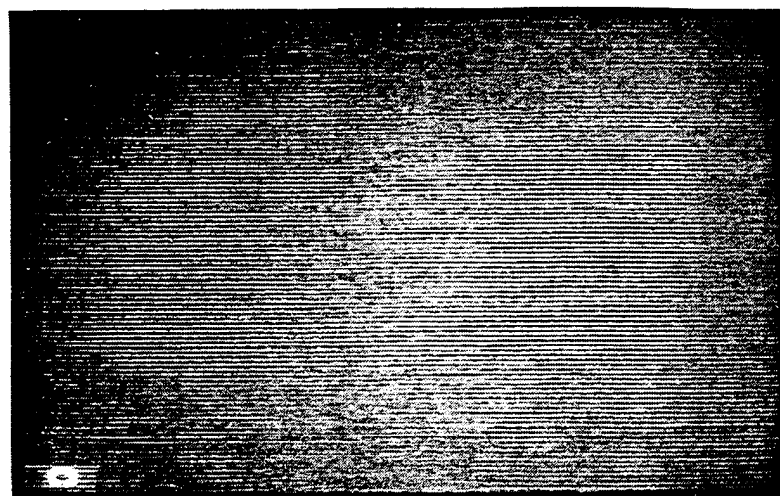


Figure 5.2 Representative ultrasonic reflector-plate C-scan of the 4-ply, unidirectional panel of SCS-6/Ti-6Al-2Sn-4Zr-2Mo composite (batch two).



**Figure 5.3** Representative radiograph (x-ray) of the 4-ply, unidirectional panel of Sigma/Ti-6Al-2Sn-4Zr-2Mo composite.



**Figure 5.4** Representative radiograph (x-ray) of the 4-ply, unidirectional panel of SCS-6/Ti-6Al-2Sn-4Zr-2Mo composite (batch two).

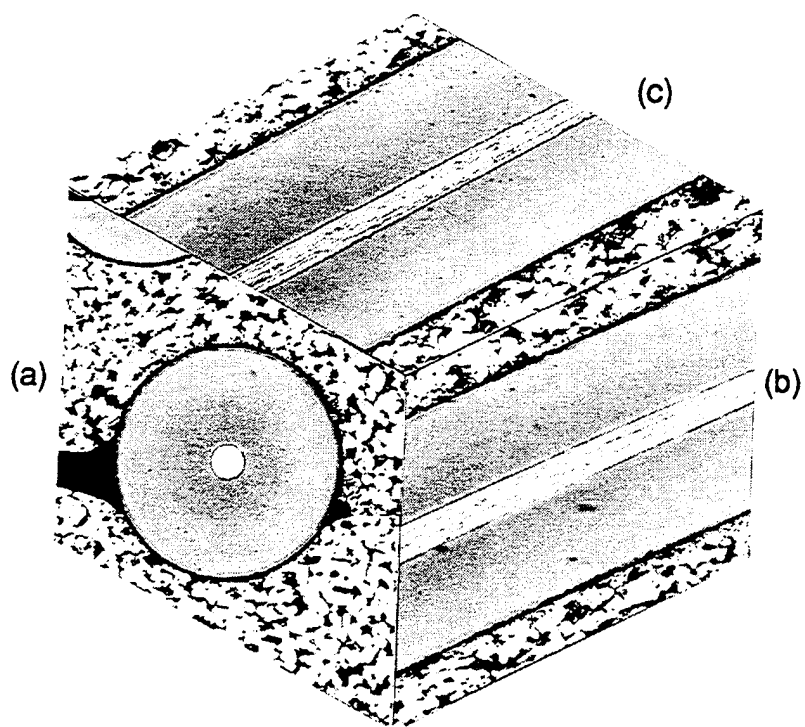


Figure 5.5 Photomicrographs of the (a) transverse, (b) longitudinal and (c) plane cross section of the Sigma/Ti-6Al-2Sn-4Zr-2Mo composite.

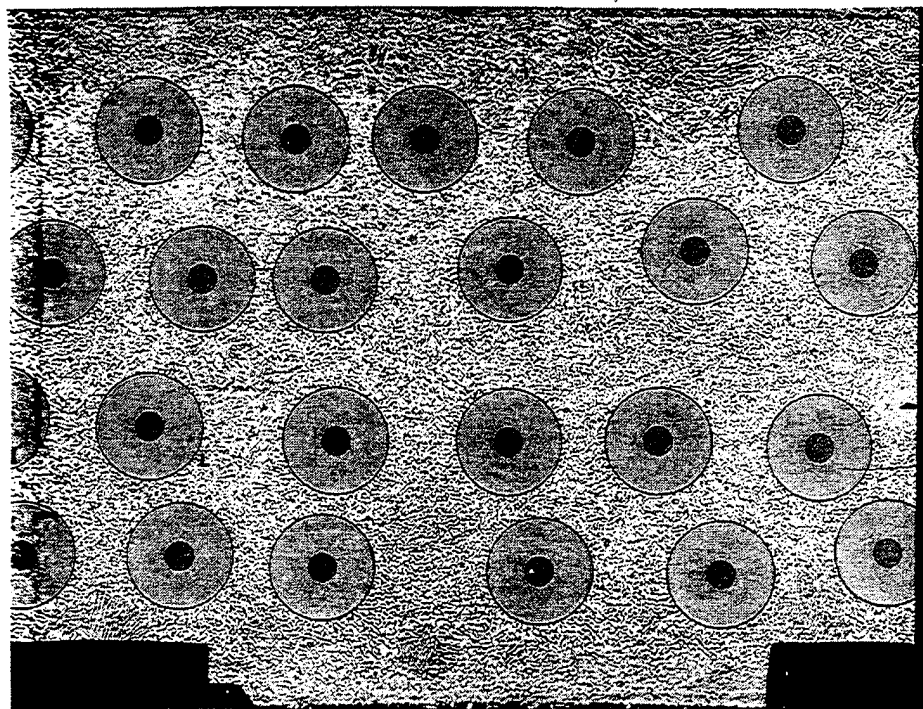


Figure 5.6 Photomicrograph of the transverse cross section of the SCS-6/Ti-6Al-2Sn-4Zr-2Mo composite (batch two).

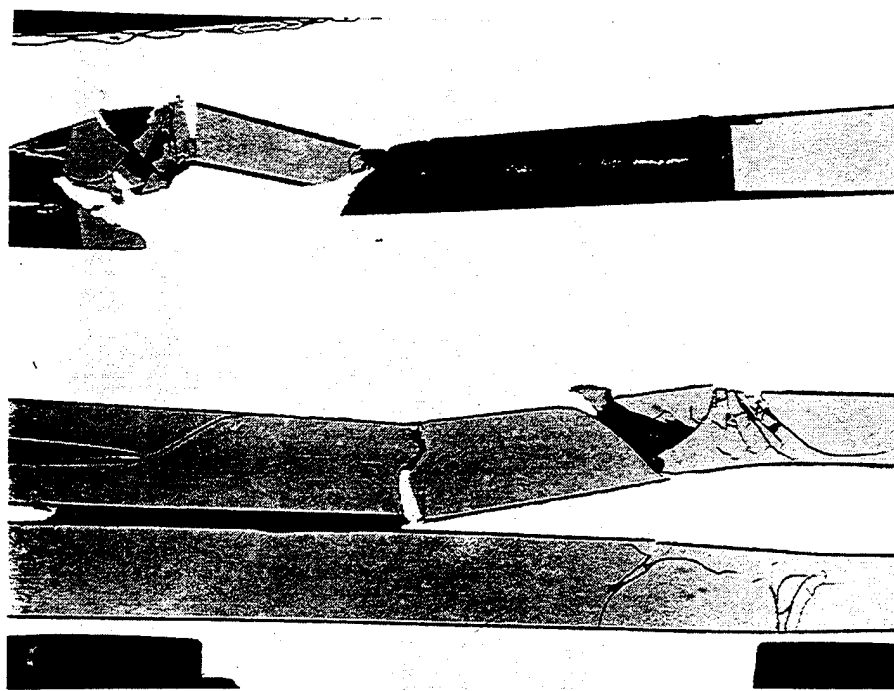


Figure 5.7 Photomicrograph of the longitudinal cross section of the SCS-6/Ti-6Al-2Sn-4Zr-2Mo composite (batch two).

## CHAPTER 6

### DEVELOPMENT OF A NEW STRESS INTENSITY FACTOR SOLUTION

This chapter explains the necessity and methodology for developing stress intensity factor and compliance solutions for a single edge notch specimen with clamped ends. Much of the discussion that follows is taken from two publications [47, 48] co-authored by the author and his colleagues.

Recent experimental work has shown that the single edge notched (SE(T)) geometry with clamped ends is well suited for fatigue crack growth testing of metal matrix composites and thin monolithic materials [49, 50]. In conventional fatigue crack growth tests of monolithic materials, the SE(T) specimens are generally pin-loaded allowing unconstrained rotation at the ends. However, for fiber reinforced composites the pin-loaded end-condition is unsuitable because of the likelihood of bearing failure at the hole. Such failure at the hole can be avoided by using friction grips (see Figure 3.5) to load the SE(T) specimen resulting in a *clamped* end condition.

Automated fatigue crack growth testing requires an expression for the stress intensity factor and a nonvisual method for determining crack length. The load versus crack mouth opening displacement (CMOD) data provide a convenient measure of specimen compliance from which the crack length can be computed. Several investigators [51-55] have proposed linear elastic fracture mechanics (LEFM) solutions of the stress intensity factor for the SE(T)

specimen with clamped ends for various height-to-width ratios. However, LEFM solutions for the CMOD of an SE(T) with clamped ends are not available in the literature.

### 6.1 Available LEFM Solutions

The clamped end condition implies rotationally constrained ends with uniform end displacements. A schematic of the SE(T) with clamped ends is shown in Figure 6.1, in which W=width, H=height, B=thickness, a=crack length, and  $\sigma_{app}$ =far-field stress applied at the clamped ends. The analyses by Marchand, et al. [53] and Ahmad, et al. [54] produced stress intensity factor solutions for a wide range of H/W and a/W. Those solutions are based on the superposition of stress intensity factors due to remote uniform stress and bending stress distributions such that the resultant rotations of the edges are zero, and the displacements ( $v$ ) at  $y = \pm H/2$  are uniform as shown in Figure 6.1. Using the above conditions, Marchand, et al. [53] and Ahmad, et al. [54] derived the following equations for the stress intensity factor (K) for an SE(T) with clamped ends,

$$K = \sigma_{app} \sqrt{\pi a} F \quad (6.1)$$

where

$$F = F_T - 6 \xi_1 F_B \quad (6.2)$$

The functions  $F_T(a/W)$  and  $F_B(a/W)$  are the geometry correction factors found in Ref. [36] for a pin-loaded SE(T) subjected to uniform remote tension and pure bending loads, respectively. The expression for  $\xi_1$  [54] is given by

$$\xi_1 = \frac{\xi_2}{\xi_3 + 12 \frac{H}{W}} \quad (6.3)$$

where

$$\xi_2 = \frac{12\pi}{W^2} \int_0^a a' F_T(a'/W) F_B(a'/W) da' \quad (6.4)$$

$$\xi_3 = \frac{72\pi}{W^2} \int_0^a a' F_B^2(a'/W) da' \quad (6.5)$$

Solving eqs 6.1 - 6.5, we obtain stress intensity factors for any  $a/W$  and any  $H/W \geq 1.0$ .

Figure 6.2 shows the function  $F$  generated using eqs 6.1 - 6.5, for  $H/W = 4$  and  $24$ . Eqs 6.4 and 6.5 were numerically integrated using the Chebyshev scheme. Alternate series expressions for  $\xi_2$  and  $\xi_3$  are given in Ref. [54]. The analytical solution of Marchand et al. [53] compares well with the finite element results of Dao and Mettu [55], as shown in Figure 6.2. The solution for an SE(T) with pin-loaded ends [36] is also shown in the same figure. The absence of free rotation at the ends of the clamped geometry significantly decreases the value of  $K$  for a given crack length compared with an SE(T) with pin-loaded ends. The difference increases with increasing  $a/W$  and decreasing  $H/W$ . Harris' [51] asymptotic solution based on an external circumferential crack in an infinitely long cylinder appears to yield a lower bound solution as shown in Figure 6.2. The solutions of Marchand et al. [53] and Dao and Mettu [55] also correlate well with the results of Bowie et al. [52], which are available for  $a/W$  up to 0.7.

The stress intensity factor solution for an SE(T) with clamped ends is significantly dependent on the height-to-width ratio as shown in Figure 6.2. The ratio of  $F$  for a clamped SE(T) to  $F$  for a pin-loaded SE(T), i.e.  $F/F_T$ , is plotted as a function of  $H/W$  for different values of  $a/W$  in Figure 6.3. Note that both geometries are subjected to remote tension stress. The ratio of 1.0 implies that the clamped SE(T) behaves like the pin-loaded SE(T). As shown in Figure 6.3, the  $K$  for a clamped SE(T) is significantly lower than that of a pin-loaded SE(T), even for  $H/W > 10$ .

## 6.2 Finite Element Analysis

A linear elastic finite element analysis was conducted to obtain the crack mouth opening displacement as a function of  $a/W$  for the SE(T) with clamped ends. A by-product of the analysis was an independent check of the stress intensity factor solutions found in ref. [53-55]. The finite element package ADINA [56] was used to conduct the analysis for crack length to width ratios ranging from 0.05 to 0.95. A typical finite element mesh is shown in Figure 6.4a, where  $H/2 = 2.0$  mm,  $W = 1.0$  mm, and  $a/W = 0.5$ . The value of  $H/W = 4$  was chosen based on the optimum usage of material and dimensions required to conduct elevated temperature tests using the quartz heating lamps. In the finite element model, eight-noded plane stress quadrilateral elements were used with Young's modulus ( $E$ ) of  $1.0 \times 10^4$  Pa, Poisson's ratio ( $\nu$ ) of 0.3 and a thickness ( $B$ ) of 0.125 mm. Around the crack tip, quarter-point singular elements [57] were used to simulate the singularity at the crack tip as shown in Figure 6.4b.

The stress intensity factor ( $K$ ) was computed from the crack tip quarter point displacements using [57-59],

$$K = \frac{2G}{\lambda+1} \sqrt{\frac{8\pi}{L}} v_b \quad (6.6)$$

Here  $v_b$  is the displacement of the quarter-point node of the crack tip element on the crack face,  $L$  is the length of the quarter-point element,  $G$  is the shear modulus, and for plane stress conditions

$$\lambda = (3 - \nu) / (1 + \nu) \quad (6.7)$$

The geometry correction factor,  $F$ , was calculated from the finite element results by rearranging eq. 6.1 as

$$F = \frac{K}{\sigma_{app} \sqrt{\pi a}} . \quad (6.8)$$

The accuracy of the finite element mesh used in this study was verified by simulating the pin-loaded end condition with a constant tension stress. The ends were allowed to rotate freely and the mesh anchored at the crack tip. The  $K$  values from the finite element analysis for  $0.1 \leq a/W \leq 0.9$  were within 1% of the handbook solutions [36]. In the finite element analysis conducted by Dao and Mettu [55], a uniform displacement was applied at the clamped ends and the average stress along the ends was used to determine the geometry correction factor. For this study, a constant stress was applied along the ends and the multipoint constraint (MPC) feature available in ADINA was used to ensure uniform displacement along the ends. The MPC condition forced the nodes along the top edge to displace the same amount as the corner node in

the loading direction. An additional condition ensuring zero displacement in the x-direction along the top edge was also imposed. For  $a/W = 0.5$ , the two methods gave almost identical results for  $K$ .

Using the MPC method, the finite element analysis was used to determine the geometry correction factors and nondimensionalized CMOD for different  $a/W$ . The geometry correction factors determined from the finite element analysis are compared with the results of Marchand et al. [53], Ahmad et al. [54], Dao and Mettu [55] and Bowie et al. [52] in Table 6.1. The difference between the results is within 1.5 % up to  $a/W = 0.95$ . A seventh order polynomial was fit to the finite element results to obtain a series expression for  $F(a/W)$ . The polynomial is of the form

$$F(\alpha) = \frac{1}{(1-\alpha)^{3/2}} \sum_{i=1}^8 m_i \alpha^{i-1} \quad (6.9)$$

where  $\alpha = a/W$ . The coefficients,  $m_i$ , for eq. 6.9 are reported in Table 6.2. The coefficient  $m_1$  was fixed at 1.122 to agree with the limiting value of  $F$  when  $a/W \rightarrow 0$  [36]. Equation 6.9 agrees with the finite element results within  $\pm 0.10\%$ . Note that eq. 6.9 is valid for  $H/W = 4.0$  only. As discussed earlier, single edge notched specimens with different height-to-width ratios will have different coefficients for eq. 6.9.

The nondimensionalized CMOD from the finite element analysis was fit with a polynomial of the form

$$\frac{a}{W}(U) = \sum_{i=1}^6 q_i U^{i-1} \quad (6.10)$$

where

$$U = \frac{1}{\sqrt{EBC} + 1} \quad (6.11)$$

and C is the compliance = CMOD/(\sigma<sub>app</sub>BW). Equation 6.10 is valid in the range 0.1 ≤ a/W ≤ 0.95. The coefficients, q<sub>i</sub>, in eq. 6.10 are reported in Table 2. Equation 6.10 agrees with the finite element results within ±0.45 %. Figure 6.5 shows a plot of a/W as a function of compliance for the SE(T) with clamped and pin-loaded ends. For short crack lengths the compliance is almost identical for both end conditions, but the difference becomes significantly greater at longer crack lengths (a/W > 0.3).

Another useful expression is the compliance as a function of crack length, as given by the following equation,

$$U(a/W) = \sum_{i=1}^6 t_i (a/W)^{i-1} \quad (6.12)$$

valid in the range 0.1 ≤ a/W ≤ 0.95. The coefficients, t<sub>i</sub>, in eq. 6.12 are reported in Table 6.2. Equation 6.12 agrees with the finite element results within ±0.15 %. The experimental validation of the above LEFM solutions for K and CMOD is discussed next.

### 6.3 Experimental Validation

Equation 6.1 implies that the effect of K produced by low stress and long crack length is equivalent to the effect of K produced by high stress and short crack length if the K values at both crack tips are the same. For a material that behaves according to LEFM, the fatigue crack growth rate should be

independent of crack length if the K values and other test conditions are identical. A valid K solution must satisfy the above condition of fatigue crack growth rate being only a function of the applied stress intensity factor range and independent of geometry under identical environmental conditions. Therefore, fatigue crack growth tests were conducted using SE(T) specimens with clamped ends to verify eqs (6.1) and (6.10).

### 6.3.1 Material and Test Specifications

The experimental results described in this study are from two different materials: a monolithic titanium alloy, Ti-1100; and a silicon carbide fiber reinforced titanium matrix composite, SCS-6/Ti-24Al-11Nb. The composite layup was [90]<sub>8</sub> with the crack growing parallel to the fibers. Since the cracks grew parallel to the fiber, no fiber bridging was possible or observed. In effect, the SCS-6/Ti-24-11 behaved similar to a monolithic material. Note that the crack growth data from the SCS-6/Ti-24Al-11Nb were generated by another investigator at the USAF Wright Laboratory Materials Directorate. All fatigue crack growth tests were conducted using closed-loop servo-hydraulic load frames controlled with PC-based automation system [60, 61]. During the tests, the CMOD was periodically measured using a quartz rod high-temperature extensometer. A schematic of the friction grip system is shown in Figure 3.5 [3]. The friction grips clamped the specimen ends and allowed no longitudinal rotation or transverse displacement. The width and thickness for the Ti-1100 is 25.34 mm and 2.06 mm, respectively, and for the SCS-6/Ti-24Al-11Nb 19.20 mm and 1.98 mm, respectively. The specimens were gripped such that H/W = 4. The initial saw-cut notch length to width ratio was 0.30 and 0.20 for the Ti-1100 and the SCS-6/Ti-24Al-11Nb, respectively. All the tests

were conducted at room temperature in laboratory air at a frequency of 2.0 Hz with a load ratio, R, of 0.1.

### 6.3.2 Validation of Compliance Solution

When the specimen is first loaded at low elastic loads, prior to any crack extension from the saw-cut notch, the load versus CMOD is a straight line. Substituting the elastic unloading compliance data from the first cycle, the thickness and the initial crack length in eq. 6.12, a value for the Young's modulus (E) was obtained. Note that eq. 6.12 was used assuming that the saw cut notch was equivalent to a crack of the same length. The compliance based value of E was 118 and 123 GPa for the Ti-1100 and [90]<sub>8</sub> SCS-6/Ti-24Al-11Nb, respectively. These values of E compare well with the results from uniaxial tension tests of Ti-1100 [62] and estimations based on the rule of mixtures for [90]<sub>8</sub> SCS-6/Ti-24Al-11Nb [63].

The compliance crack lengths calculated using eq. 6.10 were compared with optical measurements for Ti-1100 and SCS-6/Ti-24Al-11Nb specimens in Figure 6.6 and 6.7, respectively. Both figures show that the CMOD expression, eq. 6.10, developed for the SE(T) geometry with clamped ends was able to accurately predict the crack length over the range tested ( $0.2 \leq a/W < 0.9$ ). The accuracy of the crack length predicted from compliance measurements was validated by plotting the normalized compliance crack length versus the normalized optical measurements in Figure 6.8. The nearly one-to-one correlation shown in the figure clearly demonstrates the high accuracy of the newly developed compliance equation for crack lengths up to  $a/W = 0.90$ .

### 6.3.3 Validation of K Solution

From the crack length versus cycles data shown in Figures 6.6 and 6.7, the fatigue crack growth behavior was determined for Ti-1100 and SCS-6/Ti-24Al-11Nb. In Figure 6.9, the crack growth rate ( $da/dN$ ) for Ti-1100 and SCS-6/Ti-24Al-11Nb is plotted as a function of applied stress intensity factor range ( $\Delta K$ ) for the decreasing  $K_{max}$  and constant  $P_{max}$  portions of the test. The crack growth rates over one decade of  $da/dN$  representing the constant  $P_{max}$  section of the test were similar to those established in the decreasing  $K_{max}$  section. The reproducibility of the  $da/dN$  versus  $\Delta K$  response over different crack lengths confirms the validity of the newly developed stress intensity factor equation for the SE(T) with clamped ends.

The data obtained using the SE(T) geometry with clamped ends were compared with that obtained using the compact tension (C(T)) geometry [34, 35, 62] under similar test conditions for Ti-1100 in Figure 6.10. Figure 6.11 compares the data for SCS-6/Ti-24Al-11Nb for the present study with the results from the C(T) geometry [63]. Figures 6.10 and 6.11 show that the  $da/dN$  versus  $\Delta K$  response at low and high  $\Delta K$  is independent of geometry for both the materials. The excellent correlation of the  $da/dN$  versus  $\Delta K$  data obtained using distinctly different geometries establishes the validity of the newly developed compliance and stress intensity factor solution for the SE(T) geometry with clamped ends.

## 6.4 Discussion of Findings

As discussed earlier, the increase in  $K$  with increasing crack length for the SE(T) geometry with clamped ends and  $H/W = 4$ , was significantly slower than that with pin-loaded ends. Thus, the SE(T) with clamped ends facilitates

fracture and fatigue testing over long crack lengths prior to failure. This behavior was shown in Figures 6.6 and 6.8 for the Ti-1100 specimen in which the compliance crack length correlated well with the optical measurements up to  $a/W \approx 0.90$ .

In the above sections, the K values for the SCS-6/Ti-24Al-11Nb composite were calculated using the eqs 6.1 and 6.9. Equation 6.9 was developed for an isotropic material. John and Ashbaugh [63] showed that since the longitudinal to transverse modulus ratio was 1.5 for the [90]<sub>8</sub> SCS-6/Ti-24Al-11Nb composite the effect of orthotropy on the K solution was negligible. The K values for the C(T) geometry shown in Figure 6.10 were calculated using the corresponding isotropic K solutions.

The primary objective of developing the K and CMOD solutions was to facilitate crack growth testing of metal matrix composites in the SE(T) clamped-end configuration. A matrix crack growing perpendicular to fibers reinforcing a composite is often bridged across the crack surfaces by fibers. The direct current electric potential technique can be used to monitor the matrix crack length in the composite [64]. Knowing the matrix crack length and the CMOD, the extent of fiber bridging can be estimated. The difference in CMOD of the composite and the corresponding fiberless matrix specimen can be used to validate the bridging stress distributions in the composite. Crack growth tests of other composite systems, like SCS-6/TIMETAL®21S, currently use the SE(T)-geometry with clamped ends [64].

Table 6.1 Geometry correction factors ( $F$ ) and nondimensionalized CMOD for an SE(T) with clamped ends  $H/W = 4.0$ .

$a/W$	This Study- finite element	Marchand et al. [53] and Ahmad et al. [54]	Dao and Mettu [55]	Bowie et al. [52]	$E^*CMOD$ $\sigma_{app} * W$
0.05	1.1227 †	1.140	1.1389	1.13	0.2928
0.10	1.1528	1.166	1.1581	1.16	0.6013
0.20	1.2411	1.251	1.2291	1.25	1.3170
0.30	1.3654	1.378	1.3604	1.37	2.2373
0.40	1.5147	1.539	1.5178	1.52	3.4596
0.50	1.6951	1.726	1.7029	1.70	5.1039
0.60	1.9026	1.934	1.9192	1.91	7.3142
0.70	2.1569	2.171	2.1801	2.17	10.2808
0.80	2.4980	2.481	2.5322	—	14.2765
0.90	3.1502	3.113	3.1637	—	19.9658
0.95	4.0864	4.052	4.1370	—	24.4116

† not used in determining coefficients  $m_i$  in eq. 6.9

Table 6.2 Coefficients used to define  $F(a/W)$ ,  $a/W(U)$  and  $U(a/W)$ .

$i$	$m_i$	$q_i$	$t_i$
1	1.122	1.293	0.7166
2	-1.775	2.344	-1.931
3	5.324	-46.97	4.656
4	-15.64	161.0	-7.484
5	25.23	-236.8	6.297
6	-24.85	131.5	-2.104
7	13.56	—	—
8	-2.964	—	—

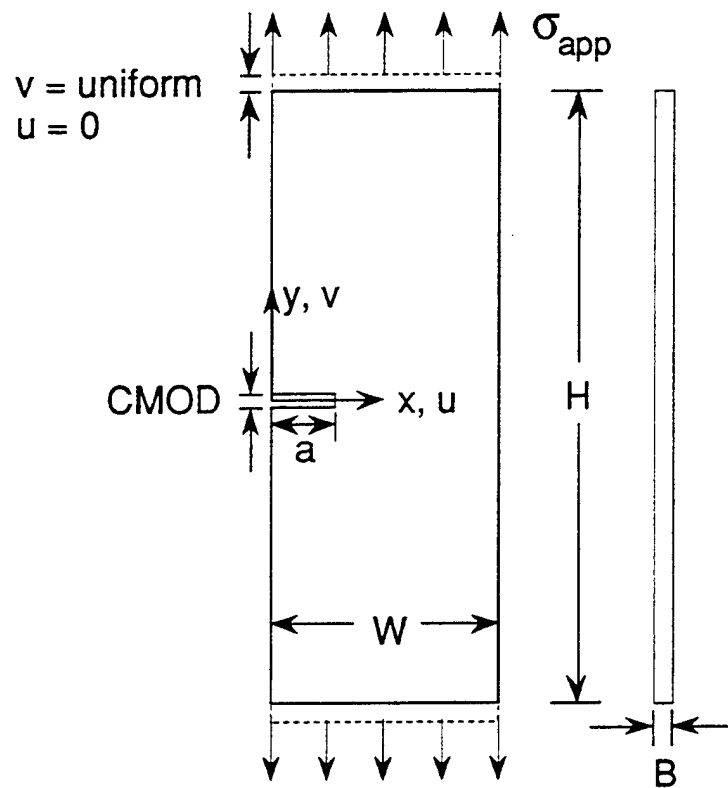


Figure 6.1 Schematic of SE(T) specimen with appropriate boundary conditions used for the finite element analysis.

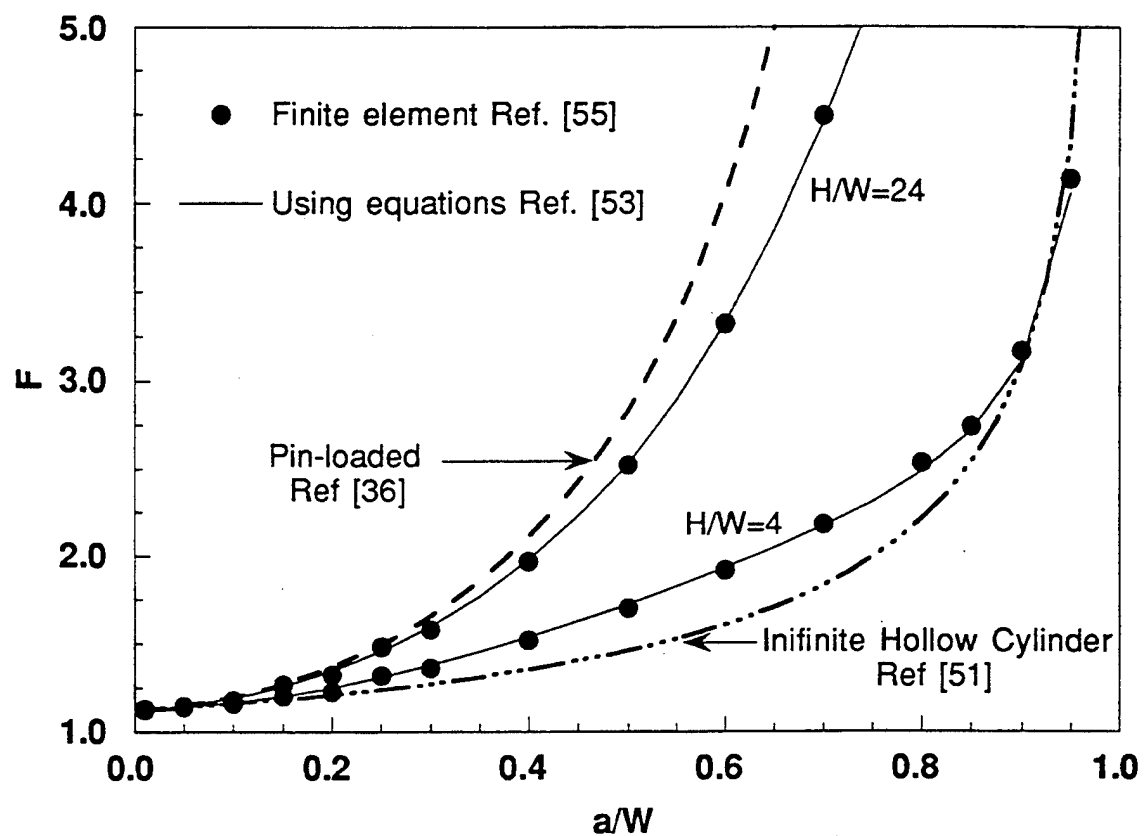


Figure 6.2 Geometry correction factor for a tension loaded SE(T) geometry with different boundary conditions and height-to-width ratios.

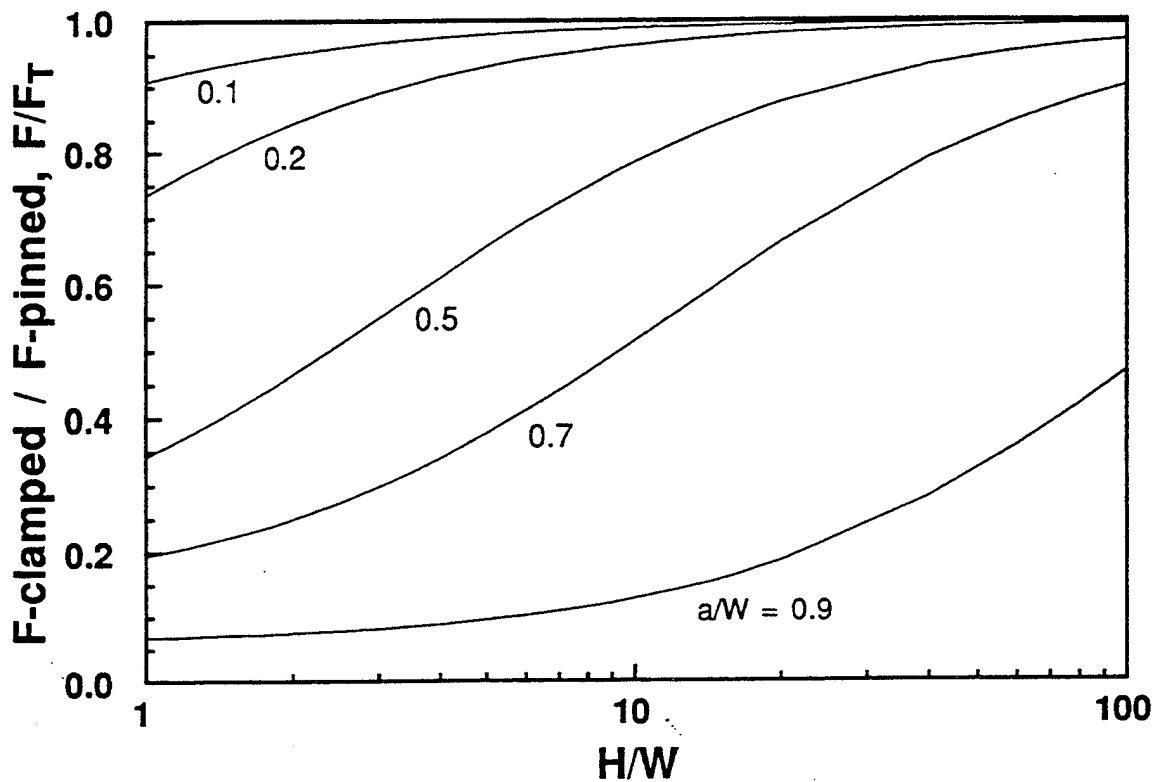
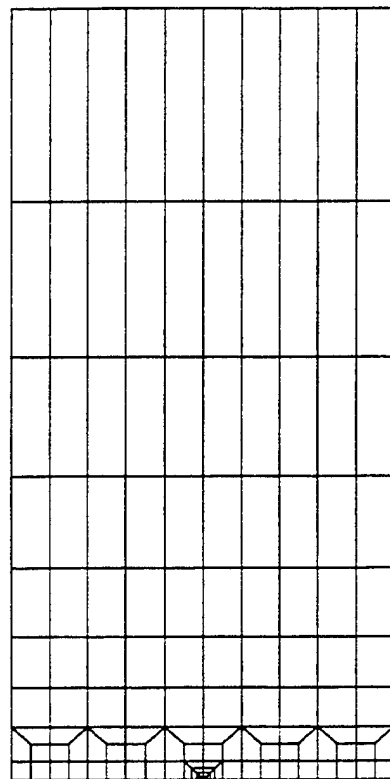
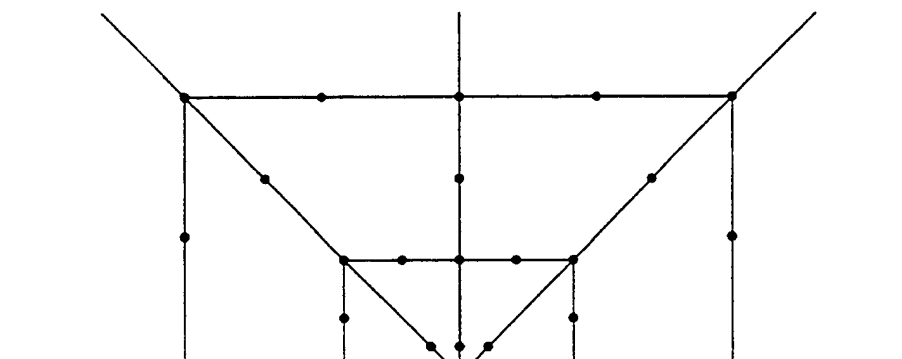


Figure 6.3 Effect of  $H/W$  on the ratio of geometry correction factors for a clamped SE(T) to a pin-loaded SE(T).



(a)



(b)

Figure 6.4 (a) Typical half-body finite element mesh ( $a/W = 0.5$ ) and (b) close-up view near the crack tip.

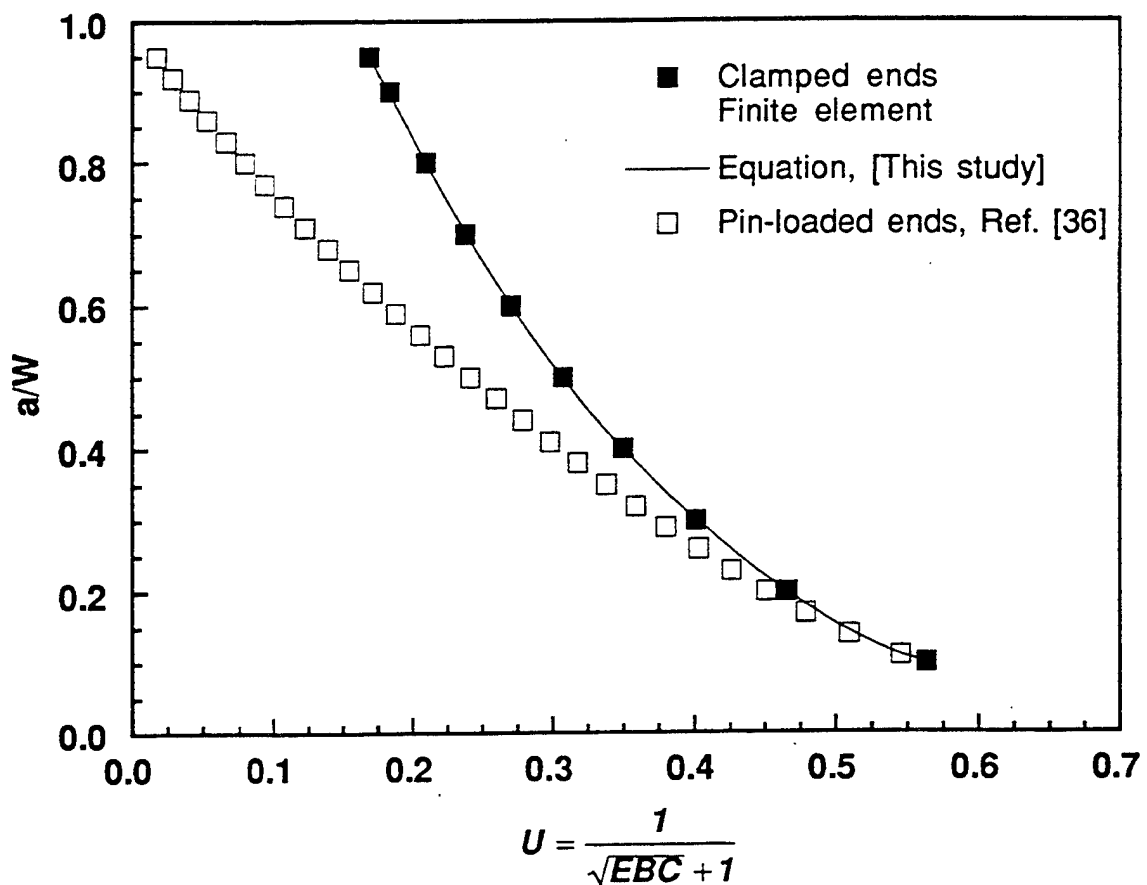


Figure 6.5 Nondimensional crack length as a function of the compliance.

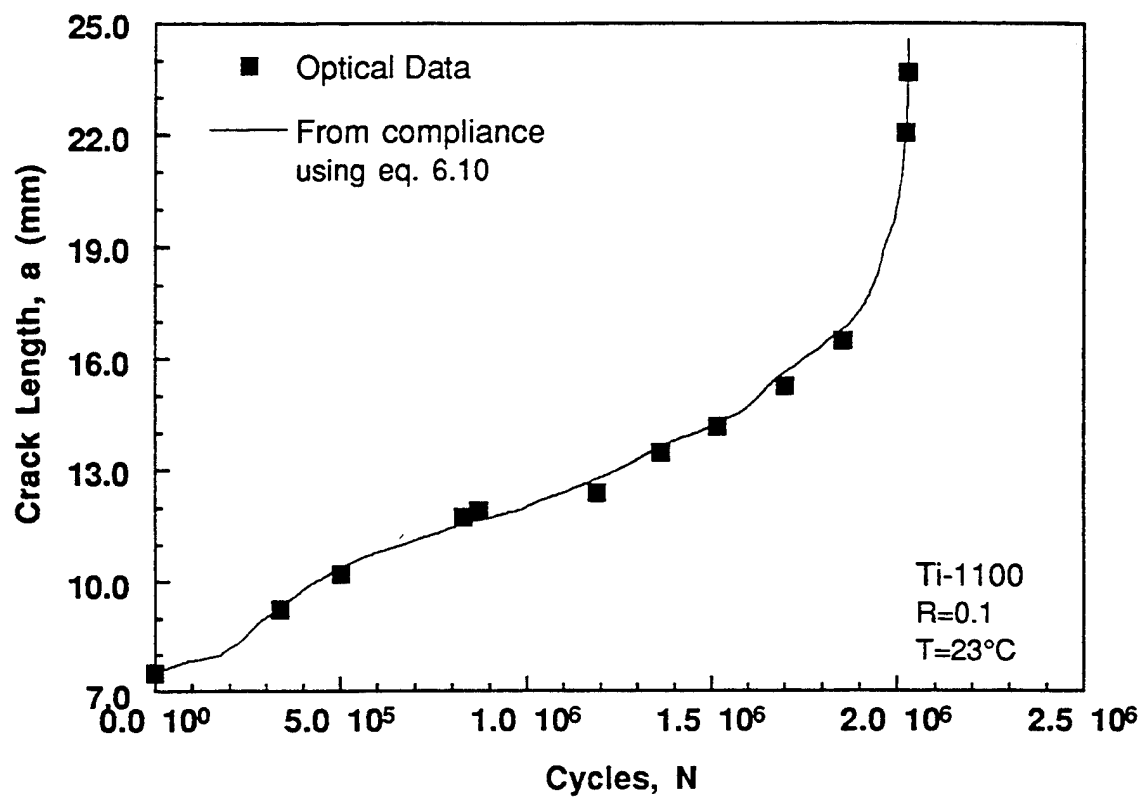


Figure 6.6 Comparison of compliance crack length with optical measurements over the life of the Ti-1100 specimen.

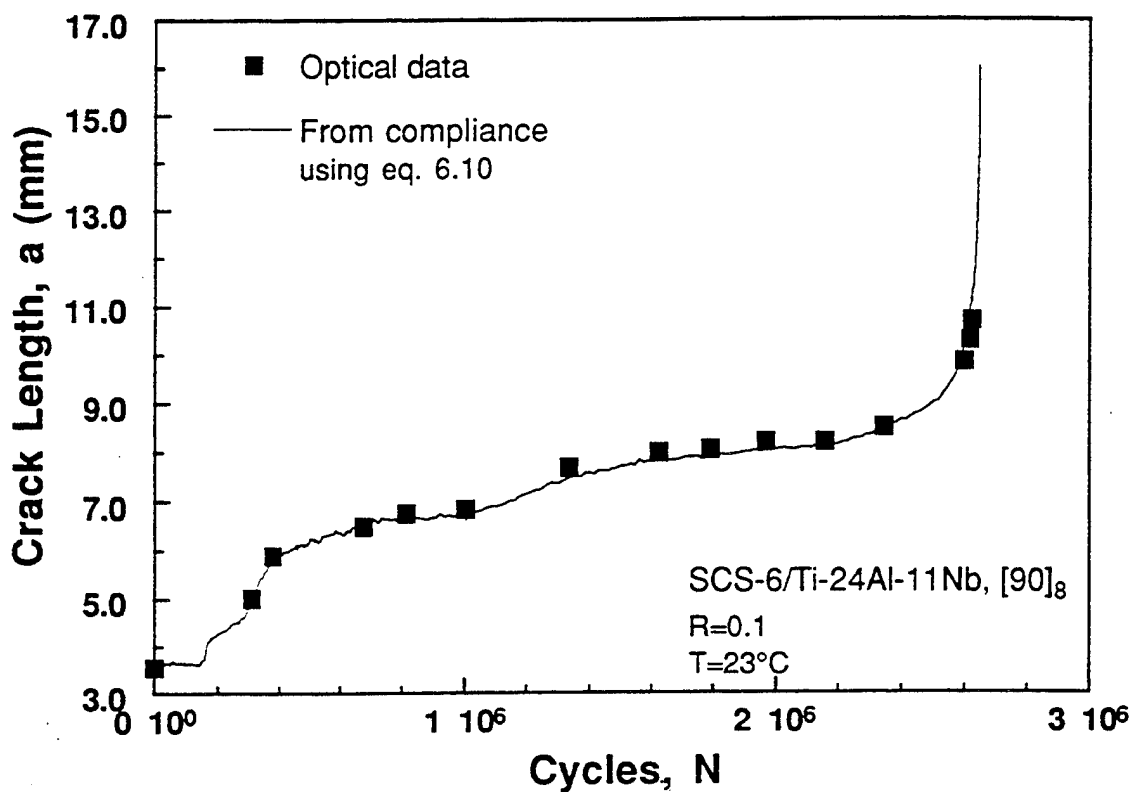


Figure 6.7 Comparison of compliance crack length with optical measurements over the life of the SCS-6/Ti-24Al-11Nb specimen.

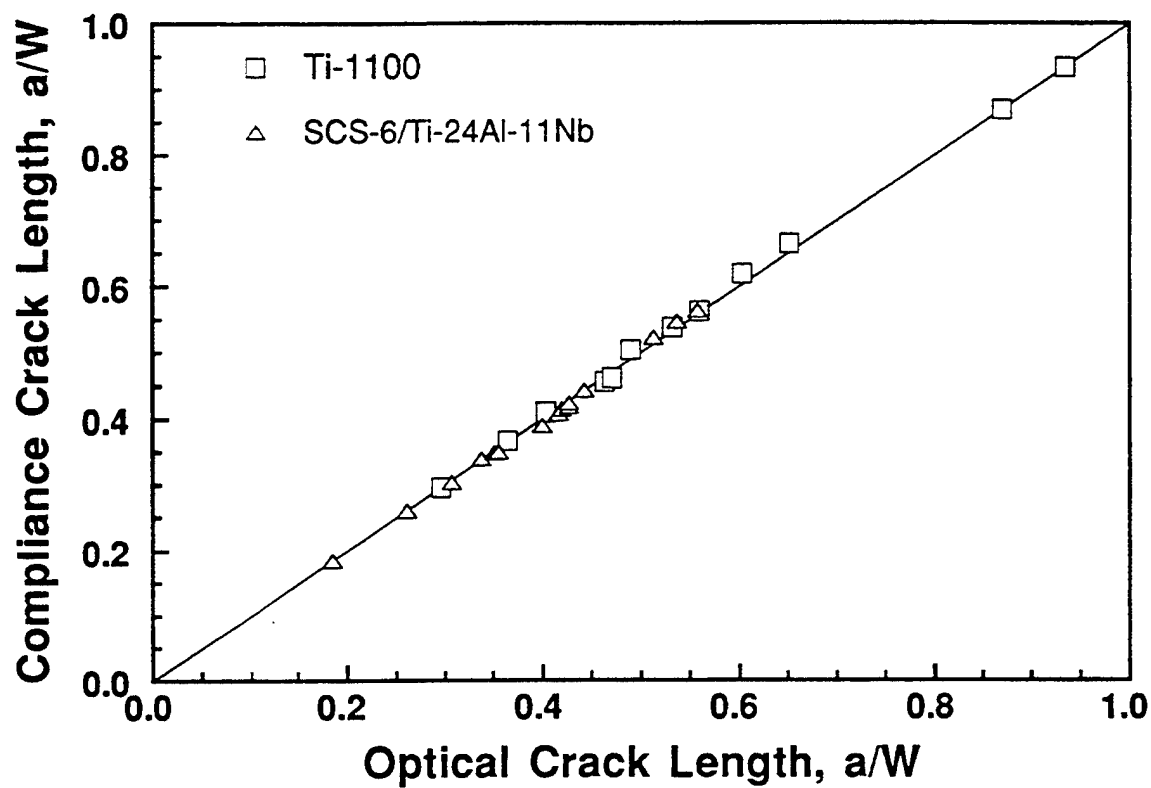


Figure 6.8 Correlation of compliance crack length with optically measured crack length.

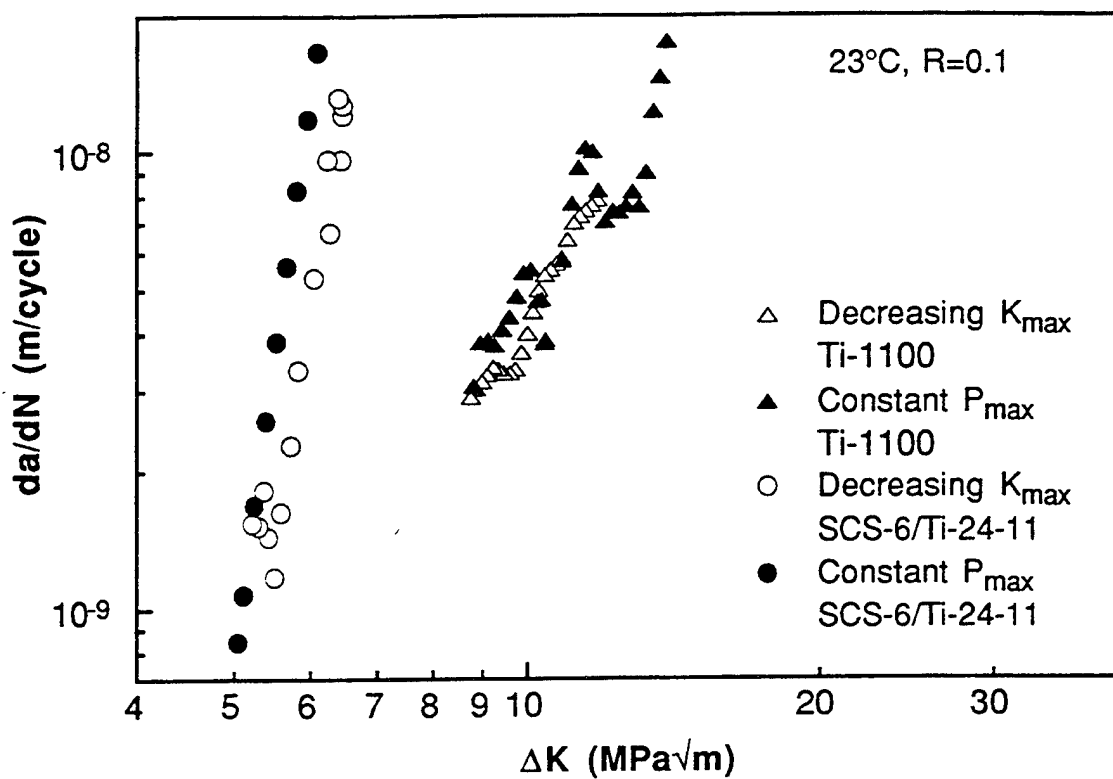


Figure 6.9 Room temperature crack growth rate as a function of applied stress intensity factor range for Ti-1100 and SCS-6/Ti-24Al-11Nb.

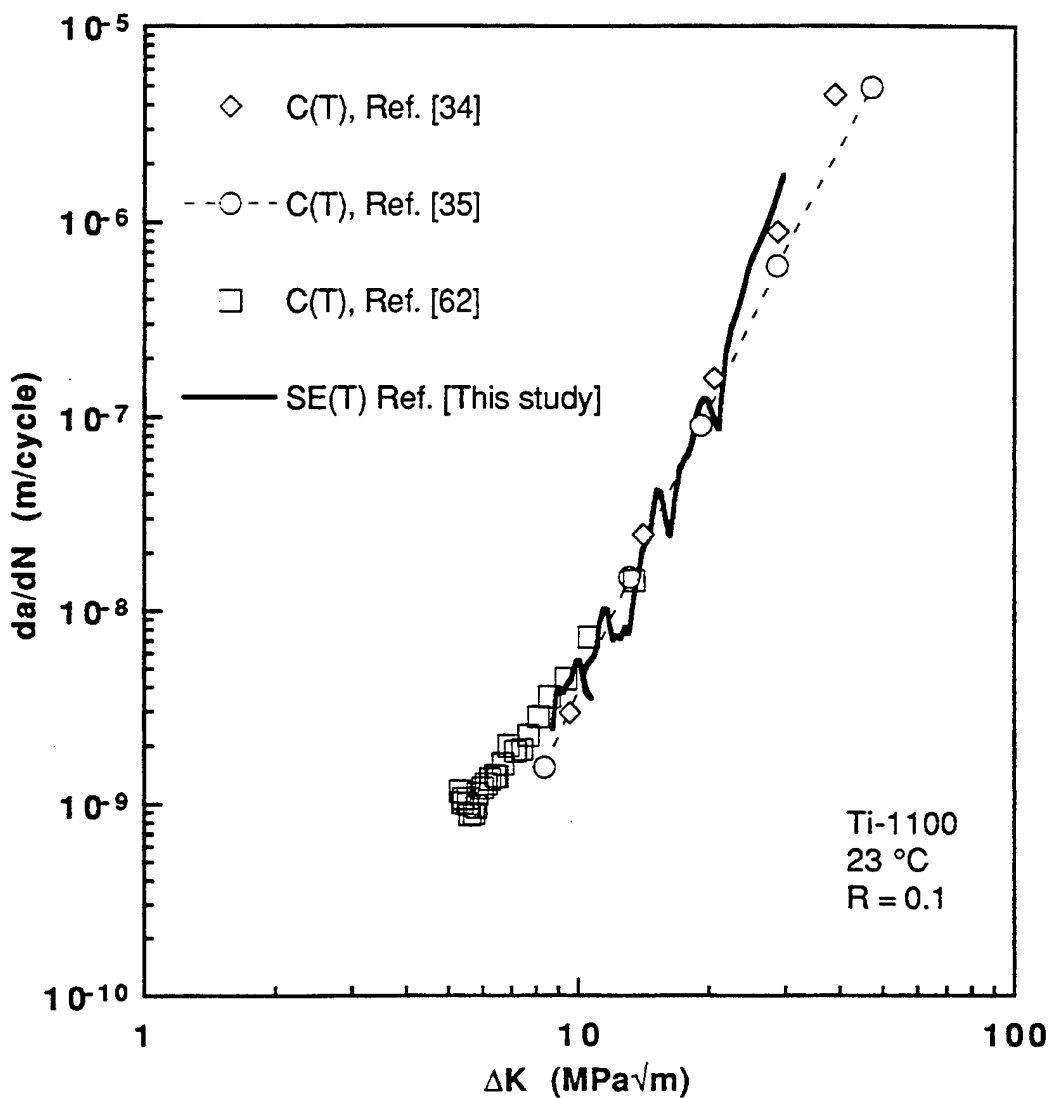


Figure 6.10 Comparison fatigue crack growth rate data obtained using the SE(T) and C(T) geometries for Ti-1100.

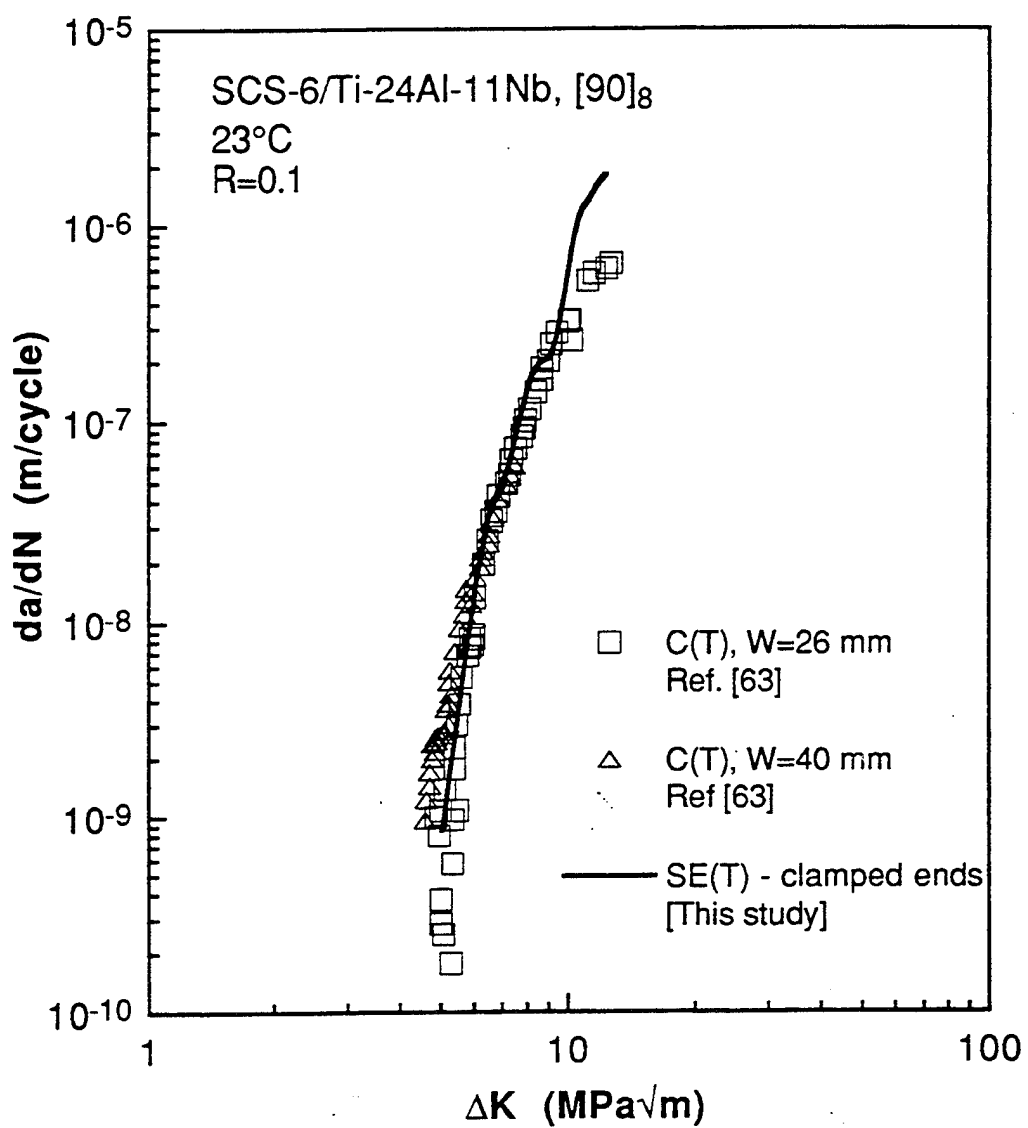


Figure 6.11 Comparison fatigue crack growth rate data obtained using the SE(T) and C(T) geometries for SCS-6/Ti-24Al-11Nb.

## CHAPTER 7

### RESULTS AND DISCUSSION OF FATIGUE CRACK GROWTH TESTS

This chapter presents the experimental results from the isothermal and thermomechanical fatigue (TMF) crack growth tests performed with the metal matrix composite material, as well as an explanation of the data reduction techniques. The material used throughout this study was a 4-ply, unidirectional, plasma sprayed composite of silicon carbide fibers, SCS-6, and a titanium based matrix, Ti-6Al-2Sn-4Zr-2Mo (Ti-6242).

#### 7.1 Summary of Tests Performed

All experiments performed for this study are listed in the order in which they were performed in Table 7.1. Seven different baseline conditions were tested; a list of those conditions are shown in Table 7.2. The 11 experimental data sets for this study, including baseline and proof tests, was generated over a seven month period. Since the cycle periods were high, sometimes as long as 20 minutes per cycle, at least 4 tests were over 20 days long with one test lasting 47 days.

The test results came from either a single-edge notch geometry (SE(T)) or a center-cracked geometry (M(T)) and are so indicated in the table. The M(T) geometry was used in addition to the SE(T) geometry to ensure self-similar crack growth across the specimen, perpendicular to the fibers. Under

certain test conditions using the SE(T) (e.g., low-temperature isothermal, low applied stress tests), cracks began to propagate along (parallel to) the fibers directly ahead of the machined notch. Crack propagation in the loading direction was observed in other studies using the SE(T) geometry [65, 66]. Fracture mechanics analyses [66, 67] show that the SE(T) geometry propagation behavior is dependent upon shear modulus and Poisson's ratio of the matrix and the fiber. The analyses pointed out that the microcracking along the fiber/matrix interface introduces a Mode II behavior. The Mode II crack then tends to decrease the Mode I driving force and the crack continues to grow along the fiber/matrix interface and not across the fiber. This mode of damage never occurred with the M(T) geometry regardless of test conditions primarily because the loading was symmetric and the Mode II driving force was negligible along the fiber/matrix interface. All fatigue crack growth tests (both SE(T) and M(T) geometries) were performed under constant maximum load,  $P_{max}$ , conditions and at a load ratio of 0.1. The typical decreasing  $K_{max}$  precrack routine was not followed because in the presence of crack bridging, an accurate determination of the crack tip stress intensity factor would have been difficult. Therefore, the specimen was started at constant  $P_{max}$  and then continued in this manner until fracture of the specimen occurred. Using guidelines set by ASTM E647 [40], the initial 1 mm of the crack growth from the machined notch was not used when computing fatigue crack growth rates.

## 7.2 Fatigue Crack Growth Data of SCS-6/Ti-6Al-2Sn-4Zr-2Mo

In this section, the fatigue crack growth rate data as function of applied stress intensity factor range are presented. This section is divided into three parts: (1) a vs. N and data reduction techniques; (2) fatigue crack growth data

gathered under isothermal conditions and; (3) fatigue crack growth data gathered under TMF conditions. The fastest cycle time that was achieved for the thermomechanical tests was 120 seconds or  $v = 0.0083$  Hz. This was governed by the maximum, controllable cooling rate of the specimen as discussed earlier in Section 3.4.2. For this reason, the 120 second cycle-time tests were considered the baseline, and all other tests were referenced to the tests conducted at that period.

### 7.2.1 Reduction of Crack Length-Cycle Data

Fatigue crack growth rates were determined, in general, from crack lengths computed from a direct-current electric-potential (DCEP) technique. Compliance crack lengths were not available for the M(T) geometry since the heating lamps' proximity to the specimen did not permit the use of extensometry to measure the crack mouth opening displacement (CMOD), an essential quantity for determining the compliance crack length. The compliance crack lengths determined from the initial SE(T) tests did not correlate well with the optical or DCEP crack lengths. Since good correlation was shown in Chapter 6 for monolithic Ti-1100 and [90]4 SCS-6/Ti-24Al-11Nb, the difference here was attributed to (1) crack opening profiles altered by small scale fiber bridging (one-two fibers) near the crack tip and (2) the inability to accurately correct crack opening displacements for thermal strains. With this in mind, compliance crack lengths were not calculated in favor of DCEP crack lengths. The DCEP crack lengths were verified by periodic optical measurement of the surface crack length on both sides of the specimen.

Plots of crack length versus cycles from each of the tests are shown in Figures 7.1-7.9. For some of the tests, the DCEP computed crack length was

nearly identical to the optically measured value, and no correction to the DCEP crack length was required. Occasionally, the DCEP crack length deviated sufficiently from the optical crack length such that the DCEP crack lengths were adjusted to match the optical crack lengths. This assured that the fatigue crack growth rate and stress intensity factor range were properly calculated. The discrepancies in DCEP measurements is attributed to pretest initialization of the control software. During the initialization of the control software, the notch length is inputted, and from this the software computes the initial excitation voltage,  $V_0$ , needed to produce the input notch length based on the specimen geometry and material resistivity (determined on the first cycle). The assumption was that  $V_0$  was constant for the remainder of the test. If the value of  $V_0$  changed during the test, the predicted crack length would differ from the actual (or optically measured) crack length. For instance, the DCEP crack lengths for specimens G8A-4-FCG and G8A-5-FCG were corrected using the optical crack length data as indicated in Figures 7.7 and 7.8, respectively. For specimen G8A-1-FCG (Figure 7.2) only, the DCEP data were corrupt due to a hardware error in the data acquisition equipment, so the optical crack length measurements were used exclusively to determine the crack growth rates. While optical crack length measurements were a valid method to determine the growth rate, the DCEP methodology for crack length measurement was the preferred method since it was easily automated and controlled by software. The optical method for this study was implemented to allow "spot checks" of the DCEP measurements.

The fatigue crack growth rates were determined using the DCEP crack length (possibly optically corrected) and the corresponding cycle count. The FORTRAN code SMOOTH, developed at the Materials Behavior Branch of the

Materials Directorate [68], was used for this calculation. Originally, this software was developed to calculate the fatigue crack growth rate from small-crack data. Discontinuities in the small-crack data are due to crack interactions with microstructure as well as inherent errors in the measurements. The goal of the software was to statistically minimize the effect of measurement errors while maintaining the actual crack growth behavior. The crack growth rate calculation algorithm followed the procedure recommended by ASTM E-647 [40], but with a notable modification. A full explanation of this modification is given in Ref [68]. In brief, this modified procedure produces a uniformly spaced series of fatigue crack growth rate calculations that minimizes the noise due to measurement precision (or lack of precision), yet retains the actual variations in crack growth rate [68].

The raw data from each test are given in tabular form in Appendix A. The data include the crack lengths and corresponding cycle counts from both DCEP and optical methods. The DCEP crack lengths in the appendix were generated by the SMOOTH code based on the raw test data. The data listed in the appendix are the same as the data shown in graphical form in Figures 7.1-7.8.

### 7.2.2 Isothermal Fatigue Crack Growth Data

Ideally, any predictive thermomechanical fatigue crack growth model would make all predictions based on isothermal data only since generating isothermal crack growth data is less complicated and less time consuming than generating similar data in a TMF mode. Therefore, isothermal data were generated at the maximum temperature,  $T_{max} = 538^{\circ}\text{C}$  ( $1000^{\circ}\text{F}$ ), and at the minimum temperature,  $T_{min} = 150^{\circ}\text{C}$  ( $300^{\circ}\text{F}$ ), of the TMF cycles.

Consequently, two empirical constants needed for the model described in Chapter 8 were determined directly from the two isothermal tests completed at 0.0083 Hz. The mechanical frequency during the isothermal tests was 0.0083 Hz. This allowed for direct comparison to the TMF crack growth rates also generated at that frequency. From this comparison the effect of the time-at-temperature or environment was assessed.

The crack growth rate data for the isothermal tests at  $T = 538\text{ }^{\circ}\text{C}$  (1000 °F) and  $150\text{ }^{\circ}\text{C}$  (300 °F) and  $\nu = 0.0083\text{ Hz}$  are compared in Figure 7.10. This figure plots the measured fatigue crack growth rate (meters/cycle) as a function of the correlating parameter, the applied stress intensity factor range,  $\Delta K$  ( $\text{MPa}\sqrt{\text{m}}$ ). From the figure, it is seen that the crack growth rates for the  $538\text{ }^{\circ}\text{C}$  (1000 °F) test are consistently higher than the rates generated from the  $150\text{ }^{\circ}\text{C}$  (300 °F). This behavior is expected since the environmental (time-dependent) contribution to the total crack growth rate for the  $150\text{ }^{\circ}\text{C}$  (300 °F) test is almost negligible compared to the test at  $538\text{ }^{\circ}\text{C}$  (1000 °F). As will be discussed in Chapter 8, the time dependent contribution to the crack growth rate at  $150\text{ }^{\circ}\text{C}$  (300 °F) is about two orders of magnitude less than the cycle dependent contribution.

Furthermore, the shape of the  $150\text{ }^{\circ}\text{C}$  (300 °F) crack growth curve in Figure 7.10 suggests that some fiber bridging occurred early in the test. The decreasing crack growth rate with increasing applied stress intensity factor range is a normal trend for a composite in which fiber bridging is a dominate mechanism. Note, however, that approximately midway through the test (@  $\Delta K = 75\text{ MPa}\sqrt{\text{m}}$  in Figure 7.10) the crack growth rate began increasing with increasing applied stress intensity factor range; an indication that fibers began to fracture and the bridged zone diminished. Jira, et al also observed full-scale

fiber bridging at room temperature in SCS-6/Ti-24Al-11Nb [69]. More extensive fiber bridging is expected at low temperatures (e.g., 150 °C) since accumulated fiber damage leading to fiber fracture is much less likely at low temperatures. At higher temperatures, the exposed carbon-rich coating of a bridged fiber burns away and leaves the silicon carbide exposed to environmental degradation. The fiber strength decreases after extended periods at elevated temperature, and fiber bridging is nearly eliminated.

An additional 538 °C (1000 °F) isothermal test was performed at a frequency of 0.83 Hz. This test gave insight into how the isothermal crack growth rate changed as a function of frequency. Typically, isothermal fatigue crack growth rates decrease as frequency increases [22, 70-73]. In fact, for truly time-dependent behavior, an order of magnitude increase in frequency results in an order of magnitude decrease in crack growth rate. This is explained primarily by the fact that higher frequencies elapse less time per cycle and, therefore, less time for the environment to contribute per cycle to the overall fatigue crack growth rate.

The fatigue crack growth data presented in Figure 7.11 clearly indicate that the higher frequency ( $v = 0.83$  Hz) data have slower growth rates compared to the lower frequency ( $v = 0.0083$  Hz) data. However, the data suggest that the crack growth rates are not fully time dependent. The frequency was increased by a factor of 100, but the crack growth rates only differ by about a factor of 10. This observation is accounted for in the modeling effort described in Chapter 8.

For all the isothermal tests, the crack length versus cycles data (Figures 7.4 and 7.5) show little evidence of bridging during the majority of each test. In the presence of full scale bridging the crack length versus cycles plots would

show decreasing increments of crack extensions with increasing cycles producing a concave-down curve. In general, the isothermal data showed only increasing increments of crack extension and producing concave-up curves. Close scrutiny of the crack length versus cycles data (Figure 7.5) indicate that some small scale bridging may have occurred between cycles 1000 and 2400. After the crack extends beyond this region, the incremental crack extensions were monotonically increasing with applied cycles — the typical response seen in monotonic and unbridged composites.

Visual inspection of matrix surface cracks during the tests revealed that when the cracks were short (and possibly bridged) the crack opening displacements along the crack were barely perceptible. During this period the crack growth rate usually remained constant or decreased slightly with increasing applied  $\Delta K$ , a typical response for titanium matrix composites under isothermal fatigue conditions [69]. However, once crack opening displacement became noticeable, the crack growth rates usually continued to increase with increasing applied  $\Delta K$ . This may indicate that fiber bridging occurred at small crack lengths, and at some longer crack length the fibers began to fail. It was also observed that the crack opening was usually negligible in the vicinity of the crack tip. In contrast, the crack opening behind this region was usually large enough so that fractured fibers in the crack wake were easily visible. It is believed that a small fiber bridged zone (2-3 fibers wide) was always present behind the crack tip which restricted the crack opening displacement in that region.

### 7.2.3 Thermomechanical Fatigue Crack Growth Data

The author was unable to locate thermomechanical fatigue crack growth data for metal matrix composites in the literature. Therefore, TMF crack growth tests were run to observe the general behavior of the composite and to generate data to assist and verify the TMF crack growth model developed in Chapter 8. All TMF tests were cycled between 150 °C and 538 °C (300 °F and 1000 °F) at frequencies of 0.0083 and 0.00083 Hz. No load hold times were introduced into the TMF cycles. Furthermore, the phase angles were limited to 0° and 180°, or in-phase and out-of-phase, respectively. The in-phase and out-of-phase fatigue crack growth data generated for the current study are presented in Figures 7.12 and 7.13, respectively. These figures represent all the baseline TMF data. The figures plot fatigue crack growth rate as a function of applied stress intensity factor range.

The crack growth rates for the in-phase and out-of-phase tests at 0.0083 Hz are compared in Figure 7.14. As the figure shows, the crack growth rates were nearly identical. Previous TMF data of monolithic Ti-24Al-11Nb [22] and Inconel 718 [29] showed that typically the in-phase fatigue crack growth rates were higher than the out-of-phase rates. Also, the TMF tests behaved similar to the isothermal tests showing fiber bridging only when the crack size was small. The crack opening displacement profile at longer crack lengths was similar to that from the isothermal tests; near the crack tip the crack opening displacement was significantly smaller than the remaining crack wake.

In contrast to the 0.0083 Hz TMF growth rates, the crack growth rates were noticeably different between the in-phase and out-of-phase tests run at 0.00083 Hz as illustrated in Figure 7.15. This suggests that the in-phase condition is more frequency dependent than the out-of-phase. Neu saw a

similar response in the TMF behavior of unnotched SCS-6/TIMETAL®21S [74]. Micromechanical modeling of the fiber and matrix stresses during in-phase and out-of-phase conditions revealed that the fiber stresses in the in-phase condition rose more rapidly with cycle period than the out-of-phase condition. During in-phase loading at longer cycle periods, the matrix relaxes and the load is transferred to the fiber. At shorter cycle periods the load transferred to the fiber from the matrix is lower.

The crack growth curve generated by specimens G9A-2-FCG, an SE(T) geometry, and G8A-1-FCG, an M(T) geometry, was another indication that large scale fiber bridging did not occur during the TMF tests. In the presence of large scale bridging, the two out-of-phase tests would not have generated a single curve over such a wide range of applied cyclic stress intensity factor as the one shown in Figure 7.16. For a fully bridged crack, the crack growth rate correlates more appropriately with net stress intensity factor range and not the applied stress intensity factor range, where  $\Delta K_{net} = \Delta K_{app} + \Delta K_{brdg}$ . Consider two different specimen geometries with an equivalent applied stress intensity factor range and full scale bridging: since  $\Delta K_{brdg}$  is different for each geometry, the crack driving force at the crack tip,  $\Delta K_{net}$ , will be different, hence the composite crack growth rate will also be different. Since no large scale bridging occurred during any of the tests during this project, it is, therefore, acceptable to correlate all the crack growth rates with the applied stress intensity factor range.

### 7.3 Additional Crack Growth Tests

The eight fatigue crack growth tests reported in Section 7.2 represent the baseline data generated to better understand the SCS-6/Ti-6Al-2Sn-4Zr-

2Mo, 4-ply, unidirectional composite under isothermal and thermomechanical conditions. Two additional tests were also completed to study conditions beyond those chosen for the baseline tests. One test examined the crack growth behavior of an SE(T) specimen subjected to cyclic temperatures while being held at a constant load. The other test reexamined the applicability of using the applied stress intensity factor range to correlate the crack growth rates for the current study.

### 7.3.1 Cyclic Temperatures and Static Loading

An SE(T) specimen, G7A-2-FCG, was cycled between 150-538 °C at a frequency of 0.0083 Hz while a static load of 7.3 kN ( $K = 60.5 \text{ MPa}\sqrt{\text{m}}$ ) was applied ( $R = 0$ ) at an  $a/W$  of 0.3. After 1381 thermal cycles, no crack growth was observed from DCEP measurements and optical inspection. The specimen was then cycled ( $R = 0.1$ ) isothermally ( $T = 538 \text{ }^{\circ}\text{C}$ ) until  $a/W$  was equal to 0.46. The static load of 7.3 kN was reapplied yielding a  $K$  of 89  $\text{MPa}\sqrt{\text{m}}$ , and the temperature was allowed to cycled again. After 1909 additional thermal cycles, no crack growth occurred. The crack was further extended by cycling ( $R = 0.1$ ) isothermally until the normalized crack length equaled 0.56. The specimen was thermally cycled another 1402 cycles under static loading ( $P = 7.3 \text{ kN}$  and  $K = 110 \text{ MPa}\sqrt{\text{m}}$ ). Again, this type of loading produced no additional crack growth. The crack was grown once more to an  $a/W$  of 0.57 by isothermal loading ( $R = 0.1$ ). Finally, the specimen was loaded to 6.45 kN ( $K = 100 \text{ MPa}\sqrt{\text{m}}$ ) at a constant temperature of 538 °C; conditions similar to a creep crack growth test. After 27 hours of exposure, the crack showed no sign of further extension, and the test was terminated.

The results from this particular test suggest that the thermal loading ( $\Delta T = 150\text{--}538\text{ }^{\circ}\text{C}$ ) under static loading did not generate a large enough driving force at the crack tip to further propagate the crack. The composite crack growth behavior is dominated by the fiber's behavior. If the fiber does not weaken and fracture due to environmental attack and fiber stress range, it is unlikely that matrix cracking will be extensive. The thermal cycling applied to this specimen under static loading did not sufficiently influence the fiber strength, so the precracked region remains partially bridged which eliminated any further matrix crack growth.

This was a significant result that directed the course of the modeling effort discussed in Chapter 8. Before this test was conducted, it was believed that the time-dependent component of the total crack growth rate was a function of static  $K_{max}$ . If this were true, the crack growth rates of a test conducted at a given  $\Delta K_{app}$  and  $\Delta T$  should be the same for one conducted at a static equivalent  $K_{max}$  and  $\Delta T$ . The test described above did not have similar growth rates to either the in-phase or out-of-phase tests; in fact, the crack growth rate was essentially zero. Therefore, the time-dependent crack growth rate is more appropriately represented by a  $\Delta K_{app}$  term. This test also suggests that if a  $\Delta K_{thermal}$  is present during thermal cycling between 150 and 538  $^{\circ}\text{C}$ , it doesn't appear to significantly contribute to the time-dependent crack growth rate; an important finding to note when exploring the influence of other thermomechanical loading histories on crack growth behavior in metal matrix composites.

### 7.3.2 Correlation of Crack Growth Rates with $\Delta K_{app}$

A concluding test of this study investigated the applicability of  $\Delta K_{app}$  as a correlating parameter for crack growth rates at different crack lengths and test conditions. The crack growth rates generated from each of the eight baseline tests discussed in Section 7.2 were determined from cracks starting from the machined notch ( $a/W = 0.3$ ). To verify that  $\Delta K_{app}$  correlated the crack growth at longer crack lengths, an SE(T) specimen, G7A-4-FCG, was precracked isothermally at  $T = 538$  °C and 2 Hz to  $a/W = 0.5$ . The precrack procedure, following guidelines established in ASTM E647 [40], reduced  $\Delta K_{app}$  from 70 MPa $\sqrt{m}$  to 45 MPa $\sqrt{m}$  by periodically lowering the applied load as a function of crack extension. When the crack reached an  $a/W = 0.5$ , a constant amplitude  $P_{max}$  at  $R = 0.1$  was applied to begin the TMF cycling at  $\Delta K_{app} = 45$  MPa $\sqrt{m}$ . The SE(T) was thermally cycled out-of-phase with the applied load at the baseline frequency of 0.0083 Hz. The crack grown during the precrack portion was not bridged by fibers, so little transient behavior was observed between the precrack conditions and the actual TMF crack growth conditions.

The out-of-phase crack growth rates generated by longer cracks in the SE(T) geometry, specimen G7A-4-FCG, were nearly identical to the growth rates produced by the shorter cracks in the M(T) geometry, specimen G8A-1-FCG, as illustrated in Figure 7.16. The result of this test indicates that  $\Delta K_{app}$  was able to correlate the crack growth rates generated by long and short cracks and for two different geometries. The influence of different geometries on crack growth rates was also discussed previously in Section 7.2.3.

An interesting crack growth behavior was observed during the out-of-phase, 0.0083 Hz test of the SE(T) specimen G7A-4-FCG. As the data in Figure 7.9 and 7.16 indicate, the crack growth rate sharply increased at two

distinct times during the life of the specimen. The increases in crack growth rate were then followed by a return to the expected composite crack growth rate given the out-of-phase conditions. This behavior was attributed to successive fracture of the bridging fibers up to the matrix crack tip during only a few cycles. This rapid fracture was then followed by matrix crack advance leaving behind a zone of unbroken fibers. When steady crack growth was reestablished, it always followed the growth curve produced by the M(T) geometry at significantly shorter crack lengths. This phenomenon of increased crack growth rate followed by a return to the expected crack growth rate of the composite was also observed in Sigma fiber reinforced TIMETAL®21S [75]. Ghonem observed that the crack growth rate under isothermal conditions would increase and approach the rate of the unreinforced matrix material, and like the behavior of specimen G7A-4-FCG, the crack growth rate would then decrease to intersect and continue along the composite crack growth curve.

Table 7.1 Summary of tests performed on the SCS-6/Ti-6Al-2Sn-4Zr-2Mo in the order in which they were completed.

Specimen ID	Type of Test	Temperature (°C)	Period (sec/cyc)	Geometry
G9A-2-FCG	Out-of-phase	150-538	120	SE(T)
G9A-3-FCG	In-phase	150-538	120	SE(T)
G9A-4-FCG	Isothermal	538	120	SE(T)
G8A-1-FCG	Out-of-phase	150-538	120	M(T)
G8A-2-FCG	Isothermal	538	1.2	M(T)
G8A-3-FCG	Out-of-phase	150-538	1200	M(T)
G8A-4-FCG	Isothermal	150	120	M(T)
G8A-5-FCG	In-phase	538	1200	M(T)
G7A-2-FCG	Hold at P <sub>max</sub>	150-538	120	SE(T)
G7A-4-FCG	Out-of-Phase	150-538	120	SE(T)*
G8A-6-FCG	Decreasing T <sub>min</sub>	538→150	120	SE(T)

\* precracked to an a/w=0.5

Table 7.2 Summary of baseline crack growth test conditions for the SCS-6/Ti-6Al-2Sn-4Zr-2Mo.

Test Type	Temperature (°C)	Period (sec/cyc)
Isothermal	538	120
Isothermal	538	1.20
Isothermal	150	120
In-phase	150-538	120
In-phase	150-538	1200
Out-of-phase	150-538	120
Out-of-phase	150-538	1200

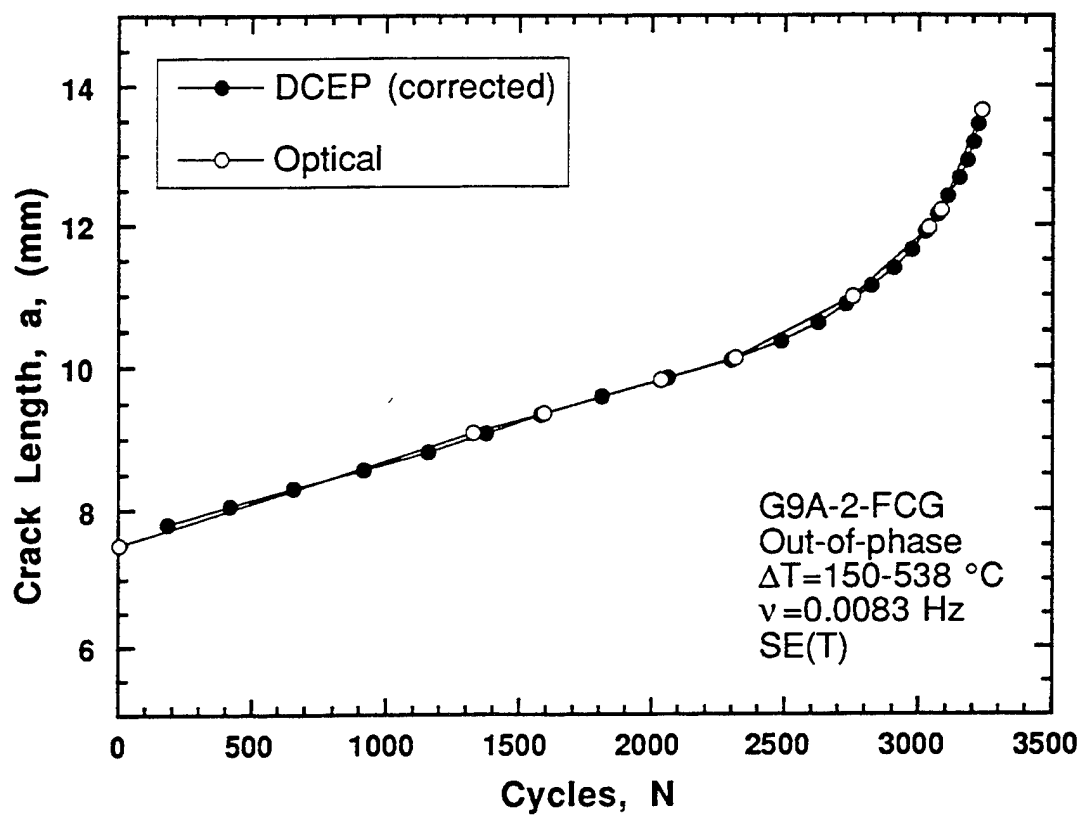


Figure 7.1 Crack length from DCEP and optical measurements as a function of applied cycles for specimen G9A-2-FCG.

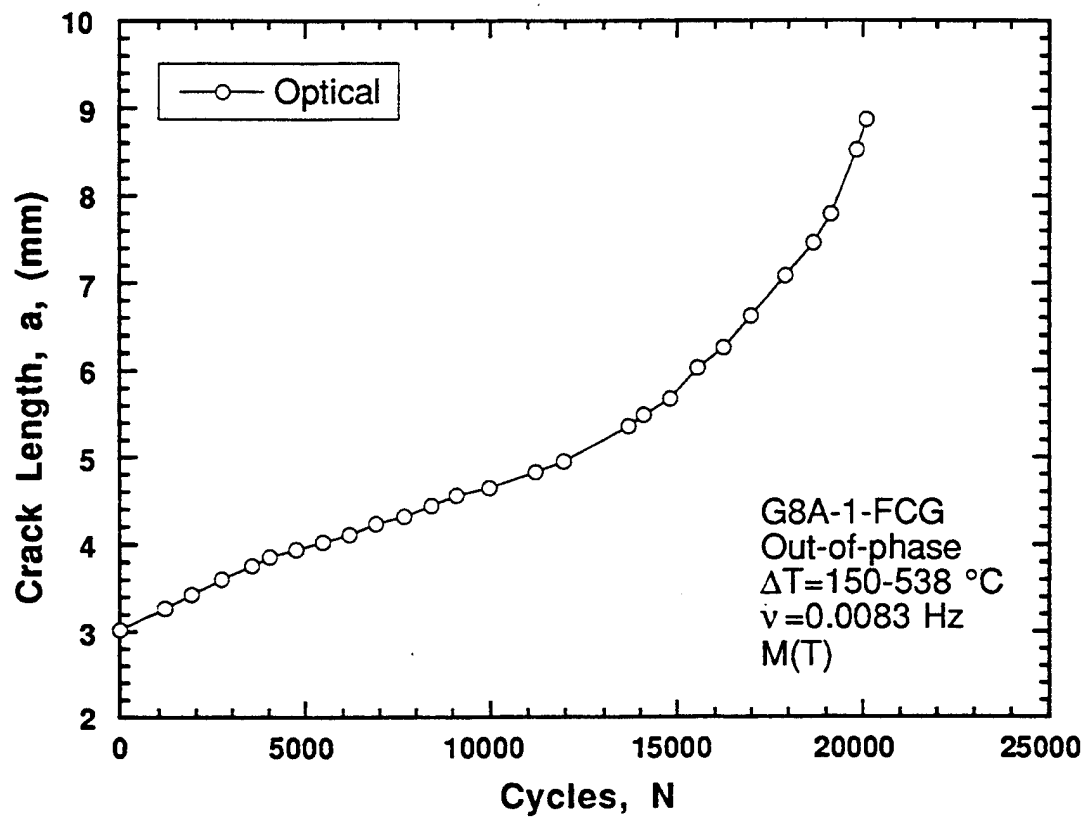


Figure 7.2 Crack length from DCEP and optical measurements as a function of applied cycles for specimen G8A-1-FCG.

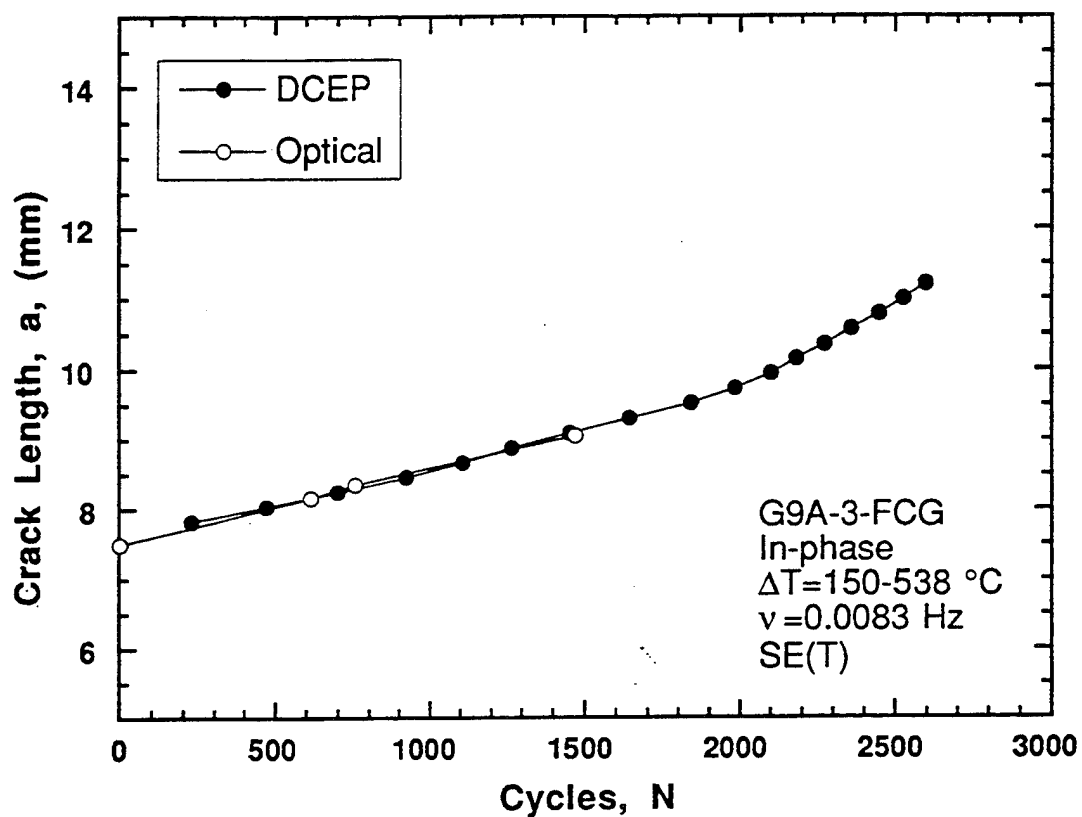


Figure 7.3 Crack length from DCEP and optical measurements as a function of applied cycles for specimen G9A-3-FCG.

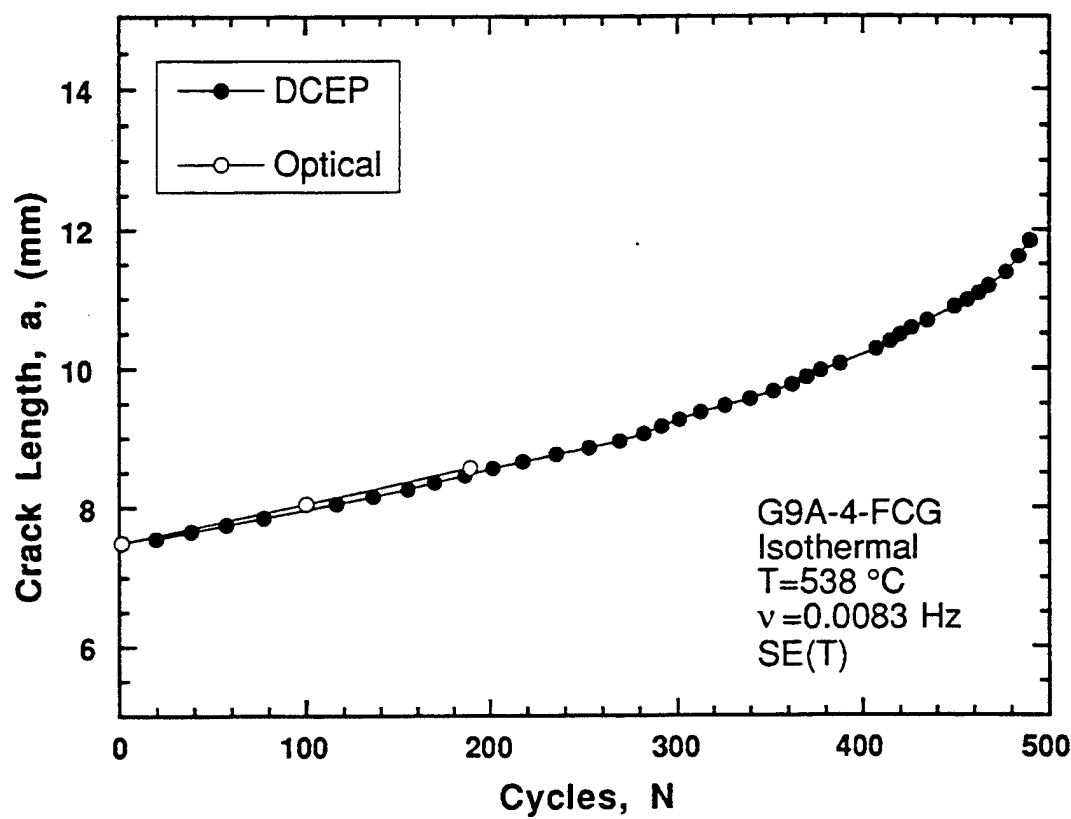


Figure 7.4 Crack length from DCEP and optical measurements as a function of applied cycles for specimen G9A-4-FCG.

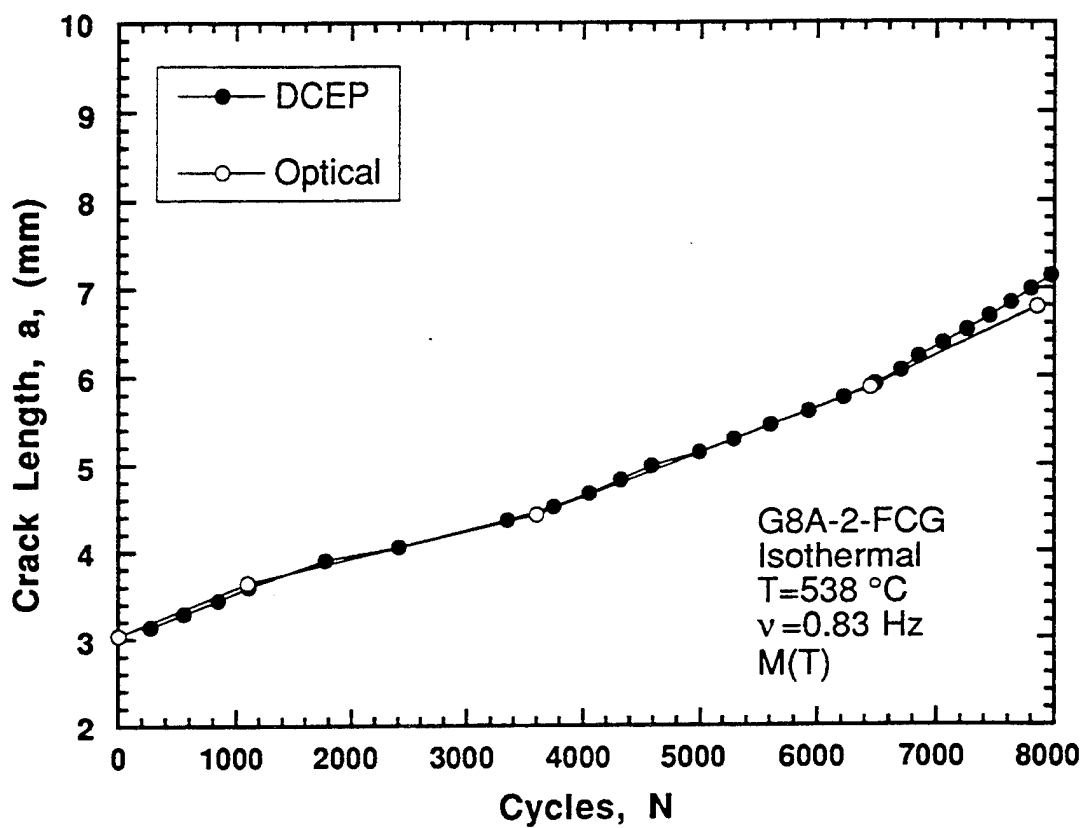


Figure 7.5 Crack length from DCEP and optical measurements as a function of applied cycles for specimen G8A-2-FCG.

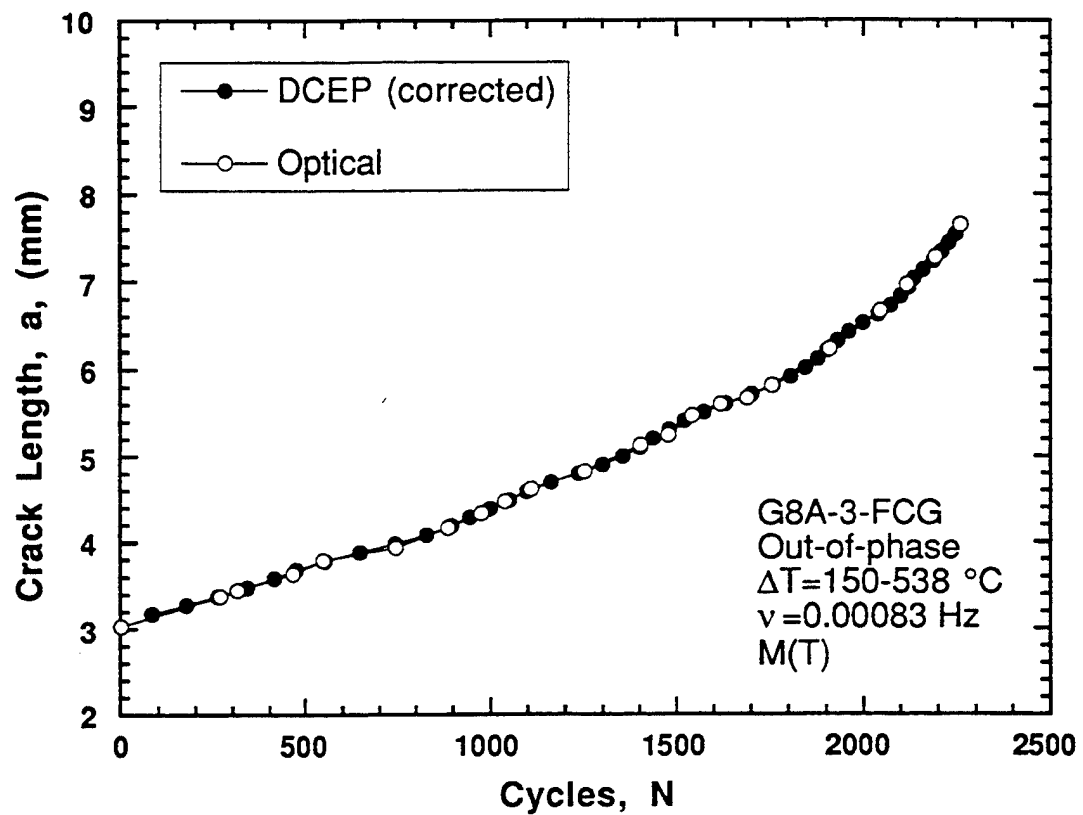


Figure 7.6 Crack length from DCEP and optical measurements as a function of applied cycles for specimen G8A-3-FCG.

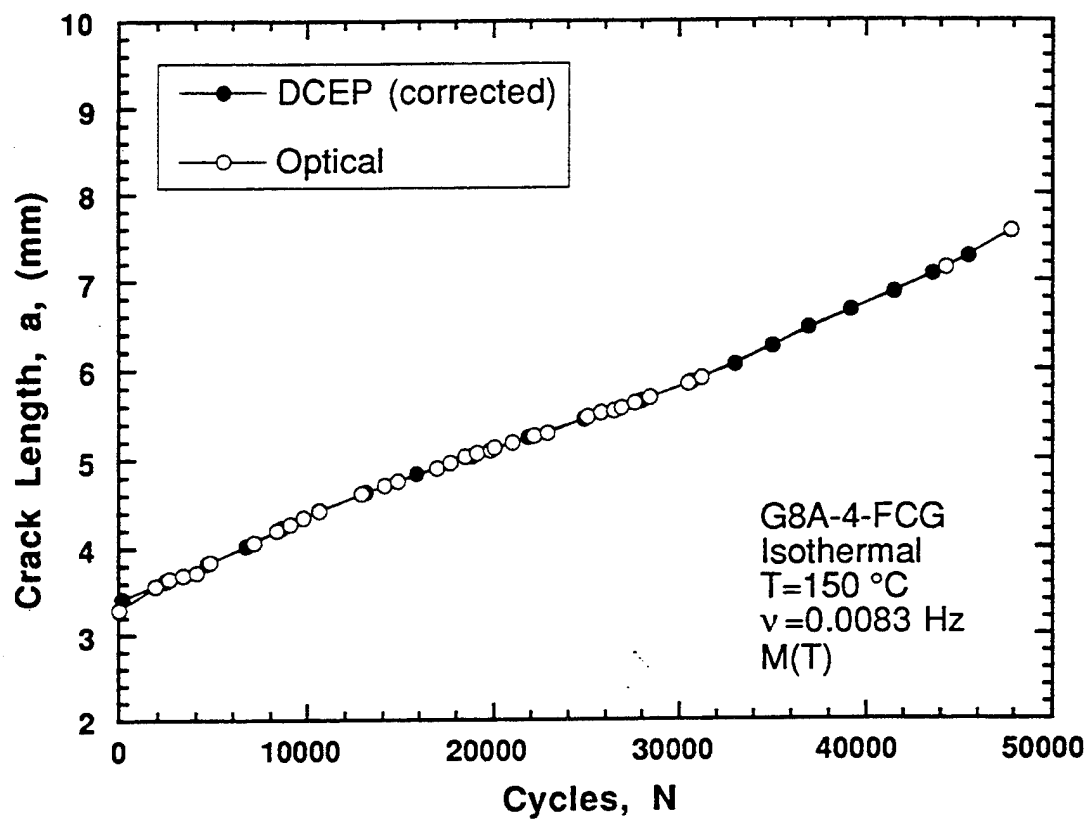


Figure 7.7 Crack length from DCEP and optical measurements as a function of applied cycles for specimen G8A-4-FCG.

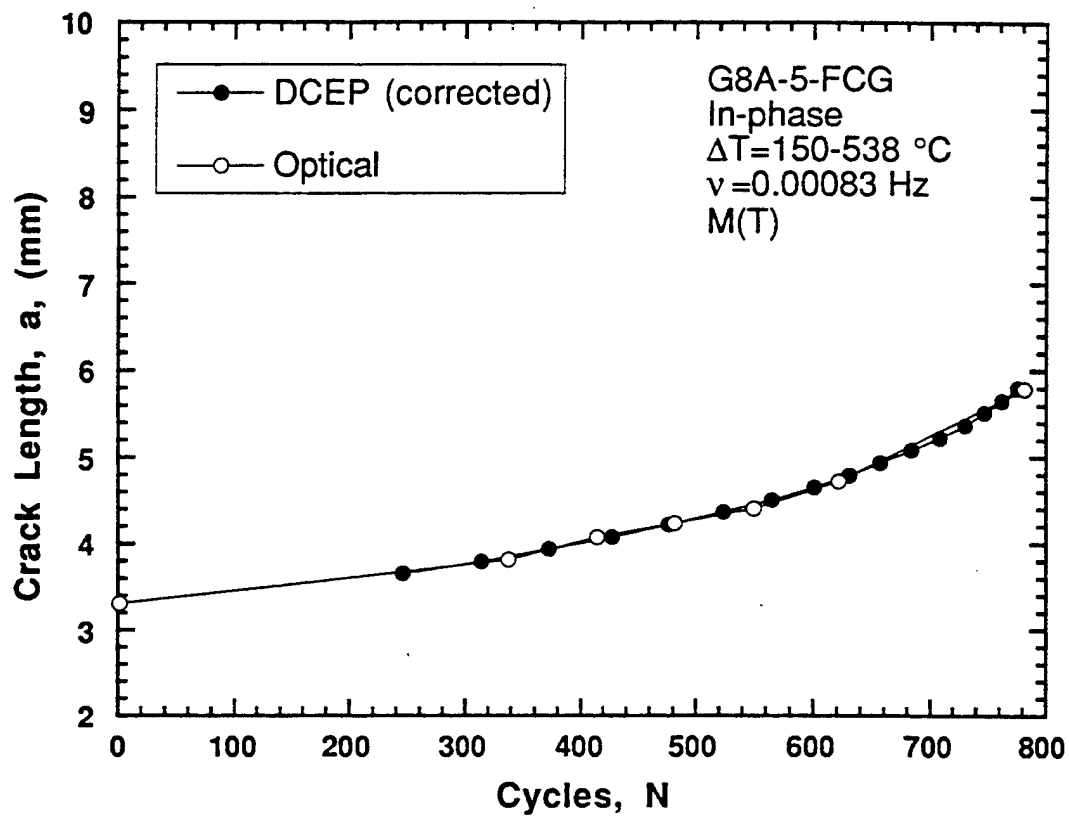


Figure 7.8 Crack length from DCEP and optical measurements as a function of applied cycles for specimen G8A-5-FCG.

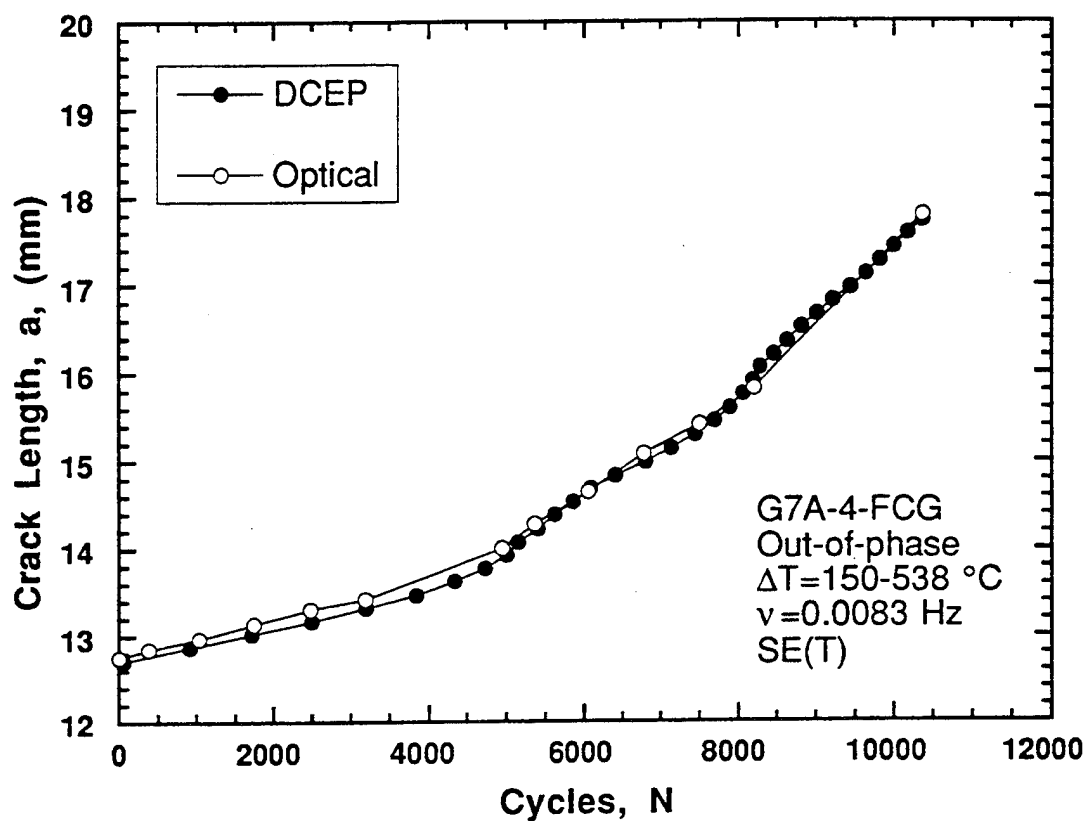


Figure 7.9 Crack length from DCEP and optical measurements as a function of applied cycles for specimen G7A-4-FCG.

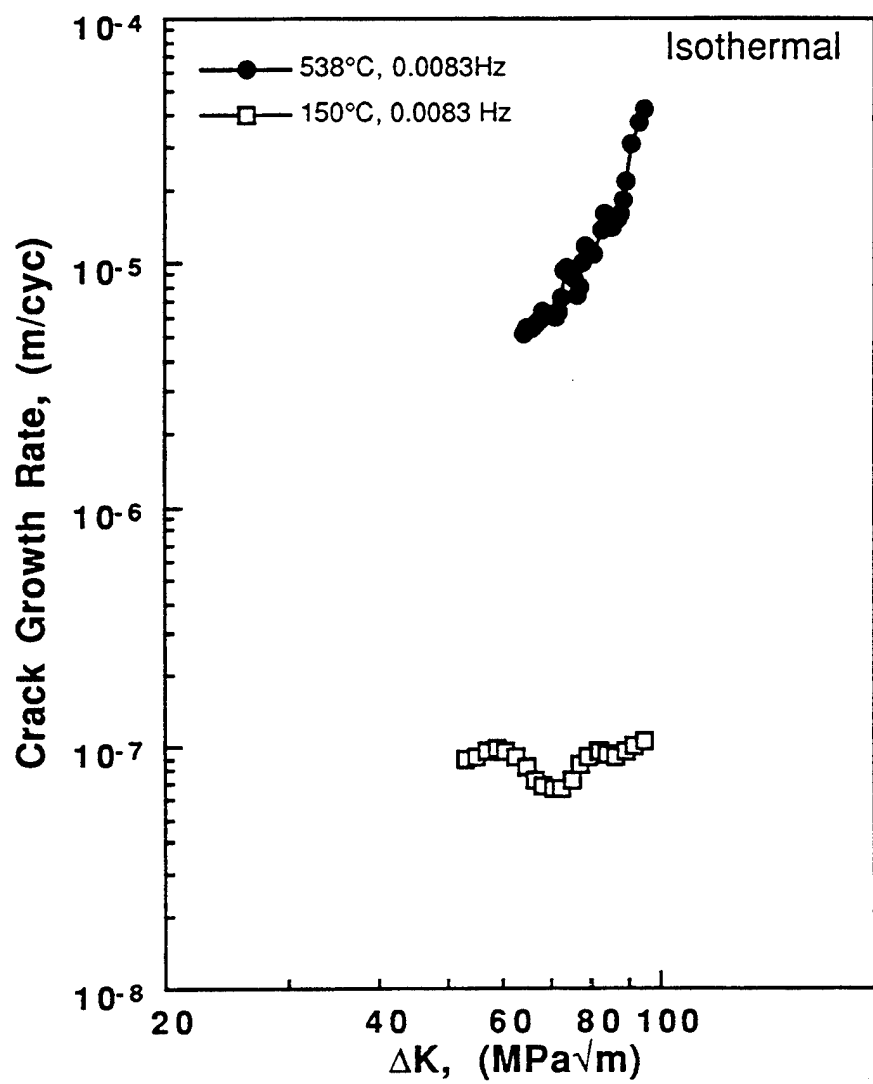


Figure 7.10 Fatigue crack growth data for SCS-6/Ti-6Al-2Sn-4Zr-2Mo at 150 and 538 °C and  $v = 0.0083$  Hz.

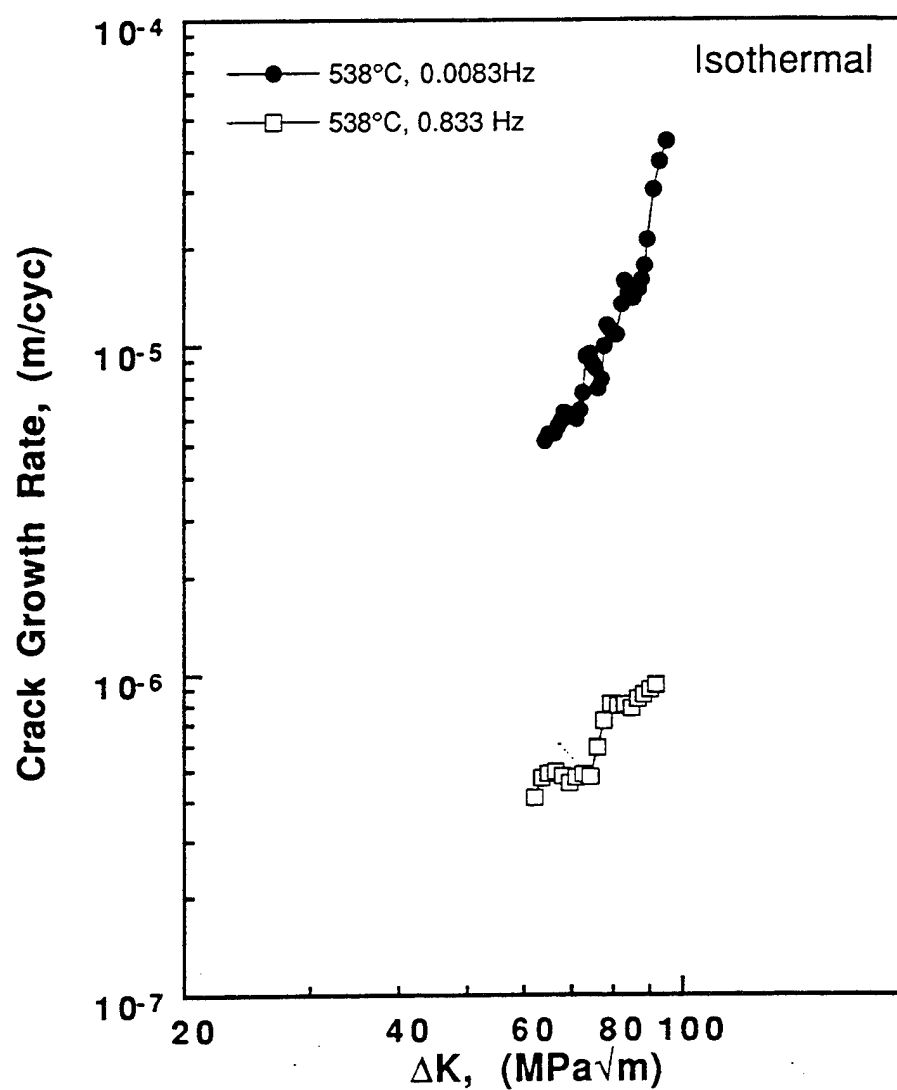


Figure 7.11 Comparison of fatigue crack growth data for SCS-6/Ti-6Al-2Sn-4Zr-2Mo generated at 538 °C and  $\nu = 0.0083$  Hz and 0.83 Hz.

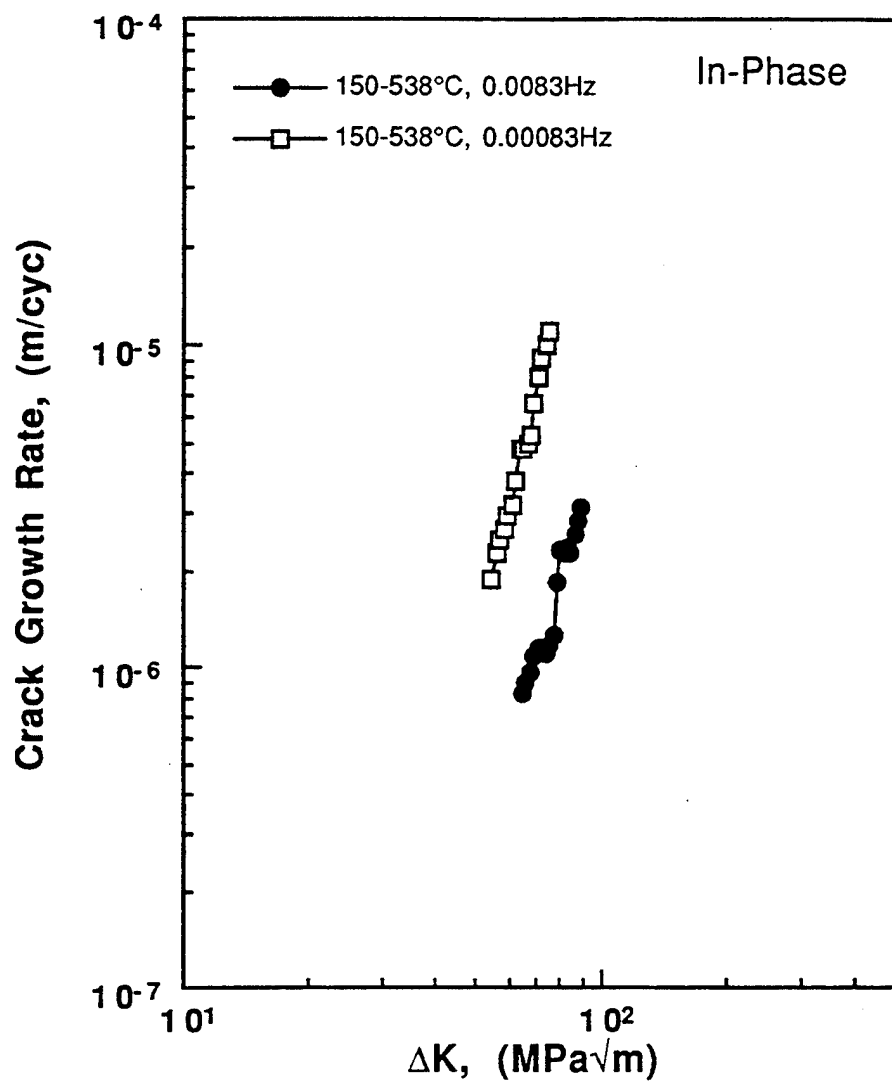


Figure 7.12 Comparison of in-phase thermomechanical fatigue crack growth data for SCS-6/Ti-6Al-2Sn-4Zr-2Mo cycled between 150 and 538 °C at 0.0083 Hz and 0.00083 Hz.

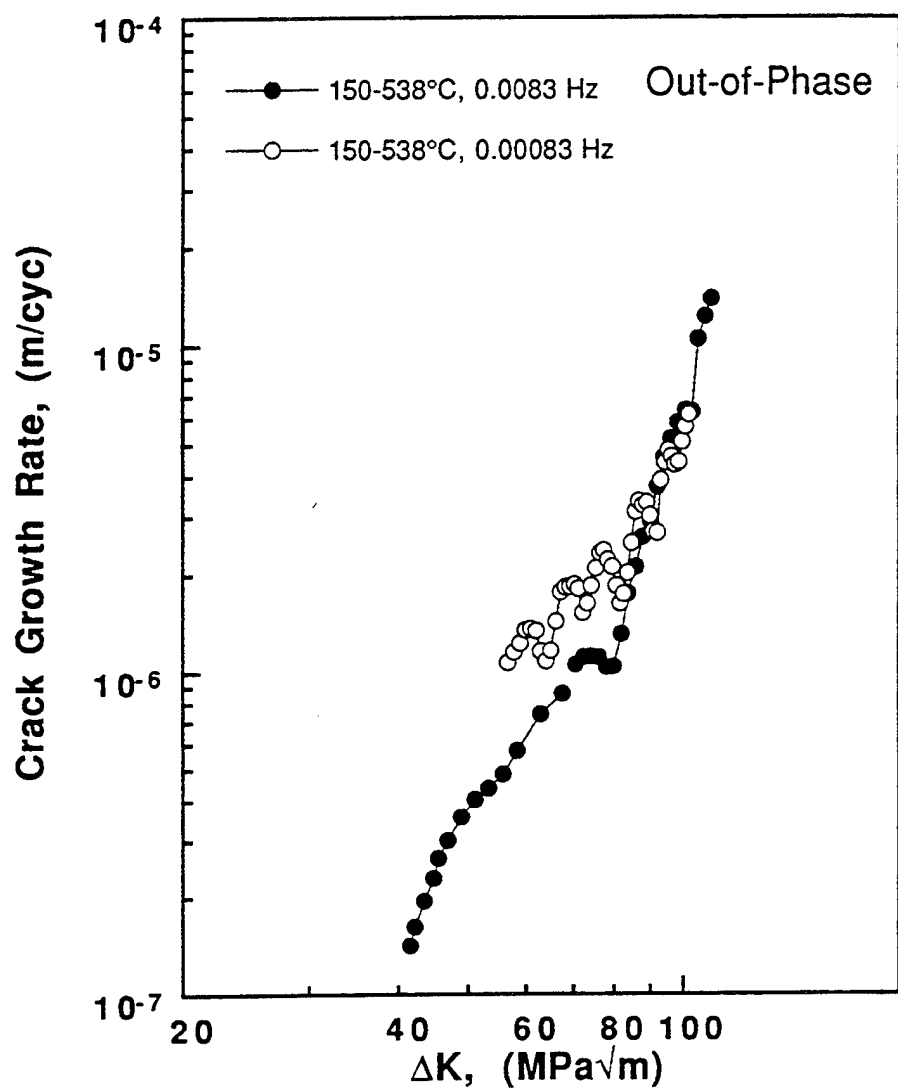


Figure 7.13 Comparison of out-of-phase thermomechanical fatigue crack growth data for SCS-6/Ti-6Al-2Sn-4Zr-2Mo cycled between 150 and 538 °C at 0.0083 Hz and 0.00083 Hz.

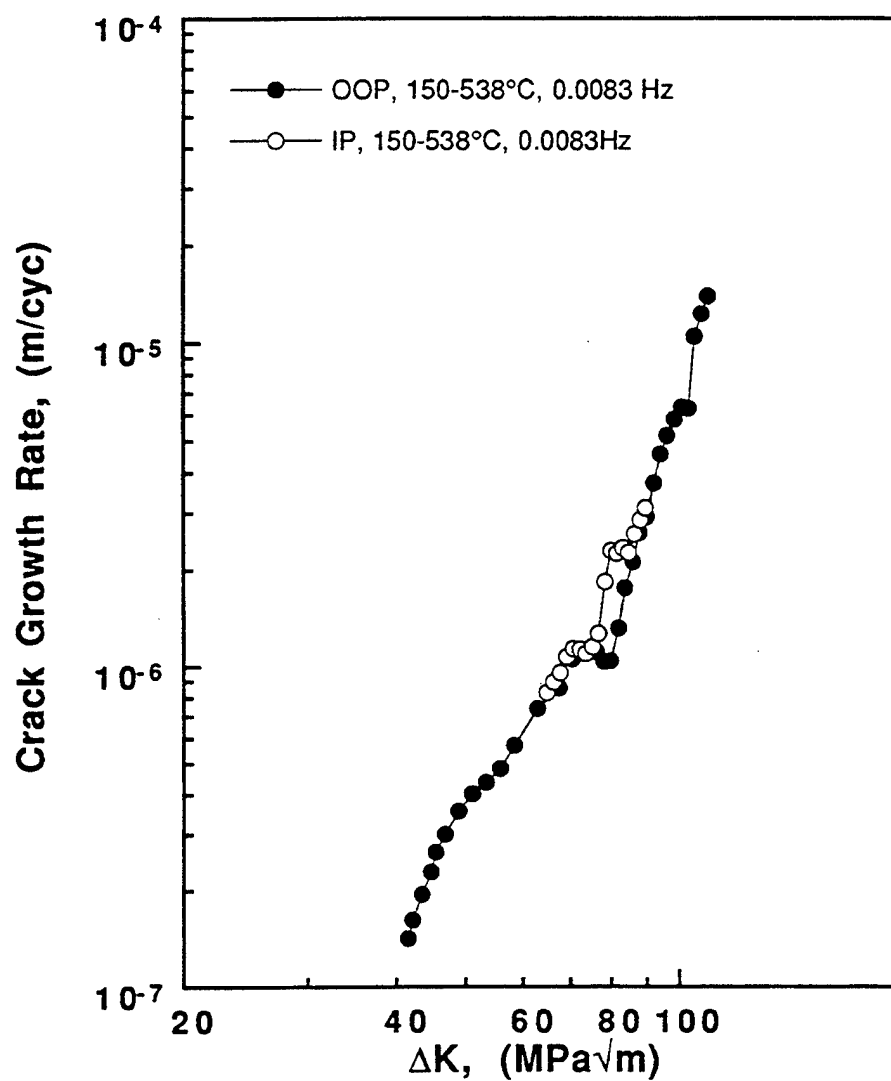


Figure 7.14 Comparison of in-phase and out-of-phase thermomechanical fatigue crack growth data for SCS-6/Ti-6Al-2Sn-4Zr-2Mo cycled between 150 and 538 °C at 0.0083 Hz.

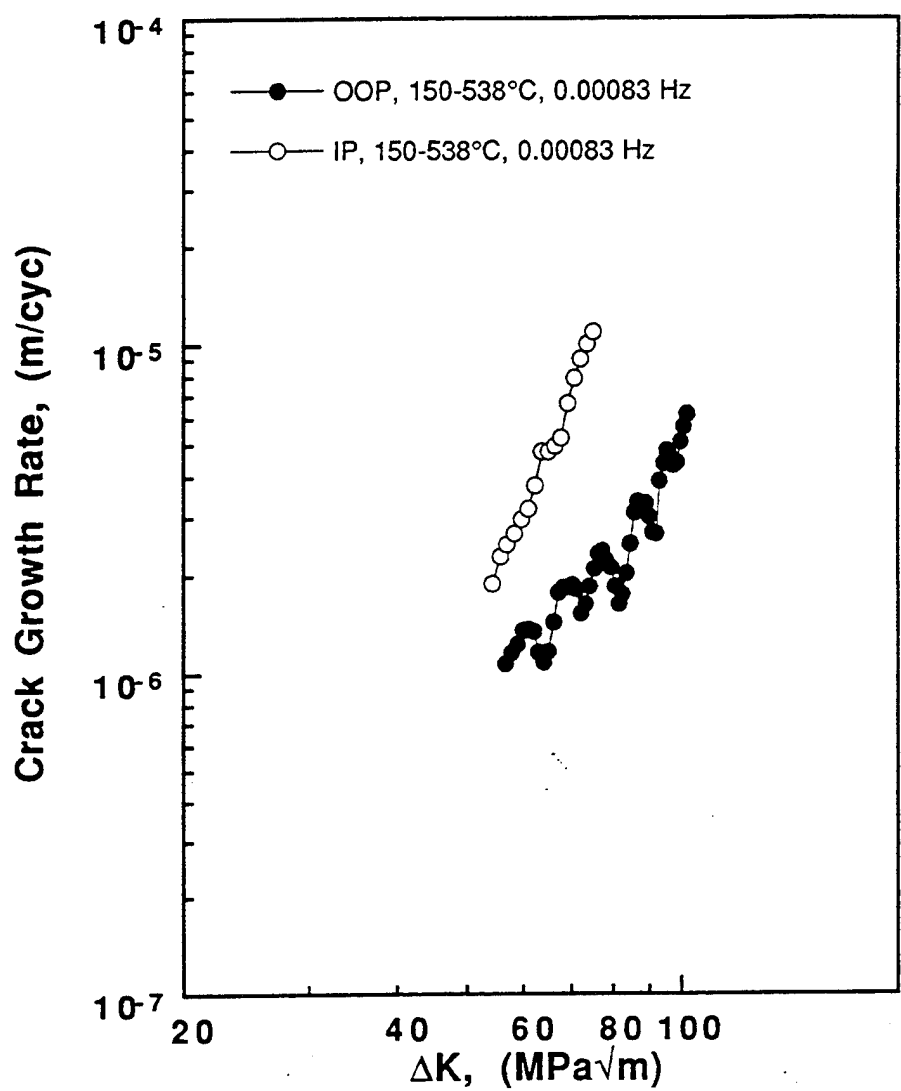


Figure 7.15 Comparison of in-phase and out-of-phase thermomechanical fatigue crack growth data for SCS-6/Ti-6Al-2Sn-4Zr-2Mo cycled between 150 and 538 °C at 0.00083 Hz.

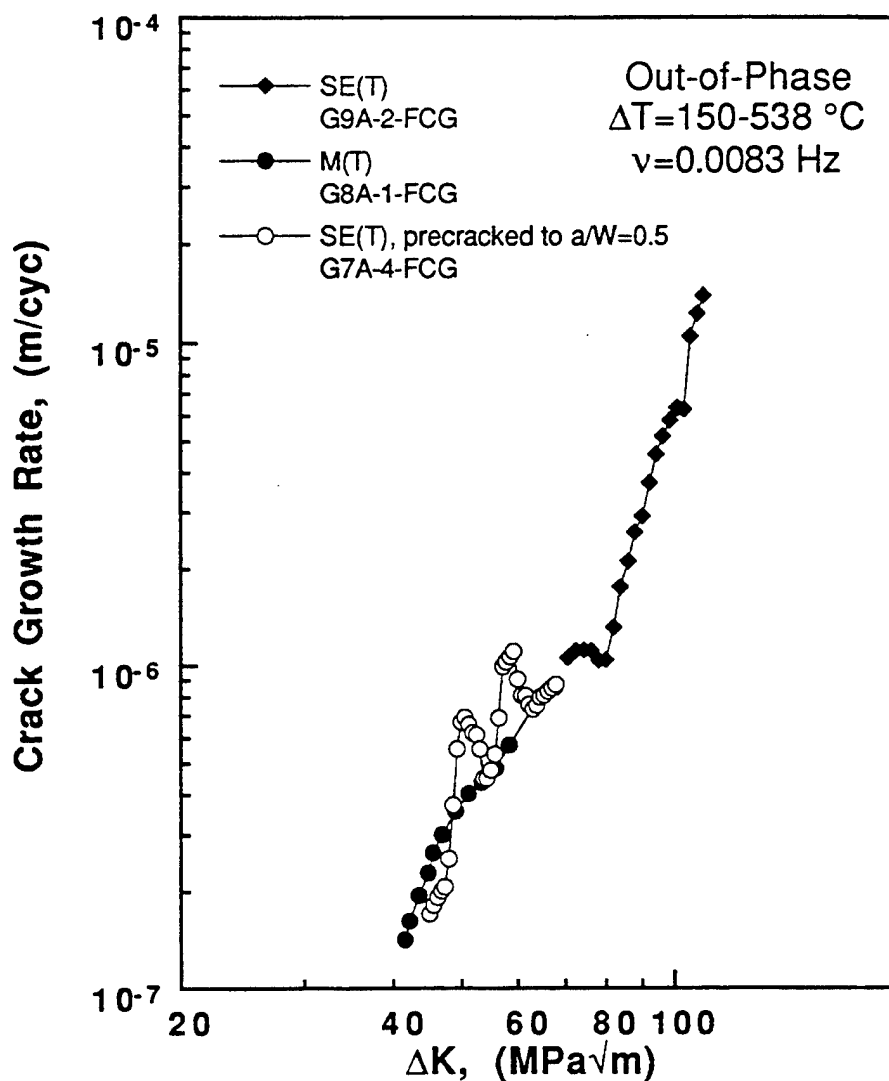


Figure 7.16 Comparison of SE(T) and M(T) geometries for out-of-phase thermomechanical fatigue crack growth data for SCS-6/Ti-6Al-2Sn-4Zr-2Mo cycled between 150 and 538 °C at 0.0083 Hz.

## CHAPTER 8

## MODELING OF TMF CRACK GROWTH IN SCS-6/Ti-6Al-2Sn-4Zr-2Mo

This chapter explains the empirical model that was developed to predict the trends evident in the experimental data. The model is a logical extension of other linear summation type models (see Chapter 2) that assume that a cycle-dependent and time-dependent damage component act during each cycle to produce a total crack growth rate.

### 8.1 Development of the TMF Model

The interpolative model presented in this chapter was based on concepts developed in previous linear summation models [29-33] and on the isothermal and TMF crack growth data generated during this study. Since the author was unaware of any TMF crack growth data for metal matrix composites (MMC), and more specifically titanium matrix composites (TMC), in the literature, it was difficult to foresee the outcome of the initial crack growth tests. Unusual crack growth behavior in some MMC, such as crack propagation along the loading direction or fiber fracture ahead of the crack tip, occur when, for example, the fiber/matrix interface is very strong or very weak, or when the crack growth is geometry dependent. Not until the initial TMF crack growth tests were complete, did a clearer understanding of the composite's behavior become apparent. The modeling effort was guided by the experimental data

generated during this study as well as by the ideas put forth in the models mentioned above.

The model presented in this chapter is capable of predicting fatigue crack growth rates for isothermal and thermomechanical fatigue conditions in the [0]4, SCS-6/Ti-6242. The model is valid for a range of temperatures between 150 and 538 °C (300 and 1000 °F) and for a range of frequencies between 0.83 and 0.00083 Hz. No experiments were conducted which incorporated hold times. While no load hold times were considered in this study, the current model is able to predict crack growth rates for load histories with hold times.

## 8.2 Explanation of TMF Modeling Expressions

The basic assumption for linear summation models for TMF fatigue crack growth behavior is that damage for any given cycle is a combination of a cycle-dependent and time-dependent damage component [11, 29-33]. Mathematically, the expression takes the form

$$\frac{da}{dN} \Big|_{total} = \frac{da}{dN} \Big|_{cycle-dependent} + \frac{da}{dN} \Big|_{time-dependent} \quad (8.1)$$

where  $a$  and  $N$  are crack length and number of cycles, respectively. As described in Chapter 2 (Section 2.3), the expressions to define  $(da/dN)_{cyc-dep}$  and  $(da/dN)_{time-dep}$  vary widely depending on the type of behavior they attempt to model. The remaining discussion will focus on the forms chosen to represent the behavior of the experimental data obtained here.

### 8.2.1 Determination of the Cycle-Dependent Term

The cycle-dependent term represents the pure mechanical fatigue experienced during a given cycle of the matrix material in its composite form. In general, the cycle-dependent term in a monolithic analysis is a function of  $\Delta K_{\text{Applied}}$ , the stress ratio ( $R$ ), and the temperature ( $T$ ) [29, 33]. Because purely cycle-dependent fatigue crack growth data for this composite was unavailable as a function of temperature and stress ratio, the cycle-dependent term was assumed to be a function of  $\Delta K_{\text{Applied}}$  only. Vesier and Antolovich [76] reported that for monolithic Ti-6242, stress ratio did affect fatigue crack growth rates for a given temperature, whereas temperature only slightly affected the fatigue crack growth rates for temperatures in the range used in this study. Since only one stress ratio is used during all fatigue crack growth tests for this study, and temperature does not influence the matrix crack growth rate, the assumption that the cycle-dependent term is only a function of  $\Delta K_{\text{Applied}}$  is probably sufficient to describe the results generated in this study.

In the TMF modeling efforts by Heil et al. [29] and Pernot et al. [33] a modified sigmodial equation, MSE, was used to describe the cycle-dependent term. Heil et al. [29] made the cycle-dependent MSE a function of  $\Delta K_{\text{Applied}}$  and stress ratio, whereas Pernot et al. [33] made the cycle-dependent MSE a function of  $\Delta K_{\text{Applied}}$  and temperature. The modified sigmodial equation (Eqn. 2.4) described in Chapter 2 has six independent empirical parameters, typically determined from experimental data. Again, since sufficient data were not available to determine these constants, a simple Paris Law was used for the cycle-dependent term. Since the Paris Law is valid only in Region II (see Figure 2.2), only the TMF crack growth data in this region is modeled in this study. Predictions of crack growth rates in Regions I and III were not attempted

because insufficient crack growth data were generated in those regions to determine an expression which would represent all the conditions used in this study.

Recall that the Paris Law has the form:

$$\frac{da}{dN} = C(\Delta K_{\text{applied}})^n \quad (8.2)$$

where C and n are empirical constants. The constant n was determined by considering the slope of the isothermal and TMF crack growth data generated for this study (Figures 7.11-7.13) between  $\Delta K = 50$  to  $80 \text{ MPa}\sqrt{\text{m}}$ , with the exception of the  $150^\circ\text{C}$  ( $300^\circ\text{F}$ ) isothermal data, where n was nearly zero. In general, the slope of the linear portion of each data set was similar enough to be considered a constant, and not a function of temperature, frequency or phase angle. The exponent n was set to equal 2.7. The coefficient C was fixed so that, along with n = 2.7, the cycle-dependent crack growth rates were slightly less than the isothermal,  $150^\circ\text{C}$  ( $300^\circ\text{F}$ ), 0.0083 Hz fatigue crack growth data (Figure 7.10). When the time-dependent contribution is negligible, such as at low isothermal temperatures, the model will represent the  $150^\circ\text{C}$  ( $300^\circ\text{F}$ ) data. Note, however, that the Paris Law does not accurately represent the data in Figure 7.10 because fiber bridging is not accounted for by the Paris Law. The fit to the  $150^\circ\text{C}$  ( $300^\circ\text{F}$ ) data represents an idealization of the behavior as if there were no bridging occurring. With this understanding, C was set equal to  $7.9 \times 10^{-13}$  (where  $\Delta K$  is in units of  $\text{MPa}\sqrt{\text{m}}$  and da/dN is in  $\text{m/cycle}$ ). The cycle-dependent term is now defined as:

$$\frac{da}{dN} = 7.9 \times 10^{-13} (\Delta K_{\text{applied}})^{2.7} \quad (8.3)$$

Note that Equation 8.3 represents only the TMF crack growth data ranging from  $\Delta K_{\text{applied}}$  of 50 to 80 MPa $\sqrt{\text{m}}$ ; outside this range the Paris Law does not accurately represent the data.

### 8.2.2 Determination of the Time-Dependent Term

As more and more of the TMF crack growth tests were completed, the contribution of the time-dependent term became evident. Specimen G9A-4-FCG (Figures 7.10 and 7.11), isothermally cycled at 538 °C (1000 °F) and 0.0083 Hz, experienced the highest crack growth rate of all the conditions tested in this study, whereas specimen G8A-4-FCG (Figure 7.10), isothermally cycled at 150 °C (300 °F), gave fatigue crack growth rates which were approximately one and a half orders of magnitude slower. The in-phase and out-of-phase tests cycled between 150 °C and 538 °C (300 °F and 1000 °F) had crack growth rates approximately a half an order of magnitude slower than specimen G9A-4-FCG cycled isothermally at 538 °C (1000 °F). This behavior suggests that the time-dependent contribution to the total crack growth rate is not a linear function in temperature, since as the temperature approaches  $T_{\max}$  (typically 538 °C=1000 °F), the time-dependent contribution greatly dominates the total crack growth rate.

An expression similar to the fiber damage term in Neu's model [77] for TMF in titanium matrix composite was used to model the time-dependent crack growth behavior. Neu suggested an Arrhenius-type expression to represent the weakening of a fiber because of time, temperature, and fiber stress. In general, the fatigue and fatigue crack growth behavior of titanium based composites reinforced with silicon-carbide fibers are greatly dependent upon

the fibers' behavior [69, 78]. Even the creep behavior of TMC's with SCS-6 fibers is associated with stress-assisted environmental degradation of the carbon-rich layers of the SCS-6 fibers, followed by subsequent weakening and fracture of the fibers [79]. With this understanding, the time-dependent component resembled a form similar to Neu's Arrhenius expression, except the fiber-stress component was replaced with an applied  $\Delta K$  dependence. The time-dependent term had the form:

$$\frac{da}{dN} = \int_{\text{cycle}} \frac{da}{dt} dt = \int_0^{t_{\text{nd}}} C_1 e^{\frac{-C_2}{T_{\text{abs}}}} (\Delta K)^n dt \quad (8.4)$$

where  $C_1$  is an empirical constant,  $T_{\text{abs}}$  is the absolute temperature ( $T$  °C + 273 K) at any instant during the cycle, and  $n$  is the same exponent used in Equation 8.1. The exponent  $n$  is assumed here to be independent of temperature. In some materials  $n$  will increase with increasing temperature, but fatigue crack growth data for monolithic Ti-6242 [76] show only a small variation of  $n$  between room temperature and 538 ° (1000 °F). The constant  $C_2$  actually represents the ratio  $Q_{\text{fib}}/R$ , where  $Q_{\text{fib}}$  is the apparent activation energy for environmental attack of the fiber (with units of kJ/mol) and  $R$  is the gas constant (with units of kJ/mol/deg). The term,  $t_{\text{nd}}$ , represents the sum of the time which the load is increasing and held at  $P_{\text{max}}$ . This is the same upper limit of integration used by Pernot et al. [33] on the time-dependent term. The TMF crack growth work of Pernot et al. included the effects of hold times; they found that the hold times at max load had to be accounted for in the time-dependent term for the predictions to match the experimental data. Since no hold times

are included in this study,  $t_{nd}$  is actually equivalent to  $t_{inc}$ , the time the load is increasing.

With an Arrhenius type expression like Equation 8.4, the effect of elevated temperatures on the total crack growth rate is greatly influenced by the value of  $C_2$  or  $Q_{fib}$ . The effect on the exponential term of varying  $C_2$  is clearly evident in Figure 8.1. As  $C_2$  increases, the function from the mid to lower temperatures ( $325\text{ }^{\circ}\text{C}$  to  $150\text{ }^{\circ}\text{C}$  or  $617\text{ }^{\circ}\text{F}$  to  $300\text{ }^{\circ}\text{F}$ ) becomes negligible compared to the function at higher temperatures. As  $C_2$  is decreased the function behaves more linearly over a wide range of temperatures. The coefficient  $C_1$  only serves to shift the entire curve up or down in a linear fashion.

To determine  $C_2$ , two of the TMF crack growth tests were used: the isothermal,  $538\text{ }^{\circ}\text{C}$  ( $1000\text{ }^{\circ}\text{F}$ ),  $0.0083\text{ Hz}$  condition; and the in-phase  $150$ - $538\text{ }^{\circ}\text{C}$  ( $300$ - $538\text{ }^{\circ}\text{F}$ ),  $0.0083\text{ Hz}$  condition. A value of  $C_1$  was also found during this process, but it was later modified in Section 8.2.3 when frequency effects were taken into account. To simplify the process of determining the model constants, the total crack growth rate was first calculated only at  $\Delta K_{\text{applied}} = 60\text{ MPa}\sqrt{\text{m}}$ . After all the constants were determined, the growth rates were calculated for a range of  $\Delta K$ 's between  $50$  and  $80\text{ MPa}\sqrt{\text{m}}$ . The correlation between the experimental data and the model's calculations is discussed later in this chapter.

Initially,  $C_1$  and  $C_2$  were simply estimated. Through trial and error, both  $C_1$  and  $C_2$  were adjusted such that the total crack growth rates for the isothermal and in-phase conditions matched the experimental data based on a best-eye fit. The values of  $C_1$  and  $C_2$  were calculated to be  $2.27\text{E-}5$  and  $12000$ , respectively. The units of  $C_1$  and  $C_2$  are  $(\text{m}^{(n-2)/n})/(\text{cyc}\cdot\text{sec}^{\gamma}\cdot\text{MPa}^n)$  and

K degrees, respectively. Interestingly enough, the value of  $Q_{fib}$  calculated from  $C_2$  is 100 kJ/mol which is similar to the  $Q_{fib}$  used in Neu's [77] TMF fatigue model of 112.9 kJ/mol. The initial form of the time-dependent term was

$$\frac{da}{dN} = \int_0^{t_{nd}} 1.70E - 5e^{\frac{-12000}{T_{abs}}} (\Delta K)^{2.7} dt \quad (8.5)$$

The relatively large value of  $C_2$  suggests that the majority of the damage occurs when the temperature is at or near the maximum temperature. In fact, the time-dependent contribution calculated for the isothermal condition at 150 °C is about two orders of magnitude smaller than the cycle-dependent term. In contrast, the time-dependent term is about an order of magnitude greater than the cycle-dependent contribution for the isothermal 538 °C condition. Note that predictions based on Equations 8.3 and 8.5 would produce crack growth rates that are equivalent regardless of the phase angle (i.e., in-phase or out-of-phase). After properly accounting for frequency the model will predict different crack growth rates due to different phase angles.

### 8.2.3 Accounting for Frequency

The time-dependent constants,  $C_1$  and  $C_2$ , were determined from data gathered at the same frequency (0.0083 Hz). Until now frequency effects were not explicitly considered. In general, the cycle-dependent term is independent of frequency, but since the time-dependent term in Equation 8.4 is implicit in time ( $T_{abs}$  depends on time during a TMF cycle), it is a function of frequency. While the data reveal that the crack growth behavior was affected by a change in frequency, the data never exhibited a completely time-dependent behavior for the conditions tested. For a given  $\Delta K$ , a completely time-dependent crack

growth rate would increase linearly with cycle period (1/frequency). The crack growth rates for the isothermal test at 538 °C cycled at 0.83 Hz (specimen G8A-2-FCG) were approximately an order of magnitude faster than the test conducted at 0.0083 Hz (specimen G9A-4-FCG). In this example, the crack growth rates increased only an order of magnitude for a two order of magnitude decrease in frequency.

To account for a similar behavior when modeling fatigue crack growth with sustained hold times in a titanium-aluminide, Nicholas and Mall [32] modified the time-dependent term in their linear summation model by a coefficient of the form  $T^{\gamma-1}$ , where  $T$  is the total cycle time (or period). They used  $\gamma = 0.5$ , which yielded a time-dependent term that would vary with frequency as  $\sqrt{T}$ . A similar modification was used in the current study to account for frequency effects. The time-dependent term was modified to take the form

$$\frac{da}{dN} = T^{\gamma-1} \int_0^{t_{nd}} 1.70E - 5e^{\frac{-12000}{T_{abs}}} (\Delta K)^{2.7} dt \quad (8.6)$$

where  $T$  is equivalent to  $t_{\text{nondecreasing}}$  in seconds and  $\gamma$  is determined by the type of test.

The value of  $\gamma$  for each type of test was determined by comparing the total crack growth rates for isothermal, in-phase, and out-of-phase conditions at two different frequencies. The value of  $\gamma$  was initially estimated to be 0.5 as used by Nicholas and Mall [32]. The value of  $\gamma$  was adjusted (along with  $C_1$ ) such that the model correctly correlated the crack growth rates of the 538 °C isothermal data generated at 0.0083 Hz and 0.83 Hz. During this process the constant  $C_1$  was also determined and fixed for the remainder of the crack

growth calculations. The value of  $\gamma_{iso}$  and  $C_1$  were fixed at 0.57 and 1.70E-5. In a similar fashion  $\gamma_{IP}$  and  $\gamma_{OOP}$  were determined. Again, the initial value of  $\gamma$  was set equal to 0.5, and then adjusted so that the in-phase and out-of-phase data generated between 150-538 °C at 0.0083 Hz and 0.00083 Hz were reasonably correlated by the linear summation model. The values of  $\gamma_{IP}$  and  $\gamma_{OOP}$  were determined to be 0.62 and 0.52, respectively.

The  $\gamma$ -term is not a constant because the frequency affects the magnitude of the fiber stress range at or near the crack tip over the life of the test according to the test type. The crack growth rate in most fiber reinforced metal matrix composites is governed largely by the fracture behavior of the fiber. If the fiber bridges the crack (i.e., does not fracture), the crack growth rate will tend to remain constant or decrease for increasing values of applied stress intensity factor range. If, however, the fiber fractures readily as the matrix crack passes by, the crack growth rate of the composite will behave similarly to a fiberless material.

Micromechanical modeling by Neu [74] of SCS-6/TIMETAL®21S [0]4 under thermomechanical loading investigated the effect of frequency on the stress in the matrix and fiber. That study showed that during in-phase loading the fiber stress range became noticeably higher at a longer cycle period (30 min/cyc) than at the shorter cycle period (3 min/cyc). The fiber stress range increase was due to relaxation of stresses in the matrix at the longer cycle periods requiring the fiber to carry a greater percentage of the applied load. The out-of-phase condition showed very little change in fiber stress range between the long and short cycle periods. In the out-of-phase loading the maximum temperature occurs at the minimum load; a condition that does not lend itself to matrix stress relaxation.

The value of  $\gamma$  is largest for the in-phase condition and lowest for the out-of-phase cycling with the isothermal condition lying in between the two. This layering of  $\gamma$  was anticipated since the influence of frequency on the in-phase condition on the fiber stress range is greater than on the other two conditions. However, the difference between the different  $\gamma$ 's is not very large, only spanning 0.52 to 0.62. This small range in  $\gamma$  indicates that while the frequency does affect the fiber stress range depending on the test conditions, the effect is not as pronounced as the micromechanical modeling of the SCS-6/TIMETAL®21S showed [74]. The change in fiber stress range due to a frequency change was not as pronounced during the fatigue crack growth tests because the applied loads and temperatures were not conducive to large scale matrix plastic deformation and stress relaxation away from the crack tip region.

#### 8.2.4 Final Form of the TMF Linear Summation Model

After the values of  $\gamma$  were determined, the linear summation model to predict the fatigue crack growth rates under isothermal and thermomechanical fatigue was complete. The model took the final form

$$\frac{da}{dN} = 7.9E - 13(\Delta K)^{2.7} + T^{\gamma-1} \int_0^{t_{upld}} 1.70E - 5e^{-12000/(T+273)} (\Delta K)^{2.7} dt \quad (8.7)$$

where  $\gamma$  equals 0.62, 0.57 and 0.52 for the in-phase, isothermal and out-of-phase conditions, respectively. The model in this form has four constants ( $C$ ,  $n$ ,  $C_1$  and  $C_2$ ) which are fixed for all conditions, and one constant,  $\gamma$ , which is test-type dependent. In effect, there are seven constants in all since there were three different test-types.

### 8.3 Crack Growth Rate Correlations and Predictions

All the constants in Equation 8.7 were based on the crack growth rate at an applied  $\Delta K = 60 \text{ MPa}\sqrt{\text{m}}$ . This simplified the procedure for determining a particular constant. A  $\Delta K = 60 \text{ MPa}\sqrt{\text{m}}$  was chosen first because it seemed to best represent Region II for all the crack growth rate data generated. Recall that this model only attempts to predict the crack growth rates for Region II of the  $da/dN - \Delta K$  relationship. In the following sections the accuracy of the correlation is shown for each of the seven conditions tested for a range of  $\Delta K$ 's between 30 and 100  $\text{MPa}\sqrt{\text{m}}$ . Region II, however, is only valid between about 50 and 85  $\text{MPa}\sqrt{\text{m}}$ . Note the term "correlation" is used here as opposed to "prediction" since all of the baseline data (seven different conditions) were needed to determine the seven constants used in the predictive model. An additional test was run at a condition different from the baseline conditions to prove the predictive capability of the model, and is described in detail later in this section.

#### **8.3.1 Isothermal Crack Growth Correlations**

The goal of this modeling effort was to predict the crack growth rates of SCS-6/Ti-6242 under thermomechanical loading based on isothermal data. Three baseline isothermal tests were conducted: two at the same temperature ( $538^\circ\text{C} = 1000^\circ\text{F}$ ), but with different frequencies (0.0083 Hz and 0.00083 Hz); and two at the same frequency (0.0083 Hz) but different temperatures ( $150^\circ\text{C}$  and  $538^\circ\text{C} = 300^\circ\text{F}$  and  $1000^\circ\text{F}$ ). Using the final form of the predictive model given in Equation 8.6, crack growth rates were calculated for each of isothermal conditions. The correlation is shown in Figures 8.2 and 8.3. As expected, the crack growth rates calculated from the model for each of the

isothermal conditions correlate well with the experimental data in Region II. However, since the experimental data represent both Region II and Region III, the calculated growth rates do not correlate well when  $\Delta K_{app}$  is greater than about 85 MPa $\sqrt{m}$ .

### 8.3.2 TMF Crack Growth Correlations

Four baseline thermomechanical conditions were studied: two in-phase at 0.0083 Hz and 0.00083 Hz and two out-of-phase also at 0.0083 Hz and 0.00083 Hz. Each of the TMF tests were cycled between 150 °C to 538 °C (300 °F to 1000 °F). The crack growth rates were calculated using the model for each of the four different TMF conditions. The computed crack growth rates are plotted along with the experimental TMF data in Figures 8.4 and 8.5. Again, since the seven constants were adjusted to fit the seven baseline conditions, the computed crack growth rates correlate well with the experimental data in Region II.

## 8.4 Experimental Proof of Linear Summation Model

As explained earlier, the computed crack growth rates shown in Figures 8.2-8.5 were correlations and not predictions. To ensure that the linear summation model was capable of predicting crack growth rates for a condition different from the baseline conditions, one additional test was completed. After all the baseline isothermal and thermomechanical fatigue crack growth tests were completed, only one crack growth specimen remained. This fact mandated that the single proof test of the model's predictive capability be designed to exercise as much of the model's capabilities as possible. The

following sections describe the process that went into designing the proof test, and the success of the predictive capability based on the experimental results.

#### 8.4.1 Designing the Proof Test

In general, the crack growth rate of SCS-6/Ti-6242 is most influenced by the time spent at elevated temperatures, especially those temperatures approaching the maximum use temperature of 538 °C (1000 °F). Cycling isothermally at  $T_{max}$  produces the highest crack growth rates since environmental degradation is more active over the entire cycle than during a TMF cycle. During a TMF cycle the amount of time spent at higher temperatures is always less than an equivalent isothermal cycle. Slower TMF frequencies, however, do spend more time at higher temperatures, producing faster crack growth rates.

With this in mind, it is obvious that constant- $\Delta K_{app}$ , TMF conditions will produce slower growth rates than isothermal conditions at the same frequency and  $T_{max}$ . Now consider a series of TMF tests in which  $T_{max}$  is constant and the minimum temperature,  $T_{min}$ , is increased in each successive test. As  $T_{min}$  approaches  $T_{max}$ , the difference between the crack growth rates of the isothermal test at  $T_{max}$  and the TMF test with  $T_{min}$  nearly equal to  $T_{max}$  will be negligible. This reasoning is shown graphically in Figure 8.6, and lead to the design of the proof test conditions.

The goal of the proof test was to use the predictive model to develop a complex TMF history which would yield a constant crack growth rate,  $da/dN$ . Experimentally, the proof test would begin under isothermal ( $T_{max}=T_{min}=538$  °C) conditions, continue with  $T_{min}$  decreasing throughout the test and end under in-phase conditions with  $T_{min}=150$  °C (300 °F). Interestingly, if  $T_{min}$  is

decreased according to a predefined profile the crack growth rate will remain constant throughout the test. A schematic representation of this is shown in Figure 8.7. This constant crack growth rate is possible since two competing damage mechanisms are acting. As the matrix crack grows through the composite (assuming no fiber bridging) the stress intensity factor range increases which leads to an increase in the crack growth rate. If during this same test, the minimum temperature is decreased the crack growth rate will tend to decrease. Appropriately combining these two opposing mechanisms into one test allows a constant growth rate test to be achieved.

The critical factor in achieving a constant crack growth rate test is to determine the minimum temperature profile as a function of elapsed cycles. To determine the exact  $T_{min}$  profile for the proof test, the linear summation model (Equation 8.6) was used. The proof test, using an M(T) geometry, was planned to start at  $T=538^{\circ}\text{C}$  with a constant cyclic force,  $\Delta P$ , of 10 kN. The desired constant crack growth rate was  $1.41 \times 10^{-6} \text{ m/cycle}$ . Knowing the beginning and ending  $\Delta K_{app}$ , 42 and  $80 \text{ MPa}\sqrt{\text{m}}$ , respectively, the number of cycles the test would run was found to be 2750. Using Equation 8.7, the growth rate ( $1.41 \times 10^{-6} \text{ m/cycle}$ ) for several different  $\Delta K$ 's between 42 and  $80 \text{ MPa}\sqrt{\text{m}}$  was calculated. To achieve the desired growth rate at each  $\Delta K$ , the minimum temperature was reduced sufficiently so that the model predicted the growth rate to be approximately  $1.41 \times 10^{-6} \text{ m/cycle}$ . This process would, therefore, follow the dashed line in Figure 8.7 moving from an isothermal condition to an in-phase condition. From this exercise the cyclic rate at which the minimum temperature should decrease over the expected 2750 cycles was determined.

Each crack growth curve corresponding to a minimum temperature needed to produce the desired crack growth rate at a given  $\Delta K$  was described

by a Paris Law as indicated in Figure 8.7. Each crack growth curve was described by the equation

$$\frac{da}{dN} = C^* (\Delta K)^n \quad (8.8)$$

where  $C^*$  is a different for each value of  $T_{min}$ . A fourth order polynomial was fit to the values of  $C^*$  and  $T_{min}$  and is given by the equation

$$C^* = 1.9792 \times 10^{-11} - 1.8151 \times 10^{-13} T_{min} + 1.2018 \times 10^{-15} T_{min}^2 - 3.1316 \times 10^{-18} T_{min}^3 + 3.3921 \times 10^{-21} T_{min}^4 \quad (8.9)$$

Figure 8.8 plots this functional relationship between  $C^*$  and  $T_{min}$ . Using this relationship, the proof test was then performed "on paper" to find the appropriate  $T_{min}$  profile for the proof test.

The proof test was simulated by growing the crack incrementally from its initial length to its final length using the equation

$$\Delta a = \frac{da}{dN} \Delta N \quad (8.10)$$

where  $da/dN$  is given by Equation 8.8 and  $\Delta N$  was set equal to 1. Since  $C^*$  in Equation 8.8 is a function of temperature given by Equation 8.9, the manner in which  $T_{min}$  is decreased over the life of the test determines the crack growth rate. The  $T_{min}$  profile was adjusted until at the end of 2750 cycles two conditions were met: (1) the crack growth rate over the entire simulation was constant and equal to  $1.41 \times 10^{-6}$  m/cycle and (2) the final crack length was equal to that required to produce a  $\Delta K_{app}$  of  $80 \text{ MPa}\sqrt{\text{m}}$ . The equation used to

describe the minimum temperature profile to produce a near constant crack growth rate is given as

$$T_{min} = 150 + 2.0839(2750 - N)^{0.66} (\text{°C}) \quad (8.11)$$

where  $N$  is the cycle count. Note that at  $N=2750$  the minimum temperature equals 150 °C (300 °F) as the proof test required.

#### 8.4.2 Experimental Results of Proof Test

To conduct the proof test with the desired  $T_{min}$  profile, the control software was modified so that the temperature setpoints would update each cycle according to Equation 8.11. The proof test specimen, G8A-6-FCG, was precracked at 0.0083 Hz with  $T=538$  °C (1000 °F) and  $\Delta K_{initial} = 42$  MPa·√m. This established the crack growth rate desired to begin the proof test. The model predicted that the growth rate would be approximately  $1.41 \times 10^{-6}$  m/cycle at the end of the precrack, and the measured ending precrack crack growth rate was  $1.38 \times 10^{-6}$  m/cycle. This was encouraging because there was no previous isothermal data ( $538$  °C = 1000 °F) generated at a  $\Delta K \approx 42$  MPa·√m.

After precracking, the software modifications were made to run the actual proof test. The crack growth rate measured soon after the proof test began was  $1.23 \times 10^{-6}$  m/cycle. While this apparent discrepancy in growth rate was small and within the limits of experiment scatter, it may be attributed to initial problems with the automatic adjustment of the temperature setpoints by the control software. While the temperature control software was modified, the specimen accumulated approximately 60 cycles before the final software was

in place. These 60 cycles were not recorded as part of the proof test crack growth data. During the software revisions the specimen was allowed to cool to room temperature at least three times before the corrections were completed. This type of cycling may have lead to a transient behavior and a reduction in the growth rate. Once the software was finalized the proof test ran uninterrupted. The minimum and maximum temperature followed the desired profile successfully as is illustrated in Figure 8.9.

Unfortunately, at cycle 2500 the computer experienced an input/output error with the printer and the test was allowed to cycle without the minimum temperature setpoint being adjusted. Under these conditions the growth rate did not remain constant and the specimen failed earlier than anticipated. The exact final cycle count was not recorded but it was no larger than 2710 cycles, and the final crack length based on inspection of the fracture surface was determined to be 8.182 mm. In addition, no experimental data such as DCEP crack length were recorded beyond cycle 2500. Furthermore, the  $T_{min}$  history beyond cycle 2500 was not recorded. If the temperature profile between cycle 2500 and 2710 was known, the remaining crack growth behavior could be predicted based by the model. Nonetheless, a significant portion of the test was completed and the data generated was similar to what was predicted during the simulation. The DCEP crack lengths were similar to those predicted using Equation 8.10 as shown in Figure 8.10. In fact, the model predicted that at cycle 2710 the crack length would equal 7.814 mm which is similar to the final crack length of 8.182 mm.

The crack growth rate was also plotted as a function of  $\Delta K_{app}$  and compared with the growth rate from the simulation. Figure 8.11 shows that the simulation predicted a slightly decreasing growth rate over the life of the

specimen. A nonconstant crack growth rate was predicted because the temperature profile for the predictions was not the exact one necessary to generate a constant crack growth rate. Nevertheless, the crack growth rates generated during the proof test followed the general trend predicted by the simulation. For that matter the experimental crack growth rate never deviated from the expected growth rate by more than a factor of 1.5. This deviation from the expected crack growth rate is quite small considering the amount of variability that is commonly observed in the crack growth rates [80] of monolithic materials. Depending of the data reduction technique [81] and the homogeneity of the material, fatigue growth rates can vary up to a factor of 3 [80] for replicate crack growth tests of the same material.

The results of the proof test indicate that the proposed linear summation model successfully captured the primary features which control the crack growth behavior of the SCS-6/Ti-6242. Namely, the time-at-temperature significantly influences the crack growth behavior. While a single proof test does not offer absolute evidence that the model is entirely accurate, it does strongly support the fundamental notions built into the model.

### 8.5 Parametric Study of Model

Having provided a limited experimental evaluation of the numerical model, it was decided to use it as a tool to further investigate TMF in SCS-6/Ti-6242. This section describes the results of that study. Three parametric studies were completed: the first study investigated the effect of load hold times during isothermal cycling; the second study looked at the effect of intermediate temperatures between 150 °C and 538 °C (300 °F and 1000 °F) on the isothermal crack growth rates; and the third study determined the effect of

decreasing the minimum temperature during in-phase conditions. All the studies were conducted at a  $\Delta K_{app}$  of  $60 \text{ MPa}\sqrt{\text{m}}$  since that represented the approximate middle of Region II.

The results of the load hold times study indicated, as expected, that as the load hold times increase under isothermal conditions, the crack growth rates increase. This behavior is shown in Figure 8.12 for various loading frequencies. Since the upper integration limit of the time-dependent component includes hold times, the model states that the crack growth rate should increase. What is not so obvious without the results of this study is how the different hold times influence the crack growth rates depending on the loading frequency. For the slower frequency (0.00083 Hz) an increase in hold time increases the growth rate only slightly, but at the higher frequency (8.3 Hz) the shorter hold times yielded the greatest change in crack growth rates. As the hold times increased the resulting change in crack growth rates was less and less since, at the slower frequencies, the hold times contribute less to the time-dependent component than the loading portion of the cycle. For the faster frequencies, the hold time increases the crack growth rate as  $T^{-1}$  since the loading portion of the cycle is only a small fraction of the total cycle time. The study results also suggest that the crack growth rates are nearly identical for long hold times and fast frequencies. The similarity in growth rates is because the hold time portion of the cycle dominates the time-dependent component of the total crack growth rate, and as the frequency increases the contribution of the loading portion of the cycle becomes negligible.

The results of the second study showed that as the isothermal temperatures increased the crack growth rates were affected differently depending on frequency. For example, at the highest frequency (8.3 Hz) the

isothermal crack growth rates remained almost constant for temperatures between 150 °C and 375 °C (300 °F and 707 °F) and increased thereafter with increasing temperature; however, at the slowest frequency (0.00083 Hz), the isothermal crack growth rates increased significantly for temperatures above 225 °C (437 °F). This behavior is evident in Figure 8.13 in which crack growth rate is plotted as a function of isothermal temperature for frequencies between 0.00083 Hz and 8.3 Hz. This behavior reinforces previous statements that the time-at-temperature and the temperature itself significantly influence the crack growth rate. The growth rate is more accelerated for slower frequencies than for faster frequencies because on a cycle-by-cycle basis the slower frequency elapses more time per cycle and, therefore, allows more damage (crack growth) to occur per cycle.

The third study illustrated how increasing the minimum temperature of an in-phase condition increases the crack growth rate to that of the isothermal condition at the maximum temperature (in this study, 538 °C = 1000 °F). The magnitude to which the growth rate increased as the minimum temperature was increased to a completely isothermal condition was directly influenced by the frequency. This is clearly shown in Figure 8.14 in which the growth rate, normalized with respect to the growth rate for  $T_{min} = 150$  °C (300 °F), is plotted as function of  $T_{min}$  for frequencies ranging from 0.00083 Hz to 8.3 Hz. For the fast frequency, the growth rate only increased about a factor of two when  $T_{min}$  changed from 150 °C (300 °F) to 538 °C (1000 °F) or  $T_{max}$ . For the slowest frequency, the growth rate differed by a factor of eight between  $T_{min} = 150$  °C (300 °F) and  $T_{min} = T_{max} = 538$  °C (1000 °F). Another interesting observation from this study was that the trends for 0.0083 Hz and 0.00083 Hz normalized growth rate are nearly the same as shown in Figure 8.14. The similar in

normalized growth rates suggests that as the frequency is further decreased the crack growth rate will behave similarly to those generated at 0.00083 Hz. This behavior is important to note since the generation of slow frequency crack growth data is more time consuming. Therefore, crack growth data from a slow frequency isothermal test (frequency < 0.00083 Hz) could be used to generate the growth rates at other  $T_{min}$ 's based on the scaled results of 0.00083 Hz data.

### 8.6 Computer Code for Modeling TMF Crack Growth

The computer program developed during this research was a revision of the computer code developed by J. Pernot [22] to model TMF crack growth in a monolithic titanium-aluminide. Pernot actually used many of the same algorithms employed by Heil [82], who modeled TMF crack growth in Inconel 718. The source code developed for this study is given in Appendix B. Many of the input and output routines as well as the numerical integration routine were taken, with permission, from the source code found in the Appendix of Pernot's Ph.D. dissertation [22].

Both the cycle-dependent and time-dependent terms were approximated numerically in the source code using a simple Simpson's rule found in most numerical methods books. Since the cycle-dependent term is not a function of time, it is not required that it be determined through integration. However, the program was written to allow use of a cycle-dependent term that is a function of time. The number of divisions used in the Simpson's rule to approximate the function was chosen so that each division represented no more than 0.77 °C. For example, an in-phase test cycling between 150 and 538 °C at a frequency of 0.0083 Hz requires 500 divisions per cycle segment for sufficient accuracy of the numerical integration. A cycle

segment is a time in the cycle in which the temperature is either always increasing or always decreasing.

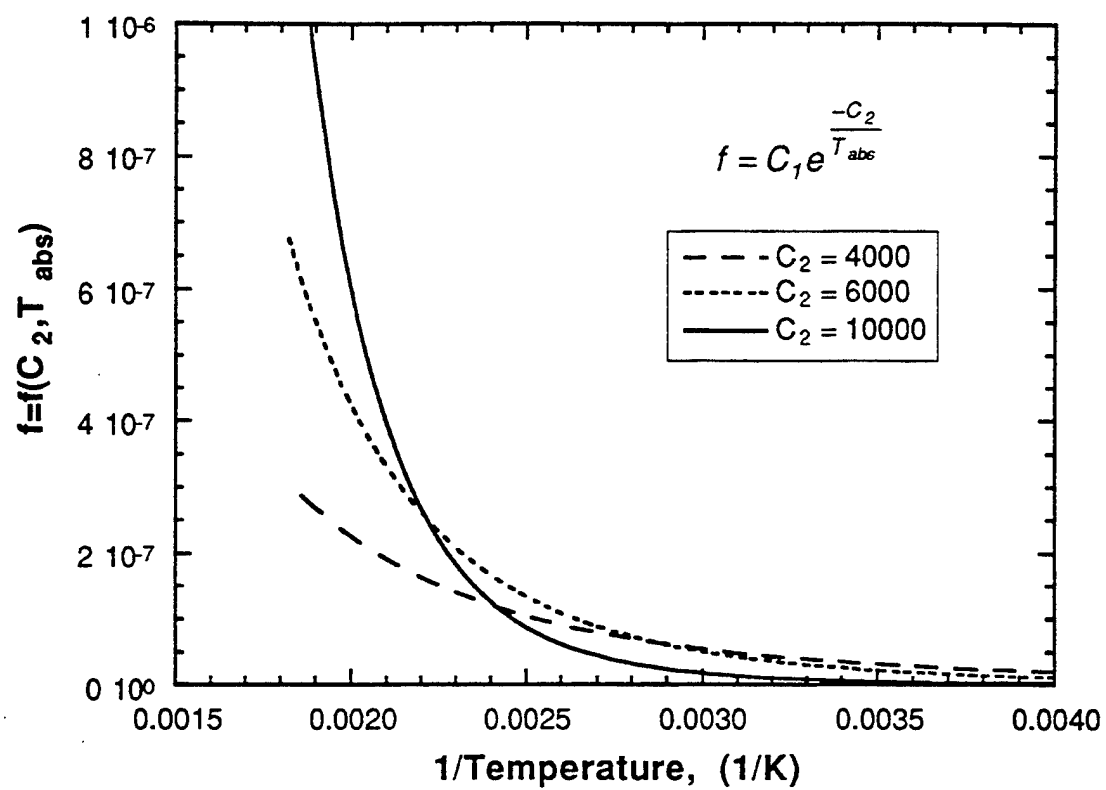


Figure 8.1 Effect of varying  $C_2$  in the Arrhenius function,  $f$ .

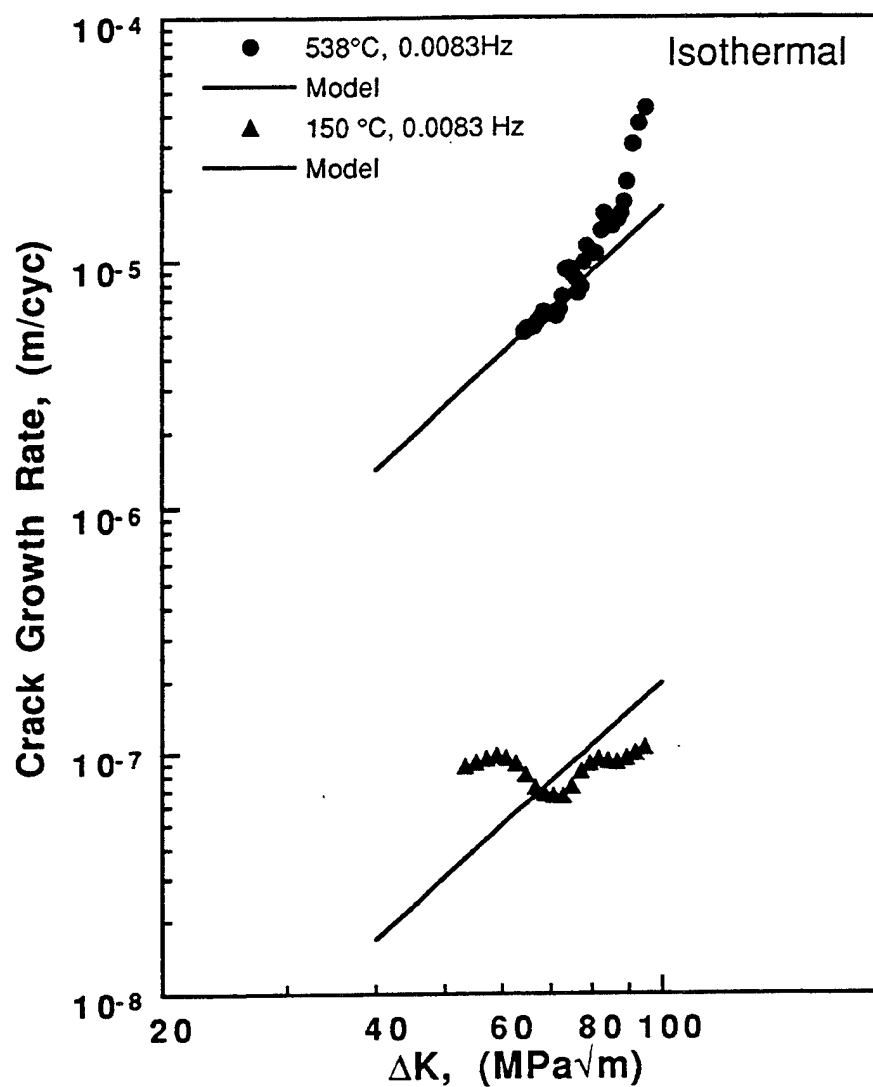


Figure 8.2 Plot showing the accuracy of the correlation between the model and the SCS-6/Ti-6Al-2Sn-4Zr-2Mo fatigue crack growth data from the isothermal tests at 150 and 538 °C and 0.0083 Hz.

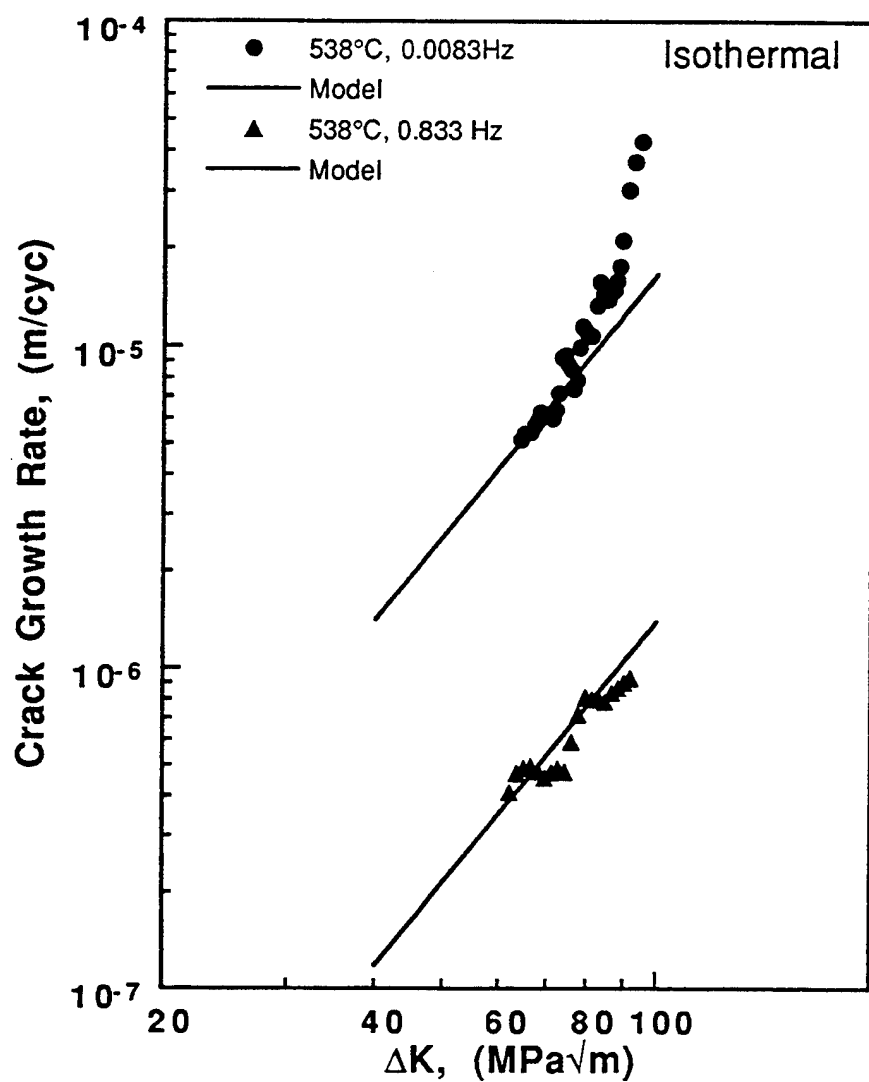


Figure 8.3 Plot showing the accuracy of the correlation between the model and the SCS-6/Ti-6Al-2Sn-4Zr-2Mo fatigue crack growth data from the isothermal tests at 538 °C and 0.0083 Hz and 0.83 Hz.

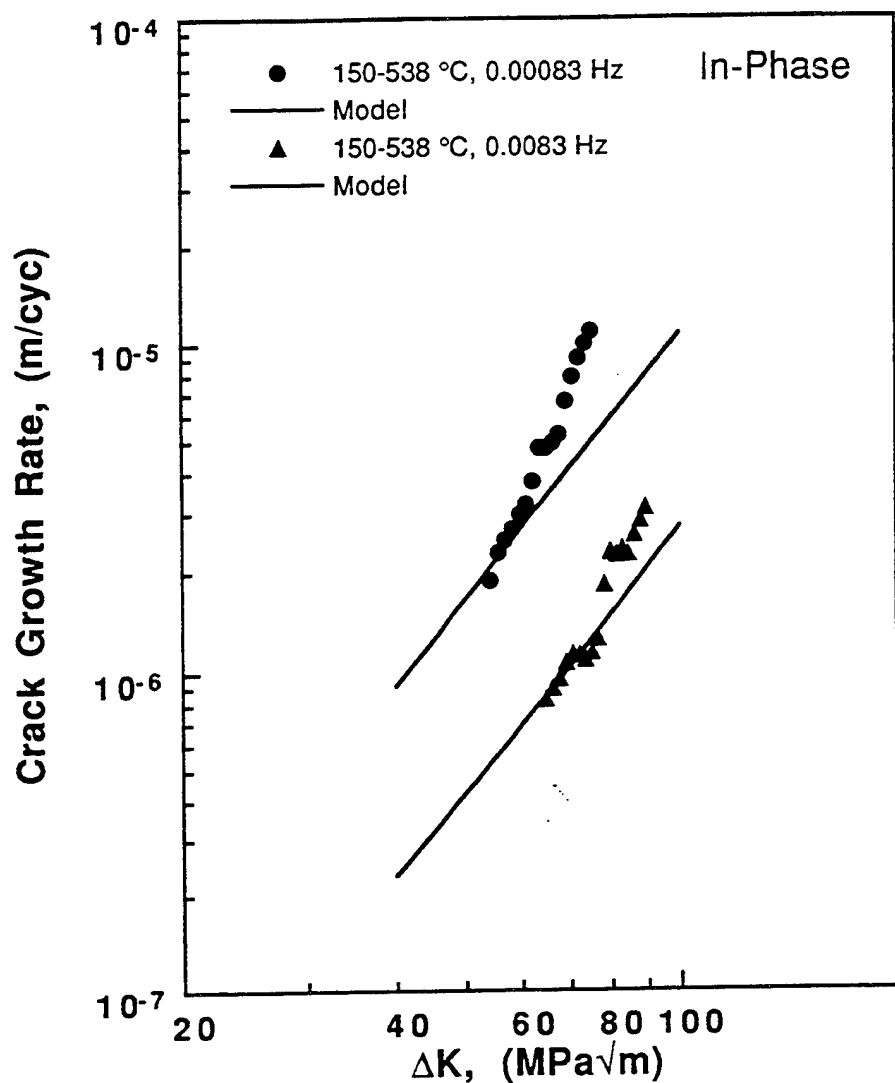


Figure 8.4 Plot showing the accuracy of the correlation between the model and the SCS-6/Ti-6Al-2Sn-4Zr-2Mo fatigue crack growth data from the in-phase tests at 0.0083 Hz and 0.00083 Hz.

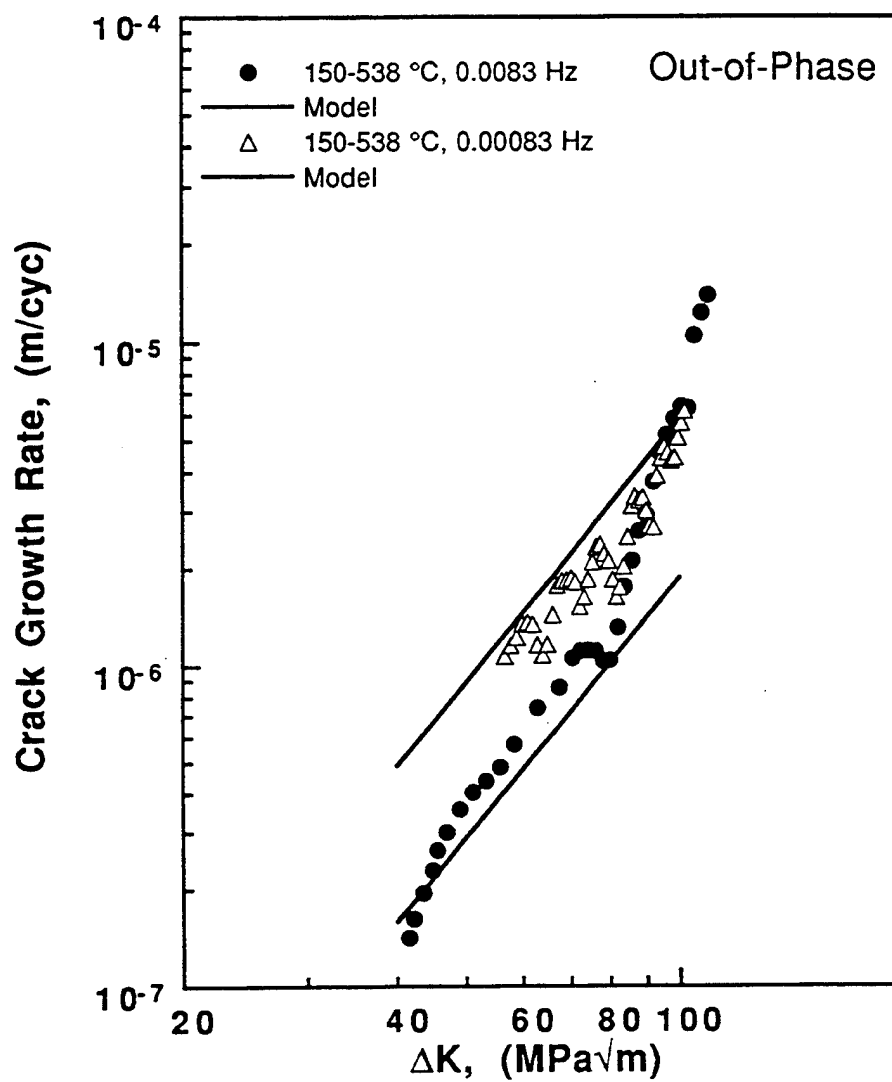


Figure 8.5 Plot showing the accuracy of the correlation between the model and the SCS-6/Ti-6Al-2Sn-4Zr-2Mo fatigue crack growth data from the out-of-phase tests at 0.0083 Hz and 0.00083 Hz.

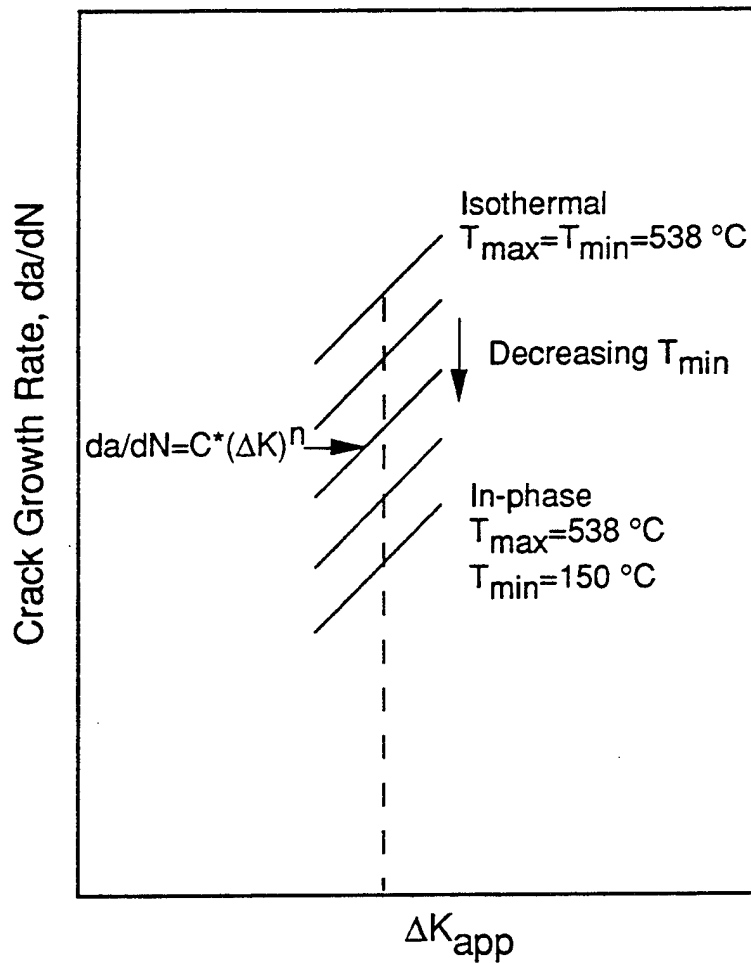


Figure 8.6 Influence of decreasing  $T_{min}$  on the crack growth rates under constant  $\Delta K_{app}$  conditions.

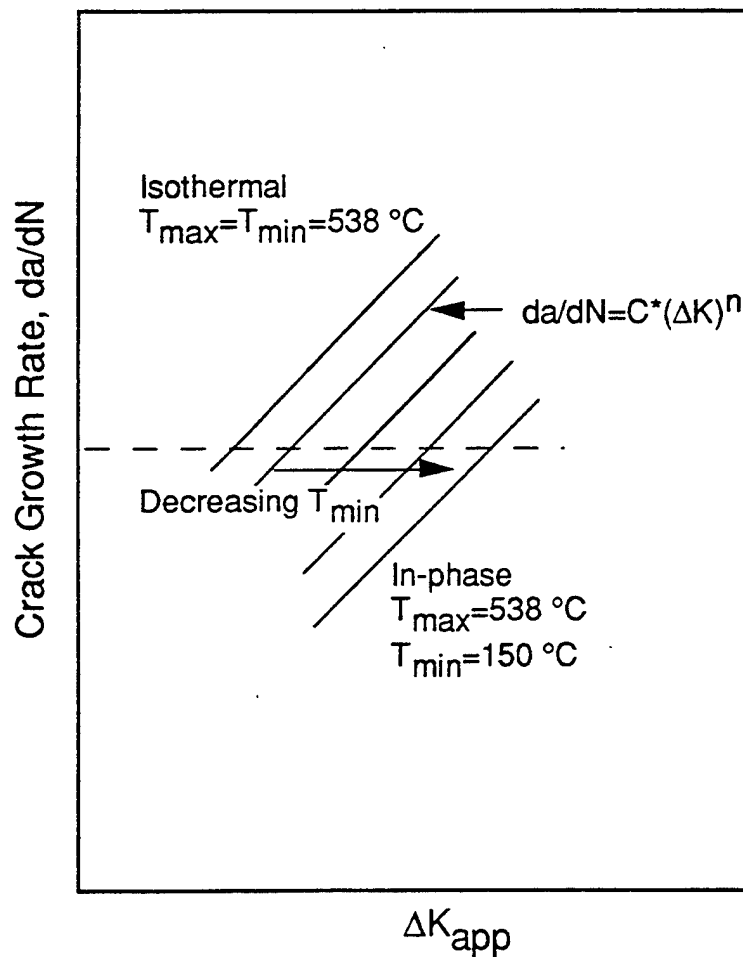


Figure 8.7 Influence of decreasing  $T_{min}$  on the crack growth behavior under constant crack growth rate conditions.

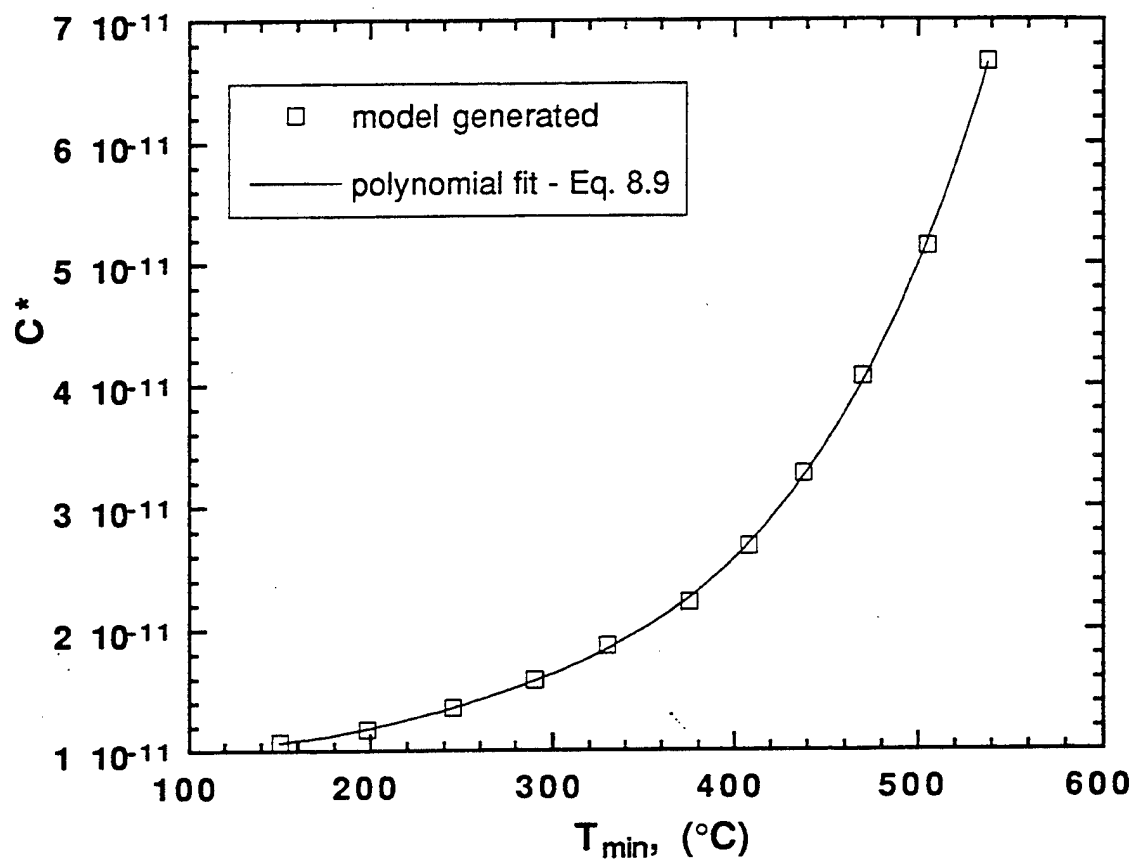


Figure 8.8 Variation of  $C^*$  as a function of the minimum cyclic temperature,  $T_{\min}$ .

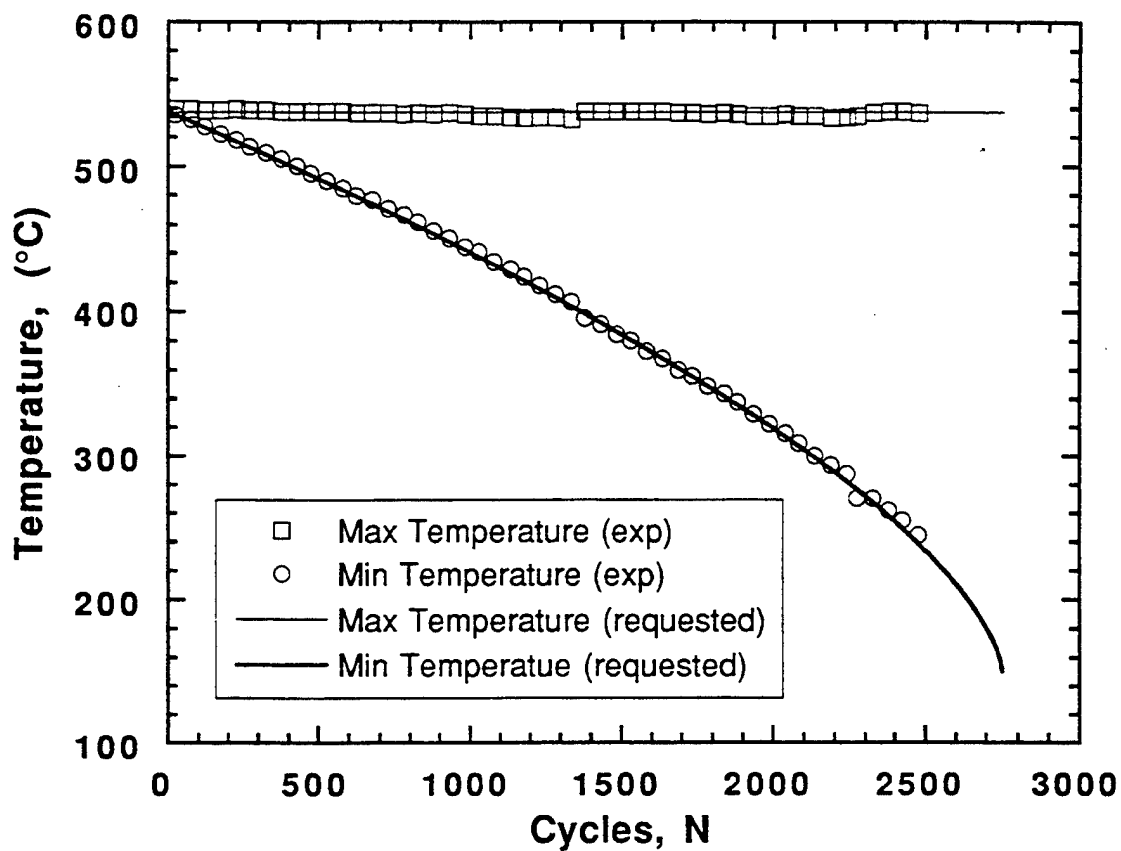


Figure 8.9 Experimental data verifying the minimum and maximum temperatures during the proof test followed the requested profiles.

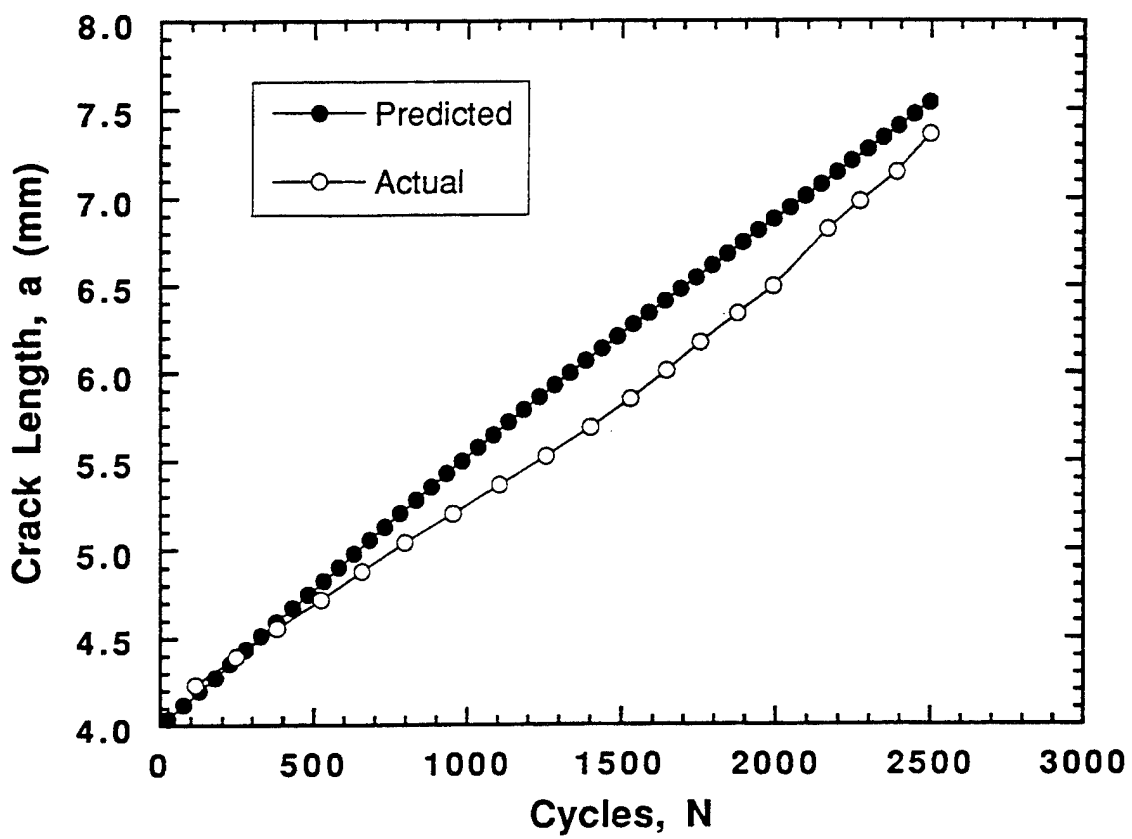


Figure 8.10 Experimental crack lengths from the proof test compared to the predicted values as a function of applied cycles.

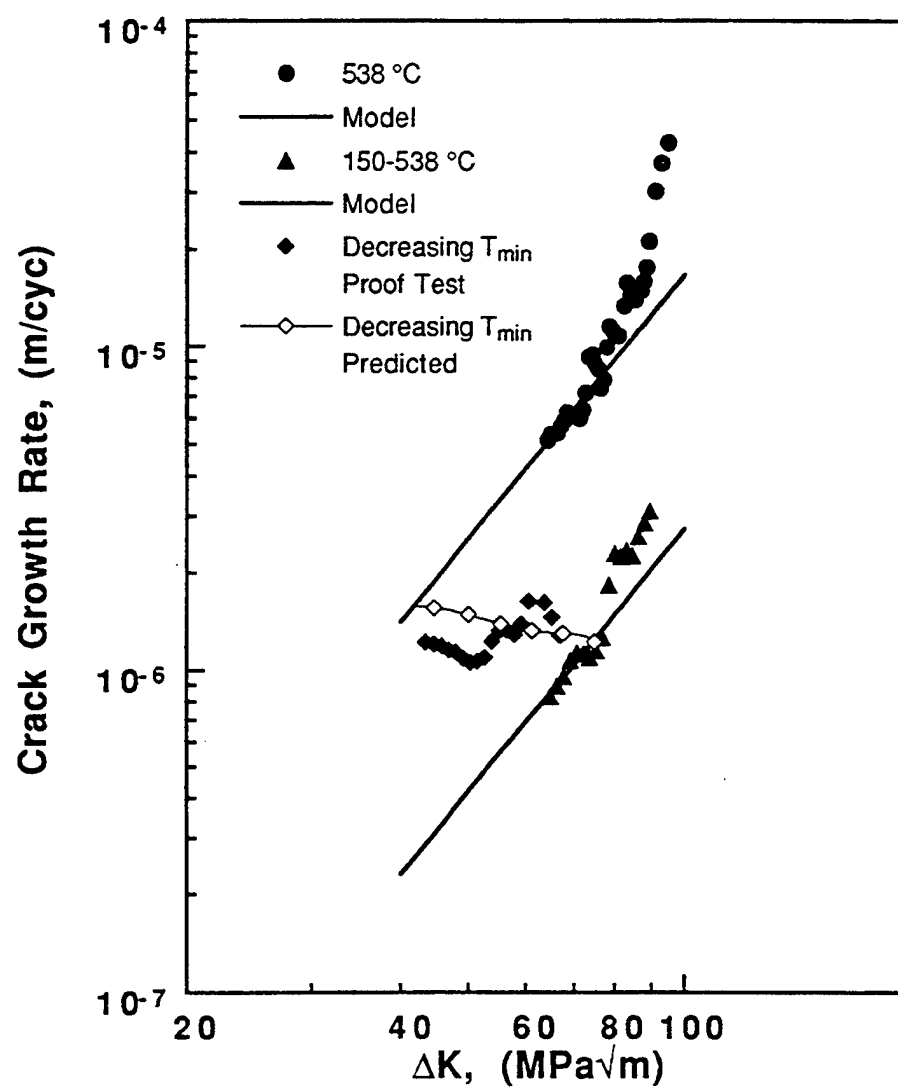


Figure 8.11 Experimental crack growth rates from the proof test compared to the predicted values as a function of  $\Delta K_{\text{app}}$ .

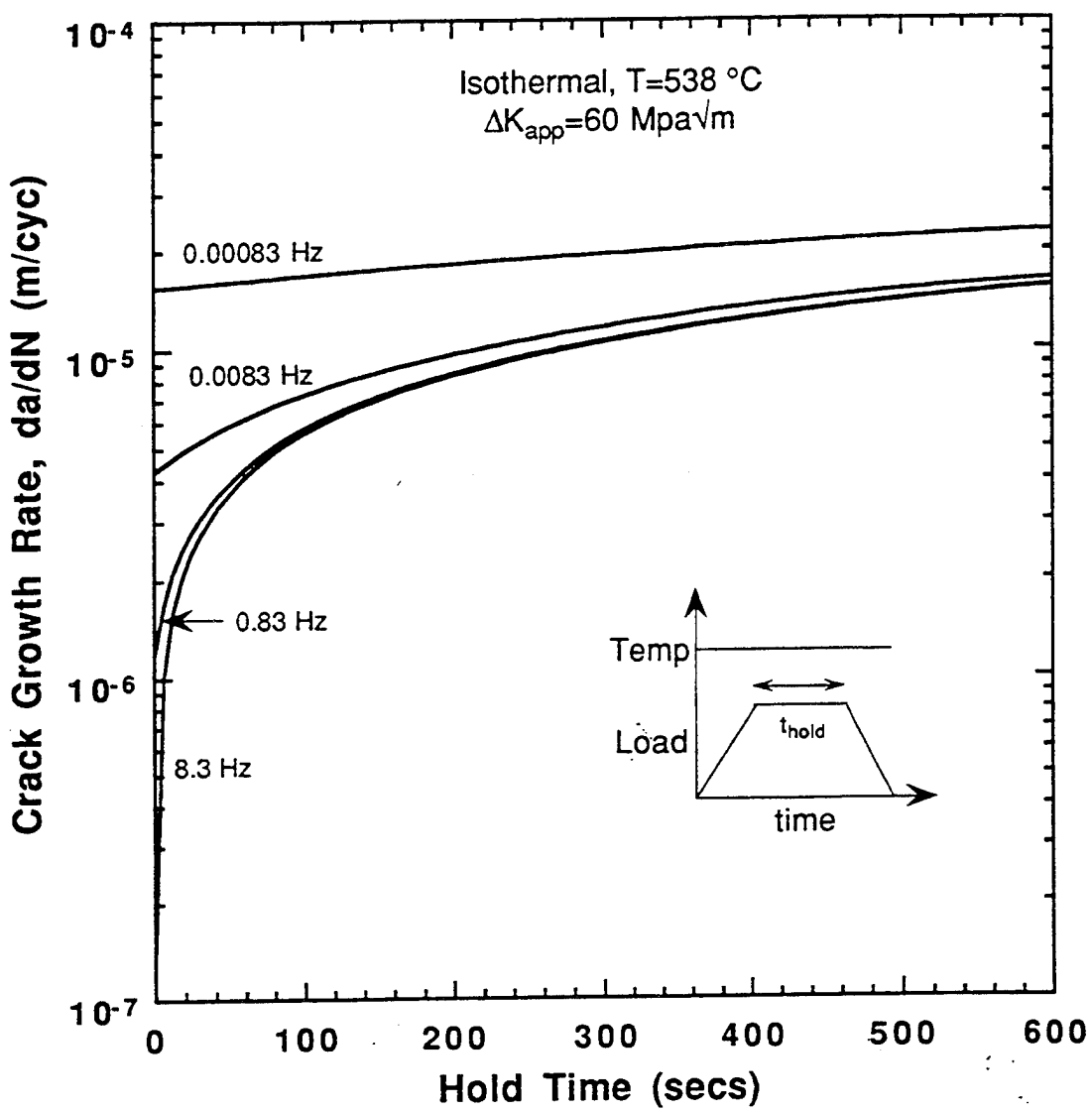


Figure 8.12 Effect of load hold times at various frequencies on the fatigue crack growth rate of [0]<sub>4</sub>, SCS-6/Ti-6Al-2Sn-4Zr-2Mo.

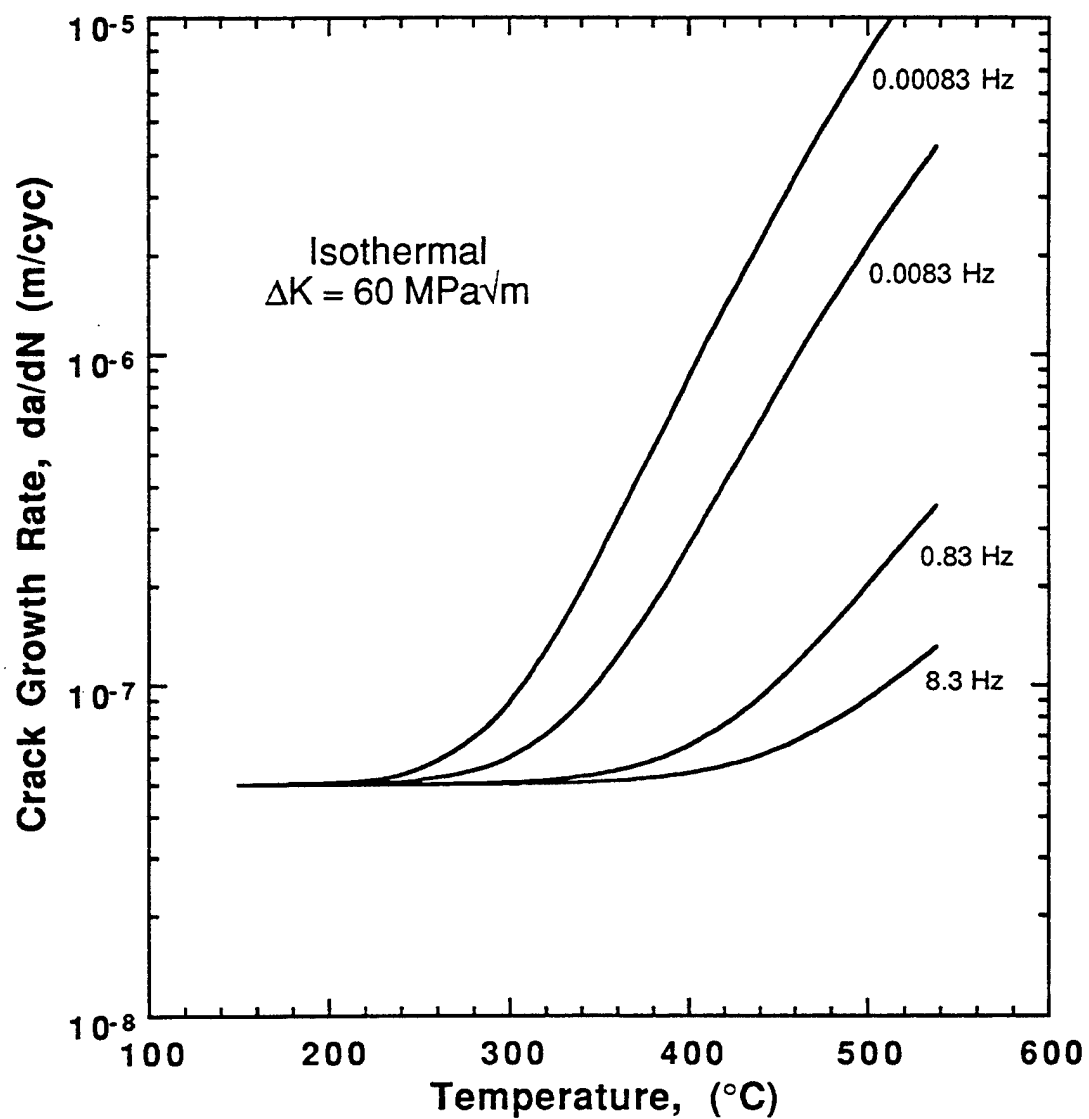


Figure 8.13 Effect of different isothermal temperatures at various frequencies on the fatigue crack growth rate of [0]4, SCS-6/Ti-6Al-2Sn-4Zr-2Mo.

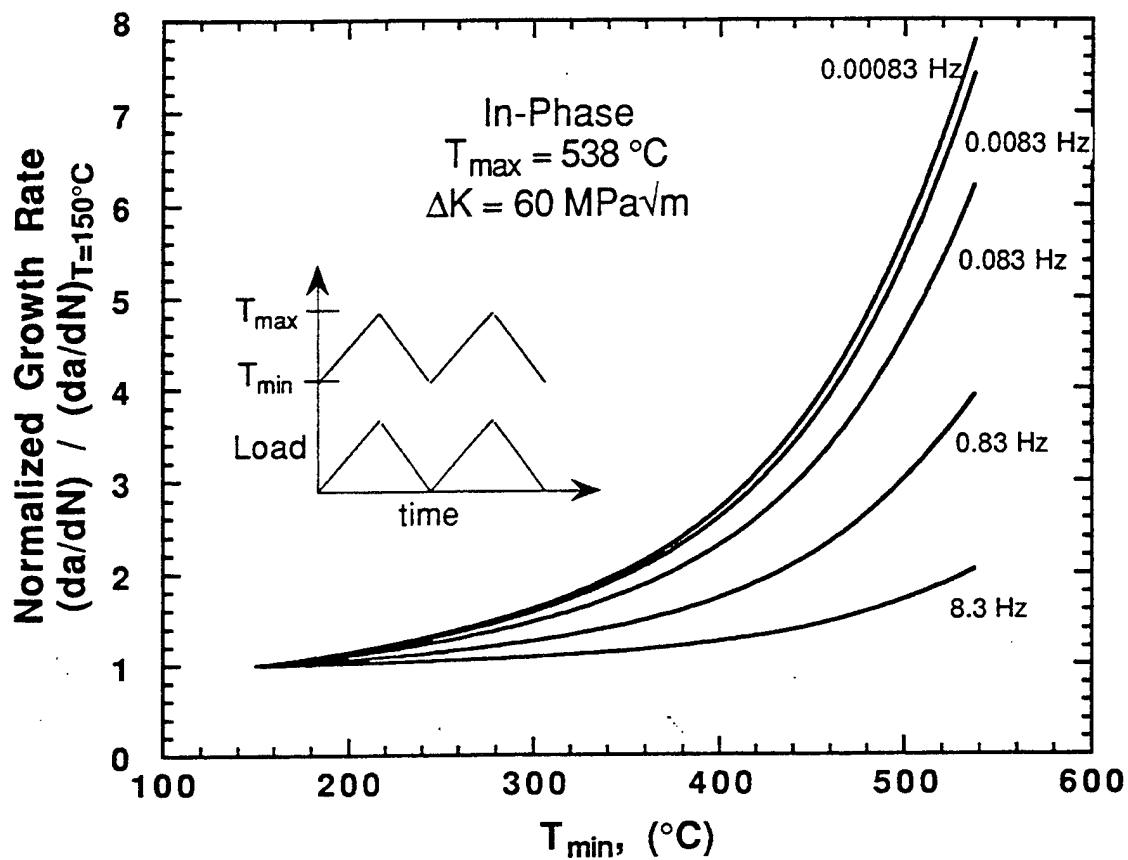


Figure 8.14 Effect of varying  $T_{\min}$  at various frequencies on the in-phase fatigue crack growth rate of  $[0]_4$ , SCS-6/Ti-6Al-2Sn-4Zr-2Mo.

## CHAPTER 9

### CONCLUSIONS

In this study, the thermomechanical fatigue (TMF) crack growth behavior of 4-ply, unidirectional SCS-6/Ti-6Al-2Sn-4Zr-2Mo was evaluated. During the study, a fully automated TMF test frame was assembled and baseline isothermal and non-isothermal fatigue crack growth data were generated. In addition, a linear summation model was developed to predict the fatigue crack growth rates of SCS-6/Ti-6242 under isothermal as well as thermomechanical fatigue conditions.

A horizontal closed-loop servohydraulic test frame was assembled in order to perform automated fatigue crack growth tests of thin-sheet composites under thermomechanical conditions. The computer controlled apparatus used quartz lamps for heating and forced air for cooling. The test frame was capable of thermal frequencies of up to 0.0083 Hz for temperatures varying between 150-650 °C. Crack lengths were measured from DCEP and correlated with optical measurements from two traveling telemicroscopes. The gripping system allowed the use of both single-edge notch and center-cracked specimen geometries.

The experimental fatigue crack growth data suggested several conclusions. One dominant factor that influenced the fatigue crack growth behavior was the time that the composite was cycled at elevated temperatures,

especially when temperatures approached 538 °C. Accordingly, the crack growth rates, all else being equal, under the thermomechanical conditions were lower than those generated isothermally at the maximum temperature of the TMF test. This result was expected since other TMF studies on monolithic materials [22, 82] demonstrated a similar behavior. The best explanation for this behavior is that the extended exposure to the elevated temperatures degraded the integrity and strength of the fiber at and behind the matrix crack tip. The degradation of the mechanical properties of the fiber led to fiber fracture and little fiber bridging.

The TMF crack growth data indicated that the test frequency influenced the growth rates depending on the phase angle. The in-phase condition tended to have higher growth rates at the slower frequency than the out-of-phase condition. This was attributed to more matrix relaxation in the in-phase condition than the out-of-phase condition which lead to higher fiber stresses. The higher fiber stresses lead to faster fiber fracture, and in turn to faster crack growth rates.

None of the crack growth tests, except for the isothermal test at 150 °C, produced evidence that full scale fiber bridging occurred. It is believed that fiber bridging was limited to approximately 2-3 fibers behind the crack tip. Based on this observation, the crack growth in this composite was modeled essentially as a monolithic material using a linear summation approach, assuming that fiber bridging only occurs on a small scale. The linear summation approach assumed that the fatigue crack growth rate could be decomposed into two different components: a cycle dependent component and a time dependent component. The cycle dependent term is dependent

upon the applied stress intensity factor range, whereas the time-dependent term also depends on the cycle period and the temperature profile.

The numerical model used five constants - one of which was dependent upon the test type. Therefore, seven baseline test conditions were used to determine the constants needed to define the model. The results from the proof test, which began under isothermal conditions and ended under in-phase conditions, support the fundamental concepts upon which the model was based.

Problems in obtaining quality test materials demonstrate that the technology to manufacture and process titanium matrix composites, even in small quantities has not matured enough to produce consistent, high-quality material. Problems such as poor matrix consolidation around fibers, fiber misalignment, and fiber fracture are common to currently manufactured titanium matrix composites. The manufacturing defects present in the first two batches of material examined here are just a few examples of the problems that must be addressed and solved before TMC can be confidently utilized in real-world applications.

Recommendations for future study of the TMF crack growth phenomenon in MMC are listed below.

1. Additional TMF crack growth tests using different titanium based composites reinforced with other continuous fibers should be performed. Using other matrices and fiber systems would allow the comparison of TMF crack growth rates between composites with varying fiber/matrix interfacial strength. The fiber/matrix interfacial properties greatly influence the crack growth characteristics of a composite, such as the amount of fiber bridging that occurs.
2. An SCS-6/Ti-6242 composite manufactured by the foil-fiber-foil technique should be tested to gain an understanding of the influence of processing techniques on fatigue crack growth characteristics. The objective here would be to

determine how the behavior of foil-fiber-foil material compares to similar material processed using induction plasma spraying.

3. Analytical modeling of the fiber bridging phenomenon during thermomechanical fatigue crack growth should be performed, since it is highly likely that fiber bridging would be a dominant mechanism in other titanium matrix composites under thermomechanical loading. Studies of SCS-6/Ti-24Al-11Nb and SCS-6/TIMETAL®21S have reported that the isothermal fatigue crack growth rates are influenced by fiber bridging [69, 78].
4. Other forms of the cycle-dependent and time-dependent formulations used in the linear summation model should be examined. The cycle-dependent term for example, should be expanded to account for R-ratio effects as well as temperature effects when applied to future materials.

## LIST OF REFERENCES

- [1] Larsen, J.M., Williams, K.A., Balsone, S.J., and Stucke, M.A. "Titanium Aluminides for Aerospace Applications", *Symposium on High Temperature Aluminides & Intermetallics*, TMS, The Minerals, Metals & Materials Society, 1989.
- [2] Ashley, S., "Titanium Aluminides: Tough Materials for Tomorrow's Engines", *Mechanical Engineering*, December, p. 49-52, 1991.
- [3] Hartman, G.A. and Russ, S.M. "Techniques for Mechanical and Thermal Testing of Ti<sub>3</sub>Al/SCS-6 Metal Matrix Composites", *Metal Matrix Composites: Testing, Analysis and Failure Modes*, Philadelphia, American Society for Testing and Materials, 1989.
- [4] Giannetti, William B. "Development of an Elevated Temperature Test Technique for Metal Matrix Composite Materials", *American Society for Composites*, Dayton, Ohio, American Society for Composites, 1989.
- [5] Johnson, W.S., "Fatigue Damage Accumulation in Various Metal Matrix Composites", *NASA Technical Memorandum 89116*, 1987.
- [6] Harmon, D.M., Saff, C.R., and Graves, D.L. "Strength Predictions for Metal Matrix Composites", *Metal Matrix Composites: Testing, Analysis, and Failure Modes*, Philadelphia, American Society for Testing and Materials, 1989.
- [7] Gabb, T.P., Gayda, J., and MacKay, R.A., "Isothermal and Nonisothermal Fatigue Behavior of a Metal Matrix Composite", *Journal of Composite Materials*, 24, June, p. 667-686, 1990.
- [8] Chan, K.S. and Davidson, D.L., "Fatigue Crack Growth in Fiber-Reinforced Metal-Matrix Composites", *submitted for publication*, 1992.
- [9] Johnson, W.S. "Mechanisms Controlling Fatigue Damage Development in Continuous Fiber Reinforced Metal Matrix Composites", *Advances in Fracture*, Pergamon Press, 1989.

- [10] Abuelfoutouh, Nader Mohamed, Verrilli, M.J., and Halford, G.R. "Isothermal Life Prediction of Composite Lamina Using a Damage Mechanics Approach", *Symposium on High Temperature Composites*, Dayton, Ohio, American Society for Composites, 1989.
- [11] Nicholas, Theodore, Heil, Michael L., and Haritos, George K., "Predicting Crack Growth Under Thermo-Mechanical Cycling", *International Journal of Fracture*, 41, p. 157-176, 1989.
- [12] Bhatt, R.T. and Grimes, H.H., "Fatigue Behavior of SiC Reinforced Ti(6Al-4V) at 650 °C", *Metallurgical Transactions A*, 13A, November, p. 1933-1938, 1982.
- [13] Gayda, John and Gabb, Timothy P., "Isothermal Fatigue Behavior of a [90]8 SiC/Ti-15-3 Composite at 426 °C", *NASA Technical Memorandum 103686*, p. 1-20, 1991.
- [14] Johnson, W.S. "Fatigue of Continuous Fiber Reinforced Titanium Matrix Composites", *An invited lecture for the Engineering Foundation Conference: Mechanical Fatigue of Advanced Materials*, Santa Barbara, California, 1991.
- [15] Paris, P.C., "The Growth of Fatigue Cracks Due to Variation in Load", Lehigh University, Ph.D. Thesis, 1962.
- [16] Forman, K.G., Kearney, V.E., and Engle, R.M., "Numerical Analysis of Crack Propagation in a Cyclic-Loaded Structure", *Journal of Basic Engineering*, 89D, p. 459, 1967.
- [17] Wallace, R.M., Annis, C.G., and Sims, D.L., "Application of Fracture Mechanics at Elevated Temperatures", Wright-Patterson AFB, Ohio, AFML-TR-76-176 Part II, 1977.
- [18] VanStone, Gooden, and Krueger, "Advanced Cumulative Damage Modeling", Wright-Patterson AFB, Ohio, AFWAL-TR-88-4146, 1988.
- [19] Larsen, J.M., Schwartz, B.J., and Annis, C.G., "Cumulative Damage Fracture Mechanics Under Engine Spectra", Wright-Patterson AFB, Ohio, AFML-TR-79-4159, 1980.
- [20] Sims, D.L., Annis, C.G., and Wallace, R.M., "Cumulative Damage Fracture Mechanics at Elevated Temperatures", Wright-Patterson AFB, Ohio, AFML-TR-76-176 Part III, 1976.
- [21] Utah, D.A., "Crack Growth Modeling in an Advanced Powder Metallurgy Alloy", Wright-Patterson AFB, Ohio, AFWAL-TR-80-4098, 1980.

- [22] Pernot, J.J., "Crack Growth Rate Modeling of a Titanium-Aluminide Alloy Under Thermal-Mechanical Cycling", Air Force Institute of Technology, Wright-Patterson AFB, Ohio, Ph.D. Thesis, 1991.
- [23] MacKay, R.A., Brindley, P.K., and Froes, F.H., "Continuous Fiber-Reinforced Titanium Aluminide Composites", *Journal of Materials*, 43(5), p. 23-29, 1991.
- [24] "Titanium Aluminide Composites", Wright-Patterson AFB, Ohio, Final Technical Report, NASP Contractor Report 1112, No. 4, Sept 1988-June 1989, 1989.
- [25] Amato, R.A., "Titanium Based Composites Fabricated by Induction Plasma Spray and Foil Fiber Foil", GE Aircraft Engines, Technical Memorandum, TM90-266, June, 1990.
- [26] Cox, B.N. and Marshall, D.B., "Crack Bridging in the Fatigue of Fibrous Composites", *Fatigue Fracture Engineering Materials and Structures*, 14(8), p. 847-861, 1991.
- [27] Ritchie, R.O., Yu, Weikang , and Bucci, R.J., "Fatigue Crack Propagation in ARALL Laminates: Measurement of the Effect of Crack-Tip Shielding from Crack Bridging", *Engineering Fracture Mechanics*, 32(3), p. 361-377, 1989.
- [28] Shang, J.K. and Ritchie, R.O., "Crack Bridging by Uncracked Ligaments During Fatigue-Crack Growth in SiC-Reinforced Aluminum-Alloy Composites", *Metallurgical Transactions A*, 20A, p. 897-908, 1989.
- [29] Heil, Michael L., Nicholas, Theodore, and Haritos, George K., "Crack Growth in Alloy 718 Under Thermal-Mechanical Cycling", *Thermal Stress, Materials Deformation and Thermo-Mechanical Fatigue*, H. Sehitoglu and S.Y. Zamrik, Editor, American Society of Mechanical Engineers, New York, p. 23-29, 1987.
- [30] Nicholas, Theodore, Weerasooriya, T., and Ashbaugh, Noel E. "A Model for Creep/Fatigue Interactions in Alloy 718", *Fracture Mechanics: Sixteenth Symposium*, American Society for Testing and Materials, 1985.
- [31] Mall, Shankar, Staubs, E.A., and Nicholas, Theodore, "Investigation of Creep/Fatigue Interaction on Crack Growth in a Titanium Aluminide Alloy", *Journal of Engineering Materials and Technology*, 112, p. 435-441, 1990.

- [32] Nicholas, Theodore and Mall, Shankar. "Elevated Temperature Crack Growth in Aircraft Engine Materials", *Advances in Fatigue Lifetime Predictive Techniques*, Philadelphia, American Society of Testing and Materials, 1992.
- [33] Pernot, J.J., Nicholas, N., and Mall, S., "Modeling Thermomechanical Fatigue Crack Growth Rates in Ti-2Al-11Nb", *International Journal of Fatigue* (in press), 1993.
- [34] Bania, P.J., "An Advanced Alloy for Elevated Temperatures", *Journal of Metals*, 40(3), p. 20-22, 1988.
- [35] Bania, P.J. "Ti-1100: A New Elevated Temperature Titanium Alloy", *Space Age Metals Technology*, SAMPE, 1988.
- [36] Tada, H., Paris, P.C., and Irwin, G.R., "The Stress Analysis of Cracks Handbook", St. Louis, Del Research Corporation, 1985.
- [37] ASTM, "E1012-89 Standard Recommended Practice for Load Train Alignment Verification", 1991 Annual Book of ASTM Standards, American Society of Testing and Materials, 1991.
- [38] Ghonem, H. and Foerch, R. "Frequency Effects on Fatigue Crack Growth Behavior in a Near Alpha Titanium Alloy", *Symposium on Elevated Temperature Crack Growth, Winter Meeting*, ASME, 1990.
- [39] Hanson, D. G., "Thermomechanical Fatigue of SCS-6/B21S [0/90]<sub>2s</sub> Composite", Air Force Institute of Technology, Wright-Patterson AFB, Ohio, Masters Thesis, 1991.
- [40] ASTM, "E-647 Standard Test Method for Measurement of Fatigue Crack Growth Rates", 1991 Annual Book of ASTM Standards, American Society for Testing and Materials, Philadelphia, 1991.
- [41] Hartman, George A. and Johnson, David A., "D-C Electric-Potential Method Applied to Thermal/Mechanical Fatigue Crack Growth", *Experimental Mechanics*, 27(1), p. 106-112, 1987.
- [42] Stubbs, David A., Russ, Stephan M., and MacLellan, Patrick T. "Examination of the Correlation Between NDE-detected Manufacturing Abnormalities in MMCs and Ultimate Tensile Strength of Thermomechanical Fatigue Life", submitted to ASTM's Second Symposium on Cyclic Deformation, Fracture, and Nondestructive Evaluation of Advanced Materials, 1992.
- [43] Boyer, H.E., ed. *Metals Handbook*. 8 ed. Nondestructive Inspection and Quality Control, Vol. 11, 1976.

- [44] Krautkramer, J. and Krautkramer, H., "Ultrasonic Testing of Materials", 4 ed. New York, Springer-Verlag, 677, 1990.
- [45] Bain, Ken R., "private communication", 1992.
- [46] Stubbs, David. "Evaluation of Wrinkles in Composite Panels Using Ultrasonic C-scans", *ASTM Fall Meeting*, 1992.
- [47] Blatt, Drew, John, Reji, and Coker, Demirkan, "Single Edge Notched Specimens with Clamped Ends for Automated Crack Growth Testing", *Presented at the 1993 Society of Experimental Mechanics Spring Conference on Experimental Mechanics*, Dearborn, Michigan, Society of Experimental Mechanics, 1993.
- [48] Blatt, Drew, John, Reji, and Coker, Demirkan, "Stress Intensity Factor and Compliance Solutions for a Single Edge Notched Specimen with Clamped Ends", *Engineering Fracture Mechanics* (in press), 1993.
- [49] Gambone, M. L., "Fatigue and Fracture of Titanium Aluminides", *WRDC-TR-89-4145*, 2, p. 1-80, 1990.
- [50] Ghosn, L.J., Kantzios, P., and Telesman, J., "Modeling of Crack Bridging in a Unidirectional Metal Matrix Composite", *International Journal of Fracture*, 54, p. 345-357, 1992.
- [51] Harris, D.O., "Stress Intensity Factors for Hollow Circumferentially Notched Round Bars", *Journal of Basic Engineering, Transactions of ASME*, 89, p. 49-54, 1969.
- [52] Bowie, I.L., Freese, C.E., and Neal, D.M., "Solution of Plane Problems of Elasticity Utilizing Partitioning Concepts", *Journal of Applied Mechanics*, Vol. 40, p. 767-772, 1973.
- [53] Marchand, N., Parks, D.M., and Pelloux, R.M., "KI-solutions for Single Edge Notch Specimens under Fixed End Displacements", *International Journal of Fracture*, 31, p. 53-65, 1986.
- [54] Ahmad, Jalees, Papaspyropoulos, V., and Hopper, A.T., "Elastic-Plastic Analysis of Edge-Notched Panels Subjected to Fixed Grip Loading", *Engineering Fracture Mechanics*, 38(4/5), p. 283-294, 1991.
- [55] Dao, T.X. and Mettu, S.R., "Analysis of an Edge-Cracked Specimen Subjected to Rotationally-Constrained End Displacements", NASA - Johnson Space Center, Technical Memorandum, NASA JSC 32171, August, 1991.

- [56] "ADINA-A Finite Element Program for Automatic Dynamic Incremental Nonlinear Analysis", ADINA R & D, Inc, Watertown, MA, Report, Report ARD 89-1, 1989.
- [57] Barsoum, R.S., "On the Use of Isoparametric Finite Elements in Linear Elastic Fracture Mechanics", *International Journal of Numerical Methods in Engineering*, 10, p. 25-37, 1976.
- [58] Ingraffea, A.R. and Manu, C., "Stress Intensity Factor Computation in Three Dimensions with Quarter Point Elements", *International Journal for Numerical Methods in Engineering*, 15, p. 1427-1445, 1980.
- [59] Yehia, N.A.B. and Shepard, M.S., "On the Effect of Quarter-Point Element Size on Fracture Criteria", *International Journal for Numerical Methods in Engineering*, 21, p. 1911-1924, 1985.
- [60] Hartman, George A., "MATE and MATE Modules — Version 2.22A, Crack Growth Analysis and Test Environments", University of Dayton Research Institute, Technical Report, UNR-TR-88-138, 1988.
- [61] Hartman, George A., Ashbaugh, Noel A., and Buchanan, Dennis J., "A Sampling of Mechanical Test Automation Methodologies used in a Basic Research Laboratory", *Automation in Fatigue and Fracture Testing and Analysis*, American Society for Testing and Materials, Philadelphia, 1993.
- [62] Zawada, Larry P., "Effect of Temperature, Frequency, and Hold Time on Fatigue Crack Propagation in Ti-Alloy IMI-834", University of Dayton, Masters Thesis, 1992.
- [63] John, Reji and Ashbaugh, Noel E. "Fatigue Crack Growth in a Silicon Carbide/Titanium Aluminide Composite", *Elevated Temperature Crack Growth*, ASME, 1990.
- [64] Hartman, George A., John, Reji, and Blatt, Drew. "Characterization of Crack Growth in Continuous Fiber Reinforced Metal Matrix Composites", *Symposium on Special Applications and Advanced Techniques for Crack Size Determination*, Atlanta, GA, American Society for Testing and Materials, 1993.
- [65] Park, Y.H., Narayen, D., Schmerling, M., and Marcus, H.L., "Fatigue Crack Growth Behavior of Ti-6Al-4V Metal Matrix/Continuous SiC and B4 C/B Fibre Composites", *Journal of Materials Science*, 19, p. 2239-2245, 1984.
- [66] Chan, K.S. and Davidson, D.L., "Driving Forces for Composite Interface Fatigue Cracks", *Engineering Fracture Mechanics*, 33(3), p. 451-466, 1989.

- [67] Chan, K.S., "A Fatigue Crack Growth Model for Fiber-Reinforced Metal-Matrix Composites", *Fatigue and Fracture of Engineering Material and Structures*, 13(2), p. 171-183, 1990.
- [68] Larsen, James M., Jira, Jay R., and Ravichandran, Kakkaveri S., "Measurement of Small Cracks by Photomicroscopy: Experiments and Analysis", *Small-Crack Test Methods*, J.M. Larsen and J.E. Allison, Editor, American Society for Testing and Materials, Philadelphia, p. 57-80, 1992.
- [69] Jira, J.R. and Larsen, J.M., "Fatigue of Unidirectional SCS-6/Ti-24Al-11Nb Composite Containing A Circular Hole (Part II)", *companion paper submitted to Metallurgical Transactions A, Carnegie Mellon University, Pittsburgh, PA*, 1993.
- [70] Balsone, Steve J., Maxwell, David C., Khobiab, Mohamed, and Nicholas, Theodore. "Frequency, Temperature, and Environmental Effects on Fatigue Crack Growth in Ti<sub>3</sub>Al", *Fatigue 90*, Hawii, 1990.
- [71] DeLuca, D.P., Cowles, B.A., Haake, F.K., and Holland, K.P., "Fatigue and Fracture of Titanium Aluminides", Wright-Patterson AFB, OH, WRDC-TR-4136, Feb, 1990.
- [72] Parida, B.K. and Nicholas, Theodore, "Growth of Fatigue Cracks Emanating from Notches in Titanium Aluminide", *Joint FEFG/ICF International Conference on Fracture of Engineering Materials and Structures*, Singapore, 1991.
- [73] Weerasooriya, T., "Effect of Frequency on Fatigue Crack Growth Rate of Inconel 718 at High Temperature", *Fracture Mechanics: Nineteenth Symposium*, American Society of Testing and Materials, p. 907-923, 1988.
- [74] Neu, Richard W., "unpublished work", USAF Materials Directorate, 1993.
- [75] Ghonem, H. and Zheng, D., "Aspects of High Temperature Damage in Fiber Reinforced Titanium Metal Matrix Composites", Air Force Office of Scientific Research, Annual Report, AFOSR-92-F49620, July, 1993.
- [76] Vesier, L.S. and Antolovich, S.D., "Fatigue Crack Propagation in Ti-6242 as a Function of Temperature and Waveform", *Engineering Fracture Mechanics*, 37(4), p. 753-775, 1990.
- [77] Neu, Richard W., "A Mechanistic-based Thermomechanical Fatigue Life Prediction Model for Metal Matrix Composites", *Fatigue and Fracture of Engineering Materials and Structures* (in press), 1993.

- [78] Larsen, J.M., Jira, J.R., and John, R., "Isothermal Fatigue Crack Growth of SCS-6/TIMETAL®21S", USAF Materials Directorate, unpublished work, 1993.
- [79] Khobaib, Mohamand. "Damage Evolution in Creep of SCS-6/Ti-24Al-11Nb Metal Matrix Composites", *American Society for Composites Sixth Technical Conference*, 1991.
- [80] Virkler, D.A., Hillberry, B.M., and Goel, P.K., "The Statistical Nature of Fatigue Crack Propagation", *Journal of Engineering Materials and Technology, Transactions of the American Society of Mechanical Engineers*, 101, p. 148-153, 1979.
- [81] Ostergaard, D.F., Thomas, J.R., and Hillberry, B.M., "Effect of  $\Delta a$ -Increment on Calculating  $da/dN$  from a versus N Data", *Fatigue Crack Growth Measurement and Data Analysis*, J. Hudak S.J. and R.J. Bucci, Editor, American Society for Testing and Materials, p. 194-204, 1981.
- [82] Heil, Mike L., "Crack Growth in Alloy 718 Under Thermomechanical Cycling", Air Force Institute of Technology, Ph.D. Thesis, 1986.

Appendix A - Tabulated Data: Cycles, Crack Lengths, and Crack Growth Rates

This appendix contains the raw data collected in each of the tests performed during this study. The data consists of the crack length and corresponding cycle count as recorded by the control software. The crack lengths from the control software were determined using the direct-current electric potential (DCEP) method as described in Chapter 3. Optical crack lengths and cycles counts are also given. The DCEP crack lengths were sometimes adjusted so they matched the optically observed crack lengths. Finally, the calculated crack growth rates are also given. These crack growth rates were taken directly from the analysis code SMOOTH as described in Chapter 7.

Specimen ID: **G9A-2-FCG**  
 Test Type: **Out-of-Phase**  
 P<sub>max</sub>: **8.7 kN**  
 R-ratio: **0.1**  
 Temperature: **150-538 °C**  
 Frequency: **0.0083 Hz**  
 Specimen Geometry: **SE(T)**

Cycles (DCEP)	DCEP Crack Length (mm)	Cycles (Optical)	Optical Crack Length (mm)	Crack Growth Rate (m/cycle)
183	7.7960	1	7.5000	1.1100e-06
416	8.0520	1328	9.0825	1.0860e-06
655	8.3080	1593	9.3550	1.0620e-06
917	8.5650	2035	9.8150	1.0590e-06
1157	8.8210	2315	10.125	1.1150e-06
1374	9.0780	2755	10.975	1.1220e-06
1581	9.3340	3039	11.960	1.1170e-06
1810	9.5900	3084	12.205	1.0410e-06
2058	9.8470	3234	13.640	1.0460e-06
2300	10.100			1.3190e-06
2488	10.360			1.7640e-06
2625	10.620			2.1230e-06
2730	10.870			2.6200e-06
2824	11.130			2.9350e-06
2908	11.380			3.7300e-06
2975	11.640			4.5730e-06
3027	11.900			5.1930e-06
3071	12.150			5.8080e-06
3109	12.410			6.3510e-06
3150	12.670			6.2900e-06
3180	12.920			1.0490e-05
3203	13.180			1.2340e-05
3222	13.440			1.3950e-05

Specimen ID: **G9A-3-FCG**  
 Test Type: **In-Phase**  
 $P_{max}$ : **8.7 KN**  
 R-ratio: **0.1**  
 Temperature: **150-538 °C**  
 Frequency: **0.0083 Hz**  
 Specimen Geometry: **SE(T)**

Cycles (DCEP)	DCEP Crack Length (mm)	Cycles (Optical)	Optical Crack Length (mm)	Crack Growth Rate (m/cycle)
224	7.8310	1	7.5000	8.3040e-07
469	8.0420	611	8.1575	8.9610e-07
696	8.2530	753	8.3550	9.5730e-07
920	8.4640	1471	9.0600	1.0750e-06
1106	8.6750			1.1370e-06
1267	8.8860			1.1350e-06
1453	9.0980			1.1010e-06
1642	9.3090			1.1570e-06
1840	9.5200			1.2670e-06
1984	9.7310			1.8410e-06
2099	9.9420			2.2980e-06
2182	10.150			2.2550e-06
2271	10.360			2.3440e-06
2358	10.580			2.2750e-06
2447	10.790			2.5940e-06
2524	11.000			2.8660e-06
2595	11.210			3.1150e-06

Specimen ID: **G9A-4-FCG**  
 Test Type: **Isothermal**  
 P<sub>max</sub>: **8.7 kN**  
 R-ratio: **0.1**  
 Temperature: **538 °C**  
 Frequency: **0.0083 Hz**  
 Specimen Geometry: **SE(T)**

Cycles (DCEP)	DCEP Crack Length (mm)	Cycles (Optical)	Optical Crack Length (mm)	Crack Growth Rate (m/cycle)
57	7.7590	1	7.5000	5.1520e-06
77	7.8600	100	8.0600	5.3630e-06
116	8.0610	189	8.5800	5.4110e-06
135	8.1620			5.6870e-06
154	8.2630			5.8920e-06
169	8.3630			6.2440e-06
186	8.4640			6.1380e-06
201	8.5640			6.1260e-06
217	8.6650			6.1160e-06
235	8.7660			5.9980e-06
253	8.8660			6.3810e-06
269	8.9670			7.1920e-06
281	9.0680			9.2920e-06
291	9.1680			9.4050e-06
301	9.2690			8.8680e-06
312	9.3700			8.5370e-06
326	9.4700			7.4140e-06
339	9.5710			7.8840e-06
352	9.6720			9.9600e-06
362	9.7720			1.1560e-05
369	9.8730			1.1150e-05
377	9.9740			1.0920e-05
387	10.070			1.0790e-05
407	10.280			1.3400e-05
414	10.380			1.5780e-05
420	10.480			1.4530e-05
426	10.580			1.4980e-05
434	10.680			1.3980e-05
449	10.880			1.4890e-05
456	10.980			1.5920e-05
462	11.080			1.7660e-05
467	11.180			2.1270e-05
477	11.380			3.0320e-05
483	11.620			3.7080e-05
489	11.850			4.2780e-05

Specimen ID: **G8A-1-FCG**  
 Test Type: **Out-of-Phase**  
 P<sub>max</sub>: **9.0 kN**  
 R-ratio: **0.1**  
 Temperature: **150-538 °C**  
 Frequency: **0.0083 Hz**  
 Specimen Geometry: **M(T)**

**NOTE:** The DCEP crack length was unavailable for this test due to hardware/software difficulties. Crack growth rates were calculated using the optical data.

Cycles (DCEP)	DCEP Crack Length (mm)	Cycles (Optical)	Optical Crack Length (mm)	Crack Growth Rate (m/cycle)
0		3.025		1.4200e-07
1162		3.267		1.6260e-07
1888		3.430		1.9590e-07
2694		3.610		2.2990e-07
3542		3.760		2.6570e-07
4027		3.862		3.0210e-07
4748		3.945		3.5670e-07
5458		4.030		4.0270e-07
6179		4.115		4.3820e-07
6893		4.240		4.8300e-07
7657		4.323		5.7180e-07
8414		4.448		7.4070e-07
9093		4.562		8.5850e-07
9963		4.642		
11203		4.828		
11945		4.957		
13669		5.363		
14088		5.492		
14799		5.675		
15524		6.028		
16227		6.265		
16976		6.622		
17904		7.082		
18659		7.460		
19120		7.795		
19828		8.520		
20096		8.872		

Specimen ID: **G8A-2-FCG**  
 Test Type: **Isothermal**  
 P<sub>max</sub>: **14.0 kN**  
 R-ratio: **0.1**  
 Temperature: **538 °C**  
 Frequency: **0.83 Hz**  
 Specimen Geometry: **M(T)**

Cycles (DCEP)	DCEP Crack Length (mm)	Cycles (Optical)	Optical Crack Length (mm)	Crack Growth Rate (m/cycle)
3315	4.4370	1	3.0390	4.0810e-07
3765	4.5880	1101	3.6465	4.2330e-07
4131	4.7400	3604	4.4290	4.4130e-07
4484	4.8910	6446	5.8765	4.5150e-07
4809	5.0430	7855	6.7915	4.6730e-07
5396	5.3460			5.1980e-07
5689	5.4980			5.4950e-07
6011	5.6490			5.9430e-07
6271	5.8010			6.3850e-07
6506	5.9520			6.7470e-07
6729	6.1040			7.1510e-07
6933	6.2550			7.5990e-07
7133	6.4070			8.0790e-07
7313	6.5590			8.3800e-07
7415	6.6450			8.5900e-07
7515	6.7320			8.7950e-07
7612	6.8180			8.9950e-07
7708	6.9050			9.1900e-07
7801	6.9920			9.3820e-07
7892	7.0780			9.5690e-07

Specimen ID: **G8A-3-FCG**  
 Test Type: **Out-of-Phase**  
 $P_{max}$ : **14.0 kN**  
 R-ratio: **0.1**  
 Temperature: **150-538 °C**  
 Frequency: **0.00083 Hz**  
 Specimen Geometry: **M(T)**

Cycles (DCEP)	DCEP Crack Length (mm)	Cycles (Optical)	Optical Crack Length (mm)	Crack Growth Rate (m/cycle)
84	3.1740	1	3.0330	1.0760e-06
174	3.2760	266	3.3730	1.1590e-06
259	3.3770	312	3.4480	1.2370e-06
339	3.4790	464	3.6380	1.3540e-06
414	3.5800	547	3.7930	1.3710e-06
474	3.6820	744	3.9330	1.3500e-06
553	3.7830	886	4.1680	1.1650e-06
647	3.8840	975	4.3380	1.0850e-06
742	3.9860	1037	4.4780	1.1720e-06
829	4.0870	1109	4.6230	1.4420e-06
895	4.1890	1252	4.8230	1.7770e-06
944	4.2900	1401	5.1280	1.8390e-06
997	4.3920	1475	5.2480	1.8510e-06
1050	4.4930	1540	5.4680	1.8760e-06
1097	4.5950	1618	5.5980	1.8190e-06
1163	4.6960	1689	5.6680	1.5340e-06
1236	4.7980	1755	5.8180	1.6410e-06
1301	4.8990	1909	6.2280	1.8590e-06
1354	5.0010	2045	6.6580	2.0980e-06
1400	5.1020	2117	6.9580	2.3410e-06
1435	5.2040	2194	7.2780	2.3850e-06
1477	5.3050	2259	7.6430	2.2290e-06
1519	5.4070			2.1280e-06
1573	5.5080			1.8600e-06
1632	5.6100			1.6380e-06
1701	5.7110			1.7520e-06
1757	5.8130			2.0340e-06
1805	5.9140			2.5050e-06
1845	6.0150			3.1220e-06
1877	6.1170			3.3420e-06
1902	6.2180			3.2650e-06
1931	6.3200			3.3240e-06
1960	6.4210			3.0340e-06
1998	6.5230			2.7120e-06
2039	6.6240			2.6860e-06

2074	6.7260	3.8890e-06
2101	6.8270	4.3940e-06
2121	6.9290	4.7860e-06
2136	7.0300	4.6000e-06
2161	7.1320	4.3230e-06
2187	7.2330	4.4150e-06
2210	7.3350	5.0900e-06
2229	7.4360	5.6510e-06
2246	7.5380	6.1620e-06

Specimen ID: **G8A-4-FCG**  
 Test Type: **Isothermal**  
 P<sub>max</sub>: **14.0 kN**  
 R-ratio: **0.1**  
 Temperature: **150 °C**  
 Frequency: **0.0083 Hz**  
 Specimen Geometry: **M(T)**

Cycles (DCEP)	DCEP Crack Length (mm)	Cycles (Optical)	Optical Crack Length (mm)	Crack Growth Rate (m/cycle)
186	3.4260	1	3.2950	8.8540e-08
2432	3.6290	1885	3.5700	9.1910e-08
4598	3.8310	2603	3.6550	9.5150e-08
6692	4.0340	3331	3.6950	9.8300e-08
8592	4.2370	4036	3.7250	9.5710e-08
10620	4.4390	4747	3.8450	9.1040e-08
13080	4.6420	7125	4.0650	8.1760e-08
15830	4.8440	8343	4.2100	7.2420e-08
18860	5.0470	9060	4.2800	6.8500e-08
21850	5.2500	9779	4.3550	6.7060e-08
24880	5.4520	10623	4.4300	6.6770e-08
27930	5.6550	12882	4.6250	7.2760e-08
30580	5.8570	14085	4.7150	8.4510e-08
33000	6.0600	14800	4.7600	9.1120e-08
34990	6.2620	16958	4.9100	9.5130e-08
36920	6.4650	17688	4.9700	9.3240e-08
39180	6.6680	18453	5.0350	9.1870e-08
41500	6.8700	19118	5.0750	9.5460e-08
43560	7.0730	19833	5.1050	1.0110e-07
45510	7.2750	20016	5.1350	1.0650e-07
	20990		5.1950	
	22167		5.2650	
	22894		5.3000	
	25046		5.4750	
	25763		5.5250	
	26476		5.5500	
	26875		5.5750	
	27589		5.6350	
	28415		5.6950	
	30457		5.8450	
	31172		5.9100	
	44313		7.1500	
	47830		7.5660	

Specimen ID: **G8A-5-FCG**  
 Test Type: **In-Phase**  
 P<sub>max</sub>: **14.0 kN**  
 R-ratio: **0.1**  
 Temperature: **150-538 °C**  
 Frequency: **0.00083 Hz**  
 Specimen Geometry: **M(T)**

Cycles (DCEP)	DCEP Crack Length (mm)	Cycles (Optical)	Optical Crack Length (mm)	Crack Growth Rate (m/cycle)
245	3.6500	1	3.3030	1.8910e-06
313	3.7930	337	3.8150	2.2840e-06
372	3.9360	414	4.0730	2.4990e-06
427	4.0800	481	4.2380	2.6950e-06
475	4.2230	549	4.4050	2.9750e-06
523	4.3660	621	4.7230	3.2010e-06
564	4.5100	781	5.7890	3.7660e-06
600	4.6530			4.7610e-06
630	4.7960			4.7790e-06
656	4.9390			4.9530e-06
683	5.0830			5.2300e-06
708	5.2260			6.6370e-06
729	5.3690			7.9260e-06
746	5.5130			9.0550e-06
761	5.6560			1.0060e-05
775	5.7990			1.0970e-05

Specimen ID: **G7A-4-FCG**  
 Test Type: **Out-of-Phase**  
 $P_{max}$ : **3.7 kN**  
 R-ratio: **0.1**  
 Temperature: **150-538 °C**  
 Frequency: **0.0083 Hz**  
 Specimen Geometry: **SE(T)**

Cycles (DCEP)	DCEP Crack Length (mm)	Cycles (Optical)	Optical Crack Length (mm)	Crack Growth Rate (m/cycle)
48	12.7100	0	12.7520	1.7160e-07
907	12.8700	374	12.8420	1.8260e-07
1717	13.0200	1032	12.9670	1.9300e-07
2486	13.1700	1746	13.1370	2.0280e-07
3193	13.3200	2472	13.3070	2.0870e-07
3837	13.4700	3186	13.4220	2.5400e-07
4336	13.6300	4950	14.0070	3.7250e-07
4734	13.7800	5360	14.2870	5.5370e-07
5007	13.9300	6057	14.6520	6.7040e-07
5150	14.0800	6778	15.0870	6.9460e-07
5399	14.2300	7496	15.4120	6.5850e-07
5612	14.3900	8214	15.8270	6.2350e-07
5854	14.5400	10368	17.7870	6.1290e-07
6089	14.6900			5.5530e-07
6409	14.8400			4.5110e-07
6805	14.9900			4.4900e-07
7132	15.1500			4.7620e-07
7451	15.3000			5.3330e-07
7695	15.4500			6.9010e-07
7894	15.6000			9.9520e-07
8064	15.7600			1.0290e-06
8194	15.9100			1.0710e-06
8285	16.0600			1.1100e-06
8465	16.2100			9.0820e-07
8639	16.3600			8.0980e-07
8816	16.5200			8.0850e-07
9018	16.6700			7.5880e-07
9217	16.8200			7.3500e-07
9434	16.9700			7.5630e-07
9632	17.1200			8.0000e-07
9817	17.2800			8.1230e-07
10000	17.4300			8.3430e-07
10180	17.5800			8.5570e-07
10360	17.7300			8.7660e-07

Specimen ID: **G8A-6-FCG**  
 Test Type: **Decreasing T<sub>min</sub>**  
 P<sub>max</sub>: **10.0 kN**  
 R-ratio: **0.1**  
 Temperature: **T<sub>max</sub>=538 °C T<sub>min</sub>→150 °C**  
 Frequency: **0.0083 Hz**  
 Specimen Geometry: **M(T)**

Cycles (DCEP)	DCEP Crack Length (mm)	Cycles (Optical)	Optical Crack Length (mm)	Crack Growth Rate (m/cycle)
<b>Precracked at P<sub>max</sub> = 10.5 kN and T = 538 °C</b>				
369	3.6440	0	3.2810	1.1940e-06
469	3.7670	700	4.0830	1.2620e-06
564	3.8900			1.3270e-06
654	4.0120			1.3890e-06
<b>***** Started of Decreasing T<sub>min</sub> Test *****</b>				
112	4.2340	1	4.0830	1.2290e-06
245	4.3960	230	4.3500	1.2110e-06
380	4.5570	673	4.9160	1.1920e-06
519	4.7190	1347	5.6560	1.1590e-06
655	4.8810	2039	6.5560	1.1450e-06
795	5.0430	2190	6.8210	1.0970e-06
952	5.2040	2498	7.3600	1.0610e-06
1103	5.3660			1.0700e-06
1257	5.5280			1.1020e-06
1401	5.6900			1.2350e-06
1528	5.8510			1.3280e-06
1644	6.0130			1.3400e-06
1753	6.1750			1.2970e-06
1874	6.3370			1.3980e-06
1989	6.4980			1.6420e-06
2165	6.8220			1.6260e-06
2269	6.9830			1.4670e-06
2387	7.1450			1.2880e-06

Appendix B - Computer Code to Predict TMF Crack Growth Rates

A computer code was developed to predict the crack growth rates of SCS-6/Ti-6Al-2Sn-4Zr-2Mo under isothermal fatigue and thermomechanical fatigue loading. The source code was originally developed by J. Pernot [22] who modelled the fatigue crack growth rates in Ti-24Al-11Nb under isothermal and thermomechanical loading. The code given in this appendix is a modification of his original code.

The modifications were fairly straight forward since his modelling effort also used a linear summation approach. The primary change to Pernot's code [22] was substituting his cycle-dependent and time-dependent formulations with those developed in this study (i.e., Equations 8.3 and 8.6). The code is standard Fortran 77 that is portable to any computer with an appropriate compiler. The program is self-contained requiring no external libraries.

```

C This program predicts the thermomechanical fatigue
C crack growth in SCS-6/Ti-6Al-2Sn-4Zr-2Mo [0]4 composite.
C The prediction scheme uses a cumulative damage model.
C K is used as the correlating parameter for crack
C growth rates. The thermal cycles range between 150 and
C 538 degrees C and cyclic frequencies for the TMF cycles
C range between 2 to 20 min/cycle.

C ++++++
C This version uses an Arhennius type equation to determine
C the time-dependent term. The form of the equation is coupled
C with an applied delta-K term.
C ++++++

```

```

PROGRAM TMFCG
CHARACTER*25 NAME, VERSION, TYPE, MATL
INTEGER CHECK
COMMON/BLK2/MATL
COMMON/BLK3/NUMTYPE
COMMON/BLK4/TYPE
COMMON/BLK5/NUMDIV
COMMON/BLK6/TIME(10),DKPERC(10),DTPERC(10)
COMMON/BLK7/XN(10),TMSTEP(10)
COMMON/BLK8/DKSLOPE,DTSLOPE
COMMON/BLK11/CHECK
COMMON/BLK12/DKTHRES
COMMON/BLK13/GAMMA

```

```
VERSION='2.00 08/16/1993'
```

```
101    CALL INITIAL(VERSION, TMTOT, TMUPLOAD, TMNONDEC, PA, R,
& TMIN, TMAX)
```

C Read integration parameters from the keyboard.

```
CALL INTPAR(DKINITIAL, DKFINAL, DKINCR)
```

C Open the output (plot) data file.

```
CALL NEWFILE(NAME)
```

C Write header to the output (plot) data file.

```
CALL HEADER(VERSION, PA, TMTOT, TMUPLOAD, TMNONDEC, R, TMIN,
& TMAX)
```

C Calculate initial temperature for CDPARPAR.

```
DT=TMAX-TMIN
```

```
T=TMIN+DT*DTPERC(0)
```

C Initialize delta K for all calculations.

```

IF(DKINITIAL.GE.30.0)THEN

    DK=DKINITIAL

    ELSE

C      If DKINITIAL<30.0 then calculations start at 30 MPa m^1/2.

        DK = 30.0

    ENDIF

31      WRITE(*,31)
      FORMAT(15(/),1X,60('*'),/,12X,' CRACK GROWTH RATE',
      & ' CALCULATIONS BEGIN',/,1X,60('*'),4(/))

      IF(CHECK.EQ.1)THEN

32      WRITE(*,32)
      FORMAT(2(/),5X,' DELTAK',5X,' DADNTOT',5X,' DADNCD',
      & 6X,' DADNTD',4X,/,2X,50('*'))

      ENDIF

100     CONTINUE

C      DADNCD is the cycle dependent damage
C      DADNTD is the time dependent damage

      DADNCD = CYCLEDEP(DK,R,TMIN,TMAX,TMTOT,TMUPLOAD,TMNONDEC)

C      The time dependent term is calculated based on an Arhennius-form equation.

      DADNTD = TIMEDEP(DK,R,TMIN,TMAX,TMTOT,TMUPLOAD,TMNONDEC)

C      DADNTD is adjusted by TMNONDEC^(gamma-1) so that the time dependent term
C      is not entirely time dependent. That is, a 10X increase in cyclic
C      time does not translate into a 10X increase in crack growth rate.
C      Value of gamma is dependent upon the type of test being run.
C      gamma = 0.62, 0.57, and 0.52 for an in-phase, an isothermal, and
C      out-of-phase test, respectively.

      DADNTD = TMNONDEC**(GAMMA-1) * DADNTD

C      If 1 was selected for the data print options, then da/dN
C      and delta K information is written to the screen.

      IF(CHECK.EQ.1)THEN

33      WRITE(*,33)DK,(DADNCD+DADNTD),DADNCD,DADNTD
      FORMAT(4(1X,E12.5))

      ENDIF

C      If the cycle-dependent or time-dependent damage terms
C      come from outside the experimental data range, a flag
C      value of 10 is returned and all calculations stop.

```

```

IF(DADNCD.EQ.10..OR.DADNTD.EQ.10.)THEN

        WRITE(*,41)DK
41      FORMAT(' OUTSIDE EXPERIMENTAL DATA RANGE AT DELTA',
&           ' K = ',F6.2,/, ' STOP CALCULATIONS, '/') 

        GOTO 200

ENDIF

C     The total crack growth is the sum of the cycle-
C     dependent and time-dependent damage.

DADNTOT = DADNCD+DADNTD

C     Write to the data file.

        WRITE(2,42)DK,DADNTOT,DADNCD,DADNTD
42      FORMAT(1X,E12.5,1X,E12.5,1X,E12.5,1X,E12.5)

C     Increment delta-K.

        DK=DK+DKINCR

C     Check to see if DELTA-K has reached the maximum value
C     input by the operator.

        IF(DK.GT.(DKFINAL+DKINCR/10.))GOTO 200

C     Return with the next value of delta-K for damage
C     calculations.

        GOTO 100

C     Close data file and end program.

200    CONTINUE

        REWIND(UNIT=2)
        CLOSE(UNIT=2)

        WRITE(*,51)NAME
51      FORMAT(/,' YOUR TMF DATA HAS BEEN STORED IN ',A25)

155    WRITE(*,55)
55      FORMAT(/,' DO YOU WANT TO ...',/,,' 1 - CALCULATE'
&           ' MORE VALUES OR',/,,' 2 - QUIT',/,,' 1 OR 2: ',\$)
        READ(*,*)CHOICE

        IF(CHOICE.NE.1.AND.CHOICE.NE.2)GOTO 155
        IF(CHOICE.EQ.1)GOTO 101

999    END
C     -----

```

```

SUBROUTINE INITIAL(VERSION,TMTOT,TMUPLOAD,TMNONDEC,
& PA,R,TMIN,TMAX)

CHARACTER*25 VERSION,TYPE,MATL
INTEGER CHOICE
COMMON/BLK2/MATL
COMMON/BLK3/NUMTYPE
COMMON/BLK4/TYPE
COMMON/BLK5/NUMDIV
COMMON/BLK6/TIME(10),DKPERC(10),DTPERC(10)

IF(CHOICE.EQ.1)GOTO 104

1      WRITE(*,1)VERSION
      FORMAT(/,1X,60('*'),/, ' PROGRAM TMFCG',22X,'VERSION ',
      & A21,/,1X,60('*'),/)

2      WRITE(*,2)
      FORMAT(/, ' THIS PROGRAM CALCULATES CRACK GROWTH',
      & ' RATES UNDER THERMO',/, ' MECHANICAL FATIGUE',
      & ' CONDITIONS USING A CUMULATIVE DAMAGE',/, ' MODEL',
      & ' THAT CONSIDERS CRACK RETARDATION',3(/),
      & ' CURRENTLY THIS PROGRAM CAN CALCULATE GROWTH RATES',
      & ' ONLY FOR',/, ' SCS-6/Ti-6Al-2Sn-4Zr-2Mo [0]4.',
      & /., ' THIS PROGRAM IS BASED ON PERVIOUS MODELING',
      & ' EFFORTS BY:',/,
      & '           (1) HEIL, NICHOLAS, HARITOS',/,
      & '           (2) PERNOT, NICHOLAS, MALL',2(/))

      WRITE (*,60)
60    FORMAT (' Type "1" to Continue')
      READ (*,*) PAUSE

      WRITE(*,3)
3      FORMAT(15(/))

104   CONTINUE

      CALL INTERACT(TMTOT,TMUPLOAD,TMNONDEC,PA,R,TMIN,TMAX)

C      After parameters are obtained from INTERACT
C      all parameters are written to the screen.

      WRITE(*,11)MATL,NUMTYPE,TYPE
11    FORMAT(10(/),1X,60('*'),/,8X,' THERMOMECHANICAL',
      & ' FATIGUE TEST PARAMETERS ',/,1X,60('*'),/,/,
      & ' MATERIAL: ',A25,/,/,
      & ' TEST TYPE: #',I2,' - ',A21)

      IF(NUMTYPE.EQ.4)THEN

12      WRITE(*,12)PA
      FORMAT(4X,' PHASE ANGLE = ',F6.2)

      ENDIF

      WRITE(*,13)TMTOT,TMUPLOAD,TMNONDEC
13    FORMAT(/, ' TIME PARAMETERS:',/,4X,' TOTAL TIME OF',
      & ' TMF CYCLE = ',F8.2,' SECONDS',/,4X,' TIME INTO',
      & ' CYCLE WHEN THE',/,4X,' LOAD STOPS INCREASING '

```

```

& ' = ',F8.2,' SECONDS',/,4X,' TIME INTO',
& ' CYCLE WHEN THE',/,4X,' LOAD BEGINS TO DECREASE',
& ' = ',F8.2,' SECONDS')

      IF (NUMTYPE.EQ.2) THEN

          TMHOLD=TMTOT-2*(TMTOT-TMNNONDEC)

          WRITE(*,14) TMHOLD
14      FORMAT(4X,' LENGTH OF HOLD AT P MAX = ',F8.2,
&           ' SECONDS')

          ENDIF

          WRITE(*,15) R,TMIN,TMAX
15      FORMAT(' LOAD PARAMETER:',/,4X,' LOAD RATIO',
&           ' = ',F4.2,2(/), ' TEMPERATURE PARAMETERS:',/,4X,
&           ' MINIMUM TEMPERATURE = ',F8.2,' DEGREES C',/,4X,
&           ' MAXIMUM TEMPERATURE = ',F8.2,' DEGREES C',/)

          WRITE (*,160)
160     FORMAT (' Type "1" to Continue')
          READ (*,*) PAUSE

          WRITE(*,21) NUMTYPE,TYPE
21      FORMAT(10(/),1X,60('*'),/,11X,' TIME-TEMPERATURE-',
&           'LOAD PROFILE PARAMETERS',/,1X,60('*'),/,/
&           ' TEST TYPE: #',I2,' - ',A21)

          IF (NUMTYPE.EQ.4) THEN

              WRITE(*,22) PA
22      FORMAT(4X,' PHASE ANGLE = ',F6.2)

              ENDIF

              WRITE(*,23) NUMDIV,(NUMDIV+1)
23      FORMAT( /,' THERE ARE',I2,' DIVISIONS OF THE TMF',
&           ' CYCLE',/, ' REQUIRING',I3,' DIVISION ENDPOINTS.',',
&           2(/),' THE DIVISION ENDPOINTS ARE: ')

              WRITE(*,24)
24      FORMAT( /,' END PT    TIME    LOAD FRACTION    TEMP',
&           ' FRACTION',/, '#      (SEC)      (DECIM FRACT)',',
&           '      (DECIM FRACT)' )

              DO 125 J=0,NUMDIV
              WRITE(*,25) J, TIME(J),DKPERC(J),DTPERC(J)
25      FORMAT(3X,I1,3X,F8.2,7X,F5.3,11X,F5.3)
125     CONTINUE

              WRITE(*,26)
26      FORMAT(/)

              WRITE (*,260)
260     FORMAT (' Type "1" to Continue')
              READ (*,*) PAUSE

              RETURN
              END

```

```

C      Subroutine INTERACT reads all cycle parameters
C      interactively from the keyboard.

      SUBROUTINE INTERACT(TMTOT,TMUPLOAD,TMNNONDEC,PA,R,
& TMIN,TMAX)

      CHARACTER*25 TYPE,MATL
      COMMON/BLK2/MATL
      COMMON/BLK3/NUMTYPE
      COMMON/BLK4/TYPE
      COMMON/BLK13/GAMMA

      WRITE(*,1)
1     FORMAT(13(/),1X,60('*'),/,13X,' INTERACTIVE INPUT'
& ' OF CYCLE PARAMETERS',/,1X,60('*'),/)

C      Set MATL equal to appropriate character constant.

      MATL='SCS-6/Ti-6Al-2Sn-4Zr-2Mo'

C      DKTHRES is set equal to 25. If DK < 25 then DADN set equal to 0.

      DKTHRES = 25.

C      GAMMA is inserted at this time. It is used to
C      adjust the time dependent of the time-dependent crack growth term.

      READ(*,*) GAMMA

      WRITE(*,3)
3     FORMAT(/,' INDICATE THE TYPE OF TEST',/,' 1 - ISO'
& ' THERMAL',/,' 2 - ISOTHERMAL WITH HOLD TIME IN LOAD'
& ' CYCLE',/,' 3 - IN PHASE TMF',/,' 4 - OUT OF PHASE'
& ' TMF',/,' 5 - UPPER TRIANGULAR PHASE TMF',/,' 6 -'
& ' LOWER TRIANGULAR PHASE TMF',/,' 7 - USER DEFINED',
& /,' 1-7: ',\$)
      READ(*,*) NUMTYPE

C      If NUMTYPE is not equal to 1-6, then 7 is assumed.

C      Cycle time information is determined.

      WRITE(*,14)
14    FORMAT(/,' INPUT THE TOTAL CYCLE TIME',
& ' (IN SECONDS): ',\$)
      READ(*,*) TMTOT

C      The rising portion of the loading cycle and the non-
C      decreasing load portion of the cycle are determined.

C      TMUPLOAD is the time from the initial increase in load
C      (at time = 0.) to the time when the load is no longer
C      increasing. This value is required for the cycle-
C      dependent crack growth rate calculations.

C      TMNONDEC is the time from the initial increase of load
C      (at time = 0.) to the time when the load begins to
C      decrease. This value is required for the time-dependent
C      crack growth rate calculations.

```

```
IF (NUMTYPE.EQ.1) THEN
    TMUPLOAD=TMTOT/2
    TMNONDEC=TMUPLOAD
    TYPE='ISOTHERMAL'

ELSEIF (NUMTYPE.EQ.2) THEN
    WRITE(*,15)
15   FORMAT(' INPUT THE HOLD TIME (IN SECONDS): ',\$)
    READ(*,*) TMHOLD
C     The uploading portion of the hold time cycle is
C     (TMTOT-TMHOLD)/2, and the time until the load begins to
C     decrease is (TMTOT-TMHOLD)/2+TMHOLD
    TMUPLOAD=(TMTOT-TMHOLD)/2
    TMNONDEC=TMUPLOAD+TMHOLD
    TYPE='ISOTHERMAL W/ LOAD HT'

ELSEIF (NUMTYPE.EQ.3.OR.NUMTYPE.EQ.4) THEN
    TMUPLOAD=TMTOT/2
    TMNONDEC=TMUPLOAD

    IF (NUMTYPE.EQ.3) THEN
        TYPE='IN PHASE TMF'
    ELSE
        TYPE='OUT OF PHASE TMF'
    ENDIF

ELSEIF (NUMTYPE.EQ.5) THEN
    TMUPLOAD=TMTOT/3
    TMNONDEC=2*TMUPLOAD
    TYPE='UPPER TRIAN PHASE TMF'

ELSEIF (NUMTYPE.EQ.6) THEN
    TMUPLOAD=TMTOT/3
    TMNONDEC=TMUPLOAD
```

```

TYPE='LOWER TRIAN PHASE TMF'

ELSE

17   WRITE(*,17)
      FORMAT(' INPUT THE TIME INTO THE CYCLE WHEN THE LOAD',
      & ' IS NO LONGER INCREASING',/,,' (IN SECONDS) : '$)
      READ(*,*)TMUPLOAD

18   WRITE(*,18)
      FORMAT(' INPUT THE TIME INTO THE CYCLE WHEN THE LOAD',
      & ' BEGINS TO DECREASE',/,,' (IN SECONDS) : '$)
      READ(*,*)TMNONDEC

TYPE='USER DEFINED'

C   If NUMTYPE is not equal to 1-6, then 7 is assumed.

      NUMTYPE=7

      ENDIF

C   Load-temperature phase information is determined for the
C   basic TMF cycles.

      IF (NUMTYPE.EQ.4) THEN

          WRITE(*,12)
          FORMAT(/, ' INPUT THE LOAD-TEMP PHASE ANGLE',
          & ' (P LEADS T)',/,,' (90, 180, OR 270): ',\$)
          READ(*,*)PA

          ELSE

C   PA is set equal to zero for all other cases.

          PA=0

          ENDIF

C   Input the load information.

          WRITE(*,13)
          FORMAT(/, ' INPUT THE LOAD RATIO (R): ',\$)
          READ(*,*)R

C   Input the temperature information.

          IF (NUMTYPE.EQ.1.OR.NUMTYPE.EQ.2) THEN

              WRITE(*,25)
              FORMAT(/, ' INPUT THE TEST TEMP: ',\$)
              READ(*,*)TMIN

              TMAX=TMIN

              ELSE

```

```

      WRITE(*,26)
26   FORMAT(/, ' INPUT THE MINIMUM TEMP: ',\$)
      READ(*,*)TMIN

      WRITE(*,27)
27   FORMAT(' INPUT THE MAXIMUM TEMP: ',\$)
      READ(*,*)TMAX

      ENDIF

C     Set up time-load-temperature profiles.

      CALL PROFILE(PA,TMTOT,TMHOLD)

      RETURN
      END

C -----
C     Subroutine PROFILE sets up the time-temperature-load
C     profiles for all TMF cycles.

      SUBROUTINE PROFILE(PA,TMTOT,TMHOLD)
      COMMON/BLK3/NUMTYPE
      COMMON/BLK5/NUMDIV
      COMMON/BLK6/TIME(10),DKPERC(10),DTPERC(10)

      IF(NUMTYPE.EQ.1) THEN

C     Isothermal cycle profile.

      NUMDIV=2

      TIME(0)=0.
      TIME(1)=TMTOT/2.
      TIME(2)=TMTOT

      DKPERC(0)=0.
      DKPERC(1)=1.
      DKPERC(2)=0.

      DTPERC(0)=1.
      DTPERC(1)=1.
      DTPERC(2)=1.

      ELSEIF(NUMTYPE.EQ.2) THEN

C     Isothermal with load hold-time cycle profile.

      NUMDIV=3

      TIME(0)=0.
      TIME(1)=(TMTOT-TMHOLD)/2.
      TIME(2)=TIME(1)+TMHOLD
      TIME(3)=TMTOT

      DKPERC(0)=0.
      DKPERC(1)=1.
      DKPERC(2)=1.

```

```

DKPERC(3)=0.

DTPERC(0)=1.
DTPERC(1)=1.
DTPERC(2)=1.
DTPERC(3)=1.

ELSEIF((NUMTYPE.EQ.3).OR.(NUMTYPE.EQ.4.AND.PA.EQ.0.))THEN

C     In-phase TMF cycle profile.

      NUMDIV=2

      TIME(0)=0.
      TIME(1)=TMTOT/2.
      TIME(2)=TMTOT

      DKPERC(0)=0.
      DKPERC(1)=1.
      DKPERC(2)=0.

      DTPERC(0)=0.
      DTPERC(1)=1.
      DTPERC(2)=0.

ELSEIF(NUMTYPE.EQ.4.AND.PA.NE.0.)THEN

C     Out-of phase TMF cycle profiles.

      IF(PA.EQ.180.)THEN

C     180 degrees out-of-phase cycle profile.

          NUMDIV=2

          TIME(0)=0.
          TIME(1)=TMTOT/2.
          TIME(2)=TMTOT

          DKPERC(0)=0.
          DKPERC(1)=1.
          DKPERC(2)=0.

          DTPERC(0)=1.
          DTPERC(1)=0.
          DTPERC(2)=1.

ELSEIF(PA.EQ.90..OR.PA.EQ.270.)THEN

C     90 and 270 degree TMF phases have the same time-load
C     profiles.

          NUMDIV=4

          TIME(0)=0.
          TIME(1)=TMTOT/4
          TIME(2)=TMTOT/2
          TIME(3)=3*TMTOT/4

```

```

TIME(4)=TMTOT

DKPERC(0)=0.
DKPERC(1)=.5
DKPERC(2)=1.
DKPERC(3)=.5
DKPERC(4)=0.

IF(PA.EQ.90.)THEN

C      90 degree TMF phase temperature profile.

      DTPERC(0)=.5
      DTPERC(1)=0.
      DTPERC(2)=.5
      DTPERC(3)=1.
      DTPERC(4)=.5

      ELSE

C      270 degree TMF phase temperature profile.

      DTPERC(0)=.5
      DTPERC(1)=1.
      DTPERC(2)=.5
      DTPERC(3)=0.
      DTPERC(4)=.5

      ENDIF

      ELSE

C      45, 135, 225, and 315 degree TMF cycles could fit
C      here if it is necessary to program them. 45 and 225
C      degree TMF cycles have identical load profiles, and
C      135 and 315 degree TMF cycles have identical load
C      profiles.

      ENDIF

      ELSEIF (NUMTYPE.EQ.5.OR.NUMTYPE.EQ.6) THEN

C      Upper triangular phase (UTP) and lower triangular phase
C      (LTP) TMF cycles have identical time profiles.

      NUMDIV=3

      TIME(0)=0.
      TIME(1)=TMTOT/3
      TIME(2)=2*TIME(1)
      TIME(3)=TMTOT

C      The load and temperature profiles differ only in
C      DKPERC(2) and DTPERC(2).

C      UTP load and temperature profiles.

      DKPERC(0)=0.
      DKPERC(1)=1.

```

```

DKPERC(2)=1.
DKPERC(3)=0.

DTPERC(0)=0.
DTPERC(1)=1.
DTPERC(2)=0.
DTPERC(3)=0.

C If NUMTYPE identifies the LTP, then DKPERC(2) and
C DKPERC(2) are reversed.

IF (NUMTYPE.EQ.6) THEN

C LTP TMF cycle load and temperature profile changes.

DKPERC(2)=0.
DTPERC(2)=1.

ENDIF

ELSE

C Read time-load-temperature profile from the keyboard
C for the user defined TMF cycle.

WRITE(*,1)
1 FORMAT(10(/),1X,60('*'),/,10X,' THE USER DEFINED',
& ' TMF CYCLE WAS SELECTED',//,1X,60('*'),3(/),' THIS'
& ' SELECTION REQUIRES THE TIME-LOAD-TEMPERATURE'
& ' PROFILE',//,' INFORMATION TO BE INPUT FROM THE',
& ' KEYBOARD.',2(/),' NOTE://,' 1. TIME MUST BEGIN'
& ' AT 0. AND END AT TMTOT (DEFINED PREVIOUSLY)',/
& ' 2. THE LOAD CYCLE MUST BEGIN ON A NON-DECREASING',
& ' SLOPE',//,' 3. THE INITIAL AND FINAL LOAD AND',
& ' TEMPERATURE FRACTIONS MUST',//,3X,' BE IDENTICAL',
& ' TO CLOSE THE CYCLE LOOPS.')

WRITE(*,2)
2 FORMAT(//,' INDICATE THE NUMBER OF DIVISIONS',
& '(NUMDIV) IN THE',
& ' TMF CYCLE',2(/),' NOTE://,' EACH CHANGE IN SLOPE',
& ' OF THE LOAD OR TEMPERATURE VS. TIME',//,' CURVES',
& ' REQUIRES A NEW DIVISION',2(/),
& ' NUMDIV CANNOT EXCEED 9',//,' NUMDIV: ',\$)
READ(*,*) NUMDIV

WRITE(*,3) NUMDIV, (NUMDIV+1), NUMDIV
3 FORMAT(//,' THERE ARE',I2,' DIVISIONS IN THE TMF',
& ' CYCLE',//,' REQUIRING',I3,' DIVISION ENDPOINTS',//,
& ' THESE ENDPOINTS NUMBER FROM 0 TO',I2,'.',/)

WRITE(*,4)
4 FORMAT(//,' DEFINE THE DIVISION ENDPOINTS BY',//,
& ' TIME (SECONDS), LOAD FRACTION, TEMPERATURE'
& ' FRACTION',//,
& ' THE FRACTIONS VARY FROM 0. TO 1. TO INDICATE',
& ' THE VARIATION',//,' BETWEEN MINIMUM AND MAXIMUM'
& ' , RESPECTIVELY.',/)

WRITE(*,5)
5 FORMAT(//,' DEFINE THE ENDPOINTS FOR THE TMF CYCLE',

```

```

&   ' DIVISIONS',//,' SEPARATE VALUES WITH COMMAS',//,
&   ' ENDPT: TIME, LOAD FRACTION, TEMP FRACTION',
&   //,' #      (SECS) (DECIMAL EQUIV) (DECIMAL EQUIV)',,
&   //,50('**')

DO 100 J=0,NUMDIV

      WRITE(*,6)J
6      FORMAT(1X,I2,':',\$)
      READ(*,*)TIME(J),DKPERC(J),DTPERC(J)

100    CONTINUE

      ENDIF

      RETURN
      END
C -----
C Subroutine INTPAR reads the integration parameters from
C the keyboard.

SUBROUTINE INTPAR(DKINITIAL,DKFINAL,DKINCR)
INTEGER CHOICE
COMMON/BLK3/NUMTYPE
COMMON/BLK5/NUMDIV
COMMON/BLK6/TIME(10),DKPERC(10),DTPERC(10)
COMMON/BLK7/XN(10),TMSTEP(10)

      WRITE(*,1)
1      FORMAT(10(/),1X,60('*'),/,8X,' INTERACTIVE INPUT OF',
&   ' INTEGRATION PARAMETERS',//,1X,60('*'),2(/))

100    IF(NUMTYPE.NE.2.AND.NUMTYPE.NE.7)THEN

      WRITE(*,2)NUMDIV
2      FORMAT(' THERE ARE ',I2,' DIVISIONS IN THE TMF CYCLE',
&   2(/),' INPUT THE NUMBER OF INTEGRATION STEPS OVER EACH',
&   //,' DIVISION OF THE TMF CYCLE',//,' NOTE:',
&   ' THE NUMBER MUST BE EVEN',//,' NUMBER OF STEPS: '\$)
      READ(*,*)IXN

      DO 200 I=1,NUMDIV

      XN(I)=IXN

200    CONTINUE

      ELSEIF (NUMTYPE.EQ.2) THEN

      WRITE(*,3)
3      FORMAT(' INPUT THE NUMBER OF INTEGRATION STEPS OVER THE',
&   //,' UPLOADING AND DOWNLOADING PORTIONS OF THE TMF CYCLE',
&   //,' NOTE:',
&   ' THE NUMBER MUST BE EVEN',//,' NUMBER OF STEPS: '\$)
      READ(*,*)XN(1)

```

```

XN(3)=XN(1)

4      WRITE(*,4)
      FORMAT(' INPUT THE NUMBER OF INTEGRATION STEPS OVER THE',
     &      /,' HOLD TIME PORTION OF THE TMF CYCLE',//,' NOTE:',
     &      /,' THE NUMBER MUST BE EVEN',//,' NUMBER OF STEPS: ',S)
      READ(*,*)XN(2)

      ELSE

5      WRITE(*,5)NUMDIV
      FORMAT(' THERE ARE ',I2,' DIVISIONS IN THE TMF CYCLE',
     &      2(/,' INPUT THE NUMBER OF INTEGRATION STEPS OVER EACH',
     &      /,' DIVISION OF THE TMF CYCLE',//,' NOTE:',
     &      /,' EACH NUMBER MUST BE EVEN',//,',
     &      /,' DIVISION # : NUMBER OF INTEGRATION STEPS',
     &      /,40('*'))

      DO 600 J=1,NUMDIV

      WRITE(*,6)J
      FORMAT(1X,I6,':',S)
      READ(*,*)XN(J)

600    CONTINUE

      ENDIF

      DO 700 J=1,NUMDIV
      TMSTEP(J)=(TIME(J)-TIME(J-1))/XN(J)

700    CONTINUE

108    WRITE(*,8)
8      FORMAT(/, ' THE NUMBER OF INTEGRATION STEPS AND TIME STEP',
     &      /,' SIZE',//,' FOR EACH DIVISION OF THE TMF CYCLE ARE: ',/,/,
     &      /,' DIV',3X,' INT STEPS',3X,' STEP SIZE ',/,30('*'))

      DO 900 J=1,NUMDIV

C      IFIX converts a real number to its integer form
C      That is XN(1) = 10.0 --> IFIX(XN(1)) = 10

      WRITE(*,9)J,IFIX(XN(J)),TMSTEP(J)
9      FORMAT(1X,I2,6X,I6,5X,F9.5)

900    CONTINUE

      WRITE(*,10)
10     FORMAT(/, ' DO YOU WANT TO:',//,' 1 - CONTINUE WITH',
     &      /,' THESE PARAMETERS',//,' 2 - CHANGE THEM',//,
     &      /,' 1 OR 2: ',S)

```

```

READ(*,*) CHOICE

IF(CHOICE.NE.1.AND.CHOICE.NE.2)GOTO 108

IF(CHOICE.EQ.2)GOTO 100

111    WRITE(*,11)
11     FORMAT(//,' INPUT THE VALUE OF DELTA-K WHERE THE'
&   ' CRACK GROWTH RATE',//,' CALCULATIONS WILL BEGIN',//,
&   '(DELTA-K = 0. DEFINES THRESHOLD): ',\$)
      READ(*,*) DKİNİTİAL

      WRITE(*,12)
12     FORMAT(//,' INPUT THE VALUE OF DELTA-K WHERE THE'
&   ' CRACK GROWTH RATE',//,' CALCULATIONS WILL END: ',\$)
      READ(*,*) DKFINAL

      WRITE(*,13)
13     FORMAT(//,' INPUT THE INCREMENT OF DELTA-K BETWEEN'
&   ' CRACK GROWTH RATE',//,' CALCULATIONS: ',\$)
      READ(*,*) DKİNCR

114    WRITE(*,14)DKİNİTİAL,DKFINAL,DKİNCR
14     FORMAT(//,' CRACK GROWTH RATE CALCULATIONS WILL://,
&   ' BEGIN AT DELTA-K = ',F7.3,//,' END AT DELTA-K = ',
&   ' F7.3,//,' WITH INCREMENT = ',F7.3)

      WRITE(*,15)
15     FORMAT(//,' DO YOU WANT TO://,' 1 - CONTINUE WITH',
&   ' THESE PARAMETERS',//,' 2 - CHANGE THEM',//,
&   ' 1 OR 2: ',\$)
      READ(*,*) CHOICE

      IF(CHOICE.NE.1.AND.CHOICE.NE.2)GOTO 114

      IF(CHOICE.EQ.2)GOTO 111

      RETURN
      END

C -----
C Subroutine NEWFILE opens a plot data file.

SUBROUTINE NEWFILE(NAME)
CHARACTER*25 NAME
INTEGER CHOICE,CHECK
COMMON/BLK11/CHECK

      WRITE(*,1)
1     FORMAT(14(/),1X,60('*'),/,5X,' INTERACTIVE INPUT OF',
&   ' DATA PLOT FILE INFORMATION',//,1X,60('*'),2(/))

102    WRITE(*,2)
2     FORMAT(4(/),' DO YOU WANT RESULTS WRITTEN:',2(/),' 1 - TO',
&   ' SCREEN AND DISK',//,' 2 - ONLY TO DISK',2(/),
&   ' 1 OR 2: ',\$)
      READ(*,*) CHECK

```

```

        WRITE(*,4)
4      FORMAT(2(/), ' WHAT IS THE NAME OF THE OUTPUT DATA FILE?',
& 2(/), ' 25 CHARACTER STRING, MAXIMUM',2(/), ' NAME: ',$)

        READ(*,5)NAME
5      FORMAT(A25)

109     WRITE(*,9)
9      FORMAT(13(/))

        IF (CHECK.EQ.1.OR.CHECK.EQ.2)THEN

        WRITE(*,10)NAME
10     FORMAT(2(/), ' THE NAME OF THE OUTPUT DATA FILE IS: ',A25)

        ENDIF

        WRITE(*,13)
13     FORMAT(2(/), ' DO YOU WANT TO:,,,,' 1 - CONTINUE WITH',
& ' THE FILE NAME(S) AND (OR) CHOICES',/, ' 2 - CHANGE THE',
& ' FILE NAME(S) AND (OR) CHOICES',/,/
& ' 1 OR 2: ',$)
        READ(*,*) CHOICE

        IF(CHOICE.NE.1.AND.CHOICE.NE.2)GOTO 109

        IF(CHOICE.EQ.2)GOTO 102

        IF (CHECK.EQ.1.OR.CHECK.EQ.2)THEN

        OPEN(UNIT=2,FILE=NAME,STATUS='UNKNOWN')

        ENDIF

        RETURN
        END

C -----
C Subroutine HEADER writes a header to the data file.

        SUBROUTINE HEADER(VERSION,PA,TMTOT,TMUPLOAD,
& TMNONDEC,R,TMIN,TMAX)

        CHARACTER*25 VERSION,TYPE,MATL
        COMMON/BLK2/MATL
        COMMON/BLK3/NUMTYPE
        COMMON/BLK4/TYPE
        COMMON/BLK5/NUMDIV
        COMMON/BLK7/XN(10),TMSTEP(10)

        WRITE(2,1)VERSION
1      FORMAT(1X,'DATA FILE FROM TMFCG VERSION ',A21,/)

        WRITE(2,4)MATL,NUMTYPE,TYPE
4      FORMAT(/, ' THERMOMECHANICAL',
& ' FATIGUE TEST PARAMETERS ',/,/

```

```

& 3X, ' MATERIAL: ',A25,/,
& 3X, ' TEST TYPE: #',I2,' - ',A21)

      IF(NUMTYPE.EQ.4) THEN

        WRITE(2,5) PA
5       FORMAT(6X, ' PHASE ANGLE = ',F6.2)

      ENDIF

      WRITE(2,6) TMTOT, TMUPLOAD, TMNONDEC
6      FORMAT(/,3X,
& ' TIME PARAMETERS: ',/,6X, ' TOTAL TIME OF TMF CYCLE',
& ' = ',F8.2, ' SECONDS',/,6X, ' TIME INTO CYCLE WHEN',
& ' THE ',/,6X, ' LOAD STOPS INCREASING',2X, ' = ',
& F8.2, ' SECONDS',/,6X, ' TIME INTO CYCLE WHEN THE ',/,
& 6X, ' LOAD BEGINS TO DECREASE = ',F8.2, ' SECONDS')

      IF(NUMTYPE.EQ.2) THEN

        TMHOLD=TMTOT-2*(TMTOT-TMNONDEC)

        WRITE(2,7) TMHOLD
7      FORMAT(6X, ' LENGTH OF HOLD AT P MAX = ',F8.2,
         & ' SECONDS')

      ENDIF

      WRITE(2,8) R,TMIN,TMAX
8      FORMAT(/,3X, ' LOAD PARAMETER: ',/,6X, ' LOAD RATIO',
& ' = ',F4.2,2(/),3X, ' TEMPERATURE PARAMETERS: ',/,6X,
& ' MINIMUM TEMPERATURE = ',F8.2, ' DEGREES C',/,6X,
& ' MAXIMUM TEMPERATURE = ',F8.2, ' DEGREES C')

      WRITE(2,9)
9      FORMAT(/, ' THE NUMBER OF INTEGRATION STEPS AND TIME STEP'
& ' SIZE',/, ' FOR EACH DIVISION OF THE TMF CYCLE ARE: ',2(/),
& 2X, ' DIV',3X, ' INT STEPS',3X, ' STEP SIZE (SEC)',/,,
& 3X,35('*'))

      DO 1000 J=1,NUMDIV

      WRITE(2,10) J,IFIX(XN(J)),TMSTEP(J)
10     FORMAT(3X,I2,6X,I6,6X,F9.5)

1000   CONTINUE

      WRITE(2,11)
11     FORMAT(2(/),4X, 'DELTA-K',6X, 'DADNTOT',7X, 'DADNCD',7X,
& 'DADNTD',/,3X,49('*'))

      RETURN
      END

C -----
C      Function CYCLEDEP calculates the cycle-dependent
C      damage term for a given delta K (DK) and test load

```

```

C      ratio (R) using the Paris Law. The Paris Law parameters
C      based on low temperature tests.
C      0.00833 Hz, 150 degrees C

      FUNCTION CYCLEDEP(DK,R,TMIN,TMAX,TMTOT,TMUPLOAD,TMNONDEC)
      REAL K, KMAX, KMIN, LAST
      COMMON/BLK6/TIME(10),DKPERC(10),DTPERC(10)
      COMMON/BLK7/XN(10),TMSTEP(10)
      COMMON/BLK8/DKSLOPE,DTSLOPE
      COMMON/BLK11/CHECK

C      Define the constants for the entire cycle.

C      Thi minimum K of the cycle is KMIN, and the maximum K of the
C      cycle is KMAX. The temperature range of the cycle, DT, is
C      the difference between TMAX and TMIN.

      KMAX=DK/(1.-R)
      KMIN=R*KMAX

      DT=TMAX-TMIN

C      Define the constants for the first division ( segment,
C      portion) of the cycle.

C      J is the cycle division counter. J will vary from 1 to
C      NUMDIV, the total number of divisions in the TMF cycle.

      J=1

C      The time step size, DTM, is defined as the time of the
C      integration segment divided by the number of time step
C      increments over that segment. The integrations are
C      typically stopped before the end of cycle is reached.

C      Note that DTM is not consistent with the use of DK or DT,
C      which both refer to ranges over the cycle.

C      Define DTM for the first portion (J=1) of the cycle.

      DTM=(TIME(1)-TIME(0))/XN(1)

C      Define the slopes of the DK vs. TM and the DT vs. TM
C      curves for the first segment of the cycle (J=1).

      DKSLOPE=DK*(DKPERC(1)-DKPERC(0))/(TIME(1)-TIME(0))
      DTSLOPE=DT*(DTPERC(1)-DTPERC(0))/(TIME(1)-TIME(0))

C      Initialize for the first segment of the cycle.

C      The initial time, stress intensity, and temperature are
C      determined. These are set to their values at J=0, which
C      defines the first endpoint of the first cycle increment.
C      This endpoint must be defined at TM=0.

      TM=0.
      K=KMIN+DK*DKPERC(0)

```

```

T=TMIN+DT*DTPERC(0)

C CYCLEDEP is set equal to zero initially. CYCLEDEP will be
C calculated (and subsequently summed) for each division of
C the cycle until TM reaches TMUPLOAD.

CYCLEDEP=0.0

C Set DADTPREV, da/dt for the previous (I-1) sample, equal
C to zero.

DADTPREV=0.0

C I is the time step counter. I is set equal to zero for the
C first integration step of each portion of the cycle. Here,
C I is set equal to zero only for the first division of the
C cycle.

C I will vary from 0 to (TIME(J)-TIME(J-1)/DTM).

800    CONTINUE

C Set all odd and even (except first and last) components of
C the Simpson's Rule summation to zero. This is required
C since summations start at SUMODD+(1st odd value) and
C SUMEVEN+(1st even value).

SUMODD=0.
SUMEVEN=0.

DO 110 I = 0, XN(J)

DADTCURR=CDDADT(DK,R,T,TMUPLOAD)

IF(DADTCURR.EQ.10.) THEN

CYCLEDEP=10.
GOTO 500

ENDIF

ADD=DADTCURR

C Perform the Simpson's rule summations: FIRST for the
C first term, LAST for the last term, SUMODD for the odd
C numbered terms (except the first), and SUMEVEN for the
C even numbered terms (except the last).

IF(I.EQ.0) THEN
FIRST=ADD

ELSEIF(I.EQ.IFIX(XN(J))) THEN

LAST=ADD

C MOD(I,2) checks whether the current counter is even or odd
C An even I will be returned as zero.

ELSEIF(MOD(I,2).EQ.0) THEN

```

```

SUMEVEN=SUMEVEN+ADD

ELSE

SUMODD=SUMODD+ADD

ENDIF

DADTPREV=DADTCURR

C      Increment the time step, the cycle division count (if
C      necessary), the time into cycle, the stress intensity
C      factor, and the temperature.

TM = TIME(J-1) + DTM * (I+1)
K = KMIN + DK * DKPERC(J-1) + (TM-TIME(J-1)) * DKSLOPE
T = TMIN + DT * DTPERC(J-1) + (TM-TIME(J-1)) * DTSLOPE

110    CONTINUE

C      Calculate the total cycle-dependent crack growth using
C      Simpson's rule.

CYCLEDEP=(DTM/3.)*(FIRST+4.*SUMODD+2.*SUMEVEN+LAST)+CYCLEDEP

TM=TIME(J)
IF(TM.LT.(TMUPLOAD-(DTM/10.)))THEN

DTM=(TIME(J)-TIME(J-1))/XN(J)
CALL INCREMNT(I,J,TM,DTM,K,DK,KMIN,T,DT,TMIN)
GOTO 800

ENDIF

DO 500 II = 1 , XN(J) * 5
C      I,J,TM,K, and T are incremented for the rest of the
C      cycle.

IF(TM.GE.(TMTOT-(DTM/10.))) GOTO 600

CALL INCREMNT(I,J,TM,DTM,K,DK,KMIN,T,DT,TMIN)

500    CONTINUE

600    RETURN
END

C -----
C      Function CDDADT calculates the instantaneous cycle-
C      dependent crack growth rate as a function of stress
C      intensity range, (DK), load ratio (R), temperature (T),
C      and loading time of the cycle (TMUPLOAD) using the
C      Paris law equation.

FUNCTION CDDADT(DK,R,T,TMUPLOAD)
COMMON/BLK12/DKTHRES
COMMON/BLK13/GAMMA

```

```

CALL CDPARPAR(CDCOFT,T,DKUPPER,DKTHRES)

C      If DK exceeds the experimental data range, set CDDADT equal
      IF(DK.GE.DKUPPER)THEN
          CDDADT=10.

C      If DK is less than the threshold value, there is no cycle-
C      dependent crack growth; CDDADT = 0.

      ELSEIF(DK.LE.DKTHRES)THEN
          CDDADT=0.

C      If DK is greater than threshold and less than the upper
C      limit of the data range, then the cycle-dependent
C      contribution to crack growth rate is computed using the
C      Paris law equation.

      ELSE

          CALL PARIS(CDCOFT,DK,CDDADN)
          CDDADT=CDDADN/TMUPLOAD

      ENDIF

      RETURN
      END

C -----
C      Subroutine CDPARPAR determines the Paris parameters for a
C      given material and load ratio, R. These parameters are
C      determined from low-temperature, high-frequency fatigue
C      tests and are used to establish the cycle-dependent
C      contribution to crack growth (damage). This subroutine is
C      called from the main program to establish the threshold
C      value of delta K, and is also called by the cycle-
C      dependent damage function, CYCLEDEP.

```

```

SUBROUTINE CDPARPAR(CDCOFT,T,DKUPPER,DKTHRES)

C      CDCOFT below is taken to be the lower than that of the isothermal 150 C
C      data. The cycle depedent damage is assumed to be temperature independent.

      CDCOFT = 7.9E-13

      DKUPPER = 120.0
      DKTHRES = 20.0
      RETURN
      END

C -----
C      Function TIMEDEP calculates the time-dependent damage term
C      for a given delta-K (DK), test load ratio (R), minimum
C      cycle temperature (TMIN), maximum cycle temperature (TMAX),
C      phase angle between load and temperature (PA), test
C      frequency (FREQ), and number of integration steps (XN).
C      The function integrates crack growth (da/dt)

```

C over the loading portion of the thermal-mechanical fatigue  
C cycle as the crack tip velocity is increasing using  
C Simpson's rule.

```
FUNCTION TIMEDEP(DK,R,TMIN,TMAX,TMTOT,TMUPLOAD,TMNONDEC)
REAL K,KMAX,KMIN,LAST
COMMON/BLK6/TIME(10),DKPERC(10),DTPERC(10)
COMMON/BLK7/XN(10),TMSTEP(10)
COMMON/BLK8/DKSLOPE,DTSLOPE
COMMON/BLK11/CHECK
COMMON/BLK13/GAMMA
```

C Define the constants for the entire cycle.

C The minimum K of the cycle is KMIN, and the maximum K of the  
C cycle is KMAX. The temperature range of the cycle, DT, is  
C the difference between TMAX and TMIN.

```
KMAX=DK/(1.-R)
KMIN=R*KMAX
```

```
DT=TMAX-TMIN
```

C Define the constants for the first division ( segment,  
C portion) of the cycle.

C J is the cycle division counter. J will vary from 1 to  
C NUMDIV, the total number of divisions in the TMF cycle.

```
J=1
```

C The time step size, DTM, is defined as the time of the  
C integration segment divided by the number of time step  
C increments over that segment. The integrations are  
C typically stopped before the end of cycle is reached.

C Note that DTM is not consistent with the use of DK or DT,  
C which both refer to ranges over the cycle.

C Define DTM for the first portion (J=1) of the cycle.

```
DTM=(TIME(1)-TIME(0))/XN(1)
```

C Define the slopes of the DK vs. TM and the DT vs. TM  
C curves for the first segment of the cycle (J=1).

```
DKSLOPE=DK*(DKPERC(1)-DKPERC(0))/(TIME(1)-TIME(0))
DTSLOPE=DT*(DTPERC(1)-DTPERC(0))/(TIME(1)-TIME(0))
```

C Initialize for the first segment of the cycle.

C The initial time, stress intensity, and temperature are  
C determined. These are set to their values at J=0, which  
C defines the first endpoint of the first cycle increment.  
C This endpoint must be defined at TM=0.

```
TM=0.
```

```

K=KMIN+DK*DKPERC(0)
T=TMIN+DT*DTPERC(0)

C      TIMEDEP is set equal to zero initially.  TIMEDEP will be
C      calculated (and subsequently summed) for each division of
C      the cycle until TM reaches TMNONDEC.

      TIMEDEP=0.0

C      Set DADTPREV, da/dt for the previous (I-1) sample, equal
C      to zero.

      DADTPREV=0.0

C      I is the time step counter.  I is set equal to zero for the
C      first integration step of each portion of the cycle.  Here,
C      I is set equal to zero only for the first division of the
C      cycle.

C      I will vary from 0 to (TIME(J)-TIME(J-1)/DTM).

800      CONTINUE

C      Initialize for the first calculation of each segment.

C      Set all odd and even (except first and last) components of
C      the Simpson's Rule summation to zero.  This is required
C      since summations start at SUMODD+(1st odd value) and
C      SUMEVEN+(1st even value).

      SUMODD=0.
      SUMEVEN=0.

      DO 110 I = 0, XN(J)

      DADTCURR = 1.70E-5 * EXP(-12000. / (T + 273.)) * (DK) ** 2.7

      IF(DADTCURR.EQ.10.)THEN

          TIMEDEP=10.
          GOTO 500

      ENDIF

C      If the crack tip velocity is decreasing, there is no
C      additional crack growth.

      IF(1.05*DADTCURR.LT.DADTPREV)THEN

          ADD=0.

      ELSE

          ADD=DADTCURR

      ENDIF

C      Perform the Simpson's rule summations: FIRST for the first

```

```

C      term, LAST for the last term, SUMODD for the odd numbered
C      terms (except the first), and SUMEVEN for the even numbered
C      terms (except the last).

      IF(I.EQ.0) THEN

         FIRST=ADD

      ELSEIF (I .GE. IFIX(XN(J))) THEN

         LAST=ADD

      ELSEIF (MOD(I,2).EQ.0) THEN

         SUMEVEN=SUMEVEN+ADD

      ELSE

         SUMODD=SUMODD+ADD

      ENDIF

      DADTPREV=DADTCURR

C      Increment the time step, the cycle division count (if
C      necessary), the time into cycle, the stress intensity
C      factor, and the temperature.

      IF (I .LT. IFIX(XN(J))) THEN

         TM = TIME(J-1) + DTM * (I+1)
         K = KMIN + DK * DKPERC(J-1) + (TM-TIME(J-1)) * DKSLOPE
         T = TMIN + DT * DTPERC(J-1) + (TM-TIME(J-1)) * DTSLOPE

      ENDIF

C      Return with new values of I, J, TM, K, and T for next
C      calculation of Simpsons Rule integration components.

110     CONTINUE

C      Calculate the total time-dependent crack growth using
C      Simpson's rule.
      TIMEDEP=(DTM/3.)*(FIRST+4.*SUMODD+2.*SUMEVEN+LAST)+TIMEDEP

      TM=TIME(J)
      IF(TM.LT.(TMNONDEC-(DTM/10.)))THEN
         DTM=(TIME(J)-TIME(J-1))/XN(J)
         CALL INCREMNT(I,J,TM,DTM,K,DK,KMIN,T,DT,TMIN)
         GOTO 800

      ENDIF

      DO 500 II = 1, XN(J) * 5

C      I,J,TM,K, and T are incremented for the rest of the cycle.

      IF(TM.LT.(TMTOT-(DTM/10.)))GOTO 600

      CALL INCREMNT(I,J,TM,DTM,K,DK,KMIN,T,DT,TMIN)

```

500 CONTINUE

600 RETURN  
END

C -----

```
SUBROUTINE INCREMNT(I,J,TM,DTM,K,DK,KMIN,T,DT,TMIN)
REAL K,KMIN
COMMON/BLK6/TIME(10),DKPERC(10),DTPERC(10)
COMMON/BLK7/XN(10),TMSTEP(10)
COMMON/BLK8/DKSLOPE,DTSLOPE
```

C Only increment the cycle division count if the current  
C time into the cycle exceeds the maximum time of the  
C J'th cycle division.

```
IF((TM+DTM).GT.(TIME(J)+(DTM/10.)))THEN
    TM=TIME(J)
    J=J+1
    DKSLOPE=DK*(DKPERC(J)-DKPERC(J-1))/(TIME(J)-TIME(J-1))
    DTSLOPE=DT*(DTPERC(J)-DTPERC(J-1))/(TIME(J)-TIME(J-1))
    DTM=(TIME(J)-TIME(J-1))/XN(J)
    I=0
    RETURN
ENDIF
```

C Increment the time step count, and time into cycle.

```
I=I+1
TM=TIME(J-1)+DTM*I
K=KMIN+DK*DKPERC(J-1)+(TM-TIME(J-1))*DKSLOPE
T=TMIN+DT*DTPERC(J-1)+(TM-TIME(J-1))*DTSLOPE

RETURN
END
```

C -----

C Subroutine PARIS uses a Paris law fit
C to calculate the crack growth rate, DADN, given the
C intensity range, DK, and the appropriate Paris coefficient.

C

```
SUBROUTINE PARIS(COFT,DK,DADN)
DADN = COFT * (DK) ** 2.7
RETURN
END
```

## VITA

Paul Andrew "Drew" Blatt was born in Huntington, West Virginia, on January 19, 1966. He graduated from Saint Joseph Central High School in 1984. In April of 1988, he received his Bachelor's degree in Aeronautical Engineering from Embry-Riddle Aeronautical University in Daytona Beach, Florida. Following this, he attended graduate school at Purdue University in West Lafayette, Indiana. In May of 1990, he was granted his Master's degree in Aeronautics and Astronautics. He continued his graduate work in the School of Aeronautics and Astronautics earning a Ph.D. in December, 1993.